PHYSICS OF SOCIAL INTERACTIONS

EDITED BY: Orit Peleg, Saad Bhamla, Alex Jordan, Tim Landgraf,
Natasha Mhatre and Laura Ann Miller
PUBLISHED IN: Frontiers in Physics

frontiers Research Topics

ISSN 1664-8714
ISBN 978-2-83250-428-4
DOI 10.3389/978-2-83250-428-4

About Frontiers

Frontiers is more than just an open-access publisher of scholarly articles: it is a pioneering approach to the world of academia, radically improving the way scholarly research is managed. The grand vision of Frontiers is a world where all people have an equal opportunity to seek, share and generate knowledge. Frontiers provides immediate and permanent online open access to all its publications, but this alone is not enough to realize our grand goals.

Frontiers Journal Series

The Frontiers Journal Series is a multi-tier and interdisciplinary set of open-access, online journals, promising a paradigm shift from the current review, selection and dissemination processes in academic publishing. All Frontiers journals are driven by researchers for researchers; therefore, they constitute a service to the scholarly community. At the same time, the Frontiers Journal Series operates on a revolutionary invention, the tiered publishing system, initially addressing specific communities of scholars, and gradually climbing up to broader public understanding, thus serving the interests of the lay society, too.

Dedication to Quality

Each Frontiers article is a landmark of the highest quality, thanks to genuinely collaborative interactions between authors and review editors, who include some of the world's best academicians. Research must be certified by peers before entering a stream of knowledge that may eventually reach the public - and shape society; therefore, Frontiers only applies the most rigorous and unbiased reviews.
Frontiers revolutionizes research publishing by freely delivering the most outstanding research, evaluated with no bias from both the academic and social point of view. By applying the most advanced information technologies, Frontiers is catapulting scholarly publishing into a new generation.

What are Frontiers Research Topics?

Frontiers Research Topics are very popular trademarks of the Frontiers Journals Series: they are collections of at least ten articles, all centered on a particular subject. With their unique mix of varied contributions from Original Research to Review Articles, Frontiers Research Topics unify the most influential researchers, the latest key findings and historical advances in a hot research area! Find out more on how to host your own Frontiers Research Topic or contribute to one as an author by contacting the Frontiers Editorial Office: frontiersin.org/about/contact

PHYSICS OF SOCIAL INTERACTIONS

Topic Editors:
Orit Peleg, University of Colorado Boulder, United States
Saad Bhamla, Georgia Institute of Technology, United States
Alex Jordan, Max Planck Institute of Animal Behaviour, Germany
Tim Landgraf, Freie Universität Berlin, Germany
Natasha Mhatre, Western University, Canada
Laura Ann Miller, University of Arizona, United States

Citation: Peleg, O., Bhamla, S., Jordan, A., Landgraf, T., Mhatre, N., Miller, L. A., eds. (2022). Physics of Social Interactions. Lausanne: Frontiers Media SA.
doi: 10.3389/978-2-83250-428-4

Table of Contents

frontiers in Physics

ORIGINAL RESEARCH
published: 07 June 2021
doi: 10.3389/fphy.2021.664948

A Study of Dramatic Action and Emotion Using a Systematic Scan of Stick Figure Configurations

Noa Raindel[1,2], *Yuvalal Liron*[1,2] *and Uri Alon*[1,2]*

[1] Theater Laboratory, Weizmann Institute of Science, Rehovot, Israel, [2] Department of Molecular Cell Biology, Weizmann Institute of Science, Rehovot, Israel

Comprehending the meaning of body postures is essential for social organisms such as humans. For example, it is important to understand at a glance whether two people seen at a distance are in a friendly or conflictual interaction. However, it is still unclear what fraction of the possible body configurations carry meaning, and what is the best way to characterize such meaning. Here, we address this by using stick figures as a low-dimensional, yet evocative, representation of body postures. We systematically scanned a set of 1,470 upper-body postures of stick figures in a dyad with a second stick figure with a neutral pose. We asked participants to rate the stick figure in terms of 20 emotion adjectives like sad or triumphant and in terms of eight active verbs that connote intent like to threaten and to comfort. The stick figure configuration space was dense with meaning: people strongly agreed on more than half of the configurations. The meaning was generally smooth in the sense that small changes in posture had a small effect on the meaning, but certain small changes had a large effect. Configurations carried meaning in both emotions and intent, but the intent verbs covered more configurations. The effectiveness of the intent verbs in describing body postures aligns with a theory, originating from the theater, called dramatic action theory. This suggests that, in addition to the well-studied role of emotional states in describing body language, much can be gained by using also dramatic action verbs which signal the effort to change the state of others. We provide a dictionary of stick figure configurations and their perceived meaning. This systematic scan of body configurations might be useful to teaching people and machines to decipher body postures in human interactions.

Keywords: social neuroscience, emotional body language, social psychology, human-computer interaction, emotion elicitation, physics of behavior, psychophysics

OPEN ACCESS

Edited by:
Orit Peleg,
University of Colorado Boulder, United States

Reviewed by:
Greg Stephens,
Vrije Universiteit Amsterdam, Netherlands
Yen-Ling Kuo,
Massachusetts Institute of Technology, United States
Moti Fridman,
Bar Ilan University, Israel

***Correspondence:**
Uri Alon
uri.alon@weizmann.ac.il

Specialty section:
This article was submitted to Social Physics, a section of the journal Frontiers in Physics

Received: *06 February 2021*
Accepted: *23 April 2021*
Published: *07 June 2021*

Citation:
Raindel N, Liron Y and Alon U (2021) A Study of Dramatic Action and Emotion Using a Systematic Scan of Stick Figure Configurations. Front. Phys. 9:664948. doi: 10.3389/fphy.2021.664948

INTRODUCTION

Body language pervades our lives. It helps us make sense of the state and intent of others and understand, from a distance, whether people are in a friendly or conflictual interaction. Despite its importance, we lack systematic ways to describe the meaning that body language carries. In other words, we lack ways to map the space of body configurations to fields of perceived meaning. A better understanding of body language is important for understanding basic neuroscience of how meaning is made [1–3], for improved human–machine interaction [4–11], and for training people to better understand body language.

What types of meaning are conveyed by body language is an open question. There are at least two main theories. One theory originates in psychology and considers body language as primarily expressing *emotions* [1–3, 12]. This emotional body-language theory takes ideas from the facial expression of emotion and applies them to research the perceived emotional meaning of body postures. Indeed, people can quickly understand emotion from a snapshot showing body postures, sometimes as rapidly and accurately as emotions are perceived from faces [13, 14]. Thus, according to the emotional body-language theory, body language primarily speaks in *adjectives*: happy, sad, triumphant, and sympathetic.

A second theory for body language is that it primarily conveys *dramatic actions*. A dramatic action is defined as the effort to change the state of another. Dramatic actions can be described by transitive verbs, such as to encourage, to comfort, to threaten, to scold. Unlike emotion adjective which define a state, dramatic action verbs define an effort to change the state of another. Dramatic action theory originates from the practice of theater [15], and was recently operationalized by Liron et al. [16]. Dramatic action theory and emotional body language theory are non exclusive: body language can carry both types of meaning.

Since the concept of dramatic action is not widely known in behavioral research, we provide a brief background. The field of theater often aims to create specific portrayals of human interaction. Accumulated experience shows that instructions for actors based on psychological factors such as emotion, motivation, and narrative are not enough to generate satisfactory performance [15]. Theater directors and actors rely on an additional layer, which is thought to be essential for creating believable interaction. This facet of behavior is dramatic action [17].

Dramatic actions are observable behaviors whose timescale is on the order of seconds. In this way, dramatic actions differ from internal motivations [18, 19], which last the entire play, and goals, which can last an entire scene. A character can change dramatic actions rapidly in an attempt to reach a goal. Dramatic actions are distinct from emotions because they are not states but instead are the efforts made to change the other's state. One can carry out a given dramatic action, such as threaten someone else, while experiencing different emotional states such as happy, angry, or sad.

Dramatic actions are related to a subset of Austin's concept of speech acts [20]. Many dramatic actions, however, are not speech acts, and in fact, do not require speech.

Dramatic actions need not necessarily succeed. An attempt to threaten or to comfort may or may not change the state of the other. Regardless of success or failure, one can still detect the effort made to change the state of the other: the dramatic action. Often, dramatic actions are part of people's habitual behavior and can be performed without conscious deliberation.

Dramatic actions can be conveyed by text: the same text can be said with different dramatic actions. For example, the text "come here" can have a different dramatic action if said by a parent soothing a child, or by a drill sergeant threatening a recruit. Dramatic actions are often conveyed through non-verbal signals including body language and gestures, facial expressions, speech, and physical actions. Even animals and babies can detect, carry out, and respond to dramatic actions [21]. Babies can activate surrounding adults and react to soothing voices; dogs can try to cheer people around them or threaten other dogs.

Currently, most research focuses on emotional body language theory, whereas the dramatic action theory has not been extensively tested. We set out to test both theories on the same stimuli in order to gain a more complete understanding of the range of meanings in body language.

Testing these theories requires a large and unbiased set of body posture stimuli in a social context. Most studies employ pictures of actors or cartoons which cover a small set of the range of possible postures. To obtain a systematic and unbiased set of body posture stimuli, we use stick figures. Stick figures represent the human body with a few angle coordinates [22–24]. By varying these angles, we systematically scanned 1,470 body configurations in a dyad of stick figures. Online participants scored these stick figure images for a set of eight dramatic actions and 20 emotions. Dramatic actions were found somewhat more frequently and strongly than emotions. From an applied point of view, we provide a dictionary of stick figure body postures with defined dramatic action and emotional meanings, which may be useful for research and automated image understanding, and for training people to understand body language.

METHODS

Stick Figures

We defined stick figures (SF) made of nine line segments and a circle (**Figure 1A**), representing two-segment legs (length 0.283 each, in units where SF height is 1), a torso (0.364, including a neck of length 0.055), two-segment arms (0.224 each), and a head (radius 0.07). The segment proportions were taken from average adult anthropometric proportions [25]. There was no representation of ankles, wrists, hands, shoulders, face, etc. The SF configurations were defined by five angles: the angles of the torso, two shoulders, and two elbows (**Figure 1A**). We discretized these angles in order to sample the SF configuration space: The torso angle θ_1 had two values: vertical to the floor and leaning to the left at 30°. The shoulder angles θ_2, θ_4 each had six options: 90°, 135°, 165°, 195°, 225°, and 270° relative to the neck, clockwise. The elbow angles θ_3 and θ_5 had seven values: 45°, 90°, 135°, 180°, 225°, 270°, and 315° relative to the arm, clockwise. The number of values for each angle was chosen based on pilot studies to allow for completeness at a reasonable survey size. The legs were not varied in order to allow a feasible survey size, despite the expressiveness of leg posture such as kneeling. Angle combinations in which two segments exactly overlapped were removed. Only unique configurations were included (no two sets of angles yielded the same SFs), resulting in 1,470 unique SFs.

Each stimulus included two SFs (**Figures 1B,C**). The SF with different configurations was on the right, and the SF on the left

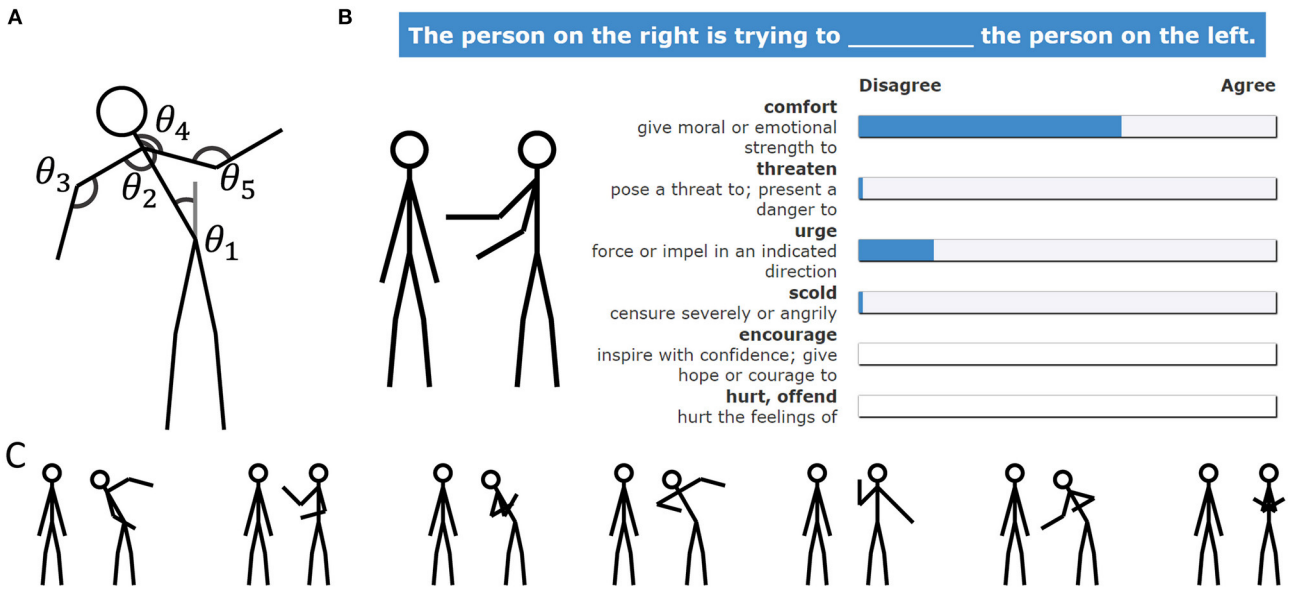

FIGURE 1 | Stimuli and survey designs. **(A)** Stick figure configurations are defined by five angles. Scanning these angles at a set of values yielded 1,470 unique SF configurations. **(B)** Schematic of the survey: A stick figure dyad was presented, in which the right SF configuration was one of 1,470 possibilities and the left SF was in a neutral configuration. Online participants marked their agreement level for completing a sentence with each of the eight DA verbs (or, in experiments 2 and 3, with emotion adjectives). **(C)** Seven typical stimuli from the set of 1,470.

had the same configuration in all images with $\theta_1 = 0°$, $\theta_2 = 195°$, $\theta_3 = 180°$, $\theta_4 = 165°$, $\theta_5 = 180°$. The distance between the two SFs was 0.55 when the right torso was upright ($\theta_1 = 0°$) and 0.64 when the right SF torso leaned to the left ($\theta_1 = 30°$). The latter distance was used to avoid contact between the SFs.

Sampling and Participants

A total of 816 (56% female) participants, recruited on the Amazon Mechanical Turk platform [26], answered the survey (324, 470, and 558 in experiments 1, 2, and 3, respectively). The survey was limited to US residents who passed an English test, with at least 100 previously approved surveys on Mechanical Turk. For every combination of a word and an image, we obtained answers from 20 different participants. The experiment was approved by the institutional review board of the Weizmann Institute of Science, Rehovot, Israel. Informed consent was obtained from all participants before answering the survey.

Survey Design

In order to avoid priming participants with dramatic actions (DA) and emotions in the same experiment, we performed separate experiments: experiment 1 for DAs, experiment 2 for basic emotions [15], and experiment 3 for social emotions. In experiment 2, we asked both for the emotion of the right SF and for the emotion of the left SF. In this analysis, we focus on the right SF. Experiment 2 was completed 4 months after experiment 1. Experiment 3 was completed 12 months after experiment 1.

The participants were shown an image of two SFs and were asked to rate how well a word completes a sentence describing the image (**Figure 1B**). The rating used a continuous "agree-disagree" slider scale. Instructions for experiment 1 (on DAs) were as follows:

"You are about to see 14 images. After viewing each image, press continue. Then, you will see the same image on the left, together with nine possible suggestions for completing the statement below, and nine bars on the right (see example). Use the bars to indicate your agreement with each statement so that it correctly describes the image, as you see it. The next image will be available only after you marked your answers in the nine bars. *"The person on the right is trying to _____ the person on the left".*"

We chose a set of DA verbs based on a previous study of 22 verbs presented with cartoon/clipart stimuli [16]. We chose verbs that were strongly perceived by participants in Liron et al. [16] and omitted verbs that were synonyms, to arrive at a list with eight DA verbs. The eight DA verbs were encourage, support, comfort, urge, hurt, bully, scold, and threaten. These eight verbs and one attention check question were provided in a random order for each image. The attention check question asked the participants to mark one of the ends of the slider scale ("agree" or "disagree").

The structure of experiment 2 was very similar to that of experiment 1 (**Supplementary Figure 1**). Instructions for experiments 2 and 3 (on emotions) were identical to experiment 1, except for six emotion adjectives instead of eight DA verbs, and the sentence *"The person on the right is feeling _____."* or "*The person on the left is feeling _____.*" The images were

identical to experiment 1, except for a small arrow indicating the SF on the right or left (**Supplementary Figure 1**). The six emotion adjectives were happy, sad, disgusted, angry, surprised, and afraid. These emotion adjectives are commonly used in emotional body language research [27].

Experiment 3 tested an additional 14 emotions that have been most commonly used in recent studies on emotions [28–31], including social emotions: amusement, awe, confusion, contempt, love, shame, sympathy, compassion, desire, embarrassment, gratitude, guilt, pride, and triumph. The basic emotion angry was used as a control to compare with the results of experiment 2.

The "agree-disagree" slider scale had no initial value. The participants had to click on the slider in order to mark their score. The scale position indicated by the participants was converted to a number between 0 (disagree) and 100 (agree) for analysis.

One unit of the survey was a sequence of 14 images in random order. Experiment 1 had 2,100 units and experiments 2 and 3 had 4,200 units. For each of the 14 visual stimuli, the participants were first presented with a stimulus at the center of the screen, and after clicking on the "next" button, the eight DA verbs or six to eight emotion adjectives and an attention check question were added, arranged in random order (**Figure 1B**, **Supplementary Figure 1**).

Data and Statistical Analysis

We removed 36 units in which a respondent failed the English test or answered more than one unit in an hour. The units in which the participants failed two or more attention check questions were removed (47/2,100, 171/4,200, and 189/4,200 of the units in experiments 1, 2, and 3, respectively, which make up 3.9% of the total units). Thus, 2,049, 2,016, and 4,011 units (of 14 images) entered the analysis for experiments 1, 2, and 3, respectively. In total, we analyzed 229,488 word–image responses for experiment 1, 337,764 for experiment 2, and 444,080 for experiment 3. The scores in these experiments showed a distribution with a peak at zero. We counted an identified word as a median score above 50, which is the midpoint between disagree and agree.

To compute the probability that a median score exceeds 50 by chance, we used bootstrapping. For each image and word, we generated 10^4 bootstrapped datasets as follows: for each participant that answered the question, we chose an answer at random from the set of all answers provided by that participant in the experiment (without attention checks). This preserves the response statistics of each participant. We found that the probability that the median score of at least one word–image pair in an image exceeded 50 in the bootstrapped data is 0.0146 for DA and $1.9{\cdot}10^{-4}$ and $1.1{\cdot}10^{-4}$ for basic and social emotions of the right SF, respectively.

For data clustering, we used the clustergram function in MATLAB R2017b (MathWorks) with correlation distance and clustering along the rows of data only.

RESULTS

Stick Figure Stimuli

In order to generate a systematic and unbiased set of stimuli, we defined stick figures (SFs) with five degrees of freedom (**Figure 1A**). We kept the legs in a fixed configuration to focus on upper body postures, which can show all emotions [32] and cover the affected space [33]. To focus on body posture and not facial expressions, the SF "head" was a circle.

In order to sample the SF configuration space, we discretized the angles, with two values for the torso angles, six for the shoulder angles, and seven for the elbow angles (**Figure 1A**). This resulted in 1,470 unique SF configurations (Methods).

To study the body posture of an SF interacting with another SF, we used images that showed two SFs (**Figures 1B,C**). The right SF had one of the 1,470 configurations, and the other had a constant neutral position.

Surveys of DA and Emotion

The online participants identified DA and emotion words for the SF dyads. We count a word as identified for a given image if its median score between participants exceeds a threshold of 50, which is the midway point between disagree (0) and agree (100). The results are robust to changes of this threshold (**Supplementary Figures 2, 3**). We find that the participants identified at least one DA or emotion in 54% of the images (798/1,470).

Participants identified at least one DA verb for 40% (591/1,470) of the images (**Figure 2A**), with an average of 1.7 DA verbs per image. A total of 57% of these images had one reported DA, 20% had two reported DAs, and 23% had three or more reported DAs (**Supplementary Figure 4**).

The participants identified at least one emotion word for 29.4% (432/1,470) of the images (**Figure 2A**), with an average of 1.4 emotion words per image. A total of 63% of these images had one reported emotion, 30% had two reported emotions, and 7% had three or more reported emotions.

The participants identified DAs but not emotions in 361 images and identified emotion but not DA in 207 images (**Figure 2B**). In general, the scores for DA were higher than the scores for emotions (Wilcoxon–Mann–Whitney test, $U > 10^6$, $p < 10^{-22}$ two-tailed, **Figure 2C**).

A potential concern is that the comparison was across participants rather than within participants. To address this, we repeated the analysis for a subset of $n = 68$ participants who participated in both experiments 1 and 2 and answered the surveys for DA and emotion for the same images. We find qualitatively similar conclusions: DAs were identified in 75% of images, emotions in 56% (one-sided paired t-test $p < 10^{-8}$). The number of cases where DA was identified but not emotion was 3.1-fold higher than the number of cases where emotion was identified but not DA (one-sided paired t-test $p < 10^{-8}$) (**Supplementary Figure 5**).

We conclude that the participants identified DAs and emotions in about half of the SF dyads. Both DAs and emotions were found frequently. DAs were perceived somewhat more frequently and strongly. To test how strongly the emotions and

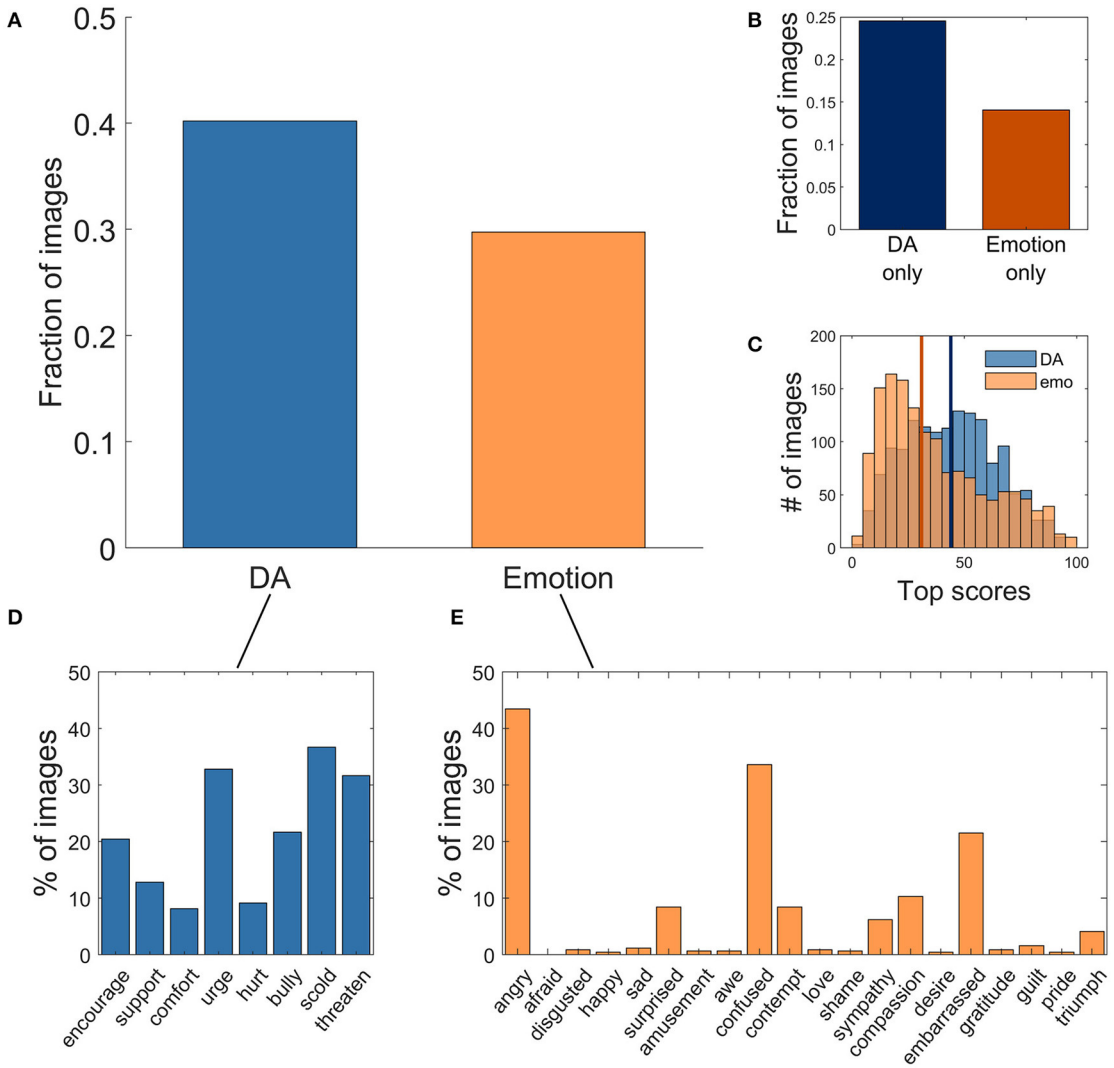

FIGURE 2 | Dramatic actions and/or emotions were found in most images, with the former found somewhat more frequently and strongly. **(A)** Fraction of the 1,470 images identified with at least one DA (blue) and at least one emotion (orange). **(B)** Fraction of images identified with at least one DA but no emotion, and at least one emotion but no DA. **(C)** Distribution of top scores. We compare the eight DA words with the eight emotion words that received the highest scores (angry, confused, surprised, contempt, embarrassed, compassion, triumph, sympathy). The distribution of the highest scores of DA words (median = 44) is different from the distribution of the highest scores of emotion words (median = 31), (Wilcoxon–Mann–Whitney $U > 10^6$, $p < 10^{-22}$ two-tailed) with a large effect size (AUC = 0.61). Vertical lines show the median of each distribution. **(D)** Percent of images, out of the images identified with at least one DA, that were identified with each of the eight DA verbs. For example, the DA 'encourage' was identified in 128 images out of the 591 images where at least one DA was identified. Note that the images were often identified with several DAs so that the histogram sums to more than 100%. **(E)** Percent of images, out of the images identified with at least one emotion, which were identified with each of the twenty emotion adjectives.

DAs are correlated, we performed regression analysis. Emotion scores were found to be able to predict 54 ± 17% of the variance of each DA verb. Conversely, DA scores were found to be able to predict 24 ± 20% of the variance of each emotion (mean ± STD, full results in **Supplementary Tables 1**, **2**). Thus, while emotions and DAs are correlated to a certain extent, the concepts are distinct [16]; both DAs and emotions are required to cover the image dataset.

Prevalence of Different DAs and Emotions

Of the 20 emotions describing the SFs, several emotions were found much more often than others: The top three emotions were angry, confused, and embarrassed, which were found in 21–44% of the images. Other emotion adjectives were rarely found, with 13 of the emotions assigned to <5% of the images (**Figure 2E**). Note that each image could be described with multiple words so that the fractions of images do not sum up to 100%.

In contrast, different DAs were identified with roughly similar frequencies (**Figure 2D**) in the range of 8–37%. Thus, the present set of DA verbs seems to allow for a more refined differentiation between these images than the present set of emotion adjectives.

In order to visualize the data, and to further see the relationship between DAs and emotions, we clustered the

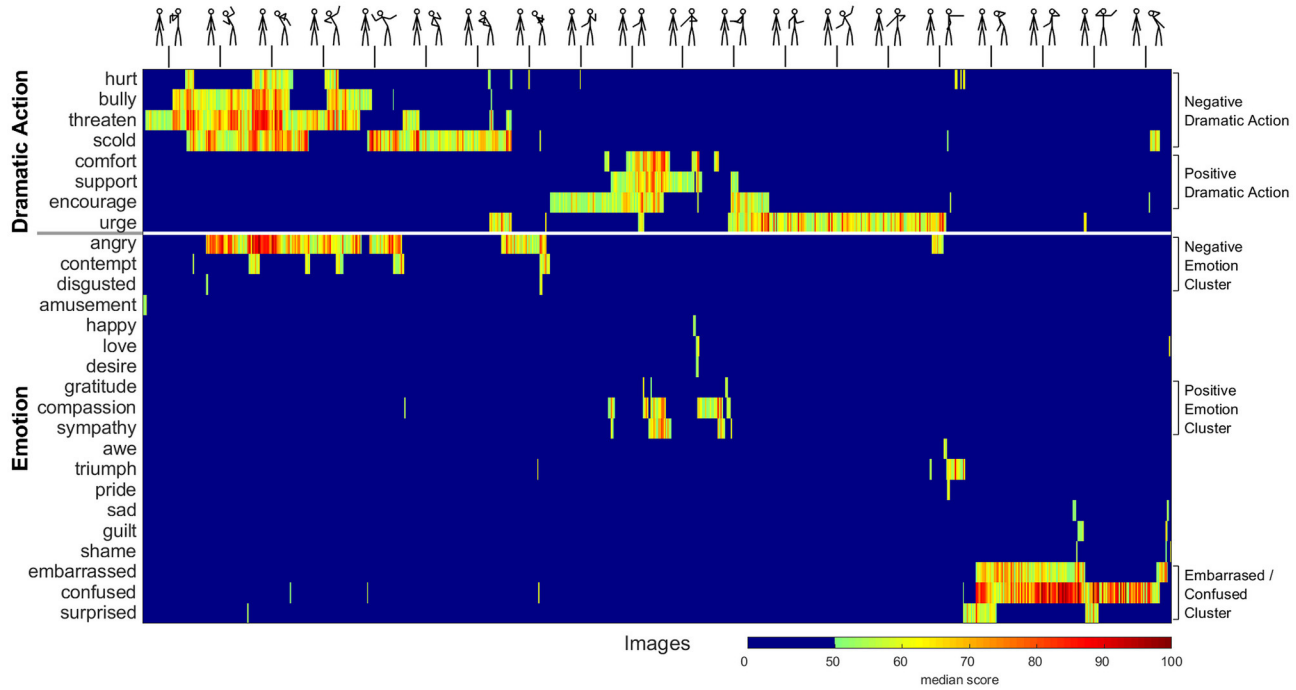

FIGURE 3 | Clustergram of all 798 images identified with at least one DA or emotion. Each column represents a single image, and each row represents a DA or emotion word, arranged by clustering. Hence, images with similar scores are placed adjacently, and DAs found in similar images are placed adjacently. Color represents median score (median scores below 50 are in blue).

images and the agreement scores (**Figure 3**). In the resulting clustergram, images with similar response scores (scores for DAs and emotions) are placed near each other [dendrogram presented in SI (**Supplementary Figure 6**)]. Similarly, DAs or emotions found in similar images are placed near each other.

We find that DAs cluster into two groups, which can be seen as two large, colored regions in the upper part of the clustergram (**Figure 3**). These groups are the negative DAs (bully, threaten, scold, and hurt) and the positive DAs (comfort, encourage, and support). The division into positive and negative valence groups is also noticeable when clustering the correlation vectors of the scores of all of the 1,470 images (**Supplementary Figure 7**). The notion of negative and positive valence for DAs is further supported by principal component analysis of the images based on their DA scores (**Supplementary Figure 8**), which shows that the first principal axis goes from the most negative to most positive in the following order: threaten, scold, bully, hurt, urge, comfort, support, encourage. The DA "urge" seems to be placed between the negative and positive valence.

Each DA has images in which it is found alone or in combination with other DAs of similar valence. For example, threaten and bully often go together (120 images). Negative DAs were never found together with positive DAs in the same image.

The bottom part of **Figure 3** shows that the emotion scores are sparser than DA scores as mentioned above, with 70% of the images showing scores below 50 for all emotions. We find that images with negative DAs are most often identified with the emotion angry (156/295 images).

Images with positive DAs (154 images) are more rarely identified with emotion; only 36 of them are identified with sympathy or compassion. A final cluster of images was scored with the emotions embarrassed and confused, usually without a DA.

We repeated the clustering analysis for all 1,470 images, without zeroing out median scores smaller than 50 (**Supplementary Figure 9**). The clustergram shows similar results; images identified with DAs are clustered in two groups of positive and negative valence, and DA scores are generally higher than emotion scores.

We conclude that both emotions and DAs are needed to fully describe the images, and that people can differentiate between DAs in the present set of stimuli to a greater extent than they can differentiate between emotions.

Mapping of Body Configuration Space to DA and Emotion

We next asked about the relationship between the SF body coordinates and the emotion and DA responses. For this purpose, we display all of the 1,470 SF configurations in a set of panels (**Figures 4A–D**).

Figure 4 displays all possible angle configurations in the study; it is a complete display of the five-dimensional stick figure configuration space. There are 5 right shoulder × 5 left shoulder × 7 right elbow × 7 left elbow × 2 torso combinations. These are displayed in a hierarchical manner. There are two columns (each for a torso angle). Each column has two subfigures, one

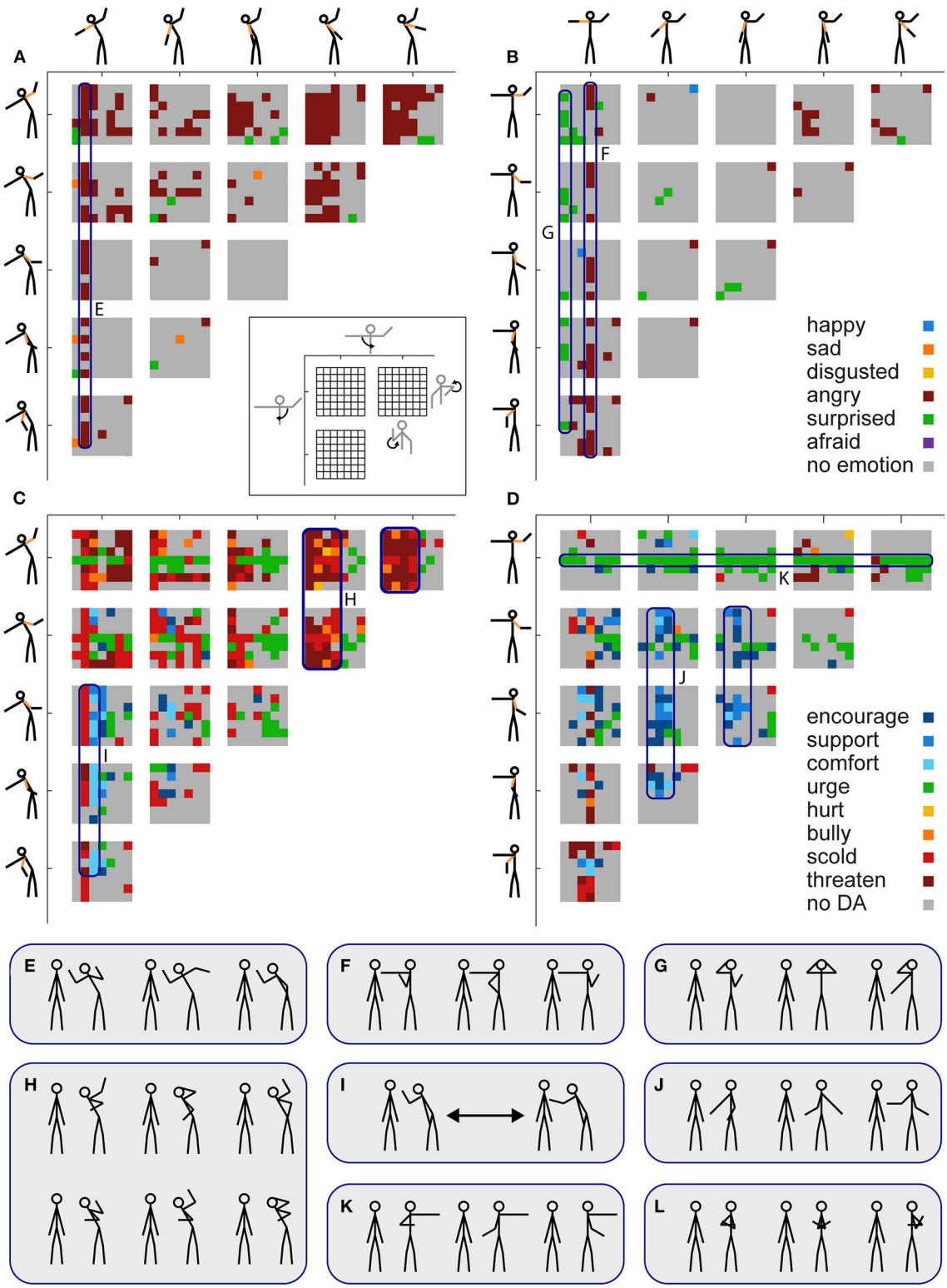

FIGURE 4 | Regions of SF configuration space map to specific emotions and DAs. All 1,470 SF configurations are displayed in a set of panels, arranged as follows. **(A,B)** indicate tilted and upright torso, respectively. The 5 × 5 combinations of the right and left shoulder angles correspond to 25 matrices, of which 15 are shown due to symmetry. Each matrix corresponds to the 7 × 7 elbow angles (axes in inset). SF configurations are color-coded according to the emotion adjective with the highest score for each image. Images in which no emotion word score exceeded 50 are in gray. **(C,D)** Same as above except that configurations are color-coded

(Continued)

FIGURE 4 | according to the DA with the highest score for each image. Images in which no DA score exceeded 50 are in gray. **(E)** A group of SFs showing the emotion angry is tilted toward the second SF with an arm at 90° and an elevated forearm (elbow at 90°). **(F)** Angry is identified in an upright position and a straight horizontal arm toward the second SF. **(G)** Upright posture together with a hand touching the head is usually identified with the emotion surprise. **(H)** Many negative DAs are identified in "W-shape" configurations, in which the elbows are high and form sharp angles. **(I)** A change of one angle (the elbow, from raised hand to low hand) transforms the score from negative valence (left) to positive valence (right). **(J)** Positive valence DAs are identified with upright configurations with low hands. **(K)** Urge is identified with a posture of horizontal arm pointing away from the second SF. **(L)** SFs with the arms crossed are often identified with the emotion angry, and with the DA scold. The figures in **(E–L)** are examples selected manually.

for emotions and the other for DA. Each subfigure shows all the arm configurations; these are ordered into 25 small matrices (5×5 shoulder configurations), but only 15 are displayed due to symmetry. Each small matrix shows the 7×7 elbow configurations.

We begin with emotions (**Figures 4A,B**) by coloring each SF configuration according to the strongest emotion identified for the right SF (gray squares have no emotion scores above 50). For simplicity, we consider the six basic emotions (happy, sad, disgusted, angry, surprised, and afraid). We find that the adjective angry is elicited primarily (77%) by the torso tilted toward the other (**Figure 4A**). It is most prevalent with one arm raised backwards at angle of 90° with respect to the torso (**Figure 4A**, upper row of panels). Another group of angry SFs with a tilted torso have a raised arm toward the other SF and the elbow is at 90° (**Figure 4E**). In SFs with an upright torso, angry is found in a stripe in which $\theta_2 = 270°$ and $\theta_3 = 180°$, where a straight horizontal arm points toward the second SF (**Figure 4F**).

The next most common emotion of the six, surprised, is identified primarily in upright SFs, with a symbolic gesture of hands touching the head (**Figure 4G**). The three SFs with the highest scores for each emotion are shown in **Figure 5A**.

We next consider the DAs assigned to the SF configurations (**Figures 4C,D**). We find that negative DAs are found primarily with the torso tilted toward the other (**Figure 4C**), especially with arms held high and away from the other in a W-like shape (**Figure 4H**). Another region with negative DAs has an arm directed toward the other with the elbow at 90° (**Figure 4I**, left). Interestingly, a move of a single angle (elbow) in this region changes the DA to a positive one (**Figure 4I**, right). This is an example of a small angle change that generates the opposite meaning. With an upright torso, negative DAs are found, for example, in a stripe with one arm pointing directly at the other, perhaps in a symbolic gesture (**Figure 4F**).

Positive DAs are elicited primarily by upright SFs with at least one arm toward the other, with an elbow angle of more than 90° (**Figure 4J**).

The DA urge, which has a neutral valence, is primarily elicited by SFs with one arm pointing horizontally away from the other SF (**Figure 4K**). This may correspond to a symbolic representation. The three SFs with the highest scores for each DA are shown in **Figure 5B**.

Although DAs were identified in more images than emotions, there are cases in which emotions were identified but not DAs. These include 33 images identified with the emotion surprised. Many of these images show SFs with at least one hand touching the head (**Figures 4B,G**). This may correspond to a symbolic representation of surprise. Another class of SFs was identified with the emotions angry and disgusted and with no DA or the DA scold. These configurations include SFs with arms crossed (**Figures 4L**, **5**). Thus, emotion and DA can serve as complementary approaches to understanding dyadic images.

For completeness, we show in the SI two additional versions of this figure. The first version (**Supplementary Figure 10**) shows the strongest emotions and DAs for all SFs, not just those with a score higher than 50. The second version (**Supplementary Figure 11**) shows the second strongest word for each stick figure.

DISCUSSION

To study the meaning of body language in terms of emotion and dramatic action, we developed a method to generate a large and unbiased dataset of body postures: a systematic scan of stick figure configurations, in a dyad where one stick figure had varying upper body configurations and the other had a neutral stance. We asked the online participants to score the images in terms of 20 emotions and eight dramatic action verbs. We find that 40% of the images were scored with dramatic actions and 29% were scored with emotions. All eight dramatic actions were found in many different images, but among the emotions, angry, confused and embarrassed were much more common than the others. We conclude that both emotions and dramatic actions are needed to understand body language. Thus, dramatic actions, which are verbs that describe the effort to change the state of another, can add to our set of concepts for the meanings of body language and complement the more widely tested emotions.

This unbiased scan of stick figure configurations confirms that stick figures are evocative stimuli: a dramatic action or emotion was identified in 54% of the images. This agrees with previous research that shows that people are able to make sense of stick figures or other schematic representations of agents [6, 34–36]. The full dictionary of the 1,470 stick figure images and their dramatic action and the scores of the six basic emotions is provided in the SI (**Supplementary Figure 12**).

Dramatic actions elicited somewhat stronger and more expressive signal than emotions in the present dataset. This may be due to the focus on body configuration rather than faces. Faces are the stimuli most commonly used to study the expression of emotion [2, 37–42]. The present list of eight dramatic action verbs can be extended to include additional dramatic actions, for example, from the list of 150 dramatic actions complied in Liron et al. [16].

The systematic scan of body configurations allowed us to ask about the continuity of the relationship between body

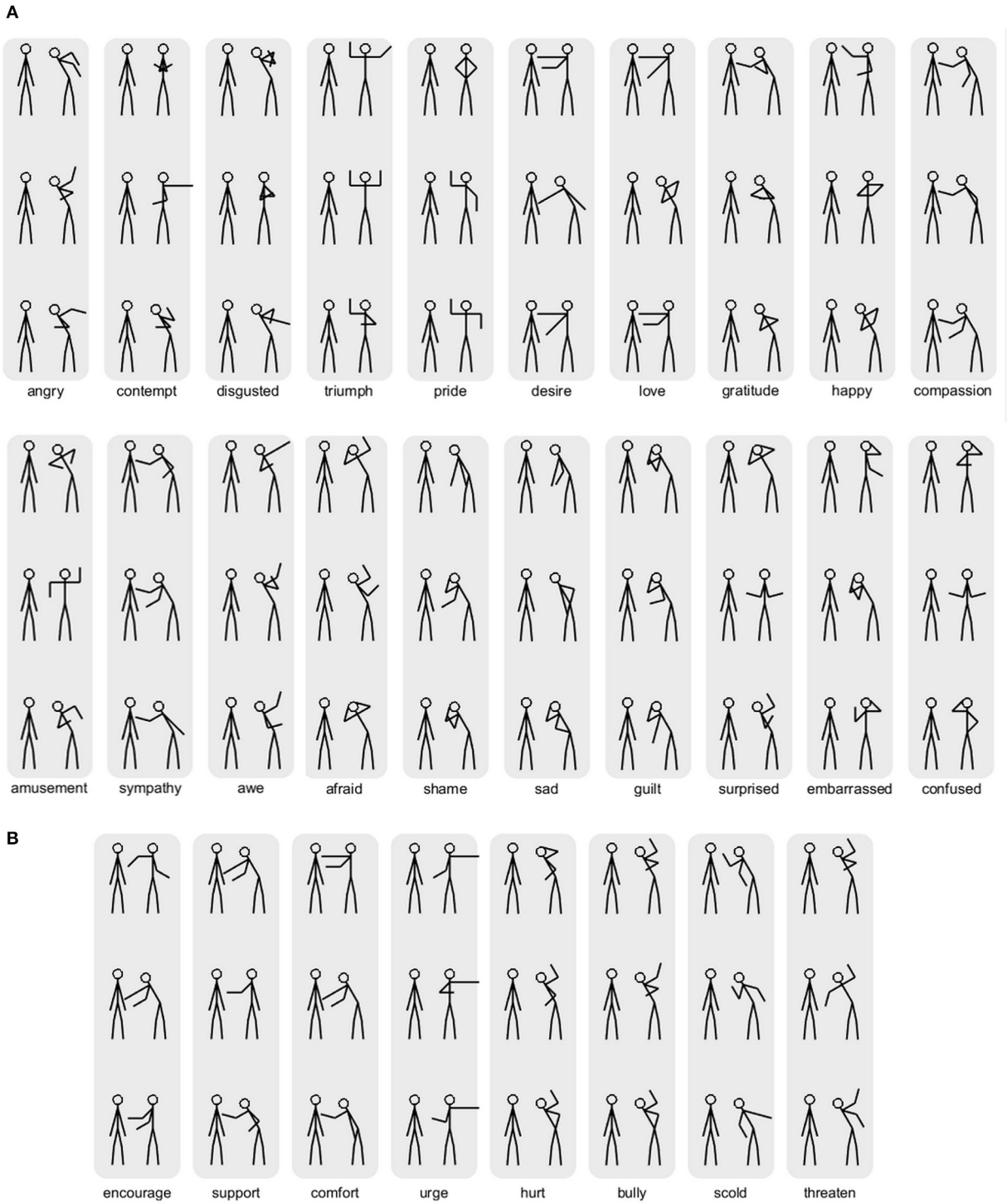

FIGURE 5 | Top images for each emotion and dramatic action. **(A)** The three top-scoring images for each emotion. For afraid (all top three images) and for the third strongest of happy and pride, the top images did not exceed a median score of 50. **(B)** The three top-scoring images for each dramatic action.

coordinates and emotions/dramatic actions. We find that similar stick figure configurations often have similar dramatic actions (**Figures 4C,D**). A wide class of configurations with the arms raised, especially with elbows at sharp angles (W-configurations, **Figure 4H**), are identified with negative dramatic actions such as bully and threaten [43]. These configurations hint at tensed

muscles. Positive dramatic actions are identified most often for configurations in which there is an arm toward the other stick figure with an elbow angle above 90° (**Figure 4J**).

There are interesting boundaries in the stick figure configuration space in which changing a single angle can change the dramatic action from positive to negative valence. For example, on the arm directed toward the other, changing the elbow angle [44] from 135° (low hand) to 90° (raised hand) can change the dramatic action valence from positive to negative (**Figure 4I**). In other cases, the configurations seem to resemble symbols, where there are one or two angles whose precise value is essential for the meaning (changing these angles changes the scoring), while other angles can be changed widely without a change in the scoring. For example, configurations in which one arm touches the head are identified with surprise, regardless of choices of the other angles (**Figure 4G**). One arm directed horizontally toward the other stick figure or hands crossed away from the other stick figure are often identified with anger (**Figure 4F**), whereas an arm directed horizontally away from the other stick figure is identified with the dramatic actions urge, despite changes in the other angles (**Figure 4K**).

The stick figures with negative dramatic actions most often (83%) had the torso leaning toward the other stick figure. Previous studies have shown contrasting findings regarding the emotional valence of leaning forward, which was identified with positive [45] or negative [34, 46, 47] valence. In comparing these results, it is important to note that the present study uses an unbiased scan of stick figure configurations, which may include configurations not sampled in other studies.

How do dramatic actions work? How does body language act to change the state of the other? One might speculate about at least two possible mechanisms, one for situations of cooperation and the other for those of competition. In a cooperative mode, dramatic actions may rely in part on the human tendency to mirror the other [48–50]. Dramatic actions can work by assuming a body configuration similar to that desired in the other, hoping to entrain the muscular system of the other [51–53]. For example, the dramatic action comfort aims to reduce the arousal and negative emotion of the other. The stick figures with this dramatic action have arms at a low position, which indicates relaxed muscles. If the entrainment is successful, the other will also relax their muscles, hopefully inducing a relaxed emotional state. In real life, to perform this dramatic action, one tends to relax the chest muscles by breathing deeply and lowering the pitch of voice, and so on.

In a competitive mode, negative dramatic actions may work by enlarging the body, a common strategy used by animals to appear more formidable [54]. An example is the W-configuration stick figures with the arms raised above the shoulder and away from the other (**Figure 4H**). Negative dramatic actions also involve configurations with activated muscles in the arms and torso [**Figures 4H,I** (left)], which may indicate readiness to attack.

In this study, the dataset of stick figures is limited in order to maintain a feasible number of configurations. The study focuses only on variations in the upper body, with a constant distance between the figures, and in each dyad the receiving stick figure is kept neutral. The study can be extended to a wider range of stick figure space, including changes in the configuration of the second stick figure in the dyad, changes in distance between the stick figures, changes in leg coordinates, and scanning more values for each angle. This can impact the range of dramatic actions and emotions found. For example, adding changes in the leg coordinates can allow kneeling figures, which can access dramatic actions with aspects of dominance such as "to beg" and "to flatter." Examples of such stick figures are provided in the SI (**Supplementary Figure 13**). Adding features such as facial expression, wrists, fingers, or indicators of gaze direction is also needed for a more complete study. Using realistic silhouettes instead of stick figures can help viewers better understand 3D postures. The study can be extended to include motion, which adds important information for the perception of action [55–61]. This study used respondents from one country (United States), and testing in other countries can help resolve how culture can make a difference [62, 63], for example, in symbols.

The present methodology allows further research to address several questions. How would the results change if the neutral stick figure were not present? What happens if participants are able to manipulate the pose directly, perhaps with a prompt to produce a particular emotion or dramatic actions? Could one direct human actors to create particular emotion/action states and then capture these states using machine vision tools? If so, would these states overlap with the states identified in the current manuscript? Another interesting question is whether the semantic relationship in the space of words corresponds to relationships in the space of stick figures. One such analysis could compute the distance between the words using WordNet or other word embeddings and check if this distance is related to distances in the space of stick figures.

We hope that the present dataset serves as a resource for further studies, for example, as stimuli for neuroscience experiments on the perception of dramatic actions or for training human recognition of dramatic actions. The top-scoring images for each dramatic action and emotion can be used as potentially strong stimuli, and the stick figures with weaker scores can be used for tests of individual differences in perception. The dictionary can also be used to label images or videos with dramatic actions and emotions by extracting stick-figure skeletons from the images using pose estimation algorithms and matching them to the present stick figure collection. It would be fascinating to learn which brain circuits perceive dramatic actions, and what cultural, situational, and individual factors contribute to how people make sense of body language.

DATA AVAILABILITY STATEMENT

The datasets generated for this study can be found in online repositories. The names of the repository/repositories and accession number(s) can be found in the article/**Supplementary Material**.

ETHICS STATEMENT

The studies involving human participants were reviewed and approved by the institutional review board of the Weizmann Institute of Science, Rehovot, Israel. The participants provided their written informed consent to participate in this study.

AUTHOR CONTRIBUTIONS

NR, YL, and UA designed the study, wrote and revised the manuscript. NR carried out online surveys. NR and YL wrote the software and analyzed the data. All authors contributed to the article and approved the submitted version.

FUNDING

Braginsky Center for the Interface between Science and the Humanities, at the Weizmann Institute of Science. The funder had no role in the design or conduct of this research.

ACKNOWLEDGMENTS

The authors thank the Braginsky Center for the Interface between Science and the Humanities, at the Weizmann Institute of Science, for support. The authors thank Yuval Hart, Yael Korem, Avi Mayo, Ruth Mayo, Michal Neeman, Lior Noy, Tzachi Pilpel, Itamar Procaccia, Hila Sheftel, Michal Shreberk, Daniel Zajfman, and the members of the Alon lab for fruitful discussions and their comments on the manuscript.

SUPPLEMENTARY MATERIAL

The Supplementary Material for this article can be found online at: https://www.frontiersin.org/articles/10.3389/fphy.2021.664948/full#supplementary-material

REFERENCES

1. de Gelder B. Towards the neurobiology of emotional body language. *Nat Rev Neurosci.* (2006) 7:242–9. doi: 10.1038/nrn1872
2. de Gelder B. Why bodies? Twelve reasons for including bodily expressions in affective neuroscience. *Philos Trans R Soc B Biol Sci.* (2009) 364:3475–84. doi: 10.1098/rstb.2009.0190
3. Kret ME, Pichon S, Grèzes J, de Gelder B. Similarities and differences in perceiving threat from dynamic faces and bodies. An fMRI study. *Neuroimage.* (2011) 54:1755–62. doi: 10.1016/j.neuroimage.2010.08.012
4. Metallinou A, Lee CC, Busso C, Carnicke S, Narayanan, et al. The USC CreativeIT database: a multimodal database of theatrical improvisation. In: *Multimodal Corpora: Advances in Capturing, Coding and Analyzing Multimodality*. Valletta: Springer (2010). p. 55.
5. Beck A, Cañamero L, Hiolle A, Damiano L, Cosi P, Tesser F, et al. Interpretation of emotional body language displayed by a humanoid robot: a case study with children. *Int J Soc Robot.* (2013) 5:325–34. doi: 10.1007/s12369-013-0193-z
6. Beck A, Stevens B, Bard KA, Cañamero, L. Emotional body language displayed by artificial agents. *ACM Trans Interact Intell Syst.* (2012) 2:1–29. doi: 10.1145/2133366.2133368
7. Poria S, Cambria E, Bajpai R, Hussain A. A review of affective computing: from unimodal analysis to multimodal fusion. *Inf Fusion.* (2017) 37:98–125. doi: 10.1016/j.inffus.2017.02.003
8. Zeng Z, Pantic M, Roisman GI, Huang TS. A survey of affect recognition methods: audio, visual, and spontaneous expressions. *IEEE Trans Pattern Anal Mach Intell.* (2009) 31:39–58. doi: 10.1109/TPAMI.2008.52
9. Calvo RA, D'Mello S. Affect detection: an interdisciplinary review of models, methods, and their applications. *IEEE Trans Affect Comput.* (2010) 1:18–37. doi: 10.1109/T-AFFC.2010.1
10. Karg M, Samadani AA, Gorbet R, Kühnlenz K, Hoey J, Kulić D, et al. Body movements for affective expression: a survey of automatic recognition and generation. *IEEE Trans Affect Comput.* (2013) 4:341–59. doi: 10.1109/T-AFFC.2013.29
11. Kleinsmith A, Bianchi-Berthouze N. Affective body expression perception and recognition: a survey. *IEEE Trans Affect Comput.* (2013) 4:15–33. doi: 10.1109/T-AFFC.2012.16
12. Darwin C. *The Expression of the Emotions in Man and Animals*. London: John Murray (1872). doi: 10.1037/10001-000
13. Meeren HKM, van Heijnsbergen CCRJ, de Gelder B. Rapid perceptual integration of facial expression and emotional body language. *Proc Natl Acad Sci USA.* (2005) 102:16518–23. doi: 10.1073/pnas.0507650102
14. Gliga T, Dehaene-Lambertz G. Structural encoding of body and face in human infants and adults. *J Cogn Neurosci.* (2005) 17:1328–40. doi: 10.1162/0898929055002481
15. Stanislavski K. *An Actor Prepares*. New York, NY: Theatre Arts (1936).
16. Liron Y, Raindel N, Alon, U. Dramatic action: a theater-based paradigm for analyzing human interactions. *PLoS ONE.* (2018) 13:e0193404. doi: 10.1371/journal.pone.0193404
17. Chubbuck I. *The Power of the Actor : The Chubbuck Technique*. New York, NY: Gotham Books (2004).
18. Maslow AH. A theory of human motivation. *Psychol Rev.* (1943) 50:370–96. doi: 10.1037/h0054346
19. Ryan RM, Deci EL. Intrinsic and extrinsic motivations: classic definitions and new directions. *Contemp Educ Psychol.* (2000) 25:54–67. doi: 10.1006/ceps.1999.1020
20. Austin JL. *How to do Things With Words*. London: Oxford University Press (1975). p. 58–64.
21. Titze IR, Martin DW. Principles of voice production. *J Acoust Soc Am.* (1998) 104:1148.
22. Aggarwal JK, Cai Q. human motion analysis: a review. *Comput Vis Image Underst.* (1999) 73:428–40.
23. Downing PE. A cortical area selective for visual processing of the human body. *Science (80-.).* (2001) 293:2470–3. doi: 10.1126/science.1063414
24. Herman M. *Understanding Body Postures of Human Stick Figures*. College Park, MD: University of Maryland at College Park (1979).
25. Roebuck JA, Kroemer KHE, Thomson WG. Engineering anthropometry methods. *Aeronaut J.* (1975) 79:555.
26. Buhrmester M, Kwang T, Gosling SD. Amazon's mechanical turk: a new source of inexpensive, yet high-quality, data? *Perspect Psychol Sci.* (2011) 6:3–5. doi: 10.1177/1745691610393980
27. Schindler K, Van Gool L, de Gelder, B. Recognizing emotions expressed by body pose: a biologically inspired neural model. *Neural Networks.* (2008) 21:1238–46. doi: 10.1016/j.neunet.2008.05.003
28. Keltner D, Cordaro DT. Understanding multimodal emotional expressions: recent advances in basic emotion theory. In: *The Science of Facial Expression*. New York, NY: Oxford University Press (2017). p. 57–75.
29. Cowen AS, Keltner D. Self-report captures 27 distinct categories of emotion bridged by continuous gradients. *Proc Natl Acad Sci USA.* (2017) 114:E7900–9. doi: 10.1073/pnas.1702247114
30. Haidt J. The moral emotions. In: Davidson RJ, Scherer KR, Goldsmith HH, editors. *Handbook of Affective Sciences*. Oxford: Oxford University Press (2003). p. 852–70.

31. Plant EA, Hyde JS, Keltner D, Devine PG. *The Gender Stereotyping of Emotions. Psychol Women Q.* (2000) 24:81–92. doi: 10.1111/j.1471-6402.2000.tb01024.x
32. Gunes H, Piccardi M. Bi-modal emotion recognition from expressive face and body gestures. *J Netw Comput Appl.* (2007) 30:1334–45. doi: 10.1016/j.jnca.2006.09.007
33. Pollick FE, Paterson HM, Bruderlin A, Sanford AJ. Perceiving affect from arm movement. *Cognition*. (2001) 82:B51–61. doi: 10.1016/S0010-0277(01)00147-0
34. Coulson M. Attributing emotion to static body postures: recognition accuracy, confusions, and viewpoint dependence. *Nonverbal Behav J*. (2004) 28:117–39. doi: 10.1023/B:JONB.0000023655.25550.be
35. Heider F, Simmel M. An experimental study of apparent behavior. *Am J Psychol*. (1944) 57:243. doi: 10.2307/1416950
36. Kleinsmith A, Bianchi-Berthouze N. Recognizing affective dimensions from body posture. In: Paiva ACR, Prada R, Picard RW, editors. *Affective Computing Intelligent Interaction: Second International Conference, ACII 2007 Lisbon, Portugal, September 12-14, 2007 Proceedings*, Berlin: Springer (2007). p. 48–58.
37. Izard CE. Facial expressions the regulation of emotions. *J Pers Soc Psychol*. (1990) 58:487. doi: 10.1037/0022-3514.58.3.487
38. Rosenberg EL, Ekman P. Coherence between expressive and experiential systems in emotion. *Cogn Emot.* (1994) 8:201–29. doi: 10.1080/02699939408408938
39. Matsumoto D, Keltner D, N.Shiota M, O'Sullivan M, Frank M. Facial expressions of emotion. In: *Handbook of Emotions*. New York, NY: The Guilford Press (2008). p. 211–34.
40. Du S, Tao Y, Martinez AM. Compound facial expressions of emotion. *Proc Natl Acad Sci USA*. (2014) 111:E1454–62. doi: 10.1073/pnas.1322355111
41. Durán JI, Reisenzein R, Fernández-Dols J-M. Coherence between emotions and facial expressions: a research synthesis. In: *The Science of Facial Expression*. New York, NY: Oxford University Press (2017). p. 107–29.
42. Rosenberg EL, Ekman P. *What the Face Reveals: Basic and Applied Studies of Spontaneous Expression Using the Facial Action Coding System (FACS)*. New York, NY: Oxford University Press (2020).
43. Aronoff J, Woike BA, Hyman LM. Which are the stimuli in facial displays of anger happiness? Configurational bases of emotion recognition. *J Pers Soc Psychol.* (1992) 62:1050–66. doi: 10.1037/0022-3514.62.6.1050
44. Ben-Yosef G, Assif L, Ullman S. Full interpretation of minimal images. *Cognition*. (2018). 171:65–84. doi: 10.1016/j.cognition.2017.10.006
45. Schouwstra SJ, Hoogstraten J. Head position and spinal position as determinants of perceived emotional state. *Percept Mot Skills.* (1995) 81:673–4. doi: 10.1177/003151259508100262
46. Harrigan JA, Rosenthal R. Physicians' head and body positions as determinants of perceived rapport. *J Appl Soc Psychol.* (1983) 13:496–509. doi: 10.1111/j.1559-1816.1983.tb02332.x
47. Mehrabian A, Friar JT. Encoding of attitude by a seated communicator via posture position cues. *J Consult Clin Psychol.* (1969) 33:330–6. doi: 10.1037/h0027576
48. Rizzolatti G, Fadiga L, Gallese V, Fogassi L. Premotor cortex and the recognition of motor actions. *Cogn Brain Res.* (1996) 3:131–41. doi: 10.1016/0926-6410(95)00038-0
49. Hasson U, Frith CD. Mirroring beyond: coupled dynamics as a generalized framework for modelling social interactions. *Philos Trans R Soc B Biol Sci.* (2016) 371:20150366. doi: 10.1098/rstb.2015.0366
50. Noy L, Dekel E, Alon U. The mirror game as a paradigm for studying the dynamics of two people improvising motion together. *Proc Natl Acad Sci USA*. (2011) 108:20947–52. doi: 10.1073/pnas.1108155108
51. Huis in 't Veld EMJ, van Boxtel GJM, de Gelder B. The Body Action Coding System II: muscle activations during the perception and expression of emotion. *Front Behav Neurosci.* (2014) 8:330. doi: 10.3389/fnbeh.2014.00330
52. Hess U, Fischer A. Emotional mimicry as social regulation. *Personal Soc Psychol Rev.* (2013) 17:142–57. doi: 10.1177/1088868312472607
53. Dimberg U, Thunberg M, Elmehed K. Unconscious facial reactions to emotional facial expressions. *Psychol Sci.* (2000) 11:86–9. doi: 10.1111/1467-9280.00221
54. Lorenz, K. *On Aggression*. London: Psychology Press (2002).
55. Atkinson AP, Dittrich WH, Gemmell AJ, Young AW. Emotion perception from dynamic and static body expressions in point-light and full-light displays. *Perception.* (2004) 33:717–46. doi: 10.1068/p5096
56. Giese MA, Poggio T. Cognitive neuroscience: neural mechanisms for the recognition of biological movements. *Nat Rev Neurosci.* (2003) 4:179–92. doi: 10.1038/nrn1057
57. Barraclough NE, Xiao D, Oram MW, Perrett DI. The sensitivity of primate STS neurons to walking sequences and to the degree of articulation in static images. *Prog Brain Res.* (2006) 154:135–48. doi: 10.1016/S0079-6123(06)54007-5
58. Bruce C, Desimone R, Gross CG. Visual properties of neurons in a polysensory area in superior temporal sulcus of the macaque. *Neurophysiol J.* (1981) 46:369–84. doi: 10.1152/jn.1981.46.2.369
59. Jellema T, Perrett DI. Neural representations of perceived bodily actions using a categorical frame of reference. *Neuropsychologia.* (2006) 44:1535–46. doi: 10.1016/j.neuropsychologia.2006.01.020
60. Oram MW, Perrett DI. Responses of Anterior Superior Temporal Polysensory (STPa) Neurons to "Biological Motion" Stimuli. *J Cogn Neurosci.* (1994) 6:99–116. doi: 10.1162/jocn.1994.6.2.99
61. Goldberg H, Christensen A, Flash T, Giese MA, Malach R. Brain activity correlates with emotional perception induced by dynamic avatars. *Neuroimage.* (2015) 122:306–17. doi: 10.1016/j.neuroimage.2015.07.056
62. de Gelder B, In 't Veld EMJ. Cultural differences in emotional expressions and body language. In: Chiao JY, Li SC, Seligman R, Turner R, editors, *The Oxford Handbook of Cultural Neuroscience*. Oxford: Oxford University Press (2015) doi: 10.1093/oxfordhb/9780199357376.013.16
63. Kleinsmith A, De Silva PR, Bianchi-Berthouze N. Cross-cultural differences in recognizing affect from body posture. *Interact Comput.* (2006) 18:1371–89. doi: 10.1016/j.intcom.2006.04.003

Conflict of Interest: The authors declare that the research was conducted in the absence of any commercial or financial relationships that could be construed as a potential conflict of interest.

frontiers in Physics

BRIEF RESEARCH REPORT
published: 10 June 2021
doi: 10.3389/fphy.2021.670555

Effects of Sinusoidal Vibrations on the Motion Response of Honeybees

Martin Stefanec[1]*, *Hannes Oberreiter*[1], *Matthias A. Becher*[1], *Gundolf Haase*[2] and *Thomas Schmickl*[1]

[1]Artificial Life Laboratory, Institute of Biology, University of Graz, Graz, Austria, [2]Institute of Mathematics and Scientific Computing, University of Graz, Graz, Austria

Vibratory signals play a major role in the organization of honeybee colonies. Due to the seemingly chaotic nature of the mechano-acoustic landscape within the hive, it is difficult to understand the exact meaning of specific substrate-borne signals. Artificially generated vibrational substrate stimuli not only allow precise frequency and amplitude control for studying the effects of specific stimuli, but could also provide an interface for human-animal interaction for bee-keeping-relevant colony interventions. We present a simple method for analyzing motion activity of honeybees and show that specifically generated vibrational signals can be used to alter honeybee behavior. Certain frequency-amplitude combinations can induce a significant decrease and other signals might trigger an increase in honeybees' motion activity. Our results demonstrate how different subtle local modulatory signals on the comb can influence individual bees in the local vicinity of the emitter. Our findings could fundamentally impact our general understanding of a major communication pathway in honeybee colonies. This pathway is based on mechanic signal emission and mechanic proprio-reception of honeybees in the bee colony. It is a candidate to be a technologically accessible gateway into the self-regulated system of the colony and thus may offer a novel information transmission interface between humans and honeybees for the next generation of "smart beehives" in future beekeeping.

Keywords: honeybees, behavior, substrate-born communication, modulatory signals, freezing responds

OPEN ACCESS

Edited by:
Natasha Mhatre,
Western University, Canada

Reviewed by:
Michael Hrncir,
University of São Paulo, Brazil
Damian Octavio Elias,
University of California, Berkeley, United States

***Correspondence:**
Martin Stefanec
martin.stefanec@uni-graz.at

Specialty section:
This article was submitted to Social Physics, a section of the journal Frontiers in Physics

Received: *21 February 2021*
Accepted: *20 May 2021*
Published: *10 June 2021*

Citation:
Stefanec M, Oberreiter H, Becher MA, Haase G and Schmickl T (2021) Effects of Sinusoidal Vibrations on the Motion Response of Honeybees. Front. Phys. 9:670555. doi: 10.3389/fphy.2021.670555

1 INTRODUCTION

Honeybees are not only economically valuable as producers of honey and wax, but most importantly they are highly efficient pollinators of wild flowers and hence they provide exceptionally important ecosystem services [1, 2]. Even beyond ecology, the economic dependency on honeybees for crop production is significant: While the demand for bee-pollinated crops is constantly on the rise, the recently reported steep increases in colony losses have raised concerns about the sustainability of honeybee populations and crop production [3].

The Western honeybee (*Apis mellifera* L.) has evolved a sophisticated communication system based on a set of very distinct locomotion behaviors, called "dances," which involve the production and a localized emission of specific mechano-acoustic vibrational patterns. These specific dance types trigger very specific reactions or behavioral modulations in those animals that perceive the emitted stimuli. These dances form, in their totality, the "dance language" of the honeybees. Most notably the "waggle dance" is used for recruiting nest mates to a specific foraging source. A dancing bee communicates the location of a food source by a repeated figure-eight shaped movement. The direction of the linear waggle phase relative to gravity represents the direction of the food source

relative to the sun, while the duration of each run increases with the distance of the food source [4]. To decode the information from such a dance, the observer bees have to closely follow the movements of the dancing bee. As the inside of a hive is usually dark, information cannot be transferred visually but instead *via* vibrations emitted during the waggling phase of each waggle dance circuit. The vibration signals are typically composed of a ca. 15 Hz body movement and a 200–300 Hz vibration produced by the flight muscles [5, 6]. It has been shown that these signals also travel through the comb which can act as an amplifier [7, 8]. Therefore the comb itself is the medium for sound transmission and the content of the cells affects the number of dance followers, with empty cells attracting more recruits [7, 9]. Other bees may not only interact with a dancer by following her runs but they can also interfere with the waggle dances and interrupt them. For example, if another bee encounters a dance advertising a food source that she already knows to be sub-optimal, she may send a "stop signal" [10]. In this case the bee bumps her head into the advertising dancer and emits another specific vibrational signal in parallel to the head-butting [11]. As a consequence, the dancing bee often stops advertising its food source. A similar effect of stopping the previously executed behavior can be triggered artificially in lab studies: When bees were stimulated with sinusoidal sound vibrations emitted onto the honeycomb, they reacted with spontaneous movement stops, what is called the "freezing response" [12–14]. While these stop and freezing signals are characterized by higher frequency vibrations, low frequency vibrations of ca. 10–40 Hz may be associated with increased activity levels of bees [15–17]. In addition, other signals and feedback mechanisms are involved in the coordination of foraging by the bee colony [18]. We pick up this line of research on the fundamental mechano-physical aspects of honeybee interaction. In our study, we aim to understand the effects of vibrations on the individual and collective behavior of honeybees. The main research question that drives our study is "How do specifically shaped vibration patterns on the combs alter the behavior of the bees that perceive these stimuli?." The answers to this research question can offer insights into the recruitment processes that governs the individual foraging behavior and the collective foraging patterns that arise from them. This might be a door opening method for novel technology to boost the pollination service, and ultimately also the ecosystem service provided by a honeybee colony in a new generation of "smart beehives."

2 MATERIALS AND METHODS

Our basic concept in the setup of our experiments was initially inspired by the setup reported in [12] and further elaborated to reflect and incorporate the technological progress we can build upon. However, these innovations allowed us to make significant improvements in the research focus and in the level of detail of our observations: Instead of subjectively evaluating the bees' behavioral responses, we use here a simple but effective pixel-based evaluation metric to measure the change in motion activity. This allowed us to quantify the behavioral responses instead of reporting only qualitative annotations. We refrained from using a modified loudspeaker to transfer the vibrational stimulus onto the comb *via* a physical/mechanical bridge, but integrated a thin piezoelectric loudspeaker into the honeycomb itself, to alter the natural environment on the honeycomb as little as possible.

2.1 Experimental Setup

All experiments were conducted on a small honeybee colony (approx. 1,500 bees) housed in a one-comb observation hive (see **Figure 1E**). The hive was located inside a building with the hive entrance being connected to the outside, allowing the bees to forage in a natural habitat. In our experimental setup, a commercially available food-grade plastic honeycomb, as frequently used by beekeepers, was modified in the following way: The outer frame elements of two plastic honeycombs were shortened on one side each and both were joined together to form a new combined double-layered honeycomb with a slim space in between the two middle layers to allow cables and devices to reside in this cavity (see **Figure 1B**). Into this cavity, which was approx 10 mm wide, four piezoelectric elements were inserted (see **Figures 1A,D**). One of these piezoelectric elements (Murata 7BB-27-4L0) served as the emitter of the vibration stimuli we tested here, while the other three elements were used for signal recording for control and adjustment purposes. The emitter was placed at a specific area of the comb, the so-called "dance floor region," the region in the hive where the majority of forager recruitment dances happen. After these preparations, the honeycomb was covered with a thin layer of wax and placed in a conventional full-sized colony beehive for 10 weeks. During this time, it was fully accepted by bees and filled with cells containing brood, pollen and nectar and received the required chemical nest-scent which is important for acceptance of the comb. The honeycomb was then transferred into the experimental observation hive, replacing the original comb that the experimental colony had in usage up until then. We waited for additional 2 weeks for the experimental colony to fully accept the modified comb before starting to conduct the experiments. The experiments were recorded digitally as video with a Canon D5 camera (see **Figure 1C**). In the experiments we report here, a python script was used for the stimulus generation (see **Figure 1G**). We tested 19 different sinusoidal frequencies: From 50 to 750 Hz in 50 Hz steps, from 1000 to 2500 Hz in 500 Hz steps, and in addition, we examined the effect of white noise. We repeated the excitation for each stimulus 12 times. The intensities used for each frequency stimulus are shown in **Figure 2C**. In addition, we tested the effect of different amplitude levels on the bees' response at 50, 500, and 5000 Hz and repeated each amplitude-frequency combination 10 times (shown in **Figures 3D–F**). These sinusoidal stimuli were passed through an audio amplifier (see **Figure 1F**) to the emitter inside the honeycomb. All experiments were carried out in continuous 30-min experiment cycles (see **Figure 1L**), which were recorded on video at 25FPS. Each cycle consisted of a series of 5 s long stimulus periods with vibrational emissions of specific frequencies and amplitudes, alternated by 10-s periods without any active stimulus emissions. The sequence of frequencies and amplitudes was produced in a randomized order.

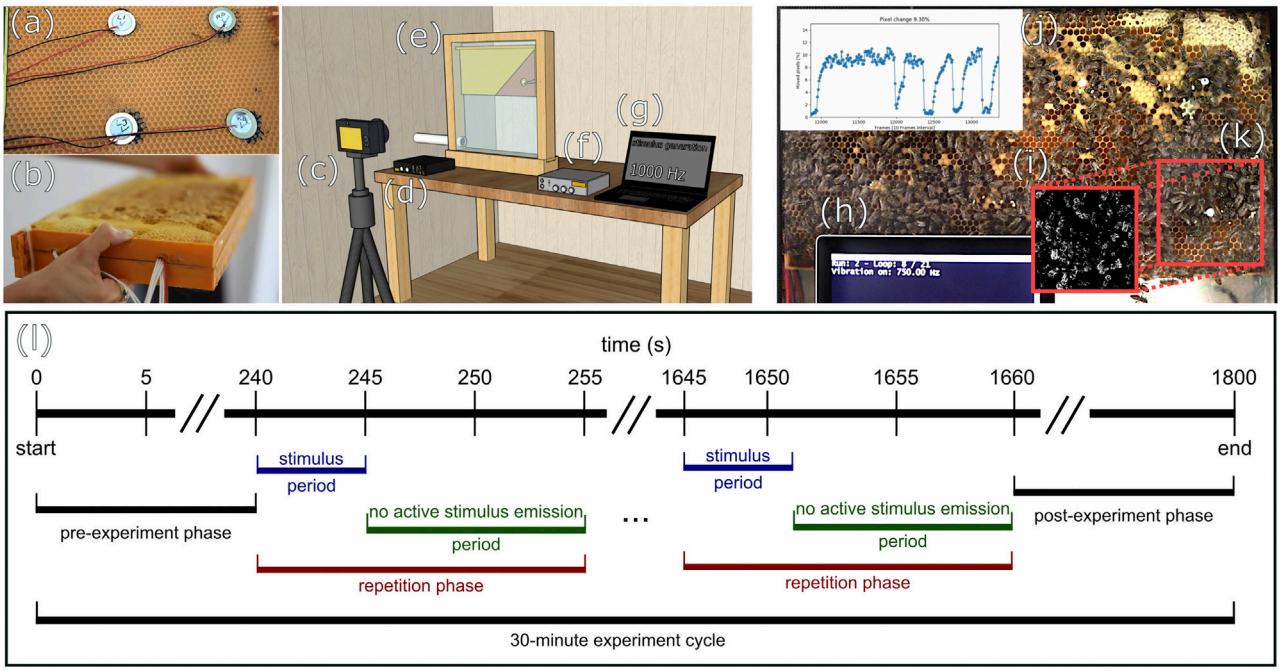

FIGURE 1 | Modified honeycomb, experimental setup, and exemplary video frame with overlays **(A)** placement of piezoelectric elements on the inner side of the comb, **(B)** closed modified comb, **(C)** camera, **(D)** sound recorder, **(E)** observation beehive (position of vibration-emitter in diagram exposed), **(F)** amplifier, **(G)** frequency generation, **(H)** information on the actuation status, **(I)** motion detection in ROI: value changes between frames below (black) and above (white) threshold, **(J)** average PMI of ROI over time, **(K)** red markings indicate the position of ROI, **(L)** diagram of exemplary experiment cycle.

2.2 Optical Motion Activity Analysis

The experimental video recordings were processed after all experiments were completed. For the evaluation of the honeybees' motion activity modulations induced by the vibrational patterns, we defined a pixel-based motion index (PMI) according to **Eqs. 2**, **3**. A square-shaped region of interest (ROI) was defined around the emitter of the vibrational stimuli, with a size of 400 × 400 pixels in each frame, respectively, 10 × 10 cm on the comb. Within this ROI, the three color (red, green blue) channels were combined into one average gray-scale image array for each frame t as ROI_t:

$$ROI_t = \begin{bmatrix} p_{1,1,t} & p_{1,2,t} & \cdots \\ \vdots & \ddots & \\ p_{K,1,t} & & p_{K,K,t} \end{bmatrix} \tag{1}$$

Each array element value of the gray-scale ROI_t was compared to the corresponding element in the consecutive video frame's array. To compensate for random noise of the image sensor, a threshold value was defined. If the difference between two corresponding array items exceeded this threshold, the change was denoted as 1, otherwise a value of 0 was denoted. This procedure resulted in a set of (significantly) changed pixel values in the ROI, which can be expressed as a fraction of changed pixels in the whole population of pixels in the ROI. This pixel-change metric can be understood as a proxy metric for the motion in the video recording, a similar metric has been shown to be useful in previous studies [19]. To additionally account for noise in the video recordings, the PMI of 10 frames each were arithmetically averaged.

$$MI_t = \frac{1}{K^2} \sum_{x=1}^{K} \sum_{y=1}^{K} p_{x,y,t} \begin{cases} 1, & \text{if } \left| p_{x,y,t} - p_{x,y,t+1} \right| > threshold \\ 0, & \text{otherwise} \end{cases} \tag{2}$$

$$PMI_{t_{10}} = \frac{1}{10} \sum_{t=1}^{10} MI_t \tag{3}$$

An exemplary frame of such a video recording with an indicated ROI is shown in **Figures 1H–K**. **Figure 4** shows four example PMI arrays at different frequency excitations before arithmetic averaging of the arrays. The experiments were conducted over the course of 2 days at the end of August 2019. To account for differences in the general motion activity levels that the bees exhibited between experimental cycles, each $MI_{i_{10}}$ was normalized to the arithmetic mean MI of all no-active stimulus emission periods of the same experiment cycle. For the Python-based implementation of the PMI calculation, multiprocessing was used for efficient data processing, the source code can be found in the repository.

2.3 Intensity Measurements

The effects of different intensities on the motion activity of the bees at various frequencies (50, 500, and 5000 Hz) were

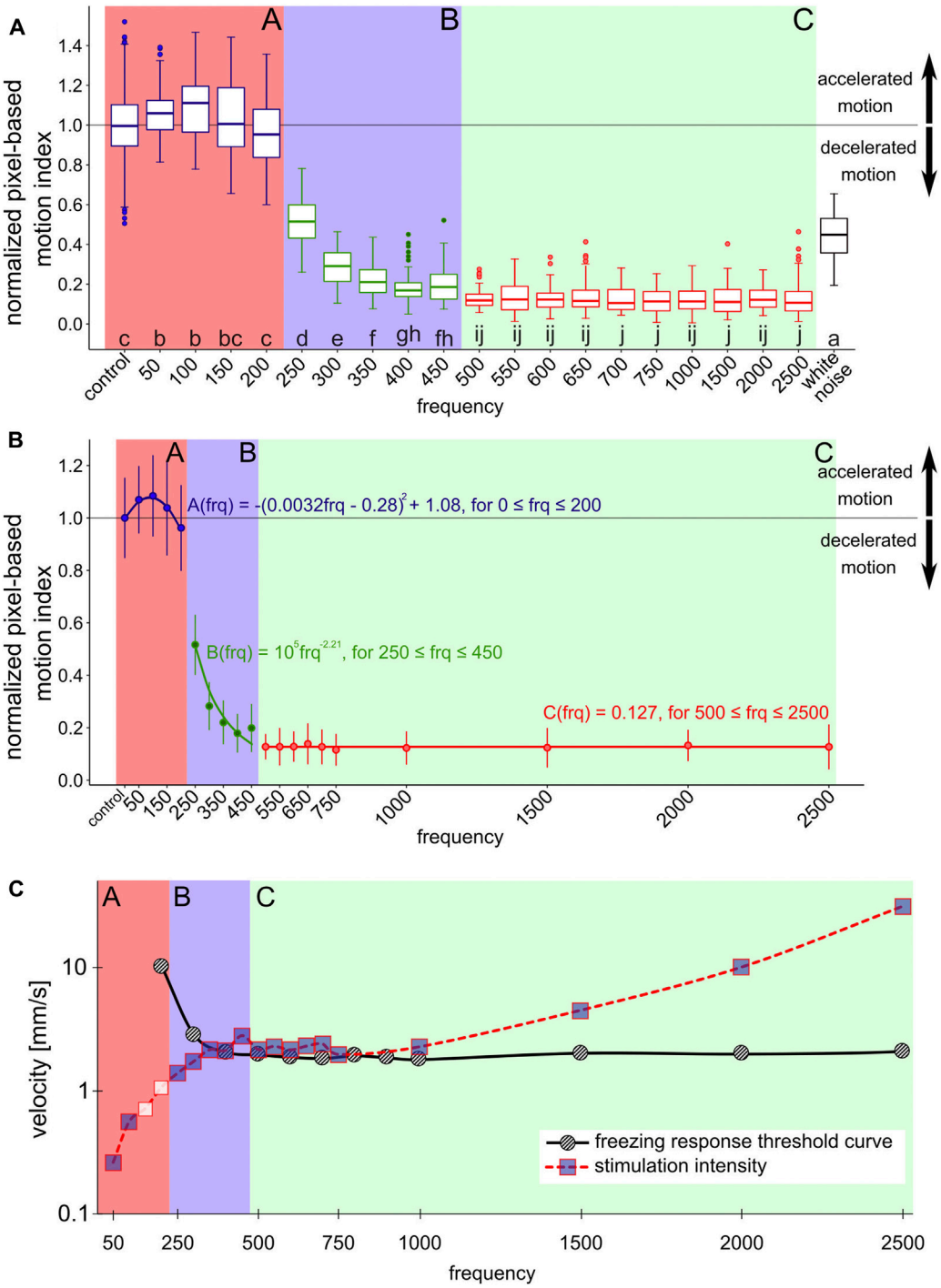

FIGURE 2 | Normalized pixel-based motion index depending on the stimulus frequency **(A)** boxplots show the distribution of normalized PMI measurements to the respective frequency stimulus. 12 repetitions per frequency, each repetition phase consists of 5 s of stimulus, filmed at 25 FPS. 10 FPS are combined into one measurement, first and last measurement of each stimulus period were discarded. Same lowercase letters indicate non-significantly different data groups (pairwise Wilcoxon tests, Bonferroni–Holm adjusted *p*-value) [25]. Colored backgrounds indicate areas with related data groups. Section A: control to 200 Hz stimulus, high basic PMI; section B: 250–450 Hz stimulus, sharply decreasing PMI; section C: 500–2500 Hz stimulus, low PMI. Outside these ranges: white noise **(B)** shows the data as mean values and the corresponding standard deviation with correctly spaced frequency intervals. Models describing the courses of frequency dependence of the PMI were fitted to the mean values for the respective data groups in section A,B,C. Section A is described by a parabolic function, section B by a power function and section C by a line **(C)** shows the intensities of the stimulations at the respective frequencies (squares and red dotted line) measured at the position of the highest intensity on the surface of the comb. The figure also includes threshold curve of the freezing response (black solid line), data adopted from [14]. Incorporated into the dependency of frequency and displacement amplitude is also the change of PMI: blue fill color of the squares indicates a change in motion activity compared to control.

measured (**Figures 3D–F**). For this purpose, intensities were chosen that were respectively lower and higher than the intensities used for the frequency-dependent experiments (which are shown in **Figure 2C**). The actual vibration intensity on the surface of a comb depends on the size of the comb, on the type of comb and foundation, on the housing and on the position of the measurement [8, 20]. Also the content of the comb, respectively the bees themselves, might influence the pervading vibrations [21]. To show the distribution of the vibration intensity on the comb surface, we measured the intensity for different frequencies (50, 500, 5000 Hz) in a 3 × 3 cm grid for the whole comb and a finer grid within the ROI (1 × 1 cm). Since intensity measurements with a laser vibrometer required direct, uninterrupted contact with the surface of the comb, these measurements could not be conducted in an inhabited hive. After the completion of the behavior experiments, the colony was removed from the comb and the bees were transferred to another hive. The same observation hive and the experimental comb, which still contained comb alterations of the bees affecting the vibration propagation (food in cells, potentially brood), was used for *post-hoc* evaluation. The intensity measurements were conducted at a later point in time, the comb was stored in a freezer in between. Changes that might alter the intensity of vibration on the front side of the comb can therefore not be ruled out. Hence, the distribution of vibration shown in **Figures 3A–C** can only indicate the actual distribution of vibration intensity in the live experimental setup. To prepare the intensity measurements, we put self-adhesive reflector tapes on the surface of the honeycomb at even intervals. We measured the intensity exactly at the center of each grid measurement point. We generated the vibration stimuli of the behavioral experiments with a piezotransducer and simultaneously recorded it with three surrounding piezoelectric sensors. To make the *post-hoc* laser-measurement evaluation as comparable as possible, the vibration generation was performed the same as in the behavior experiments and was additionally recorded by the same piezoelectric sensors. The intensities in these recordings were digitally measured to match with the previously digitally measured intensities of the behavior experiment recordings. The alignment showed comparable digital intensities at the different frequencies tested. After we were able to ensure similar vibration intensities through this step, we conducted more precise intensity measurements using a laser vibrometer (Polytec PDV 100), the measurements are shown in **Figures 2C**, **3**. The data was transmitted to the Polytec Vibrometer software (V5.2.2) *via* the USB break-out box (VIB-E-220). In this software the magnitude was measured as velocity *via* fast Fourier transform.

2.4 Statistical Analysis

We used the software package *R* [22] with the RStudio IDE [23] for the majority of our analyses. The package collection tidyverse [24] was used for graphs and exploratory data analysis. For comparing effects of different frequency stimuli, a two sided pairwise Wilcoxon rank sum test with Bonferroni–Holm family wise error rate adjustment was used. Test results are represented as lowercase letters [25], whereas the same letters indicate a nonsignificant comparison $p > 0.05$, see **Figure 2A**.

2.5 Code Availability

For reproducible code a public Github repository[1] under MIT licence was created. It includes the exported dataset, session info with packages, the code used for the statistical analysis, and the exported pairwise comparison test results.

3 RESULTS

3.1 Motion Activity Depending on the Stimulus Frequency

Figure 2 shows the normalized PMI (**Eqs. 2**, **3**) in response to the frequency of the applied vibration. All data groups were compared pairwise (**Figure 2A**). This allowed us to classify the data into three distinct frequency-defined sections that share a common behavior: When bees were stimulated with frequencies located in section A (in the range of 50–200 Hz, respectively the control group), the observed bees in the ROI did not show a significantly reduced motion activity in the normalized PMI, but even a slight increase in activity at low frequencies, with a maximum at 100 Hz. Further increasing the frequency of the signal yielded a diminishing of the reaction back again to the level observed in the control group at the highest frequency in section A, which is 200 Hz. In contrast to that, when stimulating the bees with frequencies within section B (250–450 Hz) a different pattern was observed in the reaction of the bees: They exhibited a significant decrease in their normalized PMI with increasing frequencies. A further increase of frequencies covered by section C (500–2500 Hz) resulted in a low normalized PMI, independent of the exact frequency.

To further detail the observed dependencies of behavioral modulation and bees on the frequencies of the emitted stimuli, we fitted a set of regression functions for every section. These functions model the expected behavioral modulation of the PMI with respect to the tested vibrational frequencies (**Figure 2B**), in order to allow prediction of the honeybees' responses to signals in the regions on the frequency band between the tested frequencies. The honeybees' response to signals with frequencies in section A can be predicted by a parabolic function $(A(frq) = -(0.0032frq - 0.28)^2 + 1.08)$, in response to frequencies in section B by a power function $(B(frq) = 10^5 frq^{-2.21})$ and in response to frequencies in section C by a linear function $(C(frq) = 0.127)$.

In addition to the effect of specific frequencies, we also tested the effect of white noise onto the bees' motion behavior. As **Figure 2A** shows, this signal, which is composed by the definition of a collection, or a sum of all possible frequencies, triggered again a clear, but not a maximal, response in the honeybees' motion modulation. We observed that this mixed-frequency signal reduced the

[1]https://github.com/martin-st/motion-analysis-of-honeybees

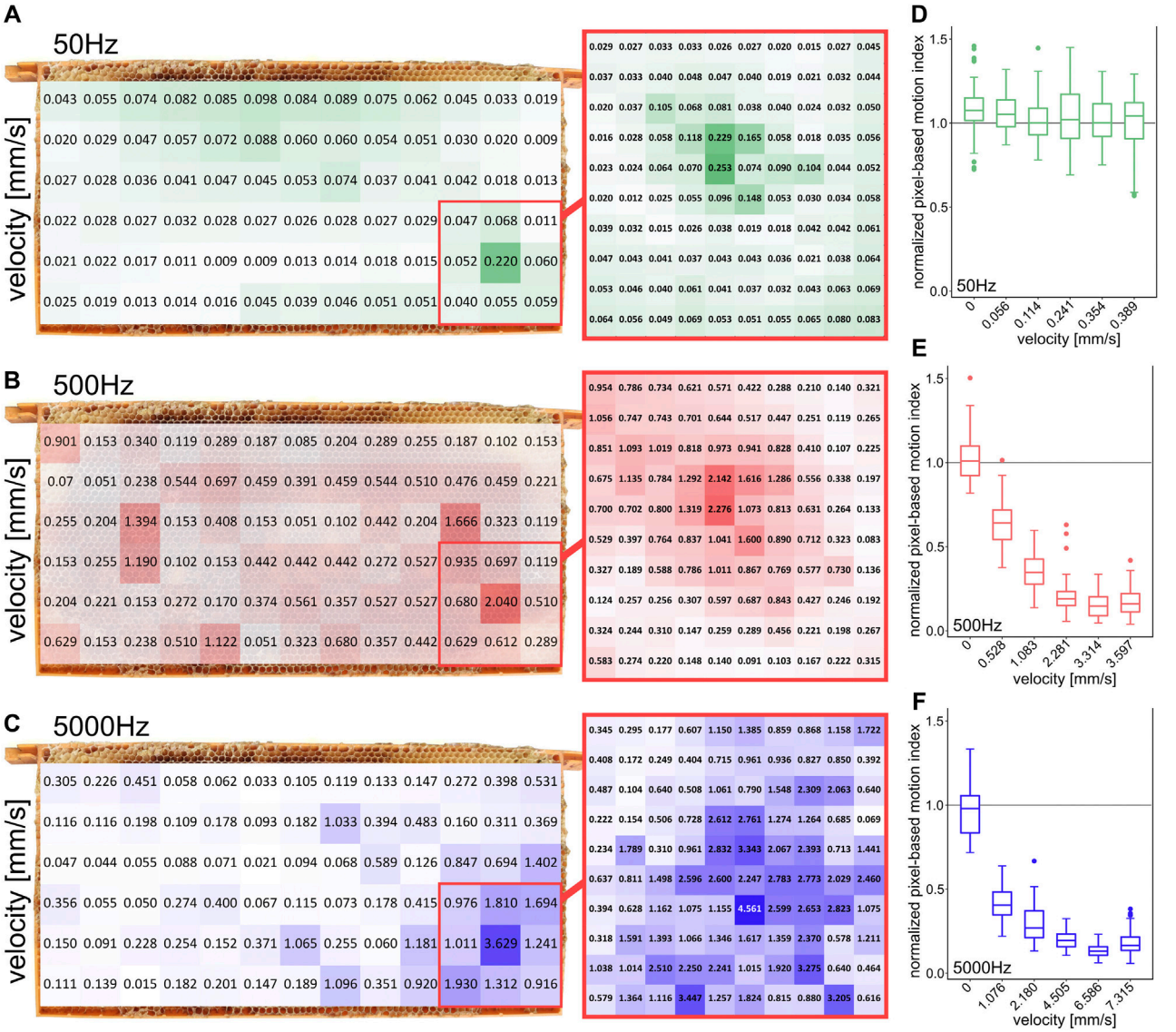

FIGURE 3 | Spatial distribution of local vibration stimulation intensities and effect of stimulation intensity on changes in honeybee movement activity **(A–C)** local intensity measurements on the comb at 50, 500, and 5000 Hz, **(D–F)** normalized pixel-based motion index of bee activity in the region of interest depending on different signal intensities for 50, 500, and 5000 Hz (10 repetitions per group). Signal intensity measured at the comb position of maximum intensity at the corresponding frequency.

PMI down to be about four times higher than the lowest observed PMI and was found to be a response similar to a clean sinusoidal signal of 250 Hz.

Exemplary results showcasing the different PMI for the control group, 100 Hz, white noise and 750 Hz are shown in **Figures 4A–D**.

3.2 Motion Activity Depending on the Stimulus Intensity

We also observed the influence of the signal's amplitude onto the observable behavioral modulation of the recipients' motion behavior. However, the actual vibration intensities on the comb surface varied significantly depending on various factors. To map an impression of the distribution of intensities on the surface of the honeycomb, we measured the intensities for three different frequencies at different locations (**Figures 3A–C**). The highest intensities were measured near the emitter in the center of the ROI for all frequencies. The emitter was placed in the inner side of the hollow honeycomb.

Figures 3D,E shows the dependence of the freezing response on the amplitude of the emitted sinusoidal signal. For three specific frequencies, the normalized PMI was determined for different intensity levels. At 50 Hz, no significant change in motion activity was detected regardless of the applied stimulus magnitude. At 500 Hz a reduction of motion activity between video frames was determined at a

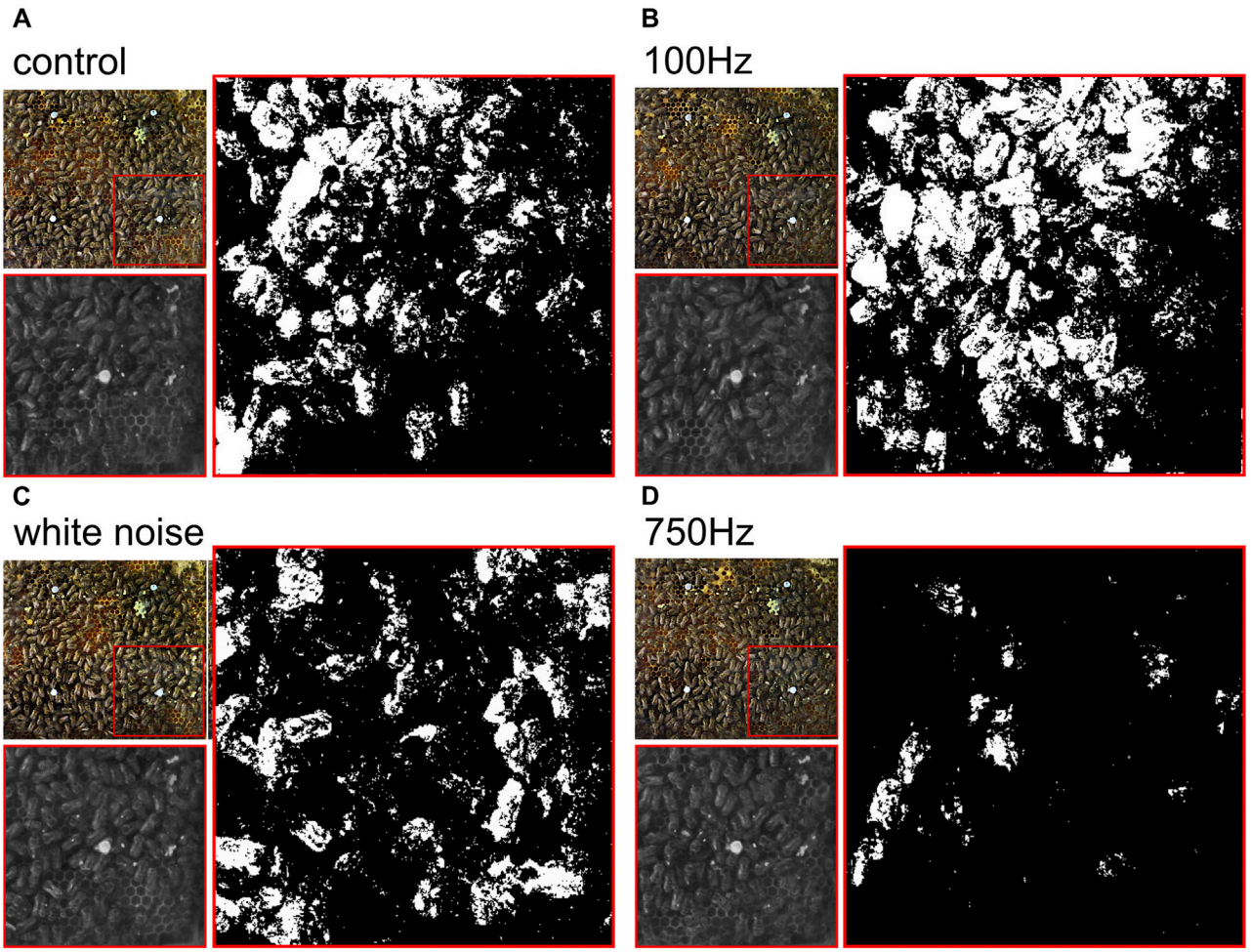

FIGURE 4 | Comparison of PMI_{10} for different frequency stimuli. For each panel: small colored top left image shows part of the frame with indicated ROI, small gray image shows gray-scale ROI, large black and white image shows PMI_{10} out of one exemplary stimulus period for **(A)** control group, **(B)** 100 Hz stimulus, **(C)** white noise, and **(D)** 750 Hz stimulus before arithmetically averaging the array, white pixels indicate movement.

velocity of 0.528 mm/s and at 5000 Hz at a velocity of 1.076 mm/s. At 500 Hz and an intensity of more than 2.281 mm/s, respectively, at 5000 Hz and an intensity of more than 4.505 mm/s no further reduction of the PMI was detected.

3.3 Correlation of Frequency and Displacement Amplitude

In order to provide a final interpretation of our data and to see its standing within the existing body of literature, we conducted a *post-hoc* meta-analysis on reference data from literature, which is shown in **Figure 2C**. This graph depicts a 3Dimensional view of our data: The X-Y plane depicts the relationship between frequencies and displacement amplitude of the stimuli in our experiments (measured directly on the emitter). The color of the data points represents our experimental results in a summarized way: data points filled in blue indicate a significant response of honeybees to a stimulus compared to the control data set. In addition to that, a threshold curve for the freezing response, redrawn from [14], has been added as a reference data set to this graph.

4 DISCUSSION

4.1 Stimuli Generation for Studying Honeybee Communication Pathways

Much research effort has been invested over the past 50 years to explore the effects of substrate-born vibrations in the honeybee colony [26–30]. One common approach of such studies has been to playback vibration signals onto the combs [31, 32]. However, these signals consist of a convolution of many frequencies, they are often modulated, and can be very complexly structured. Another approach has been to study the effects of pure-tone sinusoidal frequencies, such was the study that first reported on the freezing response of honeybees to these stimuli [12]. The study reports a decreased locomotive activity, especially with frequencies in a range of 500–1000 Hz. No such freezing response

was reported at a frequency below 100 Hz or above 2500 Hz. The excitation of the subgenual organs of a honeybee is a mechanical energy transfer, thus the energy that the signal contains is expected to be important. This energy depends on the signal's amplitude and on the frequency in combination, additionally affected by material properties in the medium it spreads and wave-based effects like interference patterns, harmonic oscillations, the geometry of the substrate and dampening effects. The behavioral response of the animals depends not only on the specific frequency, or a specific amplitude, but on the combination of these two and the measurement point on the honeycomb [14]. showed the threshold for the required signal amplitude. Such a threshold curve indicates the expected set of minimum signal prerequisites in order to expect a specific behavioral response (redrawn as a reference data set in **Figure 2C**). The stimulus intensities applied in our experiments can be grouped into three distinct regions: In the range of 50–300 Hz, the stimuli we generated were below the predicted behavior response threshold, thus if the prediction holds we should not have observed the responses that we did observe. In the region of 350–1000 Hz, the stimuli we generated were approximately at the threshold level of the behavioral response, thus also here the previous predictions we found in the existing literature need to be questioned, given that the behavioral responses we observed are too significant to assume that the sensorial or behavioral threshold was just matched. Such a match would suggest that we see weak to medium responses, as such thresholds differ across individuals and over time, thus we should expect only a fraction of the bees in the ROI reacting to such borderline signals. Only for signals in the 1500–2500 Hz range did the intensity of our signals lie above the threshold curve described in the literature and thus lead to the predicted behavioral responses. Studies have already shown that the physiological threshold of the subgenual organ of honeybees is lower than the behavioral threshold [33]. It is possible that the behavioral threshold to vibration intensity was underestimated so far due to the subjective assessment of the behavioral response.

In addition, our experiments potentially indicate that stimulus intensities well below the reported behavioral threshold for signals in the 50–100 Hz frequency range produce the opposite effect of a freezing response: The PMI showed a statistically significant increase in motion activity. This behavioral response to these vibrational stimuli was previously unknown and, to our knowledge, is the first time such a behavioral response to an artificial stimulus has been observed. Our finding result from statistical evaluation of the data and does not imply any behavioral/biological relevance of this stimulus response. In a second series of experiments measuring the effect of vibration intensity on behavioral modification, no increase in activity was detected with a pure tone of 50 Hz, regardless of intensity (see **Figure 3D**). Activating vibration signals are known to occur in natural honeybee colonies, in particular the shaking dance. This signal is reported to cause a non-specific increase in activity [16]. However, the frequencies associated with this signal are significantly lower ($\bar{x}$ = 16.3 Hz, S = ± 5.8 Hz [15]) than the frequencies we used in our experiments. The data from our experiments suggest that an increase in motion activity in response to artificial vibratory stimulation may exist, but more detailed studies are needed to confirm this assumption.

4.2 Strengths and Weaknesses of the Applied PMI Metric

In contrast to the qualitative observer-based evaluation used in the literature so far, the rather objective, as it is based on a computer algorithm, and quantitative motion index metric used here allows for a simple pixel-based assessment of the observed honeybees' motion activity. This analysis reveals more details in the evaluation of vibration signal effects on honeybee behavior. For example, without such a quantitative approach, it would not have been possible to generate a model, based on three regression functions, that allows predicting the bees' responses to specific frequencies in a quantitative way. This is a fundamental new piece of evidence that can be utilized in technological approaches of human-honeybee interaction, for example in "smart beehives." However, this method of assessment also has its weaknesses and does not evaluate strictly the actual stimulus-behaviour response of the bees themselves, but uses rather the resulting optical flow as a proxy for quantification of the video frames. But nevertheless, this simple method already allows quantification of changes in the overall movement patterns at certain areas on the comb over time, a feature that might suffice for informing mean-field model based approaches of this system in the future. For individual-based models the data would need to be extracted rather on an individual bee level, with sophisticated image tracking and individually marked bees. Such systems already exist and are proven to be effective with honeybees [34–36], however, these setups demand for much more sophisticated computer hardware than we used here, as our method could easily be performed in an all-in-one solution with a simple low-cost and low-energy computing solution, likely even operating on a live datastream and in a closed-loop setup in the near future.

In this work we show that artificially generated vibration patterns on the comb can affect the locomotor activity of bees. The surface of the honeycomb serves as a communication platform through which the vibrations are transmitted. Many factors influence the intensity of the signals on the surface of the honeycomb [8, 20, 21]. Also in our experiments, the intensity of the stimulus decreased very rapidly as a function of distance from the emitter, respectively, a very complex intensity pattern emerged, even within the ROI (see **Figures 3A–C**). Nevertheless, certain well-defined frequency-amplitude combinations result in significant downregulation of their motion, while others may result in upregulation. Understanding these responses could be a door opener for targeted interventions in the signal cascade of the colony. The dance floor, where the waggle dances occur, is not the only the location where information is passed on from returning foragers to the bees inside the colony, this information is also further processed by a network of interacting bees, shaping the foraging patterns of the colony as a whole [37]. By downregulating the locomotor activity of the bees on the dance floor *via* artificial vibrations, the information flow on the dance floor will be disturbed and changes in the foraging patterns of the colony may arise as a result of this intervention.

Especially since small interventions in the worker allocation system, which is composed of many feedback loops [18], could alter individual feedbacks and thus change the way the system works. If these interventions could be triggered automatically in a controlled way when dances to potentially hazardous forage sites (like fields freshly sprayed with pesticides) were detected, a mechanism could be established to protect the colony from a potentially fatal foraging decision. Whether or not the potential upregulation of motion activity we observed at low frequencies could potentially be used to stimulate foraging activities requires further studies.

DATA AVAILABILITY STATEMENT

The datasets presented in this study can be found at: https://github.com/martin-st/motion-analysis-of-honeybees.

ETHICS STATEMENT

According to the animal care principles of our institution and the current animal protection laws of Austria, experiments on insects do not fall under animal experiments requiring a permit. However, during our work we attach great importance to causing as little harm to the animals as possible.

AUTHOR CONTRIBUTIONS

MS developed the core hypothesis in this article together with TS and HO. MS and HO conducted the experiments and generated the Python code to determine the pixel change. MS, HO, MB, and TS wrote the text of the article together in a collaborative effort. MS designed **Figures 1**, **4** with input of MB and TS. MS and HO designed **Figures 2**, **3** with input of MB and TS. HO performed the data analyses and implemented the *R* Code for **Figures 2**, **3**. GH improved the PMI calculation performance by implementing multiprocessing.

FUNDING

This work was supported by the Field of Excellence "Complexity of Life in Basic Research and Innovation" (COLIBRI) at University of Graz and the EU H2020 FET-Proactive project "HIVEOPOLIS" (no. 824069).

REFERENCES

1. Klein A-M, Vaissière BE, Cane JH, Steffan-Dewenter I, Cunningham SA, Kremen C, et al. Importance of Pollinators in Changing Landscapes for World Crops. *Proc R Soc B* (2007) 274:303–13. doi:10.1098/rspb.2006.3721
2. Gallai N, Salles J-M, Settele J, and Vaissière BE. Economic Valuation of the Vulnerability of World Agriculture Confronted with Pollinator Decline. *Ecol Econ* (2009) 68:810–21. doi:10.1016/J.ECOLECON.2008.06.014
3. Kearns CA, Inouye DW, and Waser NM. ENDANGERED MUTUALISMS: The Conservation of Plant-Pollinator Interactions. *Annu Rev Ecol Syst* (1998) 29:83–112. doi:10.1146/annurev.ecolsys.29.1.83
4. von Frisch K. *The Dance Language And Orientation Of Bees* (Cambridge, MA: Harvard University Press 2013) (1967) doi:10.4159/harvard.9780674418776
5. Esch H. Über die Schallerzeugung beim Werbetanz der Honigbiene. *Z Vergl Physiol* (1961) 45:1–11. doi:10.1007/bf00297754
6. Michelsen A, Towne WF, Kirchner WH, and Kryger P. The Acoustic Near Field of a Dancing Honeybee. *J Comp Physiol* (1987) 161:633–43. doi:10.1007/bf00605005
7. Nieh JC, and Tautz J. Behaviour-locked Signal Analysis Reveals Weak 200-300 Hz Comb Vibrations during the Honeybee Waggle Dance. *J Exp Biol* (2000) 203:1573–9. doi:10.1242/jeb.203.10.1573
8. Tautz J, Casas J, and Sandeman D. Phase Reversal of Vibratory Signals in Honeycomb May Assist Dancing Honeybees to Attract Their Audience. *J Exp Biol* (2001) 204:3737–46. doi:10.1242/jeb.204.21.3737
9. Tautz J, and Rohrseitz K. What Attracts Honeybees to a Waggle Dancer? *J Comp Physiol A: Sensory, Neural Behav Physiol* (1998) 183:661–7. doi:10.1007/s003590050289
10. Kietzman PM, and Visscher PK. The Anti-waggle Dance: Use of the Stop Signal as Negative Feedback. *Front Ecol Evol* (2015) 3:14. doi:10.3389/fevo.2015.00014
11. Nieh JC. The Stop Signal of Honey Bees: Reconsidering its Message. *Behav Ecol Sociobiol* (1993) 33:51–6. doi:10.1007/bf00164346
12. Little HF. Reactions of the Honey Bee, *Apis mellifera* L., to Artificial Sounds and Vibrations of Known Frequencies1. *Ann Entomol Soc America* (1962) 55:82–9. doi:10.1093/aesa/55.1.82
13. Spangler HG. Suppression of Honey Bee Flight Activity with Substrate Vibration123. *J Econ Entomol* (1969) 62:1185–6. doi:10.1093/jee/62.5.1185
14. Michelsen A, Kirchner WH, and Lindauer M. Sound and Vibrational Signals in the Dance Language of the Honeybee, *Apis mellifera*. *Behav Ecol Sociobiol* (1986) 18:207–12. doi:10.1007/bf00290824
15. Gahl RA. The Shaking Dance of Honey Bee Workers: Evidence for Age Discrimination. *Anim Behav* (1975) 23:230–2. doi:10.1016/0003-3472(75)90068-8
16. Schneider SS, and Lewis LA. The Vibration Signal, Modulatory Communication and the Organization of Labor in Honey Bees, apis Mellifera. *Apidologie* (2004) 35:117–31. doi:10.1051/apido:2004006
17. Hrncir M, Maia-Silva C, and Farina WM. Honey Bee Workers Generate Low-Frequency Vibrations that Are Reliable Indicators of Their Activity Level. *J Comp Physiol A* (2019) 205:79–86. doi:10.1007/s00359-018-1305-x
18. Anderson C, and Ratnieks FLW. Worker Allocation in Insect Societies: Coordination of Nectar Foragers and Nectar Receivers in Honey Bee (*Apis mellifera*) Colonies. *Behav Ecol Sociobiol* (1999) 46:73–81. doi:10.1007/s002650050595
19. Mariano P, Salem Z, Mills R, Schönwetter-Fuchs-Schistek S, Correia L, and Schmickl T. Evolving Robot Controllers for a Bio-Hybrid System. In: *Artificial Life Conference Proceedings*. (MIT Press) (2018) p. 155–62.
20. Sandeman D, Tautz J, and Lindauer M. Transmission of Vibration across Honeycombs and its Detection by Bee Leg Receptors. *J Exp Biol* (1996) 199:2585–94. doi:10.1242/jeb.199.12.2585
21. Tautz J. Honeybee Waggle Dance: Recruitment success Depends on the Dance Floor. *J Exp Biol* (1996) 199:1375–81. doi:10.1242/jeb.199.6.1375
22. R Core Team. *R. A Language and Environment for Statistical Computing*. Vienna, Austria: R Foundation for Statistical Computing (2020).
23. RStudio Team. *RStudio: Integrated Development Environment for R*. Boston, MA: RStudio, PBC (2021).
24. Wickham H, Averick M, Bryan J, Chang W, McGowan L, François R, et al. Welcome to the Tidyverse. *Joss* (2019) 4:1686. doi:10.21105/joss.01686
25. Piepho H-P. An Algorithm for a Letter-Based Representation of All-Pairwise Comparisons. *J Comput Graphical Stat* (2004) 13:456–66. doi:10.1198/1061860043515

26. Simpson J. The Mechanism of Honey-Bee Queen Piping. *Z für vergleichende Physiologie* (1964) 48:277–82.
27. Ohtani T, and Kamada T. 'Worker Piping': The Piping Sounds Produced by Laying and Guarding Worker Honeybees. *J Apicultural Res* (1980) 19:154–63. doi:10.1080/00218839.1980.11100016
28. Hrncir M, Barth FG, and Tautz J. 32 Vibratory and Airborne-Sound Signals in Bee Communication (Hymenoptera). *Insect sounds Commun Physiol Behav Ecol Evol* (2005) 421. doi:10.1201/9781420039337.CH32
29. Seeley T, and Tautz Jx. r. Worker Piping in Honey Bee Swarms and its Role in Preparing for Liftoff. *J Comp Physiol A: Sensory, Neural Behav Physiol* (2001) 187:667–76. doi:10.1007/s00359-001-0243-0
30. Schlegel T, Visscher PK, and Seeley TD. Beeping and Piping: Characterization of Two Mechano-Acoustic Signals Used by Honey Bees in Swarming. *Naturwissenschaften* (2012) 99:1067–71. doi:10.1007/s00114-012-0990-5
31. Michelsen A, Kirchner WH, Andersen BB, and Lindauer M. The Tooting and Quacking Vibration Signals of Honeybee Queens: a Quantitative Analysis. *J Comp Physiol* (1986) 158:605–11. doi:10.1007/bf00603817
32. Kirchner W, Dreller C, and Towne W. Hearing in Honeybees: Operant Conditioning and Spontaneous Reactions to Airborne Sound. *J Comp Physiol A* (1991) 168:85–9. doi:10.1007/bf00217106
33. Kilpinen O, and Storm J. Biophysics of the Subgenual Organ of the Honeybee, apis Mellifera. *J Comp Physiol A* (1997) 181:309–18. doi:10.1007/s003590050117
34. Wario F, Wild B, Couvillon MJ, Rojas R, and Landgraf T. Automatic Methods for Long-Term Tracking and the Detection and Decoding of Communication Dances in Honeybees. *Front Ecol Evol* (2015) 3:103. doi:10.3389/fevo.2015.00103
35. Boenisch F, Rosemann B, Wild B, Dormagen D, Wario F, and Landgraf T. Tracking All Members of a Honey Bee colony over Their Lifetime Using Learned Models of Correspondence. *Front Robot AI* (2018) 5:35. doi:10.3389/frobt.2018.00035
36. Gernat T, Rao VD, Middendorf M, Dankowicz H, Goldenfeld N, and Robinson GE. Automated Monitoring of Behavior Reveals Bursty Interaction Patterns and Rapid Spreading Dynamics in Honeybee Social Networks. *Proc Natl Acad Sci USA* (2018) 115:1433–8. doi:10.1073/pnas.1713568115
37. Seeley T, Camazine S, and Sneyd J. Collective Decision-Making in Honey Bees: How Colonies Choose Among Nectar Sources. *Behav Ecol Sociobiol* (1991) 28. doi:10.1007/BF00175101

Conflict of Interest: The authors declare that the research was conducted in the absence of any commercial or financial relationships that could be construed as a potential conflict of interest.

frontiers in Physics

PERSPECTIVE
published: 14 June 2021
doi: 10.3389/fphy.2021.687823

Goals and Limitations of Modeling Collective Behavior in Biological Systems

Nicholas T. Ouellette[1]* *and Deborah M. Gordon*[2]*

[1]Department of Civil and Environmental Engineering, Stanford University, Stanford, CA, United States, [2]Department of Biology, Stanford University, Stanford, CA, United States

Local social interactions among individuals in animal groups generate collective behavior, allowing groups to adjust to changing conditions. Historically, scientists from different disciplines have taken different approaches to modeling collective behavior. We describe how each can contribute to the goal of understanding natural systems. Simple bottom-up models that describe individuals and their interactions directly have demonstrated that local interactions far from equilibrium can generate collective states. However, such simple models are not likely to describe accurately the actual mechanisms and interactions in play in any real biological system. Other classes of top-down models that describe group-level behavior directly have been proposed for groups where the function of the collective behavior is understood. Such models cannot necessarily explain why or how such functions emerge from first principles. Because modeling approaches have different strengths and weaknesses and no single approach will always be best, we argue that models of collective behavior that are aimed at understanding real biological systems should be formulated to address specific questions and to allow for validation. As examples, we discuss four forms of collective behavior that differ both in the interactions that produce the collective behavior and in ecological context, and thus require very different modeling frameworks. 1) Harvester ants use local interactions consisting of brief antennal contact, in which one ant assesses the cuticular hydrocarbon profile of another, to regulate foraging activity, which can be modeled as a closed-loop excitable system. 2) Arboreal turtle ants form trail networks in the canopy of the tropical forest, using trail pheromone; one ant detects the volatile chemical that another has recently deposited. The process that maintains and repairs the trail, which can be modeled as a distributed algorithm, is constrained by the physical configuration of the network of vegetation in which they travel. 3) Swarms of midges interact acoustically and non-locally, and can be well described as agents moving in an emergent potential well that is representative of the swarm as a whole rather than individuals. 4) Flocks of jackdaws change their effective interactions depending on ecological context, using topological distance when traveling but metric distance when mobbing. We discuss how different research questions about these systems have led to different modeling approaches.

Keywords: collective behavior, modeling, emergent phenomena, active matter, foraging behavior, midge swarms

OPEN ACCESS

Edited by:
Saad Bhamla,
Georgia Institute of Technology,
United States

Reviewed by:
Roland Bouffanais,
University of Ottawa, Canada
Olga Shishkov,
University of Colorado Boulder,
United States
Richard P Mann,
University of Leeds, United Kingdom

***Correspondence:**
Nicholas T. Ouellette
nto@stanford.edu
Deborah M. Gordon
dmgordon@stanford.edu

Specialty section:
This article was submitted to Social Physics, a section of the journal Frontiers in Physics

Received: *30 March 2021*
Accepted: *01 June 2021*
Published: *14 June 2021*

Citation:
Ouellette NT and Gordon DM (2021) Goals and Limitations of Modeling Collective Behavior in Biological Systems. Front. Phys. 9:687823. doi: 10.3389/fphy.2021.687823

INTRODUCTION

Throughout nature, molecules, cells, and organisms interact in ways that generate collective behavior. Collective behavior has been defined in many ways, but some features are generally recognized as essential. First, and perhaps most importantly, collective systems operate without central control. The group-level behavior and properties arise spontaneously from the local behavior of the individuals in the group, and no individual directs the behavior of others. The individuals interact with one another, but because individuals typically do not have global knowledge about the whereabouts and behavior of all the others, these interactions are local. Since the interactions are essential in determining the resulting collective behavior, different forms of group-level behavior arise from distinct types of interactions. Finally, collective behavior in nature (as we define it) always performs some biological function. The goal of modeling is to elucidate how local interactions, in the aggregate, allow the group to accomplish this function.

Some of the best-known examples of collective behavior are the many spectacular forms of synchronous movement in animals. Flocks of starlings wheel in the sky. Schools of fish travel together and turn sharply when a predator approaches. Clouds of locusts travel together. Similar patterns occur at the cellular level and also arise from interactions among individual cells. Groups of neural crest cells, for example, move together early in mammalian development [1]; the cells at one side contract, and the others do not, pulling the whole group of cells along. Common patterns of collective movement include flocks, where the animal motion is directionally ordered and the group has a net linear momentum; mills, where the motion is ordered and the group has a net angular momentum; and swarms, where the motion is disordered but the group remains bound together.

A second and widespread category of collective behavior regulates activity or effort to determine who does what and when, using a distributed process based on interactions [2]. For example, differentiation in a developing embryo occurs through local chemical and tactile interactions among cells, leading to the formation of distinct tissues that descend from identical cells. Another example of this type of collective behavior is task allocation in social insects, the process that determines how colonies adjust the numbers of individuals performing each of various tasks, such as foraging and care of the larvae. Individuals change tasks in response to interactions with each other and changing colony needs [3].

The patterns generated by collective animal groups, and more generally the distributed processes common to many forms of collective behavior, have captivated scientists beyond biology and have inspired diverse modeling approaches. Collective movement first caught the interest of the computer graphics and animation community [4], and has subsequently been the subject of a great deal of study in physics and applied mathematics [5, 6].

Physicists have been especially interested in the observation that when different kinds of animals in different environments with very different individual behavior are brought together in sufficiently large numbers, only a few types of group dynamics emerge. Because collective behavior in natural systems involves large numbers of discrete individuals, many physicists have considered collective behavior through the lens of statistical mechanics. The hope in this approach is that collective behavior can be understood as an emergent property that arises from averaging over large numbers of interacting individuals. This is conceptually similar to how bulk material properties emerge from averaging over atoms or molecules.

This line of thinking has been the genesis of the young but rapidly evolving field of active matter [7, 8]. In conceptualizing groups of organisms as matter, the focus of modeling has been on specifying minimal microscopic models and working to tease out how the group-level dynamics emerge. In this way, this bottom-up approach to describing collective behavior reflects the way that physicists are trained to work from first principles when possible. The goal of the modeling in this case is the development of a general understanding of how and why group-level properties emerge given knowledge about the individual-level behavior. This approach has historically been successful in allowing us to understand and link many disparate physical phenomena [9]. However, the complexities of biological systems make them different from systems traditionally considered by physicists, in ways that warrant additional care in interpreting the predictions of models.

Collective behavior in natural systems is particularly appealing to engineers, who hope to exploit it in the design of engineered distributed systems. Collective behavior operates with no individual in charge and directing the motion of the others, and the properties and functionality of the group arise from the interactions among the individuals. This means that no individual is essential for the group to function. Thus, one advantage of collective behavior is that the function performed by the group is robust to the loss of individuals. Additionally, the bottom-up, self-organized nature of collective behavior means that the group is regulated and maintains coherence without the need for any individual to have global information about the state of the others—and thus serves as a robust model of distributed control with limited communication or information sharing.

Because the emphasis in the engineering community has been on the function performed by the group rather than on scaling up the behavior of each individual, models of collective behavior formulated by engineers tend to start with the group-level dynamics and propose a simplified model that generates this behavior. In this way, these top-down engineering models can be seen as explaining *how* a collective system works (in a simplified fashion) rather than *why* it works. The resulting models can be very powerful, both because they are easily translatable to designed systems and because they lead to predictions that can be tested in the biological system. However, because such models are not based on first principles, it can be difficult to know whether they will remain valid when the system parameters or other factors change.

Modeling biological processes brings further challenges that are not typically encountered in physics or engineering. Different organisms communicate and sense their surroundings differently, imposing distinct constraints on their behavior, so that even if the structure of two groups of different organisms is

similar or they have similar functions, they may operate in very different ways. Additionally, organisms behave differently in different situations, so that a model that describes a particular group of animals well in one context may not hold when the environment changes. Moreover, organisms act to modify their environments, in ways that influence whether and how they interact, so that their behavior cannot be considered to be operating in an environment independent of the organisms [10]. Thus, models of collective behavior are unlikely to be generic, and do not fully describe the biological system. We argue that models of collective behavior that are intended to provide biological insight are most effective and useful when designed to address specific questions about collective behavior, and that it is important to remember their limitations.

To illustrate these ideas, we begin below with a broad overview of modeling trends in collective behavior, including a discussion of reasons why intuition gleaned from modeling in physics and engineering may not be sufficient to understand a biological system. We then discuss four distinct case studies that differ in organism, interactions, and ecological context: foraging by harvester ants, the formation of trail networks by arboreal turtle ants, the emergence of binding and group-size regulation in midge swarms, and collective travel and mobbing by flocking jackdaws.

MODELING COLLECTIVE BEHAVIOR

Modeling is ubiquitous in all branches of science. However, both what is meant by the term "modeling" and what its goal is differ among disciplines. Such distinctions are particularly fraught in an interdisciplinary field such as collective behavior, and they can lead to misunderstandings among scientists with different priors. Here, then, we begin by trying to elucidate some of these differences and to clarify the various starting points and perceived purposes of modeling collective behavior, before describing modeling strategies in more detail.

Modeling in physics tends to be built on the process of stripping away details, in an attempt to isolate only the most fundamental aspects of a problem or system. A "toy model" in this sense is typically not intended to reproduce the behavior of the modeled system exactly; rather, the goal is to construct a more tractable system that shares the same key features as the problem of interest but whose dynamics can be completely understood. A model of collective behavior developed in this spirit would not necessarily be expected to capture the specific behavior of any particular organism, but instead could be used to explain how individual, local interactions can scale up to produce coherent and distinct group-level behavior. We can characterize this general approach as being bottom-up: the model explicitly specifies the microscopic dynamics of the system, and the macroscopic behavior is expected to be an outcome of solving the model.

An engineer might approach modeling the same system differently. The goal of models in engineering is often to describe the actual behavior of the system, rather than why a system behaves as it does. If such a model captures enough about how the behavior works, it can then be translated into a new situation or used for a different purpose. For collective behavior, this style of modeling would entail describing in a simplified fashion what a collective group does in the aggregate, without explaining how the function of the collective behavior arises from the behavior of the individuals. In this way, this approach is more top-down: the macroscopic behavior of the group is what is explicitly specified in the model.

Here we discuss the approach to modeling used by biologists to guide empirical investigation [11]. A model is a description of a natural process that can make specific predictions. When the predictions do not fit the data, this provides an opportunity to modify the model so as to describe the natural process more accurately. However, even when the predictions of the model fit the data, this does not prove that the model is correct, because the same observed outcome could be achieved in other ways. Thus, although the physicist's modeling goal is achieved when the collective behavior can be explained as the outcome of individual behavior and the engineer's goal is reached when the operation of the system can be predicted, the biologist with a model that predicts the observed outcome will still seek to confirm that the real system actually operates in the way described by the model. In other words, for the biologist, obtaining a model that can then be studied and applied in contexts that do not occur in nature is not the goal; rather, the goal is to understand phenomena that *do* occur.

Thus, different scientific communities use models of collective behavior in different ways and to address different questions. It is important to remember that in all of these approaches, models are by their nature always limited in scope and applicability; as famously explained by the statistician George Box, "all models are wrong" [12]. In particular, no model is likely to capture all of the inherent complexity of a biological system as it adjusts to constantly changing environments. Richard Levins in *Evolution in Changing Environments* remarked that any model is either so general that it cannot be used to ask how well it fits observations or so detailed that it merely captures what is already known, and so the exercise of modeling is the attempt, through matching model results with data, to find a model that is somewhere in between [13].

Next, we contrast strategies for implementing the bottom-up and top-down approaches described above to address questions about natural systems, and then discuss case studies of models of different types of collective behavior.

Bottom-Up Modeling

The starting point of a bottom-up model of collective behavior is the individual. Each member of the group is assigned a set of behavioral rules, including interactions with others, that it executes. The goal is that the correct group-level collective behavior will emerge as the individuals follow their rules. This approach, often termed agent-based modeling, has seen widespread use in modeling collectively moving groups of animals such as flocks and schools. Designing an agent-based model of this type requires several explicit choices [14]. One must at minimum specify how each individual behaves when it is not interacting with others, which is often as simple as moving in a

straight line at a constant speed; how the individual interacts with others; and which others it interacts with. Although these rules may be fully deterministic, it is common to include some stochasticity to mimic variously the imperfections of biological sensing or the random or unexplained variation among individuals that occurs in natural groups. Any behavioral rules assigned to individuals are themselves not fundamental, as they must arise from a complex process of sensory signal transduction by each individual and subsequent internal decision-making. Some classes of bottom-up models attempt to take aspects of these internal processes into account explicitly.

Some of the earliest agent-based flocking models were developed in the computer-graphics community [4], with the goal of producing animations of group motion that looked realistic. Subsequently, the same general framework was adopted by the physics community with the goal of casting the emergence of collective motion as a kind of critical phenomenon [15], by analogy with the study of phase transitions. The focus of this work was primarily on groups that display unidirectional ordered motion (that is, flocks), but later research showed that changes to the interaction rules can produce other types of group motion such as toroidal mills or disordered swarms [16]. More generally, agent-based models have also been used to describe many forms of collective behavior beyond simple collective movement [17].

The primary goal of bottom-up modeling, however, is not simply to replicate the observed collective outcome, such as the shape of a group of moving individuals, but rather to explain how that outcome arises from the behavior of individuals and their interactions. For example, we would like to understand how interactions between individual birds give rise to the macroscopic ordered motion of a flock [18, 19], or why rafts of interlocked fire ants display an effective viscoelasticity [20].

In physics, questions about collective outcomes of interactions among individuals fit the general paradigm of statistical mechanics. Originally developed to describe thermal systems, statistical mechanics is a core tool throughout condensed matter physics, and is extremely powerful for describing the properties of materials by appropriately averaging over interactions between their constituent atoms. The purview of statistical mechanics has over the past several decades expanded enormously beyond its traditional areas of application, and has proved to be useful in understanding a broad range of topics, both physical and non-physical [9]. Researchers have attempted to apply the general methods of statistical mechanics to just about every problem involving large numbers of discrete degrees of freedom [9]. It is an obvious extension of this approach to use statistical mechanics to treat collective groups, where the degrees of freedom are the individual organisms. This is the core of the young subdiscipline of active matter physics.

Statistical mechanics is not, however, a panacea; there are many cases where its methods do not work. It is worth considering when and why this occurs, to be aware of the limitations of a statistical-mechanical approach to collective behavior. The central concept in statistical mechanics is that of an ensemble: instead of trying to predict the dynamics of a single system, we instead make statements about the average properties of a large number of identically prepared and constrained systems. Thus, the key to any statistical-mechanical approach is the specification of an appropriate ensemble. One classical way to do this is to appeal to conservation laws. For an isolated thermal system, for example, we expect that its total energy is conserved. An appropriate ensemble in this case is the microcanonical ensemble, the set of all configurations of the constituent molecules whose individual energies add up to the (conserved) total energy. We can characterize different thermal systems in this framework by specifying the relative likelihood of each of these configurations *via* a density of states. However, there are many cases where this approach fails. Without an appropriate conservation law, for example, defining an ensemble is often not possible, e.g., in highly dissipative athermal systems like granular materials [21]. In systems far from equilibrium, which is the rule for biological systems, defining an appropriate ensemble is difficult, because the macroscopic properties of such a system may change in time.

Unfortunately, both of these caveats apply in the case of collective behavior. Because each individual organism independently consumes and dissipates energy, we cannot in general assert any of our usual conservation laws such as energy or momentum. By the same token, life is inherently far from equilibrium; a biological system in equilibrium is dead. Thus, it is not obvious how to define an appropriate ensemble.

Modeling methods that originated in the study of hydrodynamics and liquid crystals (and that generally fall within the domain of nonequilibrium statistical mechanics) have been somewhat more successful in developing group-level descriptions of animal groups that exhibit net motion [8]. In this approach, one models the group with a small number of continuum fields rather than discrete individuals. The equations of motion for these fields can either be developed by coarse-graining over the discrete microscopic equations of motion, or sometimes simply by including all terms allowed by symmetry and setting their relative strengths empirically. This approach was notably recently applied to polarized human crowds [22].

To date, bottom-up, agent-based models have been quite successful in demonstrating that collective states can be generated only from simple local interactions. Such models can produce various kinds of group shapes reminiscent of those observed in nature. Advances in active matter are beginning to lead to an understanding of how these collective states arise and their properties. However, we must remain cautious about interpreting these successes as indications that simple bottom-up models accurately describe real biological systems. It is certainly tempting to do so, following intuition gained from decades of studying critical phenomena. Toy models such as the Ising model accurately describe the behavior of physical systems with much more complicated structure at the microscale because these systems are strongly constrained by conservation laws and symmetries. These constraints give rise to universality, so that in a formal sense toy models describe aspects of real physical systems exactly. Biological systems, however, need not respect conservation laws and symmetries, particularly at the whole-organism level. Thus, care must be exercised in trusting the

predictions of simple agent-based models of collective behavior, particularly when they are extrapolative. And because formal theoretical arguments cannot guarantee that models predictions will be correct, validation against observational data is essential. Finally, we note that even such validation is fraught, and comparing the output of a model with the macroscopic behavior of a real system cannot definitively confirm that the mechanisms assumed in the model are correct. Collective behavior requires interactions and is thus inherently nonlinear, and nonlinear systems are rarely invertible.

Top-Down Modeling

An alternative approach, that is characteristic of classic methods in engineering, is to use a top-down approach to describe a collective process. The goal of such models is not to discover the underlying principles that govern collective behavior, but instead to specify how to generate particular collective outcomes. It goes without saying, of course, that employing this approach requires one to know what outcome is sought. Dynamical systems theory generally aims to predict the outcomes of dynamical processes, without necessarily specifying the behavior of each component. For example, control theory was developed to specify how the flow of work, such as in a factory, possibly involving many different operations, yields a rate of production and minimizes delays or optimizes some outcome [23].

The tools of dynamical systems theory have been used to model forms of collective behavior that regulate activity. For example, many physiological processes arising from chemical interactions and interactions among cells can be considered to be collective behavior within tissues. The kinetics of such processes describe how outcomes depend on concentrations of various components, without considering the details of how the components encounter each other and interact. For example, metabolic pathways depend on interactions among various molecular actors, and their collective behavior can be described in a top-down way [24, 25].

Systems biology has developed the quantitative analysis of collective processes within and among cells [26]. In general, the dynamics of signaling pathways can be described with differential equations that specify quantities without examining the details of local interactions among the participants, ranging from transcription networks [27] to cell division. For example, Cheng and Ferrell [28] showed how, in the frog egg, a trigger wave works quickly in apoptosis by examining the change in the quantity of caspase moving across the cell. The dynamics demonstrate the mechanism; trigger waves occur faster than diffusion. This result is based on top-down modeling; the dynamics reveal the broad strokes of how the components of the system interact without describing the interactions themselves in detail.

Similarly, the study of population dynamics in ecology uses models of the outcome of interactions among individuals to explain collective processes in populations [29]. The Lotka-Volterra equations are a simple example. They describe how populations change as a function of numbers of individuals and amounts of resources in the environment, without addressing the details of the particular interactions that cause individuals to reproduce or die, or how birth and death are affected by available resources.

Here we present some examples from our own work of different approaches to modeling collective behavior.

Harvester Ants

Our investigations of the collective behavior that regulates foraging activity in harvester ants have primarily used tools from engineering to create top-down models that capture the goals and tasks of the ants.

First, we considered a model of spatial distributions of a population of harvester ant colonies. Harvester ants forage for scattered seeds and so do not use pheromone trails [30]. Colonies compete with neighboring colonies of the same species for foraging area [31]. A colony regulates its foraging activity in response to interactions with neighboring colonies and food availability. Colonies must regulate activity in response to the risk of water loss. Ants lose water to evaporation when out foraging in the desert sun, but obtain their water from metabolizing the fats in the food they eat. The extent to which one colony's foraging area overlaps with its neighbors' changes over a colony's lifetime, as colonies grow older and larger [32].

We modeled the spatial distribution of colonies to ask how competition among neighboring colonies generates the shifting spatial distribution of colonies [33]. Our goal was to capture the relevant interactions among colonies enough to predict how distributions change over time. Similar studies have been done to explain the collective outcome of spatial interactions among individuals in populations of sessile organisms that compete with their neighbors for resources, such as self-thinning in trees [34] or populations of termite colonies [35]. The basic parameter in our model was the spatial range of foraging by each age class of colony. The results show how the local neighborhood of colonies of the same species affects each colony's opportunity to expand its foraging area. A recent analysis of the effect of spatial distributions on colony foraging area and its survival supports the results of this model.

Harvester ant colonies regulate foraging collectively using local olfactory encounters. Ants smell with their antennae, and when one ant touches the antennae of another, it assesses the odor of the other ant. Ants, like many insects, spread long-chain fatty acids, cuticular hydrocarbons, on their bodies by grooming. These cuticular hydrocarbons help to prevent desiccation, and also carry specific odors. In the course of a brief antennal contact, one ant smells the cuticular hydrocarbon profile of the other [36]. Ants use the odor of cuticular hydrocarbons to recognize whether another ant is a nestmate and also to identify the task of the ants they meet.

A harvester ant forager waits inside the nest entrance between foraging trips. An outgoing forager uses the rate at which it meets returning foragers with food to decide whether to leave the nest on its new trip [37]. Because each ant searches until it finds food, the rate of forager return is a cue to food availability: more food means a shorter search time and a higher rate of forager return.

We developed a model to predict the rate at which outgoing foragers leave the nest, based on the rate of forager return [38].

We tracked the rates at which foragers left the nest and returned, including in field experiments in which we manipulated the rate of forager return. The parameters of our model were the rate at which foragers left the nest, which we treated as a Poisson process, and a variable that describes how much returning foragers stimulate the rate at which foragers leave the nest. Here we did not specify the dynamics or details of the interactions of outgoing and returning foragers. We used the data on the rate of foraging return, and the model, to simulate the rate at which foragers leave the nest. Our goal was to ask if this simple process was sufficient to predict the observed fluctuations in foraging activity. We found a good fit by the simulations with the observed rate at which foragers left the nest. The good fit between model predictions and data shows that it is plausible that the interactions of returning and outgoing foragers as they mix inside the entrance chamber generate the moment-to-moment rate at which foragers they leave the nest.

The model showed that overall the rate at which foragers leave the nest depends on the rate of forager return. We then looked more closely at the interactions of outgoing and returning foragers, to ask what is the process that individual foragers use to decide whether to leave the nest on their next trip. Each forager makes many trips in a day, and when it returns to the nest, uses its rate of encounter to decide whether to leave the nest. The encounters are antennal contacts in which it assesses the odor of the ant it meets.

We asked how a forager assesses its rate of antennal contact with other ants [39]. We used a leaky integrator model, based on drift-diffusion dynamics, from theoretical neuroscience. This choice of model was based on an analogy between ants and neurons. Just as a forager uses the rate at which it meets returning foragers to decide whether to leave the nest, so a neuron uses the rate of stimulation from other neurons to decide whether to fire. In neurons, the electrical charge leaks as it travels down the axon. We modified the leaky integrator model to explain the firing rate of neurons, to ask whether the decisions of outgoing foragers could be based on a similar process.

In our model, each encounter between a returning and outgoing forager stimulates the outgoing forager to leave the nest, and this stimulus has a decay. If enough encounters occur often enough, the stimulus reaches some stochastic threshold value and the forager is likely to decide to leave the nest to forage. We added another element to the model that does not apply to neurons. Experiments showed that when no foragers return for an extended period, about 8 min or more, the outgoing foragers leave the entrance chamber and go down to the deeper nest where they are not available to be stimulated to forage.

We were able to fit the model to data by developing a method in the field to film ant interactions inside the nest. This allowed us to obtain data on the rates of encounter of outgoing and returning foragers inside the nest, as well as the rates of encounter of ants that decided not to leave the nest on the next trip. These data fit the predictions of the model. These results show that it is plausible that a forager can assess interaction rate using a physiological process in which each interaction it experiences has a decay, and the decision depends on the accumulated stimulation from encounters over time.

Once we understood the dynamics that regulate a forager's decision to leave the nest, we were able to consider the regulation of foraging activity, and how it varies from day to day and among colonies [40]. Using a low-dimensional analytical model from control theory, we brought together the dynamics of different aspects of the system, including interactions inside the nest and foraging outside the nest [41].

The model brings together the encounters of foragers inside the nest as an open loop with the activity of foragers going out to search, retrieve seeds and return to the nest as a closed loop. It uses excitability dynamics to represent how outgoing foragers inside the nest respond to returning foragers to decide whether to leave the nest to forage, and then uses a random delay distribution to represent the activity of foragers outside the nest. The results show how feedback from outgoing foragers returning to the nest stabilizes the incoming and outgoing foraging rates to a common value determined by the volatility of available foragers. There is a critical volatility in the interactions of outgoing and returning foragers, above which foraging activity continues at a set rate, and below which foraging stops. Observations show that foraging activity adjusts to changes in temperature and humidity both within a day and from day to day. Our model suggests that these adjustments occur because foragers modify their volatility after they leave the nest and become exposed to the environment; a forager's experience on its last trip influences how it responds to encounters with returning foragers.

In these examples, modelling was used to investigate different aspects of harvester ant behavior. First, we considered how the interactions of foragers of neighboring colonies shape the spatial distribution of the population. Then a series of models, combined with field experiments, investigated the feedback that regulates foraging activity through interactions of outgoing and returning foragers. We found that interactions lead to individual forager decisions whether to leave the nest, through excitable dynamics. Then we combined these in a model that included both the excitable dynamics and the adjustment of volatility by foragers in response to the conditions they encounter outside. This series of modelling projects show the role of feedback across many timescales in the collective regulation of foraging activity, and helps to explain how evolution is shaping collective behavior through variation among colonies in individual response to interactions [42].

Arboreal Turtle Ants

Turtle ants form networks of trails in the canopy of the tropical forest. The network consists of a routing backbone that connects several nests of the same colony, along which the ants distribute resources, and temporary trails to ephemeral food sources. Ants lay pheromone trails as they go, and when they get to a junction, tend to take the edge with the most pheromone. The pheromone evaporates over time, probably with an exponential decay. While most ants follow the edge with the most pheromone, occasionally some ant takes a different edge, not the one most strongly reinforced. This allows for search and exploration, and also for repair of breaks in the vegetation that interrupt the trail network [43].

We asked what is the algorithm that the ants use to maintain and repair trails [44]. We modeled this as a distributed algorithm with two parameters: the rate of evaporation of the pheromone, and the probability that an ant leaves the trail to explore. We found that the parameter values most successful in simulations matched those from field observations [43]. This shows that this model is plausible because it is consistent with field observations.

Next, we asked what objectives are optimized by the algorithm that the ants use [45]. Unlike species that forage on the ground and can go anywhere in a 2D plane, arboreal ants never leave the tree canopy, and so the configuration of their trail networks is constrained by the vegetation. We considered what objectives the ant networks meet by comparing the observed turtle ant trail networks with simulated networks of random, hypothetical trails in the same surrounding vegetation. We made these comparisons with trails optimized for different objectives: the shortest path, the path with the least number of nodes or junctions in the vegetation, and finally the path linking nodes with a 3D configuration most likely to be reinforced by pheromone. To consider the alternatives from which the ants choose a path, we used data from maps of trail networks, tracking the path through the tree canopy that the ants used, and also the vegetation around the path. We found that the ants' trails minimize the number of nodes traversed, reducing the opportunity for ants to get lost at each node, and favor nodes with 3D configurations most likely to be reinforced by pheromone, thus keeping the ants together on the same trail. The results showed that rather than finding the shortest path, turtle ant trail networks take advantage of natural variation in the environment to favor coherence, keeping the ants together on the trails.

Next, we examined in detail what algorithm the ants use to minimize the number of nodes or junctions in the trail network, although no ant can assess the length of the trail [46]. This asks what the details of the local interactions involving trail pheromone are that have the outcome that trails minimize the number of nodes, although no ant can assess the total number of nodes in the trail.

The model is a form of a reinforced random walk on a directed graph. The ants lay pheromone on edges and at each junction, choose an edge with the most pheromone. The pheromone decays with time. Ants travel both ways on the trail. Because there is a consistent small probability that some ants explore, or choose an edge that is not reinforced, every edge not taken is an opportunity for leakage, losing ants off the trail. We found that this process converges to the path with the fewest nodes bypassed when the rate of flow of ants in both directions is constant. However, when the flow rate increases, for example, due to the discovery of a new food source, it converges to the shortest path. We showed that the combination of forward and backward flow, with ants laying pheromone (without directional signal) in both directions, is necessary for convergence. Thus this model provides a plausible explanation for how collectively the ants can minimize the number of junctions in the path, or find the shortest path, although no ant assesses the path's length or number of nodes.

These modelling projects help to explain how colonies maintain and repair trail networks that link nests and food sources using only local information based on pheromone intensity at junctions in the vegetation, how the networks are shaped by the physical configurations of the vegetation, and which aspects of the process contribute to the coherence of the trails.

Midge Swarms

Chironomid midges, like most other species in order *Diptera*, form swarms spontaneously as part of their mating process. Swarms are composed entirely of males, and are thought to provide targets for females to find mates. These swarms are transient (tending to form at dawn and dusk based on light-level cues), and form over ground-based features known as swarm markers. Unlike flocks or mills, swarms are fixed in place, in that the group as a whole does not exhibit net translational or rotational motion; however, each individual is constantly moving. Since the vector sum of the (nonzero) linear and orbital angular midge velocities must vanish, the relative motion of the midges must be either highly structured or largely random. Empirically, the latter situation is what is observed. However, the motion of individual midges is not completely arbitrary, because they remain bound to the swarm. In the wild, swarms form in free space with no external constraints; thus, the swarm boundaries, which are surprisingly tightly regulated, are dynamically set, and depend most strongly on the number of individuals in the swarm [47]. More precisely, midges behave as if they are moving in a harmonic potential well that binds them to the swarm [47]. The strength of this effective potential scales with the number of midges in the swarm. This emergence of this effective potential is one of the signatures that swarming is indeed collective despite the difficulty of identifying specific interactions between individuals [48].

Because swarms do not obviously accomplish any collective tasks (aside from staying fixed despite environmental fluctuations [49] and acting as a target for females), most models of swarms are bottom-up. Building on the body of work done to understand the Vicsek flocking model [15], one popular avenue for modeling swarms has been to treat them as Vicsek flocks in the unpolarized regime, often with additional attractive interactions [16] or a confining potential [50, 51] to keep them cohesive. However, this type of model makes predictions that do not agree with observations, displaying, for example, much stronger attraction to neighbors relative to other swarm features than is measured in real swarms [48] or suggesting that swarms may spontaneously polarize and become mobile flocks [51]. Part of the problem with these models may indeed be that they start by assuming that the collective behavior arises from direct interactions between neighboring individuals, even though evidence for significant interactions of this type is scant [48, 52].

A different modeling approach that has been more successful in capturing observed features of swarms is to begin not by assuming a particular type of behavioral interaction, but rather by considering how midges sense each other. Midges in swarms interact acoustically, perceiving the sound of the wingbeats of other midges. Indeed, this is thought to be the primary mechanism by which midges distinguish males from females, as the fundamental wingbeat frequency is very different for males

and females. Male midges transduce sound *via* their Johnston's organs, and to leading order, the strength of the sound signal they perceive will decay as the inverse square of the distance from the emitting source [53]. Inverse-square laws are, of course, very common—perhaps most notably in gravitation. This observation led us to model swarms as a kind of self-gravitating system [53–57], following a line of reasoning that goes back to Okubo [58]. This framework is very appealing, as it allows us to translate intuition gained from studying gravitation to collective behavior. Several observed features of swarms also naturally arise in a gravitational model. Gravitational systems are, for example, naturally bound together, but local interactions are difficult to discern because gravitational forces are long-range. Additionally, multi-body gravitating systems are well known to allow for chaotic motion, so that the random and disordered nature of the motion of individuals in the swarm can be captured without needing to build it into the model explicitly.

A simple, purely gravitational model, although qualitatively reasonable, does not quantitatively capture the structure of real midge swarms [56]. However, we found that we can improve the model by making an addition that is also grounded in biological sensing. Most biosensors do not have a fixed gain; rather, to avoid damage and improve sensitivity, their gain adapts to the input signal strength. This typically occurs *via* the so-called fold-change detection mechanism [59], also known as Weber's law. In the case of a gravitational swarm model, incorporating adaptivity means that midges that are not too close to their neighbors primarily respond to the net contribution of all of the other midges in the swarm, while those that are close to neighbors respond primarily to these nearby midges [53]. Note that this renormalization of the effective force felt by individuals also formally makes the model many-body, in that the adaptive force cannot be decomposed into the linear superposition of the contributions from each individual midge.

Whether implemented in a deterministic way [53, 54, 56, 57] or *via* a stochastic modelling framework [49, 55, 60, 61], adaptive-gravity models of swarms correctly reproduce many features of midge swarms. Model swarms display an emergent harmonic potential, as they must given the form of the gravitational interaction; but with adaptivity, they also reproduce the observed weakening of the strength of the potential with increasing swarm size [53]. They also reproduce the heavy tails seen in the acceleration distributions [53, 60] and the distinct behavior of midges in the swarm core as compared with those on the swarm periphery [60, 62]. What is perhaps more unexpected, since these adaptive-gravity models do not explicitly model direct interactions between individuals, is that such models also reproduce multipoint properties of swarms. For example, they display similar transient pairing of individuals as has been observed in real swarms [52, 57]. Adaptive-gravity swarms also display similar material-like properties such as effective viscoelasticity [60, 61].

To summarize, because the general function of swarms is not fully understood, we approached modeling them from the bottom up. Our primary goal was to understand a specific feature of the swarms, namely the emergence of the effective potential that binds swarms together and the way in which this potential varies with swarm size. Appealingly, our models also reproduced other empirical features of midge swarms. However, the models are certainly not full descriptions of the biology; for example, these models cannot shed light on the biological function of swarming.

Jackdaw Flocks

Jackdaws (*Corvus monedula*) are a highly social, colony-breeding corvid. In the winter, when there are no young in the nest, they roost together nightly in communal trees. At dusk, they form large "transit" flocks to travel from their daytime foraging grounds to their roosts. These flocks are highly polarized, in that the flight directions of all the individuals in the flock are close to uniform. In that sense, jackdaw transit flocks are qualitatively similar to those other species of flocking birds that have been studied such as European starlings. Unlike starlings, however, jackdaw societies are highly structured; in particular, they are known to form lifelong monogamous pair bonds [63]. Paired birds not only remain in close proximity during foraging and nesting, but also qualitatively appear to fly together during flocking [64]. Quantitative statistical analysis of jackdaw transit flocks confirms the presence of paired birds, which tend to remain unusually close together along their entire flight trajectories [65].

Agent-based, bottom-up models that assume a tendency for individuals to align their motion, such as the classic Reynolds [4] or Vicsek [15] models, were first introduced with the intent of capturing the behavior of bird flocks. Testing of these models, however, occurred only many years later, due to the difficulty of collecting detailed measurements of bird movement. Nevertheless, when tested on starling flocks, these models have been shown to perform reasonably well. They not only capture simple features of the flocks, such as their high degree of polarization, but also more subtle properties such as their long-range, scale-free velocity correlations [66, 67]. To achieve agreement between the model and the data, however, one significant modification was required—not to the way in which individuals interact, but rather to which individuals interact. Standard agent-based models such as the Vicsek model assume that a given individual responds to all others that lie within some distance of it. This way of determining the interaction range is described as being *metric*, because it depends on real, physical distance. Flocking starlings, in contrast, were found to respond to a specific number of neighbors (six or seven, empirically), regardless of their distance [68]. This kind of interaction range is termed *topological*, because it does not depend on distance.

In many ways, jackdaw transit flocks appear to be similar to starling flocks. Like starling flocks, they are highly polarized and exhibit long-range velocity correlations [65]. Jackdaws in transit flocks also interact *via* a topological distance. An individual's topological range, however, depends on whether it is part of a mated pair or not: paired birds interact with three to four others, while unpaired birds interact with seven to eight [65]. This difference has group-level consequences, as the correlation length decreases monotonically with the fraction of jackdaws in the flock that are paired. Because the correlation length can roughly be taken to be a measure of the global responsiveness of the flock, this result suggests that the more paired birds a jackdaw flock contains, the less effectively that flock can detect and evade predators. This effect can be reproduced by a Vicsek-style model with a topological interaction rule and two classes of individuals

with different interaction ranges [65]. Pairing thus appears to have an adverse effect on the group behavior, in a way that can be captured by simple modeling. That finding led us to question whether pairing also carries some advantage. And indeed, in addition to any benefits that long-term pairing may convey when not flocking, paired birds also gain individual benefits from pairing when participating in transit flocks. An analysis of the wingbeat frequencies of paired and unpaired birds shows that paired birds beat their wings more slowly on average, and thus expend less energy flying in the flock than their unpaired conspecifics [65]. This effect is not captured by simple Vicsek-style agent-based modeling, since such models do not consider energy expenditure; rather, self-propulsion is simply assumed at no cost to the individual.

Jackdaws in the winter roosting season, in contrast to the summer nesting season, roost in separate nests while taking care of their young, and transit flocks do not form. However, even in this season jackdaws will come together when responding to distinctive scolding calls to mob predators [69]. This behavior can be induced using model predators and playbacks of recorded scolding calls [70].

Mobbing flocks are qualitatively different from transit flocks. Paired birds, for example, are not evident, presumably because one member of each pair remains in the nest with the young. The more significant difference between mobbing and transit flocks, however, is that the interactions among individuals in mobbing flocks occur over metric rather than topological distances [70]. Rather than interacting with a fixed number of neighbors, jackdaws in mobbing flocks align their motion with neighbors over a real physical distance, perhaps because they need to be careful about keeping their distance from the predator. This difference has consequences for the structure of mobbing flocks. Whereas transit flocks do not show a qualitative dependence on flock size, small mobbing flocks are loose and disordered while large mobbing flocks are dense and polarized [70]. The development of this large-scale order as the flock density increases is captured remarkably well by the Vicsek model using a metric distance [71].

When tested against quantitative observational data, bottom-up, agent-based models thus capture a fairly broad range of the features of jackdaw flocks. In particular, we were able to use modeling to assess the likelihood that pairing (and, more generally, differences in local interaction range and type) was responsible for the decrease in correlation length that we observed. However, the results described here also illustrate the limitations of such models. In particular, the observation that jackdaws in transit flocks interact *via* topological distances but use metric distance in mobbing flocks dispels any notion that there may be a single model for bird flocks, or even a single model for a given species. Ecological context is an essential factor for designing appropriate models, and cannot be ignored.

DISCUSSION AND CONCLUSION

These four examples illustrate how different modeling approaches can be used to address questions about collective behavior in biological systems. For both harvester ants and turtle ants, we know at least some of the functions that the collective behavior performs: the regulation of foraging in the case of harvester ants, and the construction and maintenance of trails in the case of turtle ants. For both of these examples, modeling shows in a simplified way how these distributed systems can accomplish these tasks given only local information. For both midge swarms and jackdaw flocks, however, the situation is somewhat different because the purpose of the collective behavior is less clear. The role of modeling in these examples thus cannot be to explain how the group achieves a task. Instead, in the case of midge swarms, we used models to describe the nature and properties of their non-random aspects. For jackdaws, we used models to understand the consequences of differences in local interactions between different individuals and of different ways of determining interaction distance. Importantly, in none of our examples did we attempt to create a single, complete model for the collective behavior; rather, our models were designed to ask specific questions or test specific hypotheses.

We argue that this approach, recognizing the limitations of models and deploying them in targeted, judicious way, is not simply an expression of ignorance but instead is a necessary consequence of the characteristics of biological systems. Biology is not physics. Organisms are not all the same, and even single individuals do not always respond the same way to stimuli. However, these variations are not purely stochastic, but rather are influenced and biased by many factors. The powerful constraints of conservation laws and symmetries that give rise to universality in physics simply do not apply to biological systems. Additionally, the types of questions that are pertinent to a biologist are different from those typically asked in physics. For physicists, the consequence is that there will probably never be a single unified model of collective behavior in biology, or even of the simpler problem of collective movement. Instead, we must acknowledge that the goal of models based on the physics approach is to explicate general principles of how global properties can arise from local interactions, and perhaps to constrain what kinds of properties are possible, while making it clear that such models are not intended to reproduce the details of any particular biological system. All models are limited and imperfect. Biologists will not be able to take a model off the shelf and apply it to a new system. Instead, we can bring together the modeling tools from different approaches to learn more about how collective behavior operates, and to identify for further investigation the processes that we do not yet understand.

AUTHOR CONTRIBUTIONS

All authors listed have made a substantial, direct, and intellectual contribution to the work and approved it for publication.

FUNDING

NTO acknowledges support from the Army Research Laboratory under Grant No. W911NF-16-1–0185 and from the Human Frontier Science Program under Grant No. RGP0049/2017.

REFERENCES

1. Shellard A, Szabó A, Trepat X, and Mayor R Supracellular Contraction at the Rear of Neural Crest Cell Groups Drives Collective Chemotaxis. *Science* (2018) 362:339–43. doi:10.1126/science.aau3301
2. Gordon DM The Evolution of the Algorithms for Collective Behavior. *Cel Syst* (2016) 3:514–20. doi:10.1016/j.cels.2016.10.013
3. Gordon DM From Division of Labor to the Collective Behavior of Social Insects. *Behav Ecol Sociobiol* (2016) 70:1101–8. doi:10.1007/s00265-015-2045-3
4. Reynolds CW Flocks, Herds and Schools: A Distributed Behavioral Model. *SIGGRAPH Comput Graph* (1987) 21:25–34. doi:10.1145/37402.37406
5. Topaz CM, and Bertozzi AL Swarming Patterns in a Two-Dimensional Kinematic Model for Biological Groups. *SIAM J Appl Math* (2004) 65:152–74. doi:10.1137/s0036139903437424
6. Vicsek T, and Zafeiris A Collective Motion. *Phys Rep* (2012) 517:71–140. doi:10.1016/j.physrep.2012.03.004
7. Ramaswamy S The Mechanics and Statistics of Active Matter. *Annu Rev Condens Matter Phys* (2010) 1:323–45. doi:10.1146/annurev-conmatphys-070909-104101
8. Marchetti MC, Joanny JF, Ramaswamy S, Liverpool TB, Prost J, Rao M, et al. Hydrodynamics of Soft Active Matter. *Rev Mod Phys* (2013) 85:1143–89. doi:10.1103/revmodphys.85.1143
9. Sethna JP *Statistical Mechanics: Entropy, Order Parameters, and Complexity*. Oxford, UK: Oxford University Press (2021). doi:10.1093/oso/9780198865247.001.0001
10. Sultan SE *Organism and Environment: Ecological Development, Niche Construction and Adaptation*. New York: Oxford University Press (2015). doi:10.1093/acprof:oso/9780199587070.001.0001
11. Sumpter DJT, Mann RP, and Perna A The Modelling Cycle for Collective Animal Behaviour. *Interf Focus.* (2012) 2:764–73. doi:10.1098/rsfs.2012.0031
12. Box GEP Science and Statistics. *J Am Stat Assoc* (1976) 71:791–9. doi:10.1080/01621459.1976.10480949
13. Levins R *Evolution in Changing Environments*. Princeton: Princeton University Press (1968). doi:10.1515/9780691209418
14. Ouellette NT Empirical Questions for Collective-Behaviour Modelling. *Pramana - J Phys* (2015) 84:353–63. doi:10.1007/s12043-015-0936-5
15. Vicsek T, Czirók A, Ben-Jacob E, Cohen I, and Shochet O Novel Type of Phase Transition in a System of Self-Driven Particles. *Phys Rev Lett* (1995) 75:1226–9. doi:10.1103/physrevlett.75.1226
16. Couzin ID, Krause J, James R, Ruxton GD, and Franks NR Collective Memory and Spatial Sorting in Animal Groups. *J Theor Biol* (2002) 218:1–11. doi:10.1006/jtbi.2002.3065
17. DeAngelis DL, and Diaz SG Decision-making in Agent-Based Modeling: A Current Review and Future Prospectus. *Front Ecol Evol* (2019) 6:237. doi:10.3389/fevo.2018.00237
18. Toner J, and Tu Y Flocks, Herds, and Schools: A Quantitative Theory of Flocking. *Phys Rev E* (1998) 58:4828–58. doi:10.1103/physreve.58.4828
19. Toner J, Tu Y, and Ramaswamy S Hydrodynamics and Phases of Flocks. *Ann Phys* (2005) 318:170–244. doi:10.1016/j.aop.2005.04.011
20. Tennenbaum M, Liu Z, Hu D, and Fernandez-Nieves A Mechanics of Fire Ant Aggregations. *Nat Mater* (2016) 15:54–9. doi:10.1038/nmat4450
21. Bi D, Henkes S, Daniels KE, and Chakraborty B The Statistical Physics of Athermal Materials. *Annu Rev Condens Matter Phys* (2015) 6:63–83. doi:10.1146/annurev-conmatphys-031214-014336
22. Bain N, and Bartolo D Dynamic Response and Hydrodynamics of Polarized Crowds. *Science* (2019) 363:46–9. doi:10.1126/science.aat9891
23. Forrester JW *Industrial Dynamics*. Cambridge: MIT Press (1961)
24. Sandefur CI, Mincheva M, and Schnell S Network Representations and Methods for the Analysis of Chemical and Biochemical Pathways. *Mol Biosyst* (2013) 9:2189–200. doi:10.1039/c3mb70052f
25. Agathocleous M, and Harris WA Metabolism in Physiological Cell Proliferation and Differentiation. *Trends Cel Biol* (2013) 23:484–92. doi:10.1016/j.tcb.2013.05.004
26. Ingalls BP *Mathematical Modeling in Systems Biology: An Introduction*. Cambridge: MIT Press (2013)
27. Alon U *An Introduction to Systems Biology: Design Principles of Biological Circuits*. Boca Raton: CRC Press (2007)
28. Cheng X, and Ferrell JE, Jr. Apoptosis Propagates through the Cytoplasm as Trigger Waves. *Science* (2018) 361:607–12. doi:10.1126/science.aah4065
29. Roughgarden J *Theory of Population Genetics and Evolutionary Ecology*. Saddle River: Prentice-Hall (1979)
30. Gordon DM The Spatial Scale of Seed Collection by Harvester Ants. *Oecologia* (1993) 95:479–87. doi:10.1007/bf00317431
31. Gordon DM How colony Growth Affects Forager Intrusion between Neighboring Harvester Ant Colonies. *Behav Ecol Sociobiol* (1992) 31:417–27. doi:10.1007/bf00170609
32. Gordon DM, and Kulig AW Founding, Foraging, and Fighting: colony Size and the Spatial Distribution of Harvester Ant Nests. *Ecology* (1996) 77:2393–409. doi:10.2307/2265741
33. Adler FR, and Gordon DM Optimization, Conflict, and Nonoverlapping Foraging Ranges in Ants. *The Am Naturalist* (2003) 162:529–43. doi:10.1086/378856
34. Westoby M The Self-Thinning Rule. *Adv Ecol Res* (1984) 14:167–225. doi:10.1016/s0065-2504(08)60171-3
35. Tarnita CE, Bonachela JA, Sheffer E, Guyton JA, Coverdale TC, Long RA, et al. A Theoretical Foundation for Multi-Scale Regular Vegetation Patterns. *Nature* (2017) 541:398–401. doi:10.1038/nature20801
36. Greene MJ, and Gordon DM Cuticular Hydrocarbons Inform Task Decisions. *Nature* (2003) 423:32. doi:10.1038/423032a
37. Pinter-Wollman N, Bala A, Merrell A, Queirolo J, Stumpe MC, Holmes S, et al. Harvester Ants Use Interactions to Regulate Forager Activation and Availability. *Anim Behav* (2013) 86:197–207. doi:10.1016/j.anbehav.2013.05.012
38. Prabhakar B, Dektar KH, and Gordon DM The Regulation of Ant colony Foraging Activity without Spatial Information. *Plos Comput Biol* (2012) 8:e1002670. doi:10.1371/journal.pcbi.1002670
39. Davidson JD, Arauco-Aliaga RP, Crow S, Gordon DM, and Goldman MS Effect of Interactions between Harvester Ants on Forager Decisions. *Front Ecol Evol* (2016) 4:115. doi:10.3389/fevo.2016.00115
40. Gordon DM, Guetz A, Greene MJ, and Holmes S Colony Variation in the Collective Regulation of Foraging by Harvester Ants. *Behav Ecol* (2011) 22:429–35. doi:10.1093/beheco/arq218
41. Pagliara R, Gordon DM, and Leonard NE Regulation of Harvester Ant Foraging as a Closed-Loop Excitable System. *Plos Comput Biol* (2018) 14:e1006200. doi:10.1371/journal.pcbi.1006200
42. Gordon DM The Rewards of Restraint in the Collective Regulation of Foraging by Harvester Ant Colonies. *Nature* (2013) 498:91–3. doi:10.1038/nature12137
43. Gordon DM Local Regulation of Trail Networks of the Arboreal Turtle Ant, *Cephalotes Goniodontus*. *Am Naturalist* (2017) 190:E156–E169. doi:10.1086/693418
44. Chandrasekhar A, Gordon DM, and Navlakha S A Distributed Algorithm to Maintain and Repair the Trail Networks of Arboreal Ants. *Sci Rep* (2018) 8:9297. doi:10.1038/s41598-018-27160-3
45. Chandrasekhar A, Marshall JAR, Austin C, Navlakha S, and Gordon DM Better Tired Than Lost: Turtle Ant Trail Networks Favor Coherence over Shortest Paths. *bioRxiv*. doi:10.1101/714410
46. Charikar M, Shivam G, Gordon DM, and Shiragur K A Model for Ant Trail Formation and its Convergence Properties. In: *12th Innovations in Theoretical Computer Science Conference* (2021). p. 85
47. Kelley DH, and Ouellette NT Emergent Dynamics of Laboratory Insect Swarms. *Sci Rep* (2013) 3:1073. doi:10.1038/srep01073
48. Puckett JG, Kelley DH, and Ouellette NT Searching for Effective Forces in Laboratory Insect Swarms. *Sci Rep* (2014) 4:4766. doi:10.1038/srep04766
49. van der Vaart K, Sinhuber M, Reynolds AM, and Ouellette NT Environmental Perturbations Induce Correlations in Midge Swarms. *J R Soc Interf* (2020) 17:20200018. doi:10.1098/rsif.2020.0018
50. Attanasi A, Cavagna A, Del Castello L, Giardina I, Melillo S, Parisi L, et al. Collective Behaviour without Collective Order in Wild Swarms of Midges. *Plos Comput Biol* (2014) 10:e1003697. doi:10.1371/journal.pcbi.1003697
51. Attanasi A, Cavagna A, Del Castello L, Giardina I, Melillo S, Parisi L, et al. Finite-size Scaling as a Way to Probe Near-Criticality in Natural Swarms. *Phys Rev Lett* (2014) 113:238102. doi:10.1103/physrevlett.113.238102

52. Puckett JG, Ni R, and Ouellette NT Time-frequency Analysis Reveals Pairwise Interactions in Insect Swarms. *Phys Rev Lett* (2015) 114:258103. doi:10.1103/physrevlett.114.258103
53. Gorbonos D, Ianconescu R, Puckett JG, Ni R, Ouellette NT, and Gov NS Long-range Acoustic Interactions in Insect Swarms: An Adaptive Gravity Model. *New J Phys* (2016) 18:073042. doi:10.1088/1367-2630/18/7/073042
54. Gorbonos D, and Gov NS Stable Swarming Using Adaptive Long-Range Interactions. *Phys Rev E* (2017) 95:042405. doi:10.1103/physreve.95.042405
55. Reynolds AM, Sinhuber M, and Ouellette NT Are Midge Swarms Bound Together by an Effective Velocity-dependent Gravity? *Eur Phys J E* (2017) 40:46. doi:10.1140/epje/i2017-11531-7
56. Gorbonos D, van der Vaart K, Sinhuber M, Puckett JG, Reynolds AM, Ouellette NT, et al. Similarities between Insect Swarms and Isothermal Globular Clusters. *Phys Rev Res* (2020) 2:013271. doi:10.1103/physrevresearch.2.013271
57. Gorbonos D, Puckett JG, van der Vaart K, Sinhuber M, Ouellette NT, and Gov NS Pair Formation in Insect Swarms Driven by Adaptive Long-Range Interactions. *J R Soc Interf* (2020) 17:20200367. doi:10.1098/rsif.2020.0367
58. Okubo A Dynamical Aspects of Animal Grouping: Swarms, Schools, Flocks, and Herds. *Adv Biophys* (1986) 22:1–94. doi:10.1016/0065-227x(86)90003-1
59. Shoval O, Goentoro L, Hart Y, Mayo A, Sontag E, and Alon U Fold-change Detection and Scalar Symmetry of Sensory Input fields. *Proc Natl Acad Sci* (2010) 107:15995–6000. doi:10.1073/pnas.1002352107
60. Reynolds AM Langevin Dynamics Encapsulate the Microscopic and Emergent Macroscopic Properties of Midge Swarms. *J R Soc Interf* (2017) 15:20170806. doi:10.1098/rsif.2017.0806
61. van der Vaart K, Sinhuber M, Reynolds AM, and Ouellette NT Mechanical Spectroscopy of Insect Swarms. *Sci Adv* (2019) 5:eaaw905. doi:10.1126/sciadv.aaw9305
62. Sinhuber M, and Ouellette NT Phase Coexistence in Insect Swarms. *Phys Rev Lett* (2017) 119:178003. doi:10.1103/physrevlett.119.178003
63. Henderson IG, Hart PJB, and Burke T Strict Monogamy in a Semi-colonial Passerine: the Jackdaw *Corvus monedula*. *J Avian Biol* (2000) 31:177–82. doi:10.1034/j.1600-048x.2000.310209.x
64. Jolles JW, King AJ, Manica A, and Thornton A Heterogeneous Structure in Mixed-Species Corvid Flocks in Flight. *Anim Behav* (2013) 85:743–50. doi:10.1016/j.anbehav.2013.01.015
65. Ling H, Mclvor GE, van der Vaart K, Vaughan RT, Thornton A, and Ouellette NT Costs and Benefits of Social Relationships in the Collective Motion of Bird Flocks. *Nat Ecol Evol* (2019) 3:943–8. doi:10.1038/s41559-019-0891-5
66. Cavagna A, Cimarelli A, Giardina I, Parisi G, Santagati R, Stefanini F, et al. Scale-free Correlations in Starling Flocks. *Proc Natl Acad Sci* (2010) 107:11865–70. doi:10.1073/pnas.1005766107
67. Bialek W, Cavagna A, Giardina I, Mora T, Silvestri E, Viale M, et al. Statistical Mechanics for Natural Flocks of Birds. *Proc Natl Acad Sci* (2012) 109:4786–91. doi:10.1073/pnas.1118633109
68. Ballerini M, Cabibbo N, Candelier R, Cavagna A, Cisbani E, Giardina I, et al. Interaction Ruling Animal Collective Behavior Depends on Topological rather Than Metric Distance: Evidence from a Field Study. *Proc Natl Acad Sci* (2008) 105:1232–7. doi:10.1073/pnas.0711437105
69. Woods RD, Kings M, McIvor GE, and Thornton A Caller Characteristics Influence Recruitment to Collective Anti-predator Events in Jackdaws. *Sci Rep* (2018) 8:7343. doi:10.1038/s41598-018-25793-y
70. Ling H, McIvor GE, Westley J, van der Vaart K, Vaughan RT, Thornton A, et al. Behavioural Plasticity and the Transition to Order in Jackdaw Flocks. *Nat Commun* (2019) 10:5174. doi:10.1038/s41467-019-13281-4
71. Ginelli F, and Chaté H Relevance of Metric-free Interactions in Flocking Phenomena. *Phys Rev Lett* (2010) 105:168103. doi:10.1103/physrevlett.105.168103

Conflict of Interest: The authors declare that the research was conducted in the absence of any commercial or financial relationships that could be construed as a potential conflict of interest.

frontiers in Physics

ORIGINAL RESEARCH
published: 15 September 2021
doi: 10.3389/fphy.2021.715996

Impact of Variable Speed on Collective Movement of Animal Groups

Pascal P. Klamser[1,2†], *Luis Gómez-Nava*[1,3†], *Tim Landgraf*[3,4], *Jolle W. Jolles*[5†], *David Bierbach*[3,6,7†] *and Pawel Romanczuk*[1,2,3*†]

[1]Department of Biology, Institute for Theoretical Biology, Humboldt Universität zu Berlin, Berlin, Germany, [2]Bernstein Center for Computational Neuroscience, Berlin, Germany, [3]Cluster of Excellence, Science of Intelligence, Technische Universität Berlin, Berlin, Germany, [4]Department of Mathematics and Computer Science, Freie Universität Berlin, Berlin, Germany, [5]Center for Ecological Research and Forestry Applications (CREAF), Campus de Bellaterra (UAB), Barcelona, Spain, [6]Department of Biology and Ecology of Fishes, Leibniz-Institute of Freshwater Ecology and Inland Fisheries, Berlin, Germany, [7]Faculty of Life Sciences, Albrecht Daniel Thaer-Institute of Agricultural and Horticultural Sciences, Humboldt Universität zu Berlin, Berlin, Germany

OPEN ACCESS

Edited by:
Elena Agliari,
Sapienza University of Rome, Italy

Reviewed by:
Shradha Mishra,
Indian Institute of Technology (BHU), India
Nikolai Bode,
University of Bristol, United Kingdom

***Correspondence:**
Pawel Romanczuk
pawel.romanczuk@hu-berlin.de

†ORCID:
Pascal Klamser
orcid.org/0000-0003-2208-4391
David Bierbach
orcid.org/0000-0001-7049-2299
Pawel Romanczuk
orcid.org/0000-0002-4733-998X
Luis Gómez-Nava
orcid.org/0000-0002-2426-5906
Jolle W. Jolles
orcid.org/0000-0001-9905-2633

Specialty section:
This article was submitted to Social Physics, a section of the journal Frontiers in Physics

Received: *27 May 2021*
Accepted: *25 August 2021*
Published: *15 September 2021*

Citation:
Klamser PP, Gómez-Nava L, Landgraf T, Jolles JW, Bierbach D and Romanczuk P (2021) Impact of Variable Speed on Collective Movement of Animal Groups. Front. Phys. 9:715996. doi: 10.3389/fphy.2021.715996

The collective dynamics and structure of animal groups has attracted the attention of scientists across a broad range of fields. A variety of agent-based models have been developed to help understand the emergence of coordinated collective behavior from simple interaction rules. A common, simplifying assumption of such collective movement models, is that individual agents move with a constant speed. In this work we critically re-asses this assumption. First, we discuss experimental data showcasing the omnipresent speed variability observed in different species of live fish and artificial agents (RoboFish). Based on theoretical considerations accounting for inertia and rotational friction, we derive a functional dependence of the turning response of individuals on their instantaneous speed, which is confirmed by experimental data. We then investigate the interplay of variable speed and speed-dependent turning on self-organized collective behavior by implementing an agent-based model which accounts for both these effects. We show that, besides the average speed of individuals, the variability in individual speed can have a dramatic impact on the emergent collective dynamics: a group which differs to another only in a lower speed variability of its individuals (groups being identical in all other behavioral parameters), can be in the polarized state while the other group is disordered. We find that the local coupling between group polarization and individual speed is strongest at the order-disorder transition, and that, in contrast to fixed speed models, the group's spatial extent does not have a maximum at the transition. Furthermore, we demonstrate a decrease in polarization with group size for groups of individuals with variable speed, and a sudden decrease in mean individual speed at a critical group size ($N = 4$ for Voronoi interactions) linked to a topological transition from an all-to-all to a distributed spatial interaction network. Overall, our work highlights the importance to account for fundamental kinematic constraints in general, and variable speed in particular, when modeling self-organized collective dynamics.

Keywords: collective motion, biophysics, mathematical models, variable speed, social interactions, group size, phase transition

1 INTRODUCTION

The emergent, highly coordinated, collective movements of schools of fish, flocks of birds and insect swarms, are fascinating examples of biological self-organization. Our understanding of these collective systems has been significantly advanced over the past years through diverse research efforts in biology [1–5], mathematics [6–8], computer science [9, 10], engineering [11, 12], and statistical physics [13–17].

In addition to empirical observations, mathematical models are an important tool for studying self-organization and collective behavior, and have been instrumental in uncovering general principles of how robust, large-scale coordination can emerge from simple, local interactions between self-propelled agents [10, 18, 19].

When formulating models, in general and for animal collectives, one has to balance simplicity/generality and detailed resemblance to experimental systems. From a statistical physics point of view, it is viable to assume some sort of universality of the collective dynamics even in far-from-equilibrium situations. Thus, as long as the model accounts for crucial aspects of the microscopic dynamics, other microscopic details become irrelevant for the macroscopic behavior for sufficiently large systems over a long temporal scale. However, 1) there is no general way to tell when the system is sufficiently large, and 2) animal groups consist of tens to hundreds, rarely thousands or more, individuals. Therefore, animal collectives should be rather viewed as mesoscopic systems, where the actual details of individual movement behavior may play an important role [20], and caution is advised when simplifying modeling assumptions.

A particularly prominent simplification often encountered in models of collective behavior is the assumption of constant speed of individual agents [13, 21–23]; for exceptions see [24–28]. However, although animals may generally tend to move at a certain, often preferred, speed, they are also able to flexibly modify their speed, ranging from non-moving to the maximum of their movement capacity. Speed adaptation due to environmental factors or social interactions [2]—ignored in constant speed models—as well as heterogeneity thereof, may play a decisive role in the ability of groups to coordinate their movement and thereby the structure of animal groups [29]. Indeed, experiments demonstrated that speed influences the collective behavior strongly, via a coupling to polarization/alignment [3, 22, 25, 29–31] which could also be shown at the local scale [25], i.e. regions in the shoal with faster fish are more polarized. In most former simulation studies, agents' speed was modelled to modify the turning rate or the assumed social forces, but was generally set to be fixed rendering speed to a mere parameter [3, 21, 22, 32]. However, a couple of studies have shown that variable speed has repercussions on group-level patterns and can lead to qualitatively new, emergent phenomena on the group level as for example bi-stable behavior with respect to polarization [24, 25]. In this bistable region, the group remains in the initiated collective state (ordered vs. disordered) because 1) the strong alignment force maintains the order (stable order) or 2) the velocity alignment reduces the speed, because the magnitude of the mean neighbor velocity is low, which allows a faster turning initiated by noise (stable disorder). These findings demonstrate the important role of feedbacks between speed, turning, and social interactions for the emergence and stability of collective states.

These feedbacks incorporate both, the physics and behavioral side of collective behavior. Due to this combination, they have not been explored, to our best knowledge, in the field of 1) active aligning particle models [16, 18, 33, 34], which are often variants of the Vicsek model that either lack inertia, repulsion and/or speed variability (none of those is present in the Vicsek model), 2) active Brownian particles [35] which consider speed variablility and repulsion but operate normally in the over-damped limit (no inertia) and rarely take alignment into account, 3) burst-coast models [26–28, 36] which model swimming behavior in greater detail (distinct phases of de- and acceleration) but either speeds are picked randomly independent of social interactions and current state [27, 36] or the focus was to resemble experimentally observed individual behavior in detail without investigating emergent effects on the collective level [26, 28].

In general, individuals in a group can differ in their phenotype (e.g. animal personality) that can be strongly linked and result in differences in movement speed [3, 37–39]). The inter-individual variability in preferred movement speed has been found to influence spatial self-sorting (faster individuals sort to the front of the shoal), cohesion and polarization of groups [3, 21, 30], but its role decreases with larger group sizes [39]. Importantly, already in behaviorally homogeneous groups, with individuals having highly similar preferred speeds, their instantaneous speed will dynamically vary over time due to individuals' direct response to social and environmental cues as well as internal decision processes. Both these types of speed variability will be important for the collective movement dynamics.

In this study, we focus on investigating the role of within-individual speed variability on emergent, self-organized collective movement using an agent-based model. It is meant to represent real animal groups, and we will discuss the role of inertia and friction and how these link speed, turning and social interactions. We will first provide an experimental motivation for our modeling ansatz by showing the ubiquity of speed variability in living and robotic fish and providing evidence for coupling between turning behavior and instantaneous speed, which can be theoretically understood by considering self-propelled movement with inertia. Inspired by these results, we will then investigate an agent-based model and demonstrate how the ability of individuals to flexibly adapt their speed in response to social interactions and fluctuations has major consequence for the emergent collective dynamics.

2 METHODS

2.1 Experimental Data

In order to determine the extent of within-individual variability in movement speeds, we analyzed previously published data sets of individual movement of the Trinidadian guppy [30] and

TABLE 1 | List of previously published tracking data used in our analysis. The table lists major characteristics of the datasets we used to show within-individual speed variability. The # of tracks indicates the number of individual tracks used for the analysis. Du to the initial study designs and questions, tracks may represent repeated measures of the same (Guppy: 20 individuals, RoboFish 1 replica) or different individuals (Molly single ind, Molly groups: 8 with 4 ind. per group). Please find exact study designs in the respective references.

	RoboFish	Guppy	Molly (single)	Molly (group)
Species	—	*Poecilia reticulata*	*Poecilia formosa*	*Poecilia formosa*
# of tracks	39	40	35	32
Observation time	10 min	10 min	6 min	5 min
Arena dimensions	88 × 88 cm	88 × 88 cm	48.5 cm diameter	60 × 30 cm
Water depth	7.5 cm	7.5 cm	3 cm	5 cm
Frame acquisition	30 FPS	30 FPS	30 FPS	30 FPS
Sex	—	Female	Female	Female
Tracking method	BioTracker [41]	BioTracker	Ethovision (10.1)	Ethovision (XT12)
References	Jolles et al. [30]	Jolles et al. [30]	Bierbach et al. [38]	Doran et al. [40]

individual and group movement of the clonal Amazon molly [38, 40] as well as a biomimetic robot ("RoboFish", [3]). We include the RoboFish to highlight that the movement constraints due to inertia and turning friction are general and not limited to biological agents. All data sets consist of positional tracking data from laboratory observations with a sampling frame rate of 30 fps, circular or rectangular arenas smaller than 1 square meter in size and only female fish, as summarized in **Table 1** and explained in more detail in **Supplementary Material Section I**.

2.2 Processing of Trajectories

The tracking data obtained for the different species and the robotic fish encodes the position $\mathbf{x}_i(t) = [x_i(t), y_i(t)]^T$ of the individual i for each frame t. We approximate the velocity of each individual from subsequent positions by computing:

$$\mathbf{v}_{i,x}(t + \Delta t) = \frac{\mathbf{x}_i(t + \Delta t) - \mathbf{x}_i(t)}{\Delta t}. \tag{1}$$

We can approximate the direction of motion of individual i by $\varphi_i(t) = arctan2(v_{i,y}(t),\ v_{i,x}(t))$. Similar to **Eq. 1**, we compute the angular speed $\dot{\varphi}(t)$ of each individual.

2.3 Fundamental Relations Between Speed and Turning

The fundamental equation of motion for a self-propelled agent i reads:

$$\frac{\mathrm{d}\mathbf{v}_i(t)}{\mathrm{d}t} = \frac{1}{m}\mathbf{F}_i(t) \tag{2}$$

with $\mathbf{v}_i$ as the velocity vector of the agent, m it's mass and $\mathbf{F}_i$ being total force acting on it. Please note that, in the following, we omit the explicit time dependence for simplicity. The velocity vector can be expressed via the speed v_i and the heading angle φ_i to $\mathbf{v}_i = v_i[\cos\varphi_i, \sin\varphi_i]^T = v_i\ \hat{\mathbf{e}}_{v,i}$. We can reformulate (in detail shown in **Supplementary Material Section II**) the velocity dynamics in terms of speed and heading angle dynamics [42] to

$$\frac{\mathrm{d}v_i}{\mathrm{d}t} = \frac{\mathbf{F}_i}{m} \cdot \hat{\mathbf{e}}_{v,i} \tag{3}$$

$$\frac{\mathrm{d}\varphi_i}{\mathrm{d}t} = \frac{\mathbf{F}_i}{v_i\ m} \cdot \hat{\mathbf{e}}_{\varphi,i} \ \text{ with } \ \hat{\mathbf{e}}_{v,i} = \begin{bmatrix} \cos\varphi_i \\ \sin\varphi_i \end{bmatrix}. \tag{4}$$

Therefore, without any further assumptions, we see that the turning is inversely proportional to the current speed, i.e. $\mathrm{d}\varphi_i/\mathrm{d}t \propto 1/v_i$. However, the inverse proportionality results in instantaneous turning for $v_i = 0$, which is unrealistic and is caused by assuming a point-like object. To provide a simple correction for this unreasonable assumption, we follow [43] and introduce a rotational friction force acting on the velocity

$$\frac{\mathrm{d}\mathbf{v}_i}{\mathrm{d}t} = \frac{1}{m}\left(\mathbf{F}_i - \alpha\ \frac{\mathrm{d}\varphi_i}{\mathrm{d}t}\ \hat{\mathbf{e}}_{\varphi,i}\right) \tag{5}$$

with α as rotational friction coefficient. If we repeat the steps from above analogously, the speed dynamics remain unchanged (**Eq. 3**) but the change in heading angle reads now:

$$\frac{\mathrm{d}\varphi_i}{\mathrm{d}t} = \frac{\mathbf{F}_i}{(v_i + \alpha)\ m} \cdot \hat{\mathbf{e}}_{\varphi,i}\ . \tag{6}$$

In the context of self-propelled agents, the above relation implies that the turning rate of an individual, in response to a force $\mathbf{F}_i$ acting on the agent or generated by the agent itself, depends on its speed v_i. For a constant force $|\mathbf{F}_i| = const.$, faster agents will turn slower. Alternatively, in order to turn at the same rate, individuals moving at different speeds have to adjust the strength of their turning force linearly with their current speed. We emphasize that this fundamental relation, ignored in most models of collective behavior explicitly modeling turning rates, holds both for fixed speeds $v_i := v_{0,i} = const.$, as well as for variable speeds $v_i := v_i(t)$.

2.4 Fitting Experimental Data and Model Comparison

We introduced in the preceding **Section 2.3 Eq. 4** that accounts for inertia effects and **Eq. 6** that additionally accounts for constraints due to turning friction. Here we treat the force in angular direction $F_\varphi = \mathbf{F} \cdot \hat{\mathbf{e}}_\varphi$, and the rotational friction coefficient α as parameters. In order to fit and state which of

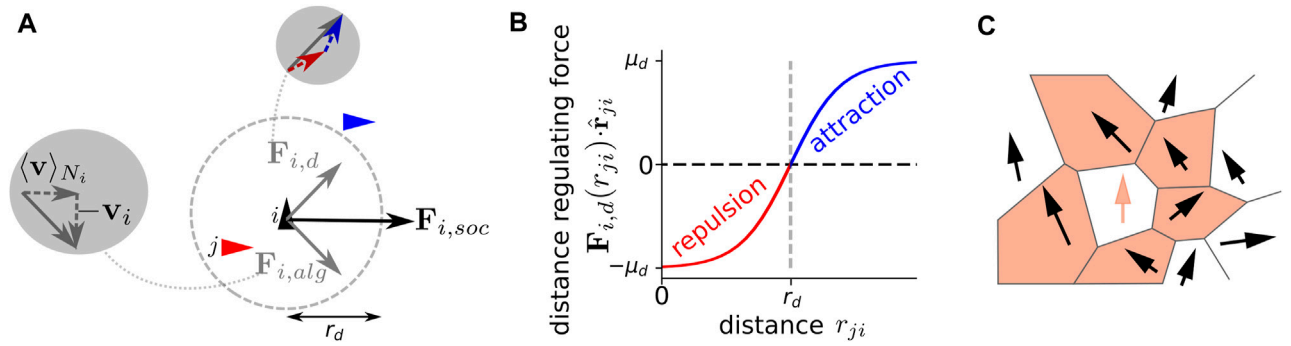

FIGURE 1 | Implementation of social interactions. A focal agent (black triangle) responds to neighbors (red and blue triangle) via a velocity alignment force $\mathbf{F}_{i,alg}$, which aims at minimizing the velocity difference to the mean neighbor velocity $\langle \mathbf{v} \rangle_{N_i}$, and a distance regulating force $\mathbf{F}_{i,d}$, their sum corresponds to the social force $\mathbf{F}_{i,soc}$ **(A)**. For simplicity the distance regulating force has a sigmoidal distance dependence: it is repulsive for distances closer, attractive for distances larger than a preferred distance r_d **(A,B)**. Note, the sign of the projection of $\mathbf{F}_{i,d}$ onto the distance vector $\hat{\mathbf{r}}_{ji}$ defines the direction towards (+) or away (–) from the respective neighbor j. The neighborhood of a focal agent (red arrow) is defined by its Voronoi neighbors (black arrows in red cells, **C**).

the two models represents the data best, we use a maximum likelihood estimation and compare both fits using the Akaike Information Criterion (AIC) [44] and the Bayesian Information Criterion (BIC) [45]. This procedure has the advantage, over an ordinary least square fit, that the AIC and BIC can be computed without requiring normally distributed residuals. Note that **Eq. 6** has one parameter more (α), and AIC and BIC penalize a larger number of parameters and therefore prevent overfitting, whereby the penalty term is larger for the BIC. The model with the lowest AIC or BIC is preferred [46, 47].

2.5 The Model

As explained in **Section 2.3**, our model mimics the movement behavior of real fish by obeying fundamental physics relations (inertia and friction). This is mathematically expressed in **Eqs 5**, **6**. Additionally, the interaction between fish is modelled by using the continuous version (i.e. overlapping instead of discrete zones) of a well established three-zone model that traditionally uses fixed speed [19]. The force acting on an individual i has a self-propulsion term (including noise) and a social term. We can express this as: $\mathbf{F}_i(t) = \mathbf{F}_{i,\mathrm{sp}}(t) + \mathbf{F}_{i,\mathrm{social}}(t)$. The self-propulsion force takes into account two main factors: 1) the tendency of an individual to keep a preferred speed v_0 and 2) the fluctuations on the linear speed v and the angular speed $\dot{\varphi}$

$$\mathbf{F}_{i,\mathrm{sp}}(t) = \left(\beta(v_0 - v_i(t)) + \sqrt{2D_v}\,\xi_v(t)\right)\hat{\mathbf{e}}_{v,i} + \left(\sqrt{2D_\varphi}\,\xi_\varphi(t)\right)\hat{\mathbf{e}}_{\varphi,i}, \tag{7}$$

where β is the speed relaxation coefficient, leading to the relaxation of the speed towards the preferred speed v_0 in the absence of other perturbations with the time constant $\tau_v = \beta^{-1}$. For solitary agents in the absence of external forces, the width of the speed distribution will be inversely proportional to β, i.e. low β corresponds to large speed variability and high β to small variability around v_0. D_v and D_φ are diffusion coefficients setting the noise intensity in v and φ, respectively, whereas ξ_v and ξ_φ are independent, Gaussian white noise processes. The social interactions are explained in detail in the following.

2.5.1 Social Interactions

We consider a social force that combines two fundamental types of interactions among individuals: 1) an alignment force $\mathbf{F}_{i,alg}$ and 2) a distance-regulating force $\mathbf{F}_{i,d}$ (**Figures 1A,B**). Thus, we can express the total social force as $\mathbf{F}_{i,\mathrm{social}}(t) = \mathbf{F}_{i,alg}(t) + \mathbf{F}_{i,d}(t)$. We use Voronoi tesselation to define the neighborhood of a focal individual i, which is labeled as $\mathbb{N}_i$ (**Figure 1C**). A Voronoi interaction network can, on the one hand, be efficiently computed, while on the other hand it is a good approximation of visual interaction networks [48]. The mathematical expression of the alignment force is:

$$\mathbf{F}_{i,alg}(t) = \frac{1}{|\mathbb{N}_i|}\sum_{j\in\mathbb{N}_i} \mu_{alg}\,\mathbf{v}_{ji}(t), \tag{8}$$

where μ_{alg} is the alignment strength and $\mathbf{v}_{ji}(t) = \mathbf{v}_j(t) - \mathbf{v}_i(t)$. The distance-regulating social force assumes a preferred distance r_d that individuals try to maintain between each other. It is defined as:

$$\mathbf{F}_{i,d}(t) = \frac{1}{|\mathbb{N}_i|}\sum_{j\in\mathbb{N}_i} \mu_d \tanh\left(m_d\left(r_{ji}(t) - r_d\right)\right)\hat{\mathbf{r}}_{ji}(t), \tag{9}$$

where $\hat{\mathbf{r}}_{ji} = (\mathbf{r}_j - \mathbf{r}_i)/|\mathbf{r}_j - \mathbf{r}_i|$ is a unitary vector from agent i to agent j, $r_{ji} = |\mathbf{r}_j - \mathbf{r}_i|$, μ_d is the strength of the force and m_d is the slope of the change from repulsion ($r_{ji} < r_d$) and attraction ($r_{ji} > r_d$) (**Figure 1B**). In principle, it is possible to extract a specific functional form of the repulsion and attraction interaction from experimental data [2, 27, 49, 50]. However, these functions will likely depend on the species and the ecological context, whereas the qualitative role of variable speed discussed below does not depend on the specific choice of the functional form of the inter-individual attraction-repulsion interactions. Therefore, for the sake of simplicity and generality, we have chosen a rather simple (sigmoidal) distance dependence for the distance regulating force controlled by only three parameters (μ_d, m_d, r_d), with the key property being a finite preferred distance r_d, which individuals try to keep to their neighbors. Note, that without the distance regulating force the

TABLE 2 | Default model parameters. If figures represent simulation with a different set of parameters, it is explicitly stated in the caption. The units are given in general length L and time T units.

Single				Collective			
preferred speed	v_0	1	$[L/T]$	group size	N	400	[1]
speed relaxation	β	0.2	$[1/T]$	alignment strength	μ_{alg}	2	$[1/T]$
turn friction	α	1	$[L/T]$	distance strength	μ_d	2	$[L/T^2]$
angular noise	D_φ	1	$[L^2/T^3]$	distance slope	m_d	2	$[1/L]$
velocity noise	D_v	0.4	$[L^2/T^3]$	preferred distance	r_d	1	$[L]$

model would be purely topological [16], but it could not reproduce the in nature omnipresent short-range repulsion and long-range attraction [2, 27, 49, 50].

2.5.2 The Equations of Motion

By considering the self-propulsion and social forces described above, we can write the explicit equations of motion for individuals, which resemble the equations in [24]:

$$\frac{\mathrm{d}v_i(t)}{\mathrm{d}t} = \beta(v_0 - v_i(t)) + F_{i,\mathrm{social},v}(t) + \sqrt{2D_v}\,\xi_v(t) \tag{10}$$

$$\frac{\mathrm{d}\varphi_i(t)}{\mathrm{d}t} = \frac{1}{v_i(t)+\alpha}\left(F_{i,\mathrm{social},\varphi}(t) + \sqrt{2D_\varphi}\,\xi_\varphi(t)\right), \tag{11}$$

with $F_{i,\mathrm{social},v}(t) = \mathbf{F}_{i,\mathrm{social}}(t)\cdot\hat{\mathbf{e}}_{v,i}(t)$ and $F_{i,\mathrm{social},\varphi}(t) = \mathbf{F}_{i,\mathrm{social}}(t)\cdot\hat{\mathbf{e}}_{\varphi,i}(t)$ beeing the projections of the social force on the heading direction $\hat{\mathbf{e}}_{v,i}$ and on the turning direction $\hat{\mathbf{e}}_{\varphi,i}$.

2.5.3 Parameter Choice and Boundary Conditions

All simulations are performed with no boundary conditions (open space) and the model parameters are summarized in **Table 2**. The length scale is defined by the preferred distance $r_d = 1$, which can be associated to the body size. With a preferred speed of $v_0 = 1$ the agents travel on average in one time unit their preferred distance. With a distance regulating force strength of $\mu_d = 2$ and $\beta \leq 2$ agents are able to prevent a collision by stopping. The angular noise $D_\varphi = 1$ is the counterpart of the alignment strength $\mu_{alg} = 2$ (same magnitude as μ_d), i.e. increasing one has the same effect as decreasing the other. Since the latter is varied in this study, the effect of both is explored. The same holds for the velocity noise $D_v = 0.4$ and the speed relaxation coefficient β. Note that with dimensionless equations, e.g. declaring the characteristic length and time as $L = r_d$ and $T = r_d/v_0$, two parameters could be reduced. However, to allow an easier interpretation, we refrain from doing so.

3 RESULTS

3.1 Experimental Data of Individual Fish

The two species of fish as well as the robotic agent exhibited qualitatively highly similar behavior: 1) non-negligible speed variability (**Figures 2A–C**), and 2) a strong decrease of turning rate with increasing speed (**Figures 2E–G**), which reflects the potential effects of inertia (see methods). Applying the same analyses on trajectories of our model simulation, we find the same patterns **Figures 2D,H**.

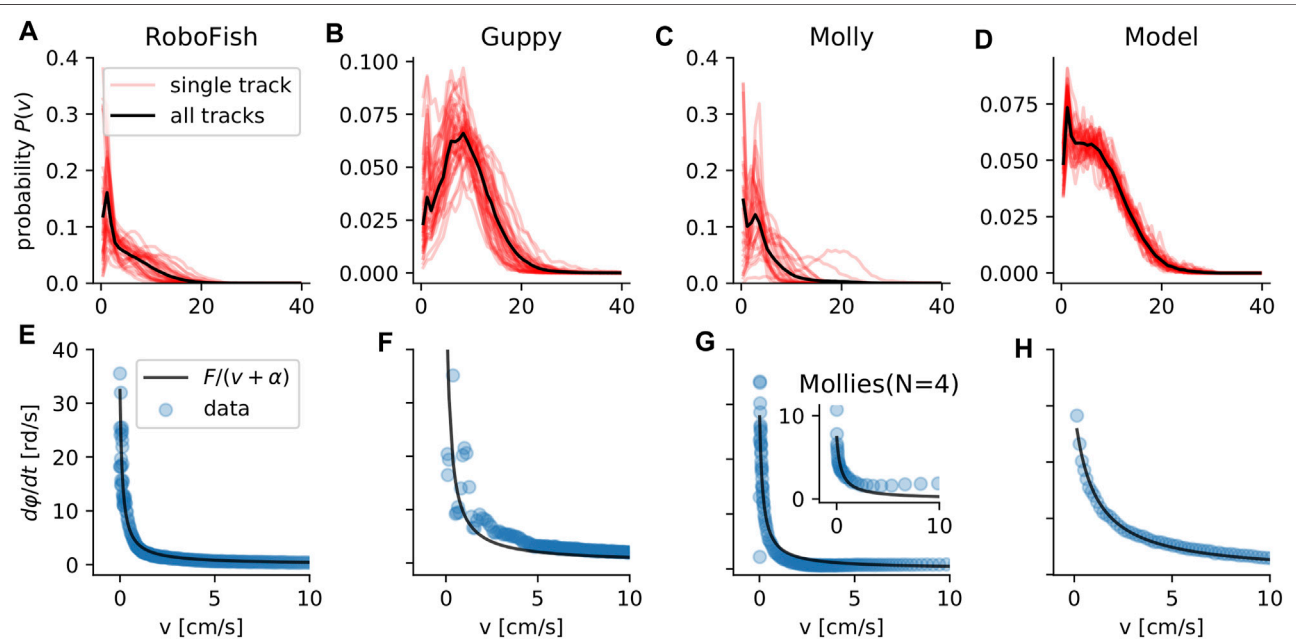

FIGURE 2 | Speed and turning of individuals. The speed probability distributions $P(v)$ for the experimental data (RoboFish, guppy, molly) and for model simulations of individuals **(A–D)**. Red transparent lines represent single tracks and the solid black line is the distribution of all tracks summarized. The absolute turning rate $\dot{\varphi}$ as a function of the speed v for the different individuals **(E–H)**. For mollies we also show the relation between turning rate speed of individuals swimming in groups of $N = 4$ (inset **G**). The parameters of the model simulations (described in **Section 2.5**) are listed in **Table 2**; **Supplementary Table S5** with the difference of a turn friction of $\alpha = 0.1$. The parameters of the model fits in **Supplementary Table S4**.

TABLE 3 | Statistical model comparison. Akaike (AIC) and Baysian (BIC) information criterion for a model without ($\frac{d\varphi}{dt} = F/v$) and with ($\frac{d\varphi}{dt} = F/(v+\alpha)$) turning-friction α for each model-species. For the same experimental data, the model with the smaller AIC or BIC is preferable, whereby the BIC penalizes additional parameters stronger and thus is more conservative. The values of the parameters α and F are listed in **Supplementary Table S4**.

	RoboFish		Guppy		Molly		Mollies (N = 4)		Model	
	AIC	BIC	AIC	BIC	AIC	BIC	AIC	BIC	AIC	BIC
$\frac{d\varphi}{dt} = F/v$	780	784	949	952	656	659	194	195	483	485
$\frac{d\varphi}{dt} = F/(v+\alpha)$	711	718	864	871	625	631	181	185	445	450

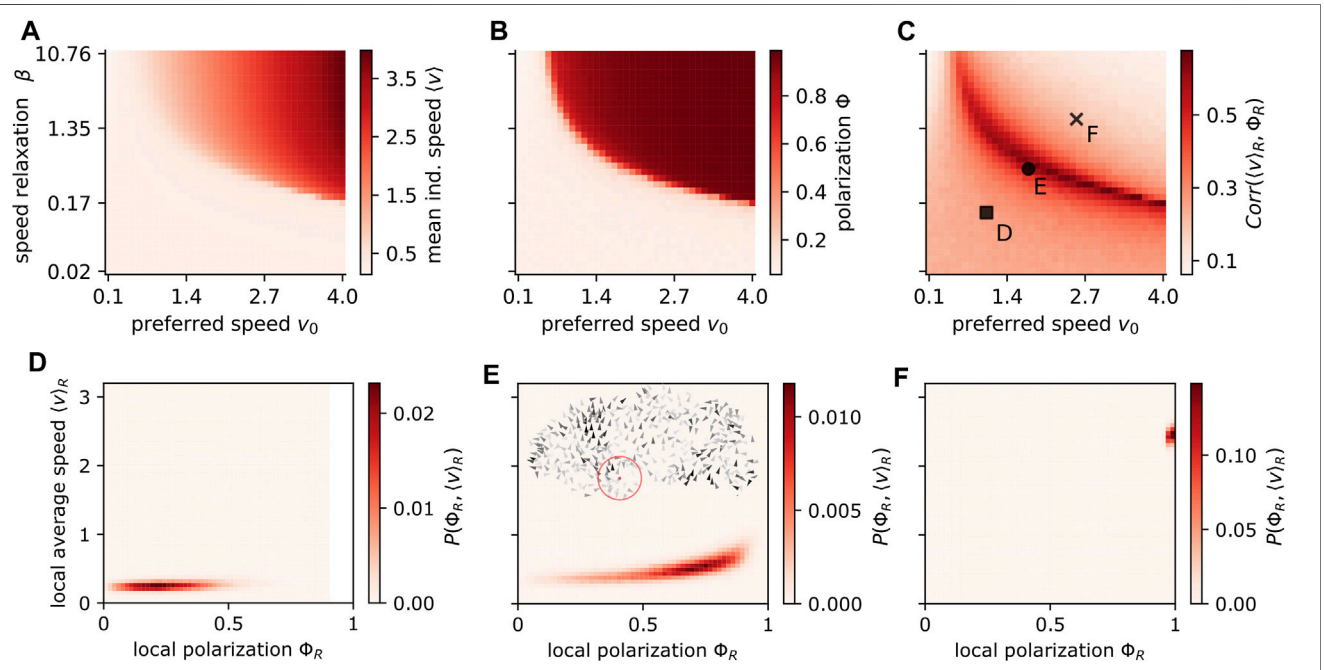

FIGURE 3 | Influence of preferred speed and speed variability on polarization and speed-polarization coupling. The preferred speed v_0 and the speed variability (modulated by the speed relaxation β) both affect the individual speed **(A)** and modulation of either of these parameters may induce orientational order marked by a high polarization Φ **(B)**. The transition to order can be understood by a local coupling between the local average speed $\langle v\rangle_R$ and the local polarization Φ_R, which we quantified via their correlation $Corr\,(\langle v\rangle_R, \Phi_R)$ **(C)**. The local averages consider all individuals within a circle of radius $R = 3$ around a focal one (red circle in inset **(E)**. Note that $\langle v\rangle_R$ is not the local group velocity (where a positive correlation with order is trivial) but the local average of the individual speed magnitudes. The specific dependence between local speed and order for three specific parameter choices (marked by square, circle and cross in **(C)** is shown for the disordered state **(D)**, the phase transition region **(E)** and the ordered state **(F)**. A snapshot of a simulation (inset **(E)**) where agents with higher speed are darker colored, with parameters corresponding to the black circle in **(C)**. The parameters of the simulations are listed in **Table 2**; **Supplementary Table S5**.

We find for all cases a speed distribution that shows a strong variation in speed (**Figures 2A–D**). The Coefficient of variation ($COV(v) = \sigma_v/\langle v\rangle$) of individual speed for the different datasets is: $COV(5) = 0.92 \pm 28$ (RoboFish), 0.57 ± 0.1 (guppy), 0.92 ± 0.78 (single molly), 0.68 ± 0.03 (model).

The model-fit to explain the four datasets was significantly ($\Delta AIC \in [31, 85]$, $\Delta BIC \in [28, 81]$) improved by taking turning friction into account (**Figures 2E–H**; **Table 3**; same for the group molly data: inset **Figure 2G**).

3.2 Collective Level Consequence of Speed Variability

The individual turning of our simulated agents resembles qualitatively (in terms of the functional dependence on speed) the behavior of real fish. This allows us now to explore how social interactions in combination with variable speed and turning restriction affect collective behavior in groups with $N = 400$.

3.2.1 Order Induced by Individual-Level Speed and Speed-Variation

Animals can vary in their preferred speed v_0, but also in their speed variability over time. We parametrized the latter by the speed relaxation coefficient β (see methods). For socially interacting agents, we find the mean individual speed $\langle v\rangle$ close to the preferred speed v_0 but only in the ordered state (**Figures 3A,B**). Interestingly, it is possible to change groups from an ordered to a disordered state by just changing the preferred speed and/or the speed variability. As shown for real, robotic and simulated fish (**Figures 2E–H**) individuals' turning rate is slower the higher their speed. This causes rotational random forces to be

damped for groups with larger speeds, facilitating order due to inertial restrictions on turning (**Figure 3B**).

In contrast, large speed-variability (low β) may lead to disorder, while a narrow individual speed distribution (large β) induces order. If the speed of an agent can vary, the velocity alignment can reduce the average speed of individuals: A focal agent i matches its velocity (direction and magnitude) with the mean velocity of its neighbors $\langle \mathbf{v} \rangle_{\mathbb{N}_i}$. However, for finite levels of directional fluctuations $|\langle \mathbf{v} \rangle_{\mathbb{N}_i}| \lessapprox v_i$, in other words, it will decelerate due to an effective social friction associated with the speed matching of the alignment interaction [24]. The reduced speed allows a faster turning and consequently enhances the angular noise and therefore disorder (**Figure 3B**). Thus, in any collective system where individuals also match their speed and not only their orientation to the local neighborhood, a group can be in different collective states only depending on the individuals' speed variability. We numerically confirmed that if agents only align their orientation and do not match their speed, the change in order by a different speed variability does not exist.

The speed variability has another highly robust emergent consequence. It allows agents of the same collective to differ in their instantaneous speed and since higher speeds induce order, we observe correlations on the local level between mean individual speed $\langle v \rangle_R$ and local polarization Φ_R with R as the radius of the circle from which the average is computed (**Figures 3C–F**). Please note that as we consider individual speed, the above correlation is different from the trivial correlation between local polarization and local group speed. The correlations between individual speed and local polarization is always positive and largest at the transition between disorder and order. The latter is a signature of phase transitions, where the susceptibility, i.e. the response to weak signals/fluctuations, is maximal. It means that information encoded in speed is best translated to a directional response at the transition region, and vice versa (likely to be beneficial in collective computation tasks).

The local coupling is an emergent consequence of the fundamental dependence of turning on speed. Thus, it is highly robust and the qualitatively same non-linear functional form was observed in experiments (compare **Figures 3D–F** with **Figure 1** in [25]). Most importantly, it weakens with low speed variability (**Figure 3C**) and does not exist for fixed speed models.

3.2.2 Mean Speed and Cohesion in Different Collective States

We have demonstrated above that the preferred speed and its variability can induce an order-disorder transition. Now, we keep the preferred speed fixed at $v_0 = 1$ and change the alignment strength μ_{alg}. By repeating this for different speed relaxation β we investigate how the collective behaves in the ordered and disordered state (controlled by μ_{alg}) under different speed variabilities.

The higher the speed variability of individuals, the larger alignment strengths are necessary for the collective to reach the ordered state (**Figure 4A**). This shift of the phase transition is more clearly depicted by shifting peaks of the susceptibility χ (**Figure 4A** inset), which is defined by the fluctuations of the polarization $\chi = N\left(\langle \Phi^2 \rangle - \langle \Phi \rangle^2\right)$.

The collective phase transition impacts the individual dynamics as well: The mean individual speed $\langle v \rangle$ shows a distinct minimum at the transition which vanishes for a high speed variability ($\beta = 1$, **Figure 4B**). The minimum in speed is related to the velocity alignment where a focal agent adjusts its velocity $\mathbf{v}_i$ to the average velocity vector of its neighbors $\langle \mathbf{v} \rangle_{\mathbb{N}_i}$. In the disordered state $\langle \mathbf{v} \rangle_{\mathbb{N}_i} \approx \mathbf{0}$, i.e. the alignment interaction induces an effective social friction $-\mu_{alg} v_i$ and thus slows the focal agent down [24]. It changes at the disorder-order transition where the neighborhood of each agent becomes increasingly polarized with increasing alignment strength. However, since there is always noise on the heading direction $|\langle \mathbf{v} \rangle_{N_i}| < v_0$, even in the strongly ordered state the individual speed is below the preferred speed v_0.

A very general qualitative change from fixed to variable speed can be observed in the group cohesion close to the phase transition. The area of the convex hull of the collective is maximal at the transition for fixed speeds. This maximum becomes less pronounced and finally vanishes with increasing speed variability (**Figure 4C**). The same holds for the nearest neighbor distance (**Figure 4C** inset). At the transition the directional correlation of the agents is maximal (i.e. susceptibility peaks, **Figure 4A** inset) and the directional fluctuations cause subgroups of the collective to head in different directions, leading to an expansion of the collective [19]. This expansion weakens with increasing speed variability because the distance regulating force can now lower the speed from a subgroup if it moves away from the shoal, effectively inhibiting expansion. A common consequence of weak cohesion is an increased probability for groups to split. However, for simplicity we assumed an unlimited attraction and alignment range, disabling fragmentation. The trend, that groups with a higher speed variability are more cohesive, is most striking at the transition, but holds in general in our model.

3.2.3 Group Size Dependent Effects

Group size is among the most biologically most important and variable parameters in the context of grouping. Thus, we investigate in this last part how group and individual measures change with group size N.

For low speed variability, the polarization remains high $\Phi \lesssim 1$ independent on N. If speed variability is high, polarization decreases with increasing group size and we expect $\Phi \to 0$ for even larger N (**Figure 5A**). Note that only in a narrow range close to the transition (marked by a large susceptibility, **Figure 5B**), the polarization saturates to intermediate values for large groups. The order-disorder transition for intermediate values of speed variability (β), is of the same nature as discussed for **Figure 3A**.

It is of particular interest, given that the size of animal groups is a key parameter of collective behaviour, if there is a specific threshold where the collective patterns of the system show a qualitative change. We find that when modelling agents with high speed variability, the mean individual speed $\langle v \rangle$ in our model undergoes a sudden change at $N = 3$ (**Figure 5C**). Until $N = 3$ the individual speed $\langle v \rangle$ is larger than v_0 and saturates towards v_0 with decreasing speed variability. The reason for $\langle v \rangle > v_0$ is that the speed distribution of individuals is asymmetric, with a

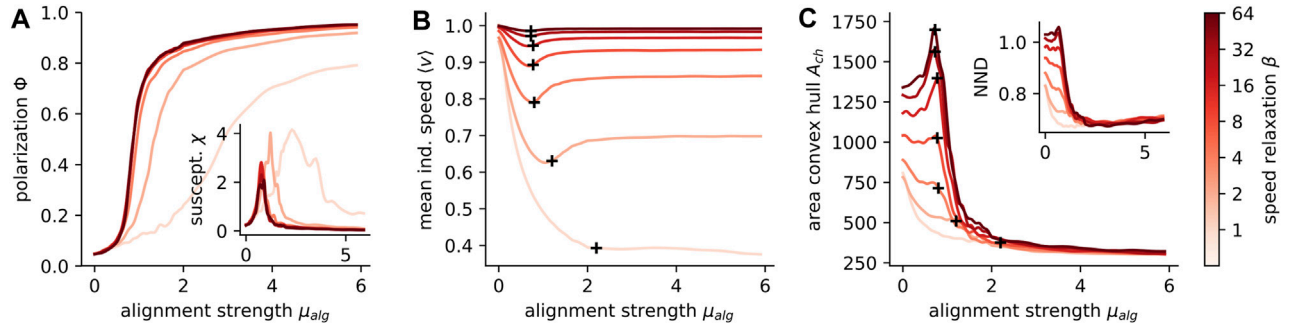

FIGURE 4 | Variable speed affects collective behavior in different states. Polarization Φ**(A)**, the susceptibility χ (inset **A**), the individual speed $\langle s \rangle$ **(B)**, the area of the convex hull **(C)** and the nearest neighbor distance *NND* (inset **C**) are shown in dependence on the velocity alignment strength μ_{alg}. Black crosses **(B,C)** mark the peak of the susceptibility, i.e. the location of the phase transition. The lines are color coded according to the speed relaxation as indicated at the colorbar, i.e. $\beta \in \{1, 2, 4, 8, 16, 32, 64\}$. The parameters of the simulations are listed in **Table 2**; **Supplementary Table S5**.

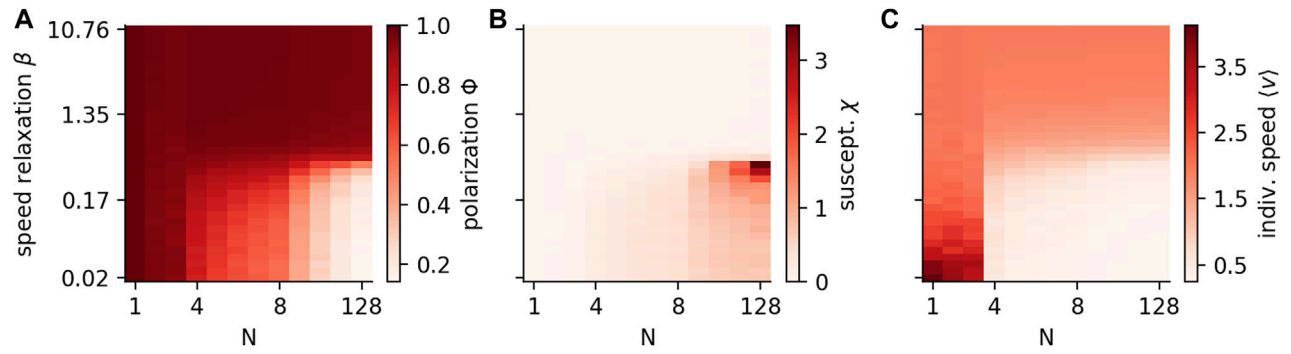

FIGURE 5 | Group size effects depend on speed variability. The polarization Φ **(A)**, the susceptibility χ **(B)** and the mean individual speed $\langle v \rangle$ **(C)** are shown for different speed relaxation β and group sizes N. The parameters of the simulations are listed in **Table 2**; **Supplementary Table S5** with the difference of a preferred speed of $v_0 = 2$.

long-tail at large speeds but cutoff at low speeds at $v = 0$ (**Figures 2A–D**), i.e. a maximum of the distribution is at $v = v_0$ but the mean is larger. For larger groups with $N \geq 4$, the speed is lower than the preferred speed but saturates also to v_0 in the fixed speed limit ($\beta \to \infty$).

This abrupt change can be understood through the interplay of individual dynamics and fundamental property of the interaction network: 1) A focal agent decelerates stronger the more its heading deviates from the average polarization of its neighborhood, i.e. $\mathrm{d}v_i/\mathrm{d}t \propto \mathbf{\Phi}_{\mathbb{N}_i} \cdot \hat{\mathbf{e}}_{v,i} - 1$ (derived in **Supplementary Material Section III**). 2) For Voronoi-type interactions and for group size $N \leq 3$, we have an all-to-all interaction network, which is not the case for $N > 3$. The second point is illustrated in **Figure 6**, where for $N > 3$ a set $\mathbb{D}_i$ of agents disconnected from the focal agent i can exists, i.e. $\mathbb{D}_i = \mathbb{A} \setminus (\mathbb{N}_i \cup \{i\}) \neq \varnothing$ for $N > 3$ with $\mathbb{A}$ as the set of all agents of the group. We confirmed this by computing the average number of neighbors during the simulations (**Figure 6**).

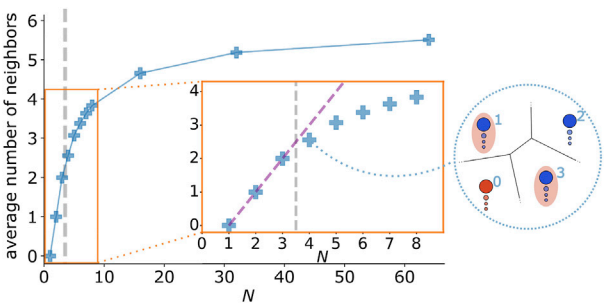

FIGURE 6 | Qualitative topological change with group size. Average Voronoi neighbor number for different group sizes. The dashed purple line (inset) marks the numbers of neighbors of a fully connected group. Illustrations of a typical spatial constellation for a group of size $N = 4$. The focal agent (0), its neighbors (1, 3) and an agent that is not connected to the focal agent (2) are shown. Note that only for group sizes $N > 3$ the latter exists, which hampers directional synchronization of the collective. The parameters of the simulations are listed in **Table 2**; **Supplementary Table S5** with the difference of a preferred speed of v0 = 2.

In summary, for $N \leq 3$ we have an all-to-all coupling, thus all agents receive the same social input, whereas for $N > 3$, centrally located individuals receive "independent" social inputs from different neighbors on different sides, which are not neighbors themselves, i.e. are not directly interacting. Thus, for $N > 3$ the centrally located individuals seek a compromise between two independent sources of information. As a consequence, the neighborhood of a focal agent located on the edge and the edge-agent itself, agree less in velocity. This results in slowing down the focal edge-agent, which in turn feeds back on the group behavior. To support this explanation we computed the vector product $\mathbf{\Phi}_{\mathbb{N}_i} \cdot \hat{\mathbf{e}}_{v,i}$ which shows a sudden decrease from $N = 3$ to $N = 4$ (**Supplementary Figure S1**).

4 DISCUSSION

We provide detailed empirical insights of speed variability in fish, providing evidence that inertia together with rotational friction explain the reduced turning ability of individuals at higher speeds. With our model that incorporates both, we explored the effect of speed variability on the emergent collective behavior. We found, among others, that 1) besides differences in (average) speed, also differences in individual speed variability (keeping preferred individual speed constant) can result in a change in polarization, 2) local coupling between speed and order is largest at the order-disorder transition, 3) individual speed variability decreases speed and increases cohesion at the phase transition and 4) the mean individual speed drops suddenly at a threshold group size ($N > 3$) but only at sufficiently high speed variability, which is intrinsically linked to the fundamental structure of the interaction network.

Our finding that higher speeds increase the polarization, is explained by the decrease of individuals turning rate at higher individual speeds that will inhibit individual directional noise, and thus facilitate stronger group polarization. Importantly, this speed-dependent turning effect comes on top of previously identified positive impact of higher speeds on group order [3]. The transition from ordered to disordered motion with speed was reported in experiments [22, 25, 29, 31]. However, corresponding models incorporating a dependence of turning rate on speed were based on fitting experimental data and not on the fundamental physics of inertia and rotational friction (see e.g. [22, 25]). This order-disorder transition induced by speed might enhance collective computation, such as the collective gradient sensing reported in golden shiners [1]: Fish swam fast in brighter and slow in darker regions and due to cohesion could collectively stay in the shade. A variable speed model that correctly accounts for inertia, could enhance the tendency of the collective to stay in the desired environment because there, low speeds increase disorder and thereby further decrease group speed prolonging the time in shade.

Additionally, we found that individual speed variability as well can change the polarization. The reason behind this dependence is speed matching, part of the social velocity alignment, that can lead to a decelerating *social friction*, where an agent adapts to the mean local group speed of its neighborhood [24]. We confirmed numerically (not shown) that this dependence vanishes if agents only align their orientation but do not match their speed. However, 1) this leads to extremely elongated groups that are unable to stay cohesive which is biologically unrealistic, 2) if agents ignore the speed of their conspecifics, flight cascades [51, 52] would not exist and 3) speed matching is experimentally confirmed for fish [3, 39]. Thus, our implementation of the alignment force, which incorporates speed matching, is very justified, and thus we also expect that the polarization dependence on speed variability is robust (implying our related findings as group size influence on speed and polarization).

We report a maximum of the local correlation between polarization and speed at the disorder-order transition and therefore elaborate the connection to collective computation by supporting the criticality hypothesis [53, 54]: information encoded in speed is most strongly linked to directional information at the transition, or the "critical point". In other words, individuals within a group show the strongest response to directional information via speed adaptations and vise versa at this transition. We also found that a minimum in cohesion at the transition exists for fixed-speed models, but weakens or even vanishes with increasing speed variability. This has important implications for studies that investigate collective behavior at criticality [19]. For example, a weak cohesion is associated with a high probability of group splits (smaller group size) and lower densities. Both effects decrease the defense against predators (safety in number [55], confusion effect [56]) and thus make the transition region less biological favorable. This effect would weaken/vanish in a variable speed model. Bode et al. [36] predict an opposite effect of speed variability on cohesion in a burst coast model where the speed variability is modulated via the length of the bursts (phases of acceleration), whereby they refer to fish with shorter bursts as more agitated fish. Shorter bursts allow more direction changes per time and thus also a better response to positional information of conspecifics, enhancing cohesion while reducing speed variability. This discrepancy shows, that it is important to clarify in future research how the general speed variability (explored in our model) plays together with the characteristics of distinct movement phases.

In our model with a high speed variability (low β), we observe a decrease in polarization with increasing group size. Linking our results again to criticality: only at the disorder-order transition does the polarization saturates for large groups to intermediate values. Recently, the same functional dependence was experimentally observed and reproduced in a model with only pairwise interactions [23]. Thus, we present an alternative explanation only based on variability in individual speed. In general, specific experimental data can be mimicked by a multitude of models which differ strongly in their microscopic interactions [21, 28, 57–59]. However, those models are most often fit to a specific experimental setup, i.e. to a certain group size, tank size and depth, and need to be recalibrated if the setup changes [22]. We avoid this with a distance regulating and alignment force that have simple, yet generic forms motivated by experimental observations [2, 27, 49, 50]. Additionally, we ensured robustness of the local coupling by repeating the simulations with circular reflecting boundary conditions.

We report a sudden speed decrease in our variable speed model at a critical group size of $N = 3$, linked to a transition from an all-to-all

network to a distributed spatial network. It might offer alternative means to test hypotheses about the underlying interaction network in real animal groups [48, 60]. In our model Voronoi-interactions cause the specific size threshold at $N = 3$, but for example for k-nearest neighbor interaction a group is all-to-all connected up to a threshold size directly set by k, i.e. for $N < k$. However, in order to observe this qualitative change the neighbors also need to match their speeds [3, 39] instead of only matching their movement direction, but, as discussed above, this assumption is reasonable. There might be also other limitations to this approach (e.g. we assume individual behavior does not change with group size [59]), however the emergent speed-interaction network coupling clearly shows how taking into account variable speed may introduce novel effects at the group level via the self-organized interplay of speed and orientation dynamics and social interactions.

To summarize, we have shown that speed variability affects polarization (on the local- and group level), cohesion (especially at the order-disorder transition) and can lead to new emergent transitions at specific groups sizes. Thus, we conclude that extreme caution should be taken when drawing strong conclusions on collective behavior of animal groups based on agent-based models with fixed speed.

DATA AVAILABILITY STATEMENT

The experimental data sets are available in repositories from previous articles ([38], [40], [30]). The code to run the agent-based model is available at github (https://github.com/PaPeK/swarm-variable-speed).

AUTHOR CONTRIBUTIONS

PK, LGN, and PR designed the analysis and wrote the paper. TL, JJ, and DB provided the experimental data and commented on the draft.

FUNDING

We received financial support by the DFG (German Research Foundation) under BI 1828/2-1, RO 4766/2-1, LA 3534/1-1 and under Germany's Excellence Strategy—EXC 2002/1 "Science of Intelligence"—project number 390523135.

ACKNOWLEDGMENTS

We are thankful to Jens Krause for stimulating discussions.

SUPPLEMENTARY MATERIAL

The Supplementary Material for this article can be found online at: https://www.frontiersin.org/articles/10.3389/fphy.2021.715996/full#supplementary-material

REFERENCES

1. Berdahl A, Torney CJ, Ioannou CC, Faria JJ, and Couzin ID. Emergent Sensing of Complex Environments by Mobile Animal Groups. *Science* (2013) 339: 574–6. doi:10.1126/science.1225883
2. Katz Y, Tunstrom K, Ioannou CC, Huepe C, and Couzin ID. Inferring the Structure and Dynamics of Interactions in Schooling Fish. *Proc Natl Acad Sci* (2011) 108:18720–5. doi:10.1073/pnas.1107583108
3. Jolles JW, Boogert NJ, Sridhar VH, Couzin ID, and Manica A. Consistent Individual Differences Drive Collective Behavior and Group Functioning of Schooling Fish. *Curr Biol* (2017) 27:2862–8. e7. doi:10.1016/j.cub.2017.08.004
4. Ward AJW, Herbert-Read JE, Sumpter DJT, and Krause J. Fast and Accurate Decisions Through Collective Vigilance in Fish shoals. *Proc Natl Acad Sci* (2011) 108:2312–5. doi:10.1073/pnas.1007102108
5. Krause J, and Godin JJ. Shoal Choice in the Banded Killifish (*Fundulus diaphanus*, Teleostei, Cyprinodontidae): Effects of Predation Risk, Fish Size, Species Composition and Size of Shoalsnkkk. *Ethology* (1994) 98:128–36. doi:10.1111/j.1439-0310.1994.tb01063.x
6. Torney CJ, Lorenzi T, Couzin ID, and Levin SA. Social Information Use and the Evolution of Unresponsiveness in Collective Systems. *J R Soc Interf* (2015) 12:20140893. doi:10.1098/rsif.2014.0893
7. Carrillo JA, Fornasier M, Toscani G, and Vecil F. Particle, Kinetic, and Hydrodynamic Models of Swarming. *Math Model collective Behav Socio-Economic Life Sci* (2010) 297–336. doi:10.1007/978-0-8176-4946-3_12
8. Ihle T. Kinetic Theory of Flocking: Derivation of Hydrodynamic Equations. *Phys Rev E Stat Nonlin Soft Matter Phys* (2011) 83:030901. doi:10.1103/PhysRevE.83.030901
9. Hidalgo J, Grilli J, Suweis S, Munoz MA, Banavar JR, and Maritan A. Information-Based Fitness and the Emergence of Criticality in Living Systems. *Proc Natl Acad Sci* (2014) 111:10095–100. doi:10.1073/pnas.1319166111
10. Olson RS, Hintze A, Dyer FC, Knoester DB, and Adami C. Predator Confusion Is Sufficient to Evolve Swarming Behaviour. *J R Soc Interf* (2013) 10:20130305. doi:10.1098/rsif.2013.0305
11. Li L, Nagy M, Graving JM, Bak-Coleman J, Xie G, and Couzin ID. Vortex Phase Matching as a Strategy for Schooling in Robots and in Fish. *Nat Commun* (2020) 11:5408. doi:10.1038/s41467-020-19086-0
12. Landgraf T, Bierbach D, Nguyen H, Muggelberg N, Romanczuk P, and Krause J. RoboFish: Increased Acceptance of Interactive Robotic Fish With Realistic Eyes and Natural Motion Patterns by Live Trinidadian Guppies. *Bioinspir Biomim* (2016) 11:015001. doi:10.1088/1748-3190/11/1/015001
13. Vicsek T, and Zafeiris A. Collective Motion. *Phys Rep* (2012) 517:71–140. doi:10.1016/j.physrep.2012.03.004
14. Cavagna A, Cimarelli A, Giardina I, Parisi G, Santagati R, Stefanini F, et al. Scale-Free Correlations in Starling Flocks. *Proc Natl Acad Sci* (2010) 107: 11865–70. doi:10.1073/pnas.1005766107
15. Feinerman O, Pinkoviezky I, Gelblum A, Fonio E, and Gov NS. The Physics of Cooperative Transport in Groups of Ants. *Nat Phys* (2018) 14:1–11. doi:10.1038/s41567-018-0107-y
16. Chaté H, Ginelli F, Grégoire G, Peruani F, and Raynaud F. Modeling Collective Motion: Variations on the Vicsek Model. *Eur Phys J B* (2008) 64:451–6. doi:10.1140/epjb/e2008-00275-9
17. Peruani F, Klauss T, Deutsch A, and Voss-Boehme A. Traffic Jams, Gliders, and Bands in the Quest for Collective Motion of Self-Propelled Particles. *Phys Rev Lett* (2011) 106:128101. doi:10.1103/physrevlett.106.128101
18. Vicsek T, Czirók A, Ben-Jacob E, Cohen I, and Shochet O. Novel Type of Phase Transition in a System of Self-Driven Particles. *Phys Rev Lett* (1995) 75:1226–9. doi:10.1103/physrevlett.75.1226
19. Klamser PP, and Romanczuk P. Collective Predator Evasion: Putting the Criticality Hypothesis to the Test. *PLOS Comput Biol* (2021) 17:1–21. doi:10.1371/journal.pcbi.1008832

20. Jolles JW, King AJ, and Killen SS. The Role of Individual Heterogeneity in Collective Animal Behaviour. *Trends Ecol Evol* (2020) 35:278–91. doi:10.1016/j.tree.2019.11.001
21. Couzin ID, Krause J, James R, Ruxton GD, and Franks NR. Collective Memory and Spatial Sorting in Animal Groups. *J Theor Biol* (2002) 218:1–11. doi:10.1006/jtbi.2002.3065
22. Gautrais J, Ginelli F, Fournier R, Blanco S, Soria M, Chaté H, et al. Deciphering Interactions in Moving Animal Groups. *Plos Comput Biol* (2012) 8: e1002678–11. doi:10.1371/journal.pcbi.1002678
23. Jhawar J, Morris RG, Amith-Kumar UR, Danny Raj M, Rogers T, Rajendran H, et al. Noise-Induced Schooling of Fish. *Nat Phys* (2020) 16. doi:10.1038/s41567-020-0787-y
24. Großmann R, Schimansky-Geier L, and Romanczuk P. Active Brownian Particles With Velocity-Alignment and Active Fluctuations. *New J Phys* (2012) 14:073033. doi:10.1088/1367-2630/14/7/073033
25. Mishra S, Tunstrøm K, Couzin ID, and Huepe C. Collective Dynamics of Self-Propelled Particles With Variable Speed. *Phys Rev E Stat Nonlin Soft Matter Phys* (2012) 86:011901. doi:10.1103/PhysRevE.86.011901
26. Harpaz R, Tkačik G, and Schneidman E. Discrete Modes of Social Information Processing Predict Individual Behavior of Fish in a Group. *Proc Natl Acad Sci USA* (2017) 114:10149–54. doi:10.1073/pnas.1703817114
27. Calovi DS, Litchinko A, Lecheval V, Lopez U, Pérez Escudero A, Chaté H, et al. Disentangling and Modeling Interactions in Fish With Burst-And-Coast Swimming Reveal Distinct Alignment and Attraction Behaviors. *Plos Comput Biol* (2018) 14:e1005933. doi:10.1371/journal.pcbi.1005933
28. Sbragaglia V, Klamser PP, Romanczuk P, and Arlinghaus R. Evolutionary Impact of Size-Selective Harvesting on Shoaling Behavior: Individual-Level Mechanisms and Possible Consequences for Natural and Fishing Mortality. *review Am Naturalist* (2020). doi:10.1101/809442
29. Kent MIA, Lukeman R, Lizier JT, and Ward AJW. Speed-Mediated Properties of Schooling. *R Soc Open Sci* (2019) 6:181482. doi:10.1098/rsos.181482
30. Jolles JW, Weimar N, Landgraf T, Romanczuk P, Krause J, and Bierbach D. Group-Level Patterns Emerge From Individual Speed as Revealed by an Extremely Social Robotic Fish. *Biol Lett* (2020) 16:20200436. doi:10.1098/rsbl.2020.0436
31. Tunstrøm K, Katz Y, Ioannou CC, Huepe C, Lutz MJ, and Couzin ID. Collective States, Multistability and Transitional Behavior in Schooling Fish. *Plos Comput Biol* (2013) 9:e1002915. doi:10.1371/journal.pcbi.1002915
32. Calovi DS, Lopez U, Ngo S, Sire C, Chaté H, and Theraulaz G. Swarming, Schooling, Milling: Phase Diagram of a Data-Driven Fish School Model. *New J Phys* (2014) 16:015026. doi:10.1088/1367-2630/16/1/015026
33. Toner J, and Tu Y. Flocks, Herds, and Schools: A Quantitative Theory of Flocking. *Phys Rev E* (1998) 58:4828–58. doi:10.1103/PhysRevE.58.4828
34. Toner J, Guttenberg N, and Tu Y. Swarming in the Dirt: Ordered Flocks With Quenched Disorder. *Phys Rev Lett* (2018) 121:248002. doi:10.1103/physrevlett.121.248002
35. Cates ME, and Tailleur J. Motility-Induced Phase Separation. *Annu Rev Condens Matter Phys* (2015) 6:219–44. doi:10.1146/annurev-conmatphys-031214-014710
36. Bode NWF, Faria JJ, Franks DW, Krause J, and Wood AJ. How Perceived Threat Increases Synchronization in Collectively Moving Animal Groups. *Proc R Soc B* (2010) 277:3065–70. doi:10.1098/rspb.2010.0855
37. Réale D, Reader SM, Sol D, McDougall PT, and Dingemanse NJ. Integrating Animal Temperament Within Ecology and Evolution. *Biol Rev* (2007) 82: 291–318. doi:10.1111/j.1469-185X.2007.00010.x
38. Bierbach D, Laskowski KL, and Wolf M. Behavioural Individuality in Clonal Fish Arises Despite Near-Identical Rearing Conditions. *Nat Commun* (2017) 8. doi:10.1038/ncomms15361
39. Herbert-Read JE, Krause S, Morrell LJ, Schaerf TM, Krause J, and Ward AJW. The Role of Individuality in Collective Group Movement. *Proc R Soc B* (2013) 280:20122564. doi:10.1098/rspb.2012.2564
40. Doran C, Bierbach D, and Laskowski KL. Familiarity Increases Aggressiveness Among Clonal Fish. *Anim Behav* (2019) 148:153–9. doi:10.1016/j.anbehav.2018.12.013
41. Mönck HJ, Jörg A, von Falkenhausen T, Tanke J, Wild B, Dormagen D, et al. BioTracker: An Open-Source Computer Vision Framework for Visual Animal Tracking. arXiv (2018).
42. Romanczuk P, Bär M, Ebeling W, Lindner B, and Schimansky-Geier L. Active Brownian Particles. *Eur Phys J Spec Top* (2012) 202:1–162. doi:10.1140/epjst/e2012-01529-y
43. Romanczuk P. *Active Motion and Swarming. From Individual to Collective Dynamics*. Berlin: Logos Verlag (2011) 12.
44. Akaike H. A New Look at the Statistical Model Identification. *IEEE Trans Automat Contr* (1974) 19:716–23. doi:10.1109/TAC.1974.1100705
45. Schwarz G. Estimating the Dimension of a Model. *Ann Statist* (1978) 6:461–4. doi:10.1214/aos/1176344136
46. Ward EJ. A Review and Comparison of Four Commonly Used Bayesian and Maximum Likelihood Model Selection Tools. *Ecol Model* (2008) 211:1–10. doi:10.1016/j.ecolmodel.2007.10.030
47. Wit E, Heuvel Ev. d., and Romeijn J-W. 'All Models Are Wrong.': an Introduction to Model Uncertainty. *Stat Neerlandica* (2012) 66:217–36. doi:10.1111/j.1467-9574.2012.00530.x
48. Strandburg-Peshkin A, Twomey CR, Bode NWF, Kao AB, Katz Y, Ioannou CC, et al. Visual Sensory Networks and Effective Information Transfer in Animal Groups. *Curr Biol* (2013) 23:R709–R711. doi:10.1016/j.cub.2013.07.059
49. Lukeman R, Li Y-X, and Edelstein-Keshet L. Inferring Individual Rules From Collective Behavior. *Proc Natl Acad Sci USA* (2010) 107:12576–80. doi:10.1073/pnas.1001763107
50. Herbert-Read JE, Perna A, Mann RP, Schaerf TM, Sumpter DJT, and Ward AJW. Inferring the Rules of Interaction of Shoaling Fish. *Proc Natl Acad Sci* (2011) 108:18726–31. doi:10.1073/pnas.1109355108
51. Rosenthal SB, Twomey CR, Hartnett AT, Wu HS, and Couzin ID. Revealing the Hidden Networks of Interaction in Mobile Animal Groups Allows Prediction of Complex Behavioral Contagion. *Proc Natl Acad Sci USA* (2015) 112:4690–5. doi:10.1073/pnas.1420068112
52. Sosna MMG, Twomey CR, Bak-Coleman J, Poel W, Daniels BC, Romanczuk P, et al. Individual and Collective Encoding of Risk in Animal Groups. *Proc Natl Acad Sci USA* (2019) 116:20556–61. doi:10.1073/pnas.1905585116
53. Mora T, and Bialek W. Are Biological Systems Poised at Criticality? *J Stat Phys* (2011) 144:268–302. doi:10.1007/s10955-011-0229-4
54. Muñoz MA. Colloquium: Criticality and Dynamical Scaling in Living Systems. *Rev Mod Phys* (2018) 90:31001. doi:10.1103/RevModPhys.90.031001
55. Krause J, and Ruxton GD. *Living in Groups*. Oxford University Press (2002).
56. Milinski M. Experiments on the Selection by Predators against Spatial Oddity of Their Prey. *Z für Tierpsychologie* (1977) 43:311–25. doi:10.1111/eth.1977.43.issue-2
57. Bastien R, and Romanczuk P. A Model of Collective Behavior Based Purely on Vision. *Sci Adv* (2020) 6:eaay0792–10. doi:10.1126/sciadv.aay0792
58. Romanczuk P, Couzin ID, and Schimansky-Geier L. Collective Motion Due to Individual Escape and Pursuit Response. *Phys Rev Lett* (2009) 102:010602. doi:10.1103/PhysRevLett.102.010602
59. Bode NWF, and Seitz MJ. Using Hidden Markov Models to Characterise Intermittent Social Behaviour in Fish shoals. *Sci Nat* (2018) 105:7. doi:10.1007/s00114-017-1534-9
60. Ballerini M, Cabibbo N, Candelier R, Cavagna A, Cisbani E, Giardina I, et al. Interaction Ruling Animal Collective Behavior Depends on Topological rather Than Metric Distance: Evidence From a Field Study. *Proc Natl Acad Sci* (2008) 105:1232–7. doi:10.1073/pnas.0711437105

Conflict of Interest: The authors declare that the research was conducted in the absence of any commercial or financial relationships that could be construed as a potential conflict of interest.

frontiers in Physics

BRIEF RESEARCH REPORT
published: 24 September 2021
doi: 10.3389/fphy.2021.678600

Larval Zebrafish Exhibit Collective Circulation in Confined Spaces

Haider Zaki[1], *Enkeleida Lushi*[2] *and Kristen E. Severi*[1]*

[1]Federated Department of Biological Sciences, New Jersey Institute of Technology, Newark, NJ, United States, [2]Department of Mathematical Sciences, New Jersey Institute of Technology, Newark, NJ, United States

Collective behavior may be elicited or can spontaneously emerge by a combination of interactions with the physical environment and conspecifics moving within that environment. To investigate the relative contributions of these factors in a small millimeter-scale swimming organism, we observed larval zebrafish, interacting at varying densities under circular confinement. If left undisturbed, larval zebrafish swim intermittently in a burst and coast manner and are socially independent at this developmental stage, before shoaling behavioral onset. Our aim was to explore the behavior these larvae as they swim together inside circular confinements. We report here our analysis of a new observation for this well-studied species: in circular confinement and at sufficiently high densities, the larvae collectively circle rapidly alongside the boundary. This is a new physical example of self-organization of mesoscale living active matter driven by boundaries and environment geometry. We believe this is a step forward toward using a prominent biological model system in a new interdisciplinary context to advance knowledge of the physics of social interactions.

Keywords: zebrafish, social interaction, living active matter, swimmers, confined collective motion

OPEN ACCESS

Edited by:
Orit Peleg,
University of Colorado Boulder,
United States

Reviewed by:
Sachit Butail,
Northern Illinois University,
United States
Ahmed El Hady,
Princeton University, United States
Patricia Yang,
Stanford University, United States

***Correspondence:**
Kristen E. Severi
severi@njit.edu

Specialty section:
This article was submitted to Social Physics, a section of the journal Frontiers in Physics

Received: *10 March 2021*
Accepted: *06 September 2021*
Published: *24 September 2021*

Citation:
Zaki H, Lushi E and Severi KE (2021) Larval Zebrafish Exhibit Collective Circulation in Confined Spaces. Front. Phys. 9:678600. doi: 10.3389/fphy.2021.678600

INTRODUCTION

The emergence of complex collective behavior of natural and artificial motile agents has long been a question of interest to scientists in many disciplines. The transition from disordered to ordered collective motion can be seen across scales, from micron long bacteria and colloids, to millimeter long ants and bees, to centimeter long crickets and bristle-bots, and even to meter-long fish and humans [1–3]. The complex behavior of flocks of birds, colonies of ants, swarms of bees and schools of fish emerges from the interactions of the constituent parts of the respective systems. While similarities in the patterns that such groups produce have suggested general principles governing the self-organization [4], it is also becoming clear that the specific patterns depend on the type of motile agent, scale, and also the type of interaction. For example, for fluid-immersed micro-scale units such as motile bacteria and colloids, it has become clear that mechanical interactions often mediated through the liquid are paramount to the type of eventual patterns [5, 6]. For larger animals such as birds, mechanics are not the only factor as others may become more prominent, e.g., visual input for birds [7], environmental factors for bees [8], sensory stimuli or social cues for humans [9].

Despite the large effort in studying the emergence of collective motion for various motile agents, little has been done to study how this behavior changes when the agents are confined, whether by hard walls or soft impediments. Recent work has shown that when swimming bacteria, colloids, spermatozoa, and even bristle-bots are placed in circular or racetrack dishes, then they will spontaneously start to circulate [5, 6, 10–13]. Even soft confinement can lead to locust milling [4] and human mosh pits [14]. Our approach was motivated by the need to develop a model where

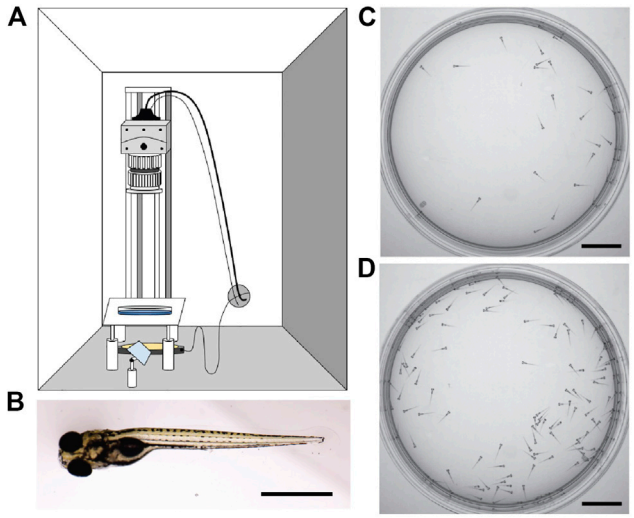

FIGURE 1 | Experimental observation of larval zebrafish swimming collectively at various densities. (A) Schematic of experimental set-up. **(B)** Image of a larval zebrafish at 6 days post-fertilization, scale bar 1 mm. Rostral (head) is to the left. **(C)** 30 larval zebrafish in the arena as captured by the camera. **(D)** 130 larval zebrafish in the arena. Scale bar for C-D 1 cm.

behavior can be observed easily, which is amenable to neurobiological perturbations, and which generates interesting and quantifiable individual and collective behavior. In the popular biological model organism *Danio rerio*, the zebrafish, swimming is influenced by fluid mechanics as well as by sensory stimuli [15–18]. Adult zebrafish have been studied extensively in both individual and collective contexts [19–24]. However, at the 5 days post-fertilization larval life stage, when zebrafish are approximately 4 mm in length, before the onset of social shoaling behavior [25, 26], they utilize different movement patterns from adult fish. Larval zebrafish, a millimeter with 2 Ls swimmer move in what is often termed a beat-and-glide or burst-and-coast discontinuous manner; they swim in bouts of movement followed by pauses [27]. This species has been extensively studied in terms of their kinematics, neurobiology, development, and behavior [28–32] but the individual or collective motion of larvae in confinement has not been explored previously.

At this life stage, larval zebrafish placed in low density have a usual social avoidance area of approximately 50 mm^2 surrounding their body and will initiate escape responses to avoid contact [33]. However, the set of observations we report here included confinement and a range of densities where larvae were forced to interact with others and did not permit them to maintain their preferred social avoidance area. These "escape" responses are short duration, high velocity movements, and can be directed away from noxious stimuli [34, 35, 36]. Here, we observed that when in confined environments at sufficiently high densities, larval zebrafish may spontaneously collectively perform a novel circling behavior or short duration "panic waves" along the confining dish. We report conditions under which the phenomenon of collective circling behavior may be elicited in larval zebrafish by use of confinement. Confined collective motion is a new and developing area of interest in the field of living active matter, where experiments at this scale and intermediate Reynolds number remain rare [36].

MATERIALS AND METHODS

Animals

Larval zebrafish used in these experiments were 5 days post-fertilization (dpf) AB wild-type (origin: ZIRC stock center, Eugene, Oregon) reared in an incubator at 28.5°C with a 14L: 10D light cycle. Larvae were generated from an adult colony maintained at NJIT in the Severi lab under Rutgers University-Newark IACUC oversight, PROTO201800041.

Acquisition

High-speed videos were collected on a custom-built setup (**Figure 1A**, **Supplemental Table S1**). A high-speed camera (Mikrotron GmbH, Germany) attached to a rail (ThorLabs) fitted with a 35 mm F1.4 lens (Fujinon) and an 850 nm bandpass filter (Midwest Optical) were used to acquire images to a Dell Precision 5820 computer fitted with a frame grabber (National Instruments) and running custom-written LabView software (National Instruments, available upon request) saving TIFF image stacks for each trial. Larvae were illuminated with 850 nm IR LEDs which are not within their visible spectra (Waveform Lighting) under an acrylic platform stabilized by Thorlabs components covered with light diffusers (Pro Gel, B&H Photo) within a custom-built enclosure (MiniTec Framing Systems, LLC) which was left open to room light. Videos were acquired at 200 Hz with 1,423 μs shutter speed at 648 × 648 pixel resolution, and trials were 6,000 frames or 30 s in duration. The same larvae were used for each trial. Videos were captured approximately 1–5 min after larvae were placed in the behavior enclosure to allow time for acclimation following handling. Animals were counted and added to the arena group before trial repeats occurred at each density stage (**Table 1**). Animals were recorded at room temperature during daytime in round petri dishes with 5.4 cm diameter.

Tracking and Trajectories

To generate tracks from raw videos, we utilized trackR, an R package written by Dr. Simon Garnier [38]. trackR is an object tracker for R allowing users to perform multi-object video tracking by background subtraction and adaptive thresholding. trackR outputted object trajectories as .csv files however with discontinuities, i.e. we could not assign particular tracks to individual larvae. These tracks were imported to MATLAB and plotted. To determine the distance traveled over tracks in separate regions within the dish, tracks were imported to MATLAB and the arena boundary and center were determined using a custom function, with a radius of 310 pixels. The inner circle was 70% of the radius (217 pixels) with the same center coordinates **Figures 2A,B**. Tracks within those regions were segregated and distances across all tracks for a given trial were calculated for three trials with 30 larvae and three trials with 130 larvae over 1,497 frames of the trial. Each trial and

TABLE 1 | Table of density across trial noting when circling behavior was observed.

Arena diameter (cm)	Number of larvae (n)	Density (larvae/cm^2)	Circling behavior	Trials
5.4	5	0.218	not observed	5
5.4	10	0.437	not observed	5
5.4	30	1.310	observed 1/5	5
5.4	50	2.183	observed 2/5	5
5.4	70	3.057	not observed	5
5.4	100	4.367	observed 3/6	6
5.4	130	5.677	observed 8/10	10

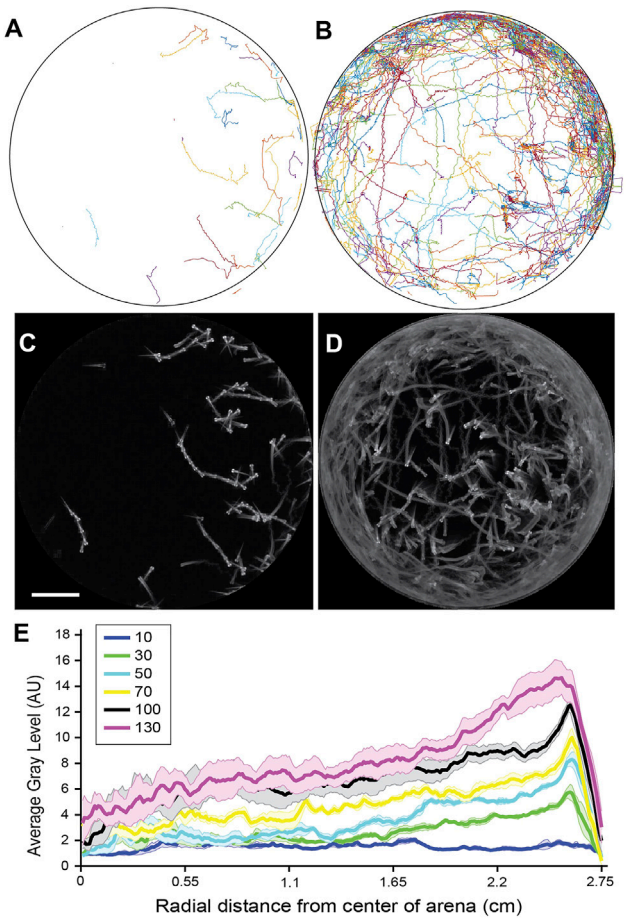

FIGURE 2 | Distribution of larval positions varies as a function of distance from the arena wall. (A) Tracked trajectories for a single trial with 30 larvae. **(B)** Tracked trajectories for a single trial with 130 larvae. **(C)** Standard deviation z-projection for the frames corresponding to A. **(D)** Standard deviation z-projection for the frames corresponding to B. **(E)** Average gray area of standard deviation z-projections plotted from the center of the arena to the border of the arena for 5 trials at each density. The mean is shown in bold and the standard error of the mean is shaded in a color corresponding to the density. Densities tested were: 10 larvae, 30 larvae, 50 larvae, 70 larvae, 100 larvae, and 130 larvae, in the same arena. Scale bar for A-D 1 cm.

the means were plotted along with the standard error of the mean **Figure 2C**. A standard *t*-test was applied between groups (ttest2 function in MATLAB) and *p*-values < 0.05 were considered significant. The mean tangential velocities and circulating order parameter were calculated using the trajectories from trackR with MATLAB custom code (**Figures 2D,E**).

Radial Distance Measure

To determine how position varied with radial distance **Figure 3E** using FIJI (NIH) and MATLAB, videos were reduced by ¼ in FIJI and cropped to exclude the pixels outside the arena. A standard deviation z-projection was applied to the image stacks to create a single image using FIJI. This process outputs a single image where each pixel represents the standard deviation value over all images in the stack at that particular pixel location (https://imagejdocu.tudor.lu/gui/image/stacks#zproject). Using the MATLAB function average_radial_profile_2 (Image Analyst, Mathworks author id:31,862) the average radial profile was calculated from a center location of each image and plotted.

Qualitative Assessment

For determination of the circling behavior (**Table 1**), a pair of qualitative assessments of the captured videos were used. First, when watching the videos at 30 Hz playback and paying attention to the region just inside the arena boundary, some collective circling instances were immediately obvious based on easily discernible rotational movement. When many conspecifics began moving in a coordinated manner around the edge of the dish in a single major direction, we took this to be circling behavior. A second qualitative identifier of circling motion was a correlate of the behavior that arises due to fluid flow. When a significant number of the larvae are circling near the boundary of the dish, a radial region of the larvae within the circling ring will exhibit larvae in counter-rotation, moving in the opposite circular direction to the major circling direction of the outer ring. This is characterized through the obvious lack of self-propelled movement (the larvae themselves are static), and oftentimes a drifting motion in a backward direction which is not a gait present in this species. Based on our understanding of fluid motion [6], this is strongly indicative of coordinated circling in one major direction. With either or both of these qualifications met, we could categorize a captured video to have circling behavior.

RESULTS

We set out to observe larval zebrafish behaving spontaneously under confinement at various densities and to determine whether

collective behavior emerged. Observing larval zebrafish behaving spontaneously at varying densities, from 5 to 130 individuals, in a 5.4 cm diameter arena (**Figure 1**), we found the animals moved freely within the arena in short bouts of swimming. We systematically tested a range of densities (**Table 1**) and found that at low densities the animals behaved relatively independently of each other, though the circular wall affected their motion as they tended to swim or stop by it more often. At high densities however the animals exhibited a high-speed circling behavior, with incidence increasing alongside density. At this density the larvae are forced to interact with other larvae as well as the boundary. The circling behavior appeared to initiate on occasions when larvae came close to each other, producing a response in the contacted larvae, and that the size and shape of the arena and the interaction with the wall produced a group of larvae circling near the edge of the arena (**Figure 2**, **Supplementary Movie S1**).

Tracking the positions of the animals confirmed there was a propensity to spend time in the outer region of the arena in proximity to the arena walls (**Figures 2A,B**). While a preference for the arena edges is well noted and was found at densities of 30 or greater larvae, the distribution in spatial position was highly biased toward the outer circumference of the arena at higher densities (**Figures 2C–E**). These higher densities of 100 larvae and greater 5.4 cm dish correlated with more frequent observation of the circling behavior (**Table 1**). We observed instances where the collective circulation slowed down, stopped, or initiated in competing directions with one direction of flow emerging as the dominant direction. This needs to be explored in future work investigating the factors that determine initiation, stopping, and direction of motion, keeping in mind that the fish can interact with others and the boundary not just through direct contact but also through fluid-mediated mechanical forces.

Indeed, when the traveled distances of each tracked position were plotted and separated into the wall-adjacent boundary region of the arena and compared to the central inner circle away from the boundary (**Figures 3A,B**), there were significant differences in the distance traveled when comparing high and low densities, and when comparing the two spatial regions at high densities (**Figure 3C**).

We quantify the active swimming bouts of the larvae by examining the azimuthal flow profile $\mathbf{v_t} = \langle \mathbf{v} \cdot \mathbf{t} \rangle_\theta$ where v is the instantaneous larva velocity measured from the trajectories, and **t** is the tangential direction at the larval position. **Figures 3D,E** show the profiles of $\mathbf{v_t}$ as a function of the distance from the dish center for three experiments each at $n = 30$ larvae (**Figure 3D**) and $n = 130$ larvae (**Figure 3E**). The positive direction is taken to be one with the dominant circulation direction (clock-wise or counter-clockwise). We notice higher $\mathbf{v_t}$, especially closer to the edge, for the higher density, meaning the larvae are moving tangentially, i.e., alongside the boundary especially since $\mathbf{v_t}$ is highest there. Negative $\mathbf{v_t}$ means counter-rotating movement, which matches the observations. We also calculate the vortex order parameter

$$\Phi = \frac{\sum_i |v_i \cdot t_i| / \left\| \sum_i v_i \right\| - 2/\pi}{1 - 2/\pi}$$

This parameter is used in many studies of confined collective motion to quantify collective circulation [6, 39]. $\Phi = 1$ means the motion is perfectly tangential/azimuthal, $\Phi = 0$ means the motion is disordered, and $\Phi < 0$ means the motion is radial. For our examples with $n = 30$ larvae, we get $\Phi = 0.0759, 0.0580, 0.0898$, whereas for $n = 130$ larvae we get $\Phi = 0.1295, 0.1327, 0.1120$. We note that Φ is higher for the higher density cases, meaning there is more circulation in those cases. While this is not as stong a signal as in the examples of bacteria [39], note that larval zebrafish do not have constant swimming speed and move in bouts.

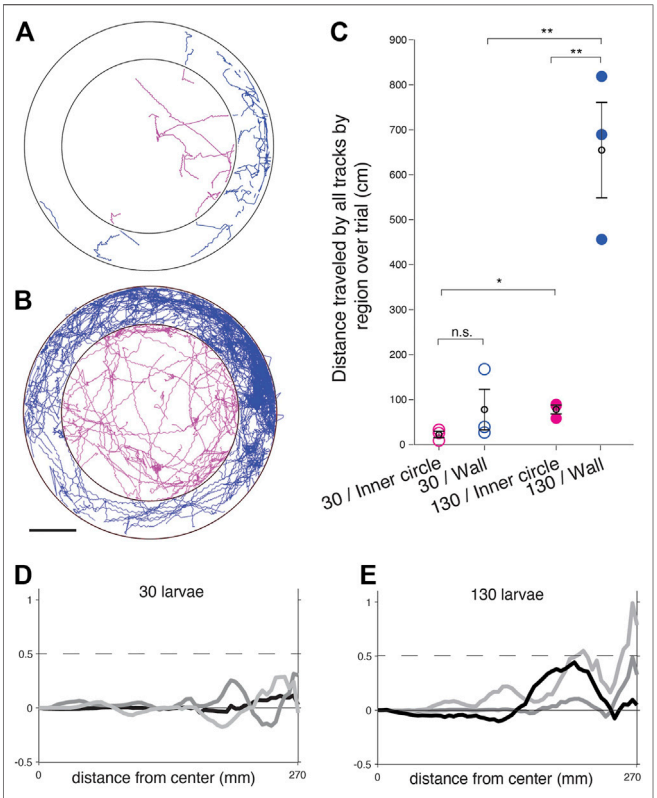

FIGURE 3 | Larval zebrafish traverse space differently at different densities when bordering the arena wall in comparison to in the center of the arena. **(A)** Trajectories for a trial with 30 larvae segregated into an outer ring adjacent to the wall (blue) and the arena center (magenta). **(B)** Trajectories for a trial with 130 larvae segregated into an outer ring adjacent to the wall (blue) and the arena center (magenta). Scale bar for A-B 1 cm. **(C)** Summed distance traveled in cm for all tracks in a trial. Trials with 30 larvae (open circles) were compared to trials of 130 larvae (filled circles) and wall-adjacent regions (blue) were compared to the inner circle of the arena (magenta). Means per group are in black open circles and error bars are the SEM. n.s. = not significant, $^*p < 0.05$, $^{**}p < 0.01$. **(D–E)**. Mean tangential velocity <v> versus the radial distance from the dish center for 3 trials each of $n = 30$ **(D)** and $n = 130$ **(E)** larvae.

DISCUSSION

The collective motion of animals and other active agents in enclosed areas is an evolving but promising area of study, as is collective

motion at the mesoscale [6, 37]. We see similarities but also differences in the self-organization of larval zebrafish to other types of motile agents under circular confinement. Here we refer to collective motion simply as an emergent group behavior that only occurs as a function of the interactions of the conspecifics and their environment and would not occur if a single larva were in isolation or in free space. At high densities the larval fish transition to short bouts of circulation alongside the dish boundary and tend to be found swimming closer to the walls than at low densities. A largely similar circulating collective motion pattern is seen across scales from single-cell organisms to humans when the motile units are placed in hard or soft circular enclosures. And yet the specific physical and neurobiological capabilities of larval fish give rise to distinct behavior. Their individual non-uniform speeds and preference for social avoidance may be influencing the non-uniform circulation or "panic wave" which at times may stop or even reverse direction. Their preferred social distancing, possible visual cues, and fluidic interactions may influence why they can mostly be found at a certain distance from the confining wall that increases with density.

Unlike smaller swimmers like bacteria, algae or spermatozoa [40], these relatively larger larval fish have more complex individual motion patterns. They are well-studied however, and much is known about their biology, locomotion, individual, and social behavior. Groneberg et al., 2020 shows that the preferred distance between animals changes due to early life social interaction, and that these responses are driven by vision and by the sensory lateral line, which senses water flow around fishes [33]. While thigmotaxis or "wall-hugging" as a response to anxiety-inducing stimuli has been well documented in larval zebrafish [41], it is interesting to consider this emergent circling behavior in the context of social anxiety caused by crowding and confinement. It was observed in work involving small groups of zebrafish at the same life stage with much smaller arenas housing seven larvae at a time, that one larva in the group could set off chain reactions of escape responses: if one animal escaped it would collide with another setting off a domino effect [42]. It's possible this emergent collective circling results from these same chains of escapes, created by the interaction with the confinement of walls and the high density of conspecifics, which then catalyze this circling behavior. In future work we are interested in identifying mechanistic drivers of transitions between states, as has been identified in other species [43].

Another interesting observation was noted just inside the extreme edges of the arena, where immobile larvae can be seen drifting rearwards, in counter-rotation with the adjacent larvae circling at the dish circumference. We presume this can be attributed to fluid flow as the animals do not appear to be oscillating their tail or actively moving, and larval zebrafish have not been observed to swim backward. This is reminiscent of the collective behavior of bacteria in circular chambers where the fluid flow disturbed by the edge-swimming bacteria pushed back the middle-swimming ones [6]. The interaction between water flow generated by the circling proportion of animals and the diameter and shape of the confinement is a point of interest which we will model and further test experimentally in the future. The study of individual or collective animal motion at intermediate Reynolds numbers remains underexplored. A better understanding of the mechanisms and interactions that give rise to the confined zebrafish collective motion will allow us to optimally direct their behavior by designing appropriate confining boundaries.

In future work, we hope to experimentally manipulate these various sensory inputs and systematically study the triggers for collective circling. It is highly advantageous to develop collective motion paradigms in a model system with an extensive genetic and optical toolkit to allow experimenters to observe and manipulate neural circuits [44–53]. Insects are also known to display a transition from disordered to ordered movement with increasing density, most famously in locusts [4]. Zebrafish sit in an advantageous space between invertebrate models where sensory systems may be easily perturbed to investigate mechanisms [54], and humans which display complex behavior but inaccesssible neurobiological underpinnings, although techniques like fMRI permit some measurement of individual human neural activity during complex social decision making [9].

Here we share a new paradigm where collective motion can be induced by confinement in a model system amenable to genetic and neurobiological tools to investigate the underlying neural circuits. By understanding what influences this collective behavior and manipulating the enclosure scales and shapes in the future, we can determine fundamental interaction rules that could be widely applicable to other organisms and systems.

DATA AVAILABILITY STATEMENT

The raw data supporting the conclusions of this article will be made available by the authors, without undue reservation.

ETHICS STATEMENT

The animal study was reviewed and approved by Rutgers-Newark IACUC protocol # PROTO201800041.

AUTHOR CONTRIBUTIONS

All the authors conceived of the project, analyzed the data, and wrote the article. HZ and KS collected the data.

FUNDING

New Jersey Institute of Technology startup funds to EL and KS. Simons Foundation for EL.

ACKNOWLEDGMENTS

We thank Dr. Simon Garnier and the Swarm lab for insightful suggestions and mentorship throughout the project, as well as

Rafael Asfour from the Swarm lab for assistance implementing trackR. Mahathi Mohan Gowda built the behavior rig setup utilized for the experiments, along with members of the Severi lab and Dr. Christoph Gebhardt assisted in designing and building the behavior rig and gave input on analysis. We thank all members of the Severi lab past and present for excellent animal care and useful discussions throughout the project. Hassan Elsaid contributed through the NJIT Research @Home program. KS acknowledges support from NJIT startup funds. EL acknowledges support from the Simons Foundation as well as NJIT startup and seed funds.

SUPPLEMENTARY MATERIAL

The Supplementary Material for this article can be found online at: https://www.frontiersin.org/articles/10.3389/fphy.2021.678600/full#supplementary-material

Supplemental Table 1 | Components for custom-built behavioral recording setup.

REFERENCES

1. Vicsek T, and Zafeiris A. Collective Motion. *Phys Rep* (2012) 517(3–4):71–140. doi:10.1016/j.physrep.2012.03.004
2. Cavagna A, Cimarelli A, Giardina I, Parisi G, Santagati R, Stefanini F, et al. Scale-free Correlations in Starling Flocks. *Proc Natl Acad Sci* (2010) 107(26): 11865–70. doi:10.1073/pnas.1005766107
3. Katz Y, Tunstrom K, Ioannou CC, Huepe C, and Couzin ID. Inferring the Structure and Dynamics of Interactions in Schooling Fish. *Proc Natl Acad Sci* (2011) 108(46):18720–5. doi:10.1073/pnas.1107583108
4. Buhl J, Sumpter DJT, Couzin ID, Hale JJ, Despland E, Miller ER, et al. From Disorder to Order in Marching Locusts. *Science* (2006) 312(5778):1402–6. doi:10.1126/science.1125142
5. Bricard A, Caussin J-B, Desreumaux N, Dauchot O, and Bartolo D. Emergence of Macroscopic Directed Motion in Populations of Motile Colloids. *Nature* (2013) 503(7474):95–8. doi:10.1038/nature12673
6. Lushi E, Wioland H, and Goldstein RE. Fluid Flows Created by Swimming Bacteria Drive Self-Organization in Confined Suspensions. *Proc Natl Acad Sci USA* (2014) 111(27):9733–8. doi:10.1073/pnas.1405698111
7. Pearce DJG, Miller AM, Rowlands G, and Turner MS. Role of Projection in the Control of Bird Flocks. *Proc Natl Acad Sci* (2014) 111(29):10422–6. doi:10.1073/pnas.1402202111
8. Peleg O, Peters JM, Salcedo MK, and Mahadevan L. Collective Mechanical Adaptation of Honeybee Swarms. *Nat Phys* (2018) 14(12):1193–8. doi:10.1038/s41567-018-0262-1
9. Charpentier CJ, Moutsiana C, Garrett N, and Sharot T. The Brain's Temporal Dynamics from a Collective Decision to Individual Action. *J Neurosci* (2014) 34(17):5816–23. doi:10.1523/jneurosci.4107-13.2014
10. Wioland H, Lushi E, and Goldstein RE. Directed Collective Motion of Bacteria under Channel Confinement. *New J Phys* (2016) 18(7). doi:10.1088/1367-2630/18/7/075002
11. Giomi L, Hawley-Weld N, and Mahadevan L. Swarming, Swirling and Stasis in Sequestered Bristle-Bots. *Proc R Soc A* (2013) 469(2151):20120637. doi:10.1098/rspa.2012.0637
12. Creppy A, Plouraboué F, Praud O, Druart X, Cazin S, Yu H, et al. Symmetry-breaking Phase Transitions in Highly Concentrated Semen. *J R Soc Interf* (2016) 13(123):20160575. doi:10.1098/rsif.2016.0575
13. Tsang ACH, and Kanso E. Density Shock Waves in Confined Microswimmers. *Phys Rev Lett* (2016) 116(4):48101. doi:10.1103/physrevlett.116.048101
14. Silverberg JL, Bierbaum M, Sethna JP, and Cohen I. Collective Motion of Humans in Mosh and circle Pits at Heavy Metal Concerts. *Phys Rev Lett* (2013) 110(22):228701–5. doi:10.1103/PhysRevLett.110.228701
15. Ehrlich DE, and Schoppik D. Control of Movement Initiation Underlies the Development of Balance. *Curr Biol [Internet]* (2017) 27(3):334. Available at: http://linkinghub.elsevier.com/retrieve/pii/S096098221631449X.doi:10.1016/j.cub.2016.12.003
16. Danos N. Locomotor Development of Zebrafish (Danio Rerio) under Novel Hydrodynamic Conditions. *J Exp Zool* (2012) 317(2):117–26. doi:10.1002/jez.1002
17. Orger MB, Smear MC, Anstis SM, and Baier H. Perception of Fourier and Non-fourier Motion by Larval Zebrafish. *Nat Neurosci* (2000) 3(11):1128–33. doi:10.1038/80649
18. Oteiza P, Odstrcil I, Lauder G, Portugues R, and Engert F. A Novel Mechanism for Mechanosensory-Based Rheotaxis in Larval Zebrafish. *Nature* (2017) 547(7664):445–8. doi:10.1038/nature23014
19. Kim C, Ruberto T, Phamduy P, and Porfiri M. Closed-loop Control of Zebrafish Behaviour in Three Dimensions Using a Robotic Stimulus. *Sci Rep* (2018) 8(1):1–15. doi:10.1038/s41598-017-19083-2
20. Heras FJH, Romero-Ferrero F, Hinz RC, and De Polavieja GG. Deep Attention Networks Reveal the Rules of Collective Motion in Zebrafish. *Plos Comput Biol* (2019) 15(9):e1007354–23. doi:10.1371/journal.pcbi.1007354
21. Romero-Ferrero F, Bergomi MG, Hinz RC, Heras FJH, and de PolaviejaAi GG. idtracker.ai: Tracking All Individuals in Small or Large Collectives of Unmarked Animals. *Nat Methods* (2019) 16(2):179–82. doi:10.1038/s41592-018-0295-5
22. Spinello C, Yang Y, Macrì S, and Porfiri M. Zebrafish Adjust Their Behavior in Response to an Interactive Robotic Predator. *Front Robot AI* (2019) 6(MAY): 1–14. doi:10.3389/frobt.2019.00038
23. Yang Y, Clément RJG, Ghirlanda S, and Porfiri M. A Comparison of Individual Learning and Social Learning in Zebrafish through an Ethorobotics Approach. *Front Robot AI* (2019) 6(August):1–13. doi:10.3389/frobt.2019.00071
24. Nunes AR, Carreira L, Anbalagan S, Blechman J, Levkowitz G, and Oliveira RF. Perceptual Mechanisms of Social Affiliation in Zebrafish. *Sci Rep* (2020) 10(1): 1–14. doi:10.1038/s41598-020-60154-8
25. Engeszer RE, Da Barbiano LA, Ryan MJ, and Parichy DM. Timing and Plasticity of Shoaling Behaviour in the Zebrafish, *Danio rerio*. *Anim Behav* (2007) 74(5):1269–75. doi:10.1016/j.anbehav.2007.01.032
26. Buske C, and Gerlai R. Shoaling Develops with Age in Zebrafish (*Danio rerio*). *Prog Neuro-Psychopharmacology Biol Psychiatry* (2011) 35(6):1409–15. doi:10.1016/j.pnpbp.2010.09.003
27. Budick SA, and O'Malley DM. Locomotor Repertoire of the Larval Zebrafish: Swimming, Turning and Prey Capture. *J Exp Biol [Internet]* (2000) 203(Pt 17): 2565–79. Available at: http://www.ncbi.nlm.nih.gov/pubmed/10934000. doi:10.1242/jeb.203.17.2565
28. Wolman M, and Granato M. Behavioral Genetics in Larval Zebrafish: Learning from the Young. *Devel Neurobio* (2012) 72:366–72. doi:10.1002/dneu.20872
29. Portugues R, and Engert F. The Neural Basis of Visual Behaviors in the Larval Zebrafish. *Curr Opin Neurobiol* (2009) 19(6):644–7. Available at: http://www.ncbi.nlm.nih.gov/pubmed/19896836. doi:10.1016/j.conb.2009.10.007
30. Portugues R, Severi KE, Wyart C, and Ahrens MB. Optogenetics in a Transparent Animal: Circuit Function in the Larval Zebrafish. *Curr Opin Neurobiol* (2013) 23(1):119–26. Available at: http://www.ncbi.nlm.nih.gov/pubmed/23246238. doi:10.1016/j.conb.2012.11.001
31. Bollmann JH. The Zebrafish Visual System: From Circuits to Behavior. *Annu Rev Vis Sci* (2019) 5:269–93. doi:10.1146/annurev-vision-091718-014723
32. Sakai C, Ijaz S, and Hoffman EJ. Zebrafish Models of Neurodevelopmental Disorders: Past, Present, and Future. *Front Mol Neurosci* (2018) 11(August): 294. doi:10.3389/fnmol.2018.00294
33. Groneberg AH, Marques JC, Martins AL, Diez del Corral R, de Polavieja GG, and Orger MB. Early-Life Social Experience Shapes Social Avoidance Reactions in Larval Zebrafish. *Curr Biol* (2020) 30(20):4009–21. doi:10.1016/j.cub.2020.07.088
34. Foreman MB, and Eaton RC. The Direction Change Concept for Reticulospinal Control of Goldfish Escape. *J Neurosci* (1993) 13(October): 4101–13. doi:10.1523/jneurosci.13-10-04101.1993
35. Dunn TW, Gebhardt C, Naumann EA, Riegler C, Ahrens MB, Engert F, et al. Neural Circuits Underlying Visually Evoked Escapes in Larval Zebrafish.

Neuron (2016) 89:613–28. Available at: http://linkinghub.elsevier.com/retrieve/pii/S089662731501123X. doi:10.1016/j.neuron.2015.12.021
36. Hale ME, Katz HR, Peek MY, Fremont RT. Neural Circuits That Drive Startle Behavior, With a Focus on the Mauthner Cells and Spiral Fiber Neurons of Fishes J Neurogenet. (2016) 30(2):89–100. doi:10.1080/01677063.2016.1182526
37. Klotsa D. As above, So below, and Also in between: Mesoscale Active Matter in Fluids. *Soft Matter* (2019) 15(44):8946–50. doi:10.1039/C9SM01019J
38. Garnier S. TrackR - Multi-Object Tracking with R. [Internet] (2021). Available at: https://swarm-lab.github.io/trackR/(Accessed Mar 5, 2021).
39. Wioland H, Woodhouse FG, Dunkel J, Kessler JO, and Goldstein RE. Confinement Stabilizes a Bacterial Suspension into a Spiral Vortex. *Phys Rev Lett* (2013) 110(26):268102–5. doi:10.1103/PhysRevLett.110.268102
40. Ostapenko T, Schwarzendahl FJ, Böddeker TJ, Kreis CT, Cammann J, Mazza MG, et al. Curvature-Guided Motility of Microalgae in Geometric Confinement. *Phys Rev Lett* (2018) 120(6):68002. doi:10.1103/physrevlett.120.068002
41. Schnörr SJ, Steenbergen PJ, Richardson MK, and Champagne DL. Measuring Thigmotaxis in Larval Zebrafish. *Behav Brain Res* (2012) 228(2):367–74. doi:10.1016/j.bbr.2011.12.016
42. Mirat O, Sternberg JR, Severi KE, and Wyart C. ZebraZoom: an Automated Program for High-Throughput Behavioral Analysis and Categorization. *Front Neural Circuits* (2013) 7:107. Available at: http://www.ncbi.nlm.nih.gov/pubmed/23781175.
43. Tunstrøm K, Katz Y, Ioannou CC, Huepe C, Lutz MJ, and Couzin ID. Collective States, Multistability and Transitional Behavior in Schooling Fish. *Plos Comput Biol* (2013) 9(2):e1002915. doi:10.1371/journal.pcbi.1002915
44. Arrenberg AB, Del Bene F, and Baier H. Optical Control of Zebrafish Behavior with Halorhodopsin. *Proc Natl Acad Sci U S A* (2009) 106(42):17968–73. Available at: http://www.ncbi.nlm.nih.gov/pubmed/19805086. doi:10.1073/pnas.0906252106
45. Wyart C, Del Bene F, Warp E, Scott EK, Trauner D, Baier H, et al. Optogenetic Dissection of a Behavioural Module in the Vertebrate Spinal Cord. *Nature* (2009) 461(7262):407–10. Available at: http://www.ncbi.nlm.nih.gov/pubmed/19759620. doi:10.1038/nature08323
46. Ahrens MB, Orger MB, Robson DN, Li JM, and Keller PJ. Whole-brain Functional Imaging at Cellular Resolution Using Light-Sheet Microscopy. *Nat Methods* (2013) 10(5):413–20. Available at: http://www.ncbi.nlm.nih.gov/pubmed/23524393. doi:10.1038/nmeth.2434
47. Satou C, Kimura Y, Hirata H, Suster ML, Kawakami K, and Higashijima S-i. Transgenic Tools to Characterize Neuronal Properties of Discrete Populations of Zebrafish Neurons. *Development* (2013) 140(18):3927–31. doi:10.1242/dev.099531
48. Kimura Y, Hisano Y, Kawahara A, and Higashijima S-i. Efficient Generation of Knock-In Transgenic Zebrafish Carrying Reporter/driver Genes by CRISPR/Cas9-mediated Genome Engineering. *Sci Rep* (2014) 4:6545. doi:10.1038/srep06545
49. Portugues R, Feierstein CE, Engert F, and Orger MB. Whole-brain Activity Maps Reveal Stereotyped, Distributed Networks for Visuomotor Behavior. *Neuron [Internet]* (2014) 81(6):1328–43. Available at: http://www.ncbi.nlm.nih.gov/pubmed/24656252. doi:10.1016/j.neuron.2014.01.019
50. Fidelin K, Djenoune L, Stokes C, Prendergast A, Gomez J, Baradel A, et al. State-Dependent Modulation of Locomotion by GABAergic Spinal Sensory Neurons. *Curr Biol* (2015) 25(23):3035–47. doi:10.1016/j.cub.2015.09.070
51. Sternberg JR, Severi KE, Fidelin K, Gomez J, Ihara H, Alcheikh Y, et al. Optimization of a Neurotoxin to Investigate the Contribution of Excitatory Interneurons to Speed Modulation *In Vivo*. *Curr Biol* (2016) 26(17):2319–28. doi:10.1016/j.cub.2016.06.037
52. Kishore S, Cadoff EB, Agha MA, and McLean DL. Orderly Compartmental Mapping of Premotor Inhibition in the Developing Zebrafish Spinal Cord. *Science* (2020) 370(6515):431–6. doi:10.1126/science.abb4608
53. Marques JC, Li M, Schaak D, Robson DN, and Li JM. Internal State Dynamics Shape Brainwide Activity and Foraging Behaviour. *Nature* (2020) 577(7789):239–43. doi:10.1038/s41586-019-1858-z
54. Jiang L, Cheng Y, Gao S, Zhong Y, Ma C, Wang T, et al. Emergence of Social Cluster by Collective Pairwise Encounters in Drosophila. *Elife* (2020) 9:e51921. doi:10.7554/eLife.51921

Conflict of Interest: The authors declare that the research was conducted in the absence of any commercial or financial relationships that could be construed as a potential conflict of interest.

frontiers in Physics

ORIGINAL RESEARCH
published: 30 September 2021
doi: 10.3389/fphy.2021.734499

Emergent Collective Locomotion in an Active Polymer Model of Entangled Worm Blobs

Chantal Nguyen[1†], *Yasemin Ozkan-Aydin*[2†], *Harry Tuazon*[3], *Daniel. I. Goldman*[4], *M. Saad Bhamla*[3*‡] *and Orit Peleg*[1,5,6*‡]

[1]*BioFrontiers Institute, University of Colorado Boulder, Boulder, CO, United States,* [2]*Department of Electrical Engineering, University of Notre Dame, Notre Dame, IN, United States,* [3]*School of Chemical and Biomolecular Engineering, Georgia Institute of Technology, Atlanta, GA, United States,* [4]*School of Physics, Georgia Institute of Technology, Atlanta, GA, United States,* [5]*Department of Computer Science, University of Colorado Boulder, Boulder, CO, United States,* [6]*Santa Fe Institute, Santa Fe, NM, United States*

OPEN ACCESS

Edited by:
Hui-Jia Li,
Beijing University of Posts and Telecommunications (BUPT), China

Reviewed by:
Rajarshi Chakrabarti,
Indian Institute of Technology Bombay, India
Wen-Xuan Wang,
Beijing University of Posts and Telecommunications (BUPT), China

***Correspondence:**
M. Saad Bhamla
saadb@chbe.gatech.edu
Orit Peleg
orit.peleg@colorado.edu

[†]These authors have contributed equally to this work and share first authorship

[‡]These authors have contributed equally to this work and share senior authorship

Specialty section:
This article was submitted to Social Physics, a section of the journal Frontiers in Physics

Received: *01 July 2021*
Accepted: *06 September 2021*
Published: *30 September 2021*

Citation:
Nguyen C, Ozkan-Aydin Y, Tuazon H, Goldman DI, Bhamla MS and Peleg O (2021) Emergent Collective Locomotion in an Active Polymer Model of Entangled Worm Blobs. Front. Phys. 9:734499. doi: 10.3389/fphy.2021.734499

Numerous worm and arthropod species form physically-connected aggregations in which interactions among individuals give rise to emergent macroscale dynamics and functionalities that enhance collective survival. In particular, some aquatic worms such as the California blackworm (*Lumbriculus variegatus*) entangle their bodies into dense blobs to shield themselves against external stressors and preserve moisture in dry conditions. Motivated by recent experiments revealing emergent locomotion in blackworm blobs, we investigate the collective worm dynamics by modeling each worm as a self-propelled Brownian polymer. Though our model is two-dimensional, compared to real three-dimensional worm blobs, we demonstrate how a simulated blob can collectively traverse temperature gradients *via* the coupling between the active motion and the environment. By performing a systematic parameter sweep over the strength of attractive forces between worms, and the magnitude of their directed self-propulsion, we obtain a rich phase diagram which reveals that effective collective locomotion emerges as a result of finely balancing a tradeoff between these two parameters. Our model brings the physics of active filaments into a new meso- and macroscale context and invites further theoretical investigation into the collective behavior of long, slender, semi-flexible organisms.

Keywords: collective behavior, active matter, locomotion, active polymers, blackworms, annelids

1 INTRODUCTION

Throughout the living world, interactions among individuals, and between individuals and the environment, give rise to emergent collective phenomena across scales: cell migration, flocking birds, schooling fish, and human crowds moving in unison [1–4]. While most examples of collective behavior occur in regimes without physical contact among individuals, many insect, arthropod, and worm species form dense aggregations, where constituent individuals are in constant physical contact with each other, for the purposes of survival, foraging, migration, and mating [5–7]. Small-scale interactions among individuals enable emergent functionalities at the group level, such as the formation of adaptive structures, including fire ant rafts [8], army ant bridges [9], and bee clusters [10], that can enhance the survival of the aggregation compared to solitary individuals. These living aggregations, where the constituents exert forces on each other or even entangle their bodies into a

single mass [6, 11], are associated with the world of soft active matter, which comprises a wide range of systems in which self-propelled individuals can convert energy from the environment into directed motion [7, 12–14].

Here, we examine the aggregation and swarming behavior of active polymer-like organisms, such as worms, that are flexible and characterized by their slender bodies (i.e., each possessing a length much longer than the width). Some species of worms can physically braid their bodies into highly entangled aggregations [11, 15–17]. In this paper, we focus on *Lumbriculus variegatus*, an aquatic worm also known as the California blackworm or mudworm. Blackworms are approximately 1 mm in diameter and up to 2–4 cm in length and live in shallow, marshy conditions across the Northern Hemisphere [11]. The physiology, neurology, biology, and behavior of individual *L. variegatus* has been extensively studied [11, 18–20], while their collective behavior has only recently been examined [17]. Blackworms can form entangled, shape-shifting blobs which allow the constituent worms to protect themselves against environmental stressors and to preserve moisture in dry conditions [17]. Recent experiments have quantified the material properties and aggregation dynamics of blackworm blobs, which can contain anywhere from a few to over tens of thousands worms and behave as a non-Newtonian fluid [17].

Most notably, these experiments resulted in the first observation of emergent locomotion in an entangled aggregation of multicellular organisms and robophysical models. While some physically-connected aggregations of worms and arthropods have been observed to demonstrate collective, coordinated movement and migration (e.g., [21, 22]), the blackworm blobs demonstrated collective self-transport in temperature gradients [17]. Under high light intensity, the worms remained a single entangled unit as they moved toward cooler environments, but only about 70% of worms moved together as an entangled blob in the absence of the spotlight [17]. It was observed in small blobs that the mechanism of this collective movement lies in a differentiation of activity, with outstretched "puller" worms in the front pulling the coiled, raised "wiggler" worms at the back [17]. This phenomenon was also captured in robophysical models of "smarticle" robots, indicating the importance of this mechanism in the self-motility of an entangled collective [17].

Other recent work has investigated the rheology and phase separation in aggregations of a similar organism, *T. tubifex*, also called the sludge worm or sewage worm. These worms also form highly entangled blobs in water to minimize exposure to poisonous dissolved oxygen, though collective locomotion has not been observed [16, 23]. The authors of this work showed that the dynamics observed in their experiments could not be captured by modeling blobs as coalescing droplets undergoing Brownian motion [16]. Namely, the diffusion constant of the blobs, which describes how quickly the blobs explore space, was observed to be independent of their size, rather than scaling as the inverse of the blob radius as would have been expected assuming completely random motion; this discrepancy was attributed to the active random motion of worms at the surface of the blob. Moreover, it was asserted that a model of collective worm behavior would likely need to account for the self-propelled tangentially-driven motion of individual worms [23].

Motivated by these experiments and insights on aggregations of blackworms and sludge worms [16, 17, 23], we pursue a theoretical model that captures the collective behavior of aquatic worms by linking together local rules governing interactions between individual worms with the emergent macroscale dynamics of the blob. Worms consume energy in order to propel themselves; hence, we look toward the extensive body of research in modeling active polymers and worm-like filaments [24, 25], where activity can be implemented in different ways, such as by immersing the polymer in a bath of colored or non-Gaussian noise [26, 30–32], or *via* monomers driven by active forces [27–29, 33]. In general, application of these models has been geared toward biopolymers and unicellular organisms in the microscopic regime, such as actin filaments, microtubules, cilia and flagella, and swarms of slender bacteria [24, 28, 34–37]. In this paper, we adapt the physics of active filaments to a macroscale, whole-organism context in order to characterize the collective behavior of worm blobs.

A similarly polymer-like organism that has also demonstrated aggregation and swarming is the nematode *C. elegans*, which is about an order of magnitude smaller than the blackworm [38]. Agent-based modeling was used to elucidate the behavioral rules governing collective *C. elegans* behavior [38], in which individual nematodes were modeled in polymer-like fashion as nodes connected by springs, with the head node undergoing a persistent random walk and the rest of the body following.

Here, we are primarily interested in tangentially-driven active filaments [27, 28], as their behavior is qualitatively similar to that of worms. Such semi-flexible, tangentially-driven filaments demonstrate a rich diversity of behavior. The bending rigidity, activity, aspect ratio, and density of filaments define phases of flocking, spiraling, clustering, jamming, and nematic laning [28].

Drawing upon these models, we model worms as two-dimensional active Brownian polymers, driven by experimental observations of the behavior of single worms (**Figure 1A**), worm blobs (**Figure 1B**), and the collective locomotion of worm blobs in temperature gradients (**Figure 1C**; [17]). We model each worm as a polymer with a tangential self-propulsion force acting only on a portion of the worm designated as the head end, as this qualitatively reflects our observations of worms being more active at the head (**Figure 1D**). After developing this single-worm model, we simulate worm blobs *via* aggregation of multiple identical worms (**Figure 1E**) attracted to each other *via* an interaction potential.

We then simulate worm blobs in a temperature gradient, which sets a preferred direction of the worm toward the cold side, reflecting real worms' preference for cooler temperatures in analogous experimental setups [17]. We perform a parameter sweep over the strength of attraction between worms and the magnitude of the tangential force. We find that from the resulting rich phase diagram, collective locomotion arises only when the attraction strength and tangential force are finely balanced (**Figure 1F**). Though our model is in 2-D, it captures the emergent collective locomotion of the worm blob as observed in experiments [17].

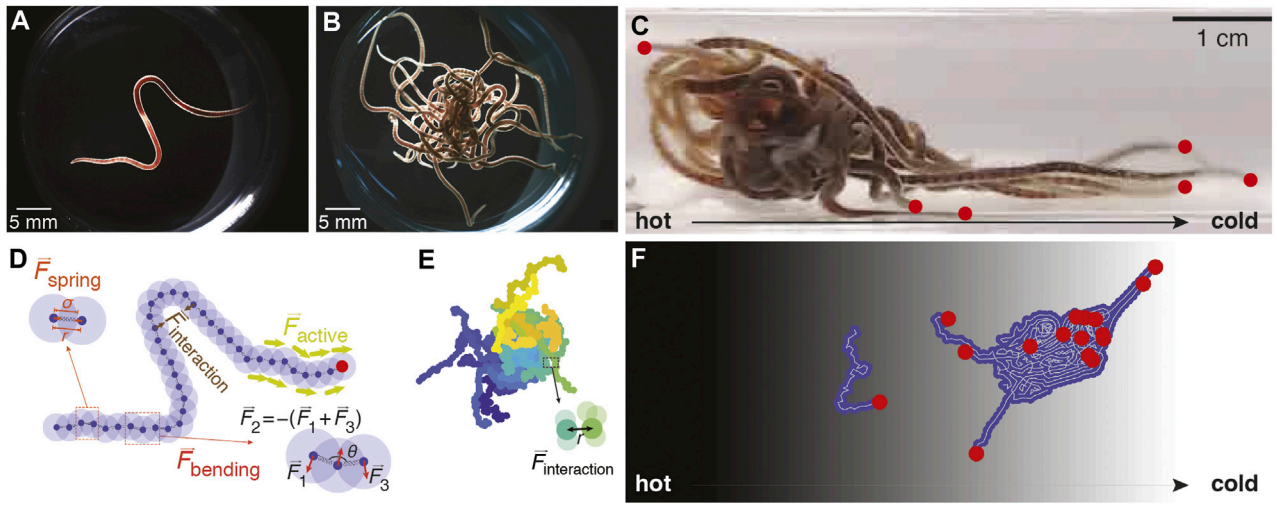

FIGURE 1 | Worm-inspired active polymer model. **(A)**. A single California blackworm (*L. variegatus*). **(B)**. An entangled worm blob consisting of 20 worms. **(C)** An entangled worm blob (~20 worms) in a temperature gradient displays collective locomotion toward the cold side **(right)**, with "puller" worms extending from the front (worm heads marked by red dots). **(D)**. Polymer model of single worm consisting of 40 monomers connected by springs with interaction potential described in **Eq. 1**. The "head" section (with the distal head node indicated by the red dot) of the worm is subject to a constant-magnitude tangential force $\vec{F}_{active}$ generating self-propulsion. The spring force $\vec{F}_{spring}$ (**Eq. 2**) is computed for adjacent pairs of monomers, and the bending force $\vec{F}_{bending}$ (**Eq. 3**) for adjacent triplets of monomers. The interaction force $\vec{F}_{interaction}$ (**Eq. 1**) is computed for every pair of monomers in a chain and is attractive if the monomers are further apart than the equilibrium distance σ and repulsive if they are closer than σ. **(E)**. Simulated worm blob consisting of 20 polymers. Each color represents a different worm. The interaction force $\vec{F}_{interaction}$ (**Eq. 6**) is computed for every pair of monomers and is stronger between monomers of different chains. **(F)**. Simulated worm blob in a temperature gradient with the hotter side on the left (black background) and the colder side on the right (white background) demonstrates collective locomotion toward the cold side. Red dots indicate the head ends of each worm; some worm heads protrude from the bulk of the blob.

TABLE 1 | List of model parameters and corresponding ranges of values used in simulations.

Parameter	Description	Range of values
N_m	Number of monomers	40
Σ	Equilibrium distance between monomers	1.189 (arb. units)
ε	Interaction coefficient, single worm	1
k_s	Spring constant	5000
k_b	Bending stiffness	10
F_{active}	Self-propulsion force magnitude	220–440
ε_{blob}	Interaction coefficient for blob (attraction parameter)	2–22

2 ACTIVE POLYMER MODEL

To construct our model, we begin by modeling a single worm as a polymer: a series of individual monomers linked together by springs of equal length (**Figure 1D**). The monomers are subject to three potentials: interaction ($U_{interaction}$), spring (U_{spring}), and bending ($U_{bending}$) [39, 40]:

$$U_{interaction} = 4\varepsilon \sum_{i=1}^{N_m} \sum_{j>i}^{N_m} \left[\left(\frac{\sigma}{|\mathbf{r}_{ij}|} \right)^8 - \left(\frac{\sigma}{|\mathbf{r}_{ij}|} \right)^4 \right] \quad (1)$$

$$U_{spring} = \frac{k_s}{2} \sum_{i=1}^{N_m} (|\mathbf{r}_{i,i+1}| - \sigma)^2 \quad (2)$$

$$U_{bending} = \frac{k_b}{2} \sum_{i=1}^{N_m-2} (\phi_{i,i+1,i+2} - \phi)^2 \quad (3)$$

where N_m is the number of monomers per chain, $\mathbf{r}_{ij} = \mathbf{r}_j - \mathbf{r}_i$ is the vector between the positions of monomers i and j, σ is the equilibrium length of the spring connecting two adjacent monomers, k_s is the spring constant, and k_b is the bending stiffness. The bending potential $U_{bending}$, described by a harmonic angle potential, is computed for every consecutive triplet of monomers i, $i + 1$, $i + 2$ whose connecting springs form an angle $\phi_{i,i+1,i+2} = \cos^{-1}(\mathbf{r}_{i+1,i} \cdot \mathbf{r}_{i+1,i+2} / |\mathbf{r}_{i+1,i}||\mathbf{r}_{i+1,i+2}|)$. ϕ_0 is the equilibrium angle of each adjacent pair of springs and is set to π.

The interaction potential is inspired by the Lennard-Jones potential used to describe interatomic interactions [39]. We use a modified form of this potential as it captures strong short-range repulsion and weaker long-range attraction, though with slightly smaller exponents that enable computational efficiency with qualitatively similar results. For two monomers with a

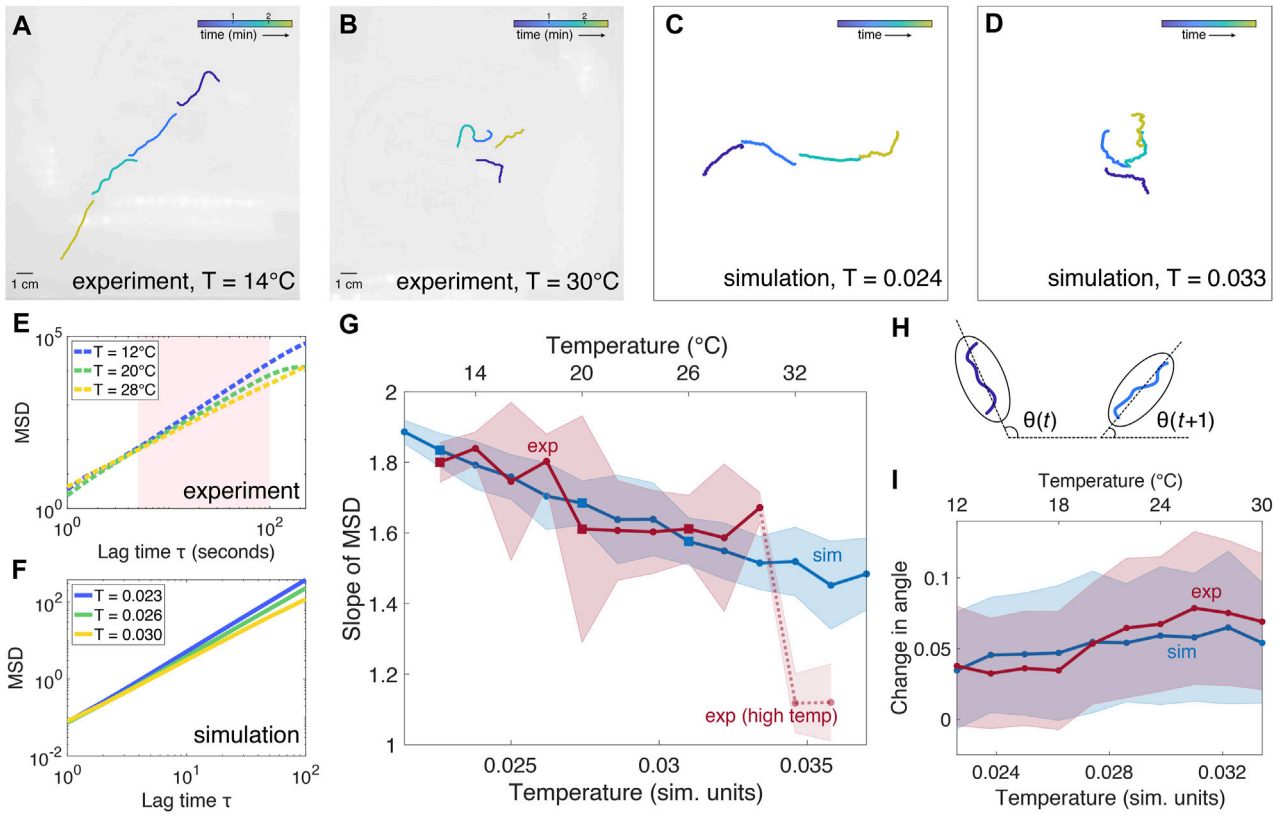

FIGURE 2 | Active polymer model of a single worm. **(A–B)**: Snapshots of single worm experiments at $T = 14^{\circ}C$ and $T = 30^{\circ}C$, respectively. Worms are colored in software to visualize time progression. **(C–D)**: Snapshots of simulated single worm conformations at $T = 0.024$ and $T = 0.033$ (simulation units), respectively. **(E)**: Examples of mean squared displacement (MSD) as a function of lag time τ from three separate experimental trials at three different temperatures, indicated by the squares in panel **(G)**. Because the MSD is not linear over the entire range of τ, the slope is computed for the region shaded in pink. **(F)**: Examples of MSD from three simulations at three different temperatures, indicated by the squares in panel **(G)**. **(G)**: Comparison of mean slope ± SD of mean squared displacement (MSD) as a function of temperature for simulation (blue) and experiment (red, 5 trials). The slope of MSD generally decreases with increasing temperature. Experimental data at $T = 32$–$34^{\circ}C$ are indicated by a dashed line, as worm physiology is likely to be affected by the high temperature. Squares indicate temperatures at which examples of MSD are plotted in panels **(E–F)**. **(H)**: The angle θ at time t is computed by fitting an ellipse to the worm and calculating the angle of the major axis with respect to the horizontal. The average change in angle between consecutive timesteps $\theta(t+1) - \theta(t)$ is used as a measure of worm fluctuations. **(I)**: For the trials analyzed in panel **(G)**, the average change in angle θ increases with temperature for both simulation and experiment.

separation $r < \sigma$, the interaction potential mimics an excluded volume mechanism to prevent the monomers from occupying the same space. For two monomers with separation $r > \sigma$, the potential is weakly attractive. This results in the polymer forming a more coiled-up conformation. The coiling up is offset partially by the bending potential, which acts to straighten the polymer.

At each step of the simulation, the force on each monomer is computed:

$$\vec{F_i} = -\vec{\nabla} U_{\text{interaction},i} - \vec{\nabla} U_{\text{spring},i} - \vec{\nabla} U_{\text{bending},i}, \tag{4}$$

and the position of each monomer is updated *via* the overdamped equation of motion

$$\vec{x_i}(t + \Delta t) = \vec{x_i}(t) + \vec{F_i}\Delta t + T\vec{\zeta}, \tag{5}$$

where $\vec{\zeta}$ is a two-dimensional random vector with each component sampled from the normal distribution $\mathcal{N}(0, 1)$ with mean 0 and variance 1, such that $T\vec{\zeta}$ represents noise with standard deviation given by a temperature value T.

L. variegatus cultivated in the laboratory measured approximately 25 ± 10 mm in length with a radius of 0.6 ± 0.1 mm, corresponding to an average length-to-radius ratio of approximately 40. In our model, each pair of monomers is connected by a spring with equilibrium length σ, which is also set to be the equilibrium distance at which the interaction potential of each monomer has value 0. In our simulations, we model worms that are $N = 40$ monomers long, such that each worm can be considered to have a length of 41 σ with radius σ, corresponding to a length-to-radius ratio of 41. We also set the spring coefficient $k_s = 5{,}000$, a relatively high value as worms do not easily stretch along their axis. We also set the bending coefficient $k_b = 10$, an intermediate value that results in more elongated worms at low temperatures and coiled worms at high temperatures (2A-D). This bending coefficient is also partially offset by a interaction of $\varepsilon = 1$. The model parameters are tabulated in **Table 1**.

The dynamics of the simulated worm-like polymer are governed by the imposed thermal fluctuations, and as such the polymer is expected to exhibit Brownian motion. However, previous studies have indicated that a Brownian depiction does not accurately describe worm behavior [16]. We also observe that simulated worms in this Brownian model demonstrate little exploration of the simulation arena (e.g., low mean squared displacement) at low temperatures, with greater exploration at high temperatures due to large random fluctuations. However, in our observations of real *L. variegatus*, blackworms often demonstrate greater exploration at low temperatures (**Figure 2A**). Thus, we add an additional active force that reflects the self-propelled forward peristaltic crawling of the worm (**Figure 1**). The force acts with equal magnitude on eight monomers at one end of the worm, denoted the head end, in the tangential direction determined by averaging the position vectors of the links on either side of the monomer; that is, $\vec{F}^{i}_{\text{active}} = f_{\text{active}}(\hat{\mathbf{r}}_{i-1,i} + \hat{\mathbf{r}}_{i,i+1})/2$. This also reflects our observation that the worms in experiments demonstrate more activity at their heads than from the rest of their bodies.

To fit the parameters of the model (**Table 1**) to reflect the observed behavior of blackworms, we compare simulations with single-worm experiments (**Figures 2A,B**). Blackworms obtained from Aquatic Foods and Blackworm Co. (CA, United States) and were cultivated in several boxes (35 cm × 20 cm × 12 cm, 25 g of worms per box) filled with spring water (at a height of approximately 2 cm) at ~4°C for at least 3 weeks. Worms were habituated to room temperature in a 50 ml beaker with spring water at ~20°C at least 6 h prior to experiments. Worms were fed with tropical fish flakes twice a week, and the water was changed 1 day after feeding them. Studies with *L. variegatus* do not require approval by the institutional animal care committee.

In these experiments, a single worm was placed in the center of a 30 cm × 30 cm × 1 cm container filled with water at a height of approximately 0.5 cm. We recorded experiments at water temperatures from 12 to 34°C ± 1°C in increments of 2°C. The worm behavior was recorded at a rate of two frames per second for 15 min. Video frames were analyzed using MATLAB Image Processing Toolbox (MathWorks, Natick, MA, United States) to extract the position and geometry of the worm. Example trajectories of the tracked worms are animated in **Supplementary Video S1–S4** and plotted in **Supplementary Figures S1–S12**.

We observe that at temperatures of 30°C or lower, the worm tends to explore the arena. Often, the worm will travel in a relatively straight path until it reaches the wall of the container, after which it will then continue to explore along the edge of the wall. In some cases, the worm fails to find the wall and continues to explore somewhat erratically. Beyond 30°C, the worm exhibits significantly less exploration, staying close to its original starting position. We attribute this to the temperature being too high for the worm to comfortably explore, and potentially even causing physiological changes to the worm [41]. Above 34°C, the worm is unlikely to survive for more than a few minutes if not seconds.

In our simulations, the self-propelled Brownian polymer remains subject to Gaussian thermal fluctuations. Most noticeably at low T, the active tangential force results in the simulated worm moving persistently in a single direction (**Figure 2C**). At high T, the thermal fluctuations tend to dominate over the bending potential, resulting in a coiled-up conformation of the simulated worm, and as such the individual tangential forces are likely to effectively cancel each other out in direction, resulting in lower overall displacement (**Figure 2D**, also see **Supplementary Video S5–S7**).

To compare simulation and experiment, we examine the mean squared displacement (MSD) as a function of lag time τ (**Figures 2E–G**; **Supplementary Figures S1–S12**). Our key observation is that the slope of the MSD, when plotted on a logarithmic scale, differs depending on the temperature. A higher MSD slope indicates that the worm undergoes more directed motion, while a lower MSD slope indicates more diffusive motion, with a slope of one representing Brownian motion. In both experiment and simulation, the slope of the MSD generally decreases as temperature increases: at low temperatures, the worm displays near-ballistic movement, which becomes increasingly less directed as temperature increases. Because the worm is confined in the experiments, the MSD is limited by the size of the arena and begins to plateau at large values of τ. Hence, we calculate the slope for the regime in which the logarithm of MSD is generally linear, for τ between 5 and 100. The simulated worm is not subject to boundary conditions and, at low T, will move persistently in the direction set by its initial orientation.

By comparing the slope of the MSD from experiments with simulations, we derive a rough scaling of the temperature between simulation units (T_{sim}) and degrees Celsius (T_{exp}): $T_{\text{exp}} = (5{,}000/3)T_{\text{sim}} - 77/3$. In determining this scaling, we excluded experimental data above 30°C, due to the drastic decrease in worm activity at high temperatures. Hence, this scaling is valid only for temperatures between 12 and 30°C inclusive.

While the slope of the MSD captures whether the worm's motion is directed or random, it does not capture higher-order measures of worm activity. To examine the amount by which a worm fluctuates over time, we calculate the average change in angle of the worm between consecutive timesteps (**Figures 2H,I**). The angle θ is determined by fitting the smallest ellipse that encloses the worm and calculating the angle of the major axis with respect to the horizontal direction (**Figure 2H**). The change in angle increases with temperature, reflecting the greater fluctuations observed in both simulation and experiment.

3 WORM BLOB AGGREGATION

To model a collective system of worms, we retain the dynamics of the single-worm model, but specify a stronger interaction potential between monomers of different chains:

$$U_{\text{interaction}} = 4\varepsilon \sum_{g=1}^{M} \sum_{i=1}^{N_m} \sum_{j>i}^{N_m} \left[\left(\frac{\sigma}{|\mathbf{r}_{i^{(g)}j^{(g)}}|} \right)^8 - \left(\frac{\sigma}{|\mathbf{r}_{i^{(g)}j^{(g)}}|} \right)^4 \right] + 4\varepsilon_{\text{blob}} \sum_{g=1}^{M} \sum_{h>g}^{M} \sum_{i=1}^{N_m} \sum_{j=i}^{N_m} \left[\left(\frac{\sigma}{|\mathbf{r}_{i^{(g)}j^{(h)}}|} \right)^8 - \left(\frac{\sigma}{|\mathbf{r}_{i^{(g)}j^{(h)}}|} \right)^4 \right] \tag{6}$$

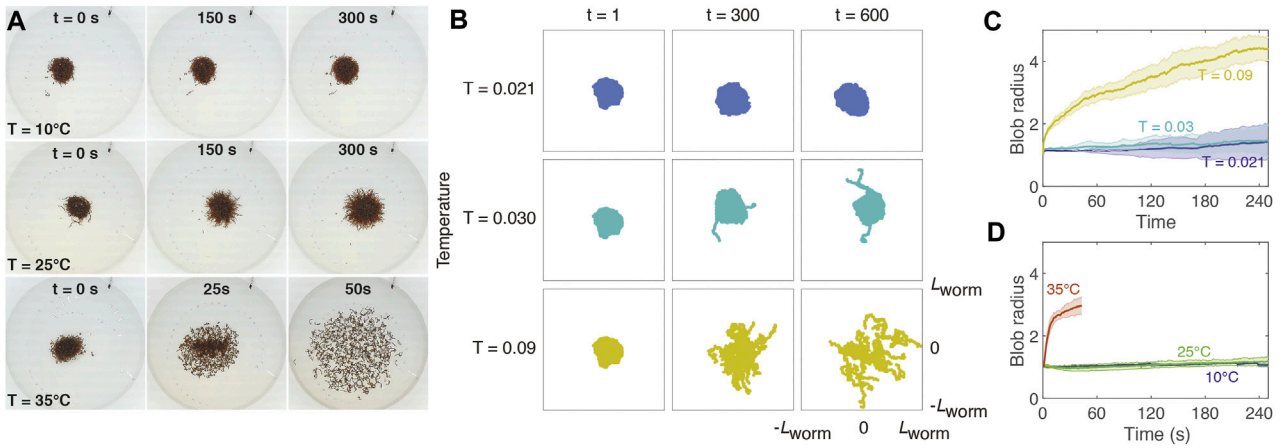

FIGURE 3 | Temperature affects cohesion of worm blobs. **(A)**: Snapshots of experimental blobs ($N \sim 600$) at 10, 25, and 35°C. Experiments at $T = 35$°C were performed for only 1 min since worms begin to die after about 2 min at this temperature. The diameter of the dish is 20 cm. **(B)**. Snapshots of simulated blobs at different temperatures (row) and time steps (column). Each box is a square with side twice the equilibrium length of one worm ($L_{worm} = 41\sigma$). Each blob contains 20 worms with attachment strength $\varepsilon_{blob} = 12$. **(C)**: Mean radius ± SD of simulated blob as a function of time for different temperatures (T = 0.021 (dark blue), 0.03 (cyan), and 0.09 (yellow)), corresponding roughly to the experimental temperatures used in panel **(A)**. For each trial, the radius is normalized to the initial radius at $t = 0$. **(D)**: Mean radius ± SD of experimental blob ($N \sim 600$) as a function of time for different temperatures (T = 10 (blue), 25 (green), 35 (red) °C). For each trial, the radius is normalized to the initial radius at $t = 0$.

where M is the number of worms in the system, N_m is the number of monomers per worm, $\mathbf{r}_{i(g)j(h)} = \mathbf{r}_{j(h)} - \mathbf{r}_{i(g)}$ is the vector between the positions of monomer i of chain g and monomer j of chain h, and the coefficient $\varepsilon_{blob} > \varepsilon$. We refer to ε_{blob} as the attraction parameter governing the strength of attractive forces between worms.

We observe in experiments that temperature affects the attachment of worms in a blob, resulting in a transition between a solid-like phase to a fluid-like phase (**Figure 3A**). At a low temperature (10°C), a tightly entangled blob remains approximately the same size over the course of several minutes. At a moderate temperature (25°C), the worms spread out slightly, though the blob remains intact; at a high temperature (35°C), the worms quickly disentangle from one another, forming a fluid of detached, coiled worms.

We simulate worm blobs at three different temperatures, $T =$ 0.021, 0.030, and 0.09 (**Figure 3**; **Supplementary Video S8–S10**). The first two temperatures roughly correspond to 10 and 25°C, respectively, following the temperature scaling described in **Section 2**. Since temperatures above 30°C result in drastic changes to worm behavior and scale differently than at moderate temperatures, we choose a high simulation temperature of 0.09 to represent 35°C. In these simulations, ε_{blob} was set to 12, and the active force magnitude was 220.

Each simulation (row of **Figure 3B**) begins from the same initial conditions shown in the $t = 1$ column. To generate these conditions, we perform a preliminary simulation starting from 20 worms initialized to random positions: the location of the head node was randomly sampled from a square with side length equal to half the worm length, with the angle of the worm sampled from the interval $[0, 2\pi)$. This ensured that the worms were close enough to aggregate into a single blob. The worms were then allowed to aggregate at a low temperature, $T = 0.02$, for a period of 20 time steps. The interaction coefficient ε_{blob} was set to a high value of 20, and the active tangential force was set to zero (i.e., the worms obeyed Brownian dynamics) to facilitate attachment. The values of the parameters in this preliminary simulation are chosen such that this "equilibration" process results in worms attaching into a stable, densely-packed blob from random conditions. This same resulting blob was used as the starting point for all simulations described below.

At $T = 0.021$, the worms remain in a compact, solid-like blob, demonstrating little activity. At $T = 0.030$, a few worms begin to detach, but most of the worms remain tightly attached. However, at $T = 0.090$, the blob "melts" into a fluid-like state, as the worms separate from each other and disperse across the arena, corroborating the experimental results (**Figure 3A**).

4 EMERGENT LOCOMOTION AND COLLECTIVE THERMOTAXIS

Previous experiments demonstrated the ability of biological worm blobs to undergo emergent collective locomotion in temperature gradients [17]. The blobs exhibited negative thermotaxis, moving from the high temperature side of the gradient to the low temperature side (**Figure 4A**). The collective locomotion was enhanced by shining a spotlight on the worms [17]: a worm blob subject to bright light conditions (5,500 lux) moved together as an entangled unit, resulting in over 90% of worms reaching the cold side over the course of the 30-min experiment. In contrast, worms under low room light conditions (400 lux) did not move as a compact blob, with most disentangling and moving individually, resulting in

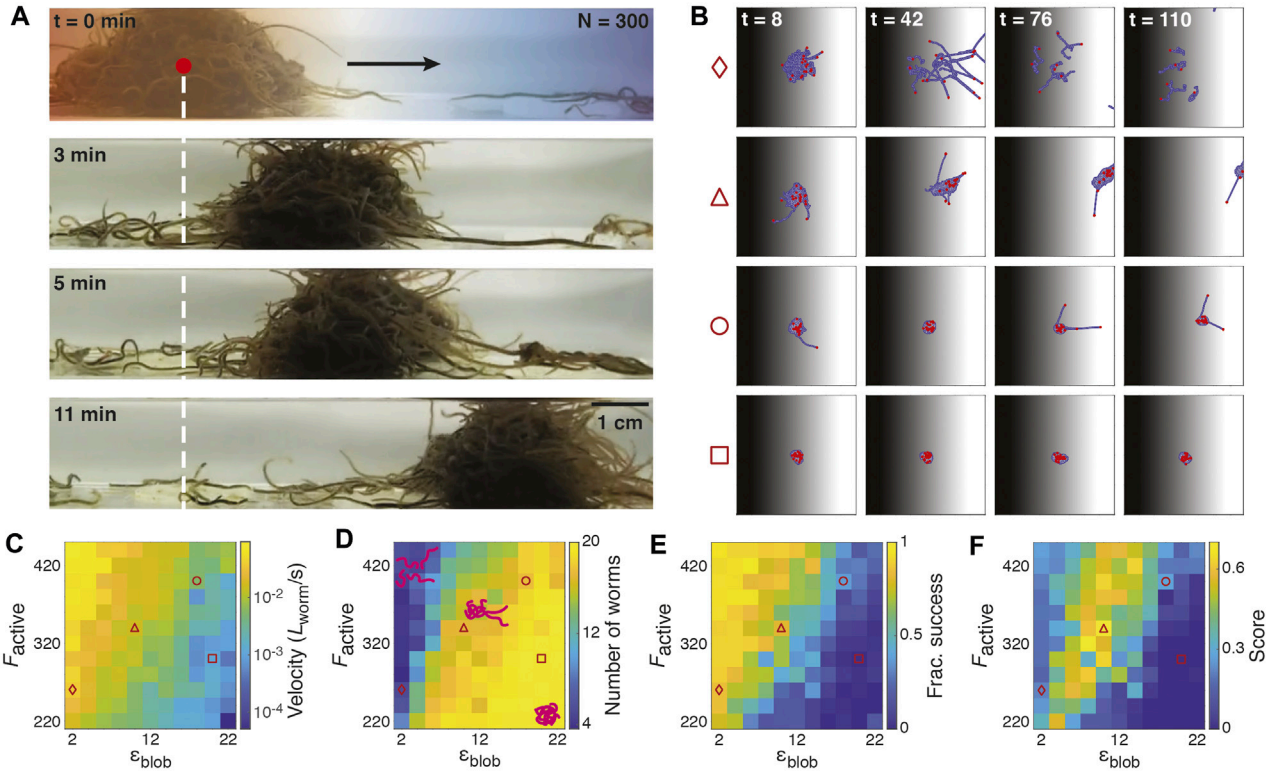

FIGURE 4 | Emergent locomotion in temperature gradients. **(A)**: Snapshots of an experimental worm blob ($N = 300$ worms) demonstrating emergent locomotion in a temperature gradient (left: high temperature; right: low temperature). **(B)**: Snapshots of blob in temperature gradient from $T = 0.08$ (black) on the left to $T = 0$ (white) on the right. Each column corresponds to a different simulation time step ($t = 8$, 42, 76, and 110 respectively). Each row corresponds to different set of attraction parameters ε_{blob} and active force magnitudes F_{active} (diamond: $\varepsilon_{blob} = 2$, $F_{active} = 260$; triangle: $\varepsilon_{blob} = 10$, $F_{active} = 340$; circle: $\varepsilon_{blob} = 18$, $F_{active} = 400$; square: $\varepsilon_{blob} = 20$, $F_{active} = 300$). Red dots indicate the heads of individual worms. Despite the three-dimensional nature of real worm blobs, our two-dimensional model captures emergent collective locomotion for some combinations of ε_{blob} and F_{active}: in the triangle sequence, the majority of worms collectively move from the hot side of the gradient to the cold side, with the heads of some worms extending into the cold side. **(C)**: Heatmap of the average x-component of the blob velocity (in worm length per second) for a range of F_{active} and ε_{blob}. The velocity is computed for the center of mass of the largest cohesive blob in the simulation. **(D)**: Heatmap of the average number of worms (maximum of 20) of the largest cohesive blob for a range of F_{active} and ε_{blob}. Cartoons indicate typical configurations of worms for different regimes of parameter space. **(E)**: Heatmap of the fraction of successful worms per simulation. Success is indicated by the fraction of worms that reach the $T = 0$ cold side of the gradient by the end of a 120-timestep simulation. **(F)**: Heatmap of the collective locomotion score, given by the product of the blob velocity, blob size, and fraction of success, with each term weighted so that its maximum is 1 (**Eq. 7**).

approximately 70% of worms successfully reaching the cold side in the same timeframe.

In the single worm case, a simulated worm has no preferred direction in the absence of a gradient; if the temperature is low enough, the worm will move in the tangential direction dictated by its head end, but this direction relies only on the initial orientation of the worm, which is randomly chosen. A temperature gradient will break this symmetry and sets a preferred direction of motion. At high temperatures, the worm's motion is largely random. However, if, *via* fluctuations, the head of the worm becomes oriented along the temperature gradient, pointing toward colder temperatures, the tangential forces will cause the worm to move in that direction. The further the worm moves toward lower temperatures, the more it will straighten out, resulting more pronounced ballistic motion. Inversely, if the worm is oriented such that it points toward warmer temperatures, the worm will continue to move in that direction if the surrounding temperature is low enough that the active force is not immediately dominated by random fluctuations. However, the component of the worm's velocity parallel to the gradient will decrease as it moves toward higher temperatures, at which point fluctuations will dominate, and the worm more frequently reorients itself (**Figure 2I**).

Here, we simulate blobs in temperature gradients and observe that the level of attachment of worms in a blob depends on a tradeoff between the interaction coefficient ε_{blob} and active force magnitude F_{active}. The higher the interaction coefficient ε_{blob}, the more compact the blob, with worms tightly adhering to one another. Increasing the active force magnitude F_{active}, on the other hand, increases the likelihood that worms will break apart from the blob.

Simulated blobs with 20 worms were placed in a temperature gradient linearly decreasing from $T = 0.08$ on the left edge of the visualization area to $T = 0$ on the other edge. The visualization area corresponds to a square arena with each edge chosen to be

120 arbitrary units long, approximately 2.5 times the equilibrium length of a single worm. While only this region is visualized, the arena extends indefinitely in each direction, with a constant $T = 0.08$ beyond the left edge and $T = 0$ beyond the right edge.

Each temperature gradient simulation was run from the same initial conditions as described previously in **Section 3**, where the initial blob aggregated in the absence of a temperature gradient. The same initial blob was used for each simulation and was subsequently placed in the temperature gradient such that its center of mass was located in the center of visualization area, corresponding to $T = 0.04$. We then performed a systematic parameter sweep over the interaction coefficient $\varepsilon_{\text{blob}}$ between values of 2–22 and the active force magnitude F_{active} between 220 and 420.

In **Figure 4B**, we highlight four examples of simulations from different regions of the explored parameter space that illustrate cases in which the blob successfully or unsuccessfully traverses the gradient as a collective. Simulations from a larger sampling of parameter space are also shown in **Supplementary Video S11**. If $\varepsilon_{\text{blob}}$ is too low (diamond sequence), the worms do not remain attached; if $\varepsilon_{\text{blob}}$ is too high (square sequence), the strong attachment forces dominate over the active forces, and the blob remains at its starting position. If $\varepsilon_{\text{blob}}$ and F_{active} are balanced, this can lead to emergent cohesive locomotion toward the cold side of the gradient (triangle sequence). If $\varepsilon_{\text{blob}}$ is slightly larger than F_{active}, collective locomotion may also occur, but at a slower speed (circle sequence).

In **Figures 4C–E**, we compare three quantities as a function of $\varepsilon_{\text{blob}}$ and F_{active}: the velocity of the center of mass of the largest worm blob in the simulation, the size of the largest blob, and the fraction of worms that successfully reach the cold side of the gradient. Generally, we observe that each of these quantities is positively correlated with F_{active} and negatively correlated with $\varepsilon_{\text{blob}}$, or vice versa.

Figure 4C is a heatmap of the blob velocity as a function of F_{active} and $\varepsilon_{\text{blob}}$; as all of the worms in a given simulation may not be attached as a single aggregation, especially for lower values of $\varepsilon_{\text{blob}}$, we report here the velocity of the center of mass of the largest cohesive blob as identified using the DBSCAN clustering algorithm [42]. We use this algorithm to identify blobs of arbitrary size and shape where the separation between two monomers in a blob is no greater than 2σ, though many other clustering methods exist, with a range of applications across fields [43, 44]. We find here that the velocity increases as F_{active} increases, but decreases as $\varepsilon_{\text{blob}}$ increases.

Meanwhile, **Figure 4D** shows a heatmap of the average number of worms in the largest blob, which shows the opposite trend as **Figure 4C**: the size of the blob is positively correlated with $\varepsilon_{\text{blob}}$ but negatively correlated with F_{active}. For high $\varepsilon_{\text{blob}}$ and low F_{active}, the blob remains completely cohesive, encompassing all 20 worms. For low $\varepsilon_{\text{blob}}$ and high F_{active}, the worms are less cohesive, with the largest blobs containing down to about four worms.

Figure 4E illustrates the fraction of worms successfully reaching the cold side of the gradient per simulation. This heatmap parallels that of **Figure 4C**, showing that the highest proportion of success occurs for low $\varepsilon_{\text{blob}}$ and high F_{active}, and the least successful blobs for high $\varepsilon_{\text{blob}}$ and low F_{active}.

In general, simulated worms are most effective at reaching the cold side when $\varepsilon_{\text{blob}}$ is low and F_{active} is high. However, they do not move cohesively, with the largest blobs containing between approximately 25–50% of the total worms in the simulation. At the other extreme, when $\varepsilon_{\text{blob}}$ is high and F_{active} is low, nearly all worms remain in a cohesive aggregation, but the blob demonstrates little to no movement toward the cold side of the gradient, due to the attachment forces dominating over the active motion. We note that for real worms, remaining in a cohesive aggregation is beneficial, especially when there is danger of moisture loss [17]. Moreover, individual blackworms can die within minutes in high temperature environments (above 30°C). Our simulations do not reflect any potential worm death; in some cases, individual simulated worms that have moved toward the hot side of the gradient become "unstuck" *via* random fluctuations and may eventually find the cold side.

Hence, we seek a regime in which the worms demonstrate a high rate of success at reaching the cold side of the gradient and move relatively quickly while remaining mostly cohesive. To do so, we compute a score for each simulation given by the product of the velocity of the center of mass, largest blob size, and fraction of success, which each of the three terms normalized such that each individual term scales between 0 and 1. All three terms are moreover equally weighted such that the score takes on values between 0 and 1:

$$\text{score} = \min(v_{\text{blob}}, v_0) \cdot N_{\text{largest blob}}/20 \cdot \text{frac. success} \tag{7}$$

where $\min(v_{\text{blob}}, v_{\max})$ represents the smaller value between the average speed of the blob in the direction of decreasing temperature v_{blob}, and v_0, which is defined as half the width of the arena divided by the total simulation time (e.g., the slowest possible speed of a successful blob); and $N_{\text{largest blob}}$ is the number of worms in the largest blob.

Figure 4F illustrates this score as a function of $\varepsilon_{\text{blob}}$ and F_{active}. The tradeoff between $\varepsilon_{\text{blob}}$ and F_{active} produces a regime in which the highest scores are achieved, along a band that roughly follows the line $F_{\text{active}} = 22\varepsilon_{\text{blob}} + 132$.

Figure 5 illustrates a phase diagram corresponding to this function overlaid with example snapshots of blob configurations from corresponding simulations, revealing the rich ensemble of behaviors across the parameter space of F_{active} and $\varepsilon_{\text{blob}}$. To generate the phase diagram, we fit the score landscape from **Figure 4F** to the following function of F_{active} and $\varepsilon_{\text{blob}}$:

$$\begin{aligned}\text{score} = \quad & \alpha_{00} + \alpha_{10}\varepsilon_{\text{blob}} + \alpha_{01}F_{\text{active}} + \alpha_{20}\varepsilon_{\text{blob}}^2 + \alpha_{11}\varepsilon_{\text{blob}}F_{\text{active}} \\ & + \alpha_{02}F_{\text{active}}^2 + \alpha_{30}\varepsilon_{\text{blob}}^3 + \alpha_{21}\varepsilon_{\text{blob}}^2F_{\text{active}} + \alpha_{12}\varepsilon_{\text{blob}}F_{\text{active}}^2 \\ & + \alpha_{03}F_{\text{active}}^3\end{aligned} \tag{8}$$

The parameters are tabulated in **Supplementary Table S1**.

The dashed lines in **Figure 5** separate three regions (I-III) characterized by the prevailing collective behavior. In region I, corresponding to the region where the highest scores are achieved, the worms consistently traverse the gradient as a

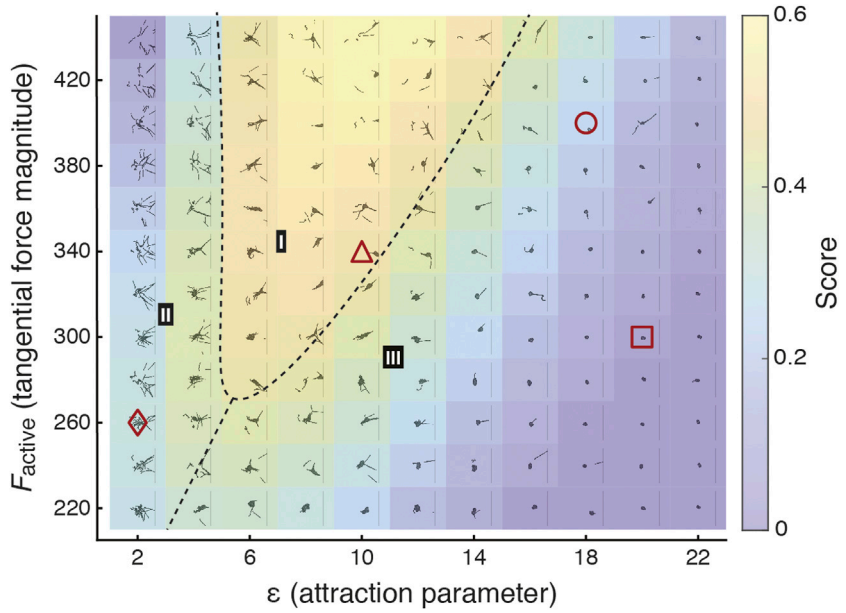

FIGURE 5 | Heatmap of score reveals parameter regime in which the most effective collective locomotion is observed. The score illustrated in **Figure 4F** is fit to the function given in **Eq. 8**. The heatmap illustrates this fitted score function and is divided into three regimes (I-III). I: consistently successful cohesive blob locomotion, reflecting observed emergent locomotion in real worm blobs (**Figure 4A**); II: generally unsuccessful blob locomotion, with failure due to dissociation of blobs; III: generally unsuccessful blob locomotion, with failure due to overly strong attachment, resulting in little collective movement. In phases II and III, parameter combinations near the boundary of phase I can intermittently lead to successful collective locomotion. Each subpanel shows an overlaid snapshot at between $t = 50$ and 150 of an example simulation with the corresponding F_{active} and ε_{blob}. Red shapes correspond to example sequences shown in **Figure 4B**.

collective. In this region, the emergent collective locomotion reflects what is observed in experiments (**Figures 1C**, **4A**; [17]). We note that while these real worm blobs inhabit three-dimensional space, our two-dimensional model nevertheless captures collective locomotion. In regions II and III, collective locomotion is generally unsuccessful, though successful cases of collective locomotion are intermittently observed near the boundary with region I. In region II, failures typically occur when the blob dissociates and worms move individually, as F_{active} is too high for the corresponding values of ε_{blob}. For failed cases in region III far from the boundary with region I, the worms are too strongly attached and as such the blob does not demonstrate any self-motility and remains near the starting position. Closer to the boundary with region I, the majority of worms may remain attached, with a few worms detaching from the blob and potentially moving toward the cold side on their own. The center of mass of the largest blob either remains close to the origin or drifts slowly to cold side, as here ε_{blob} is slightly too high compared to F_{active}.

5 DISCUSSION

Following the first observation of collective locomotion in entangled worm blobs [17], we developed a model that employs the physics of active, semi-flexible polymers and filaments in the context of the collective behavior of macroscale, multicellular organisms. We model worms as self-propelled Brownian polymers, focusing specifically on the parameter space of aspect ratio, bending rigidity, activity, and temperature that describes the California blackworm, *L. variegatus*, at temperatures between 10 and 35°C. In the simulated single worm case, the constant-magnitude tangential force F_{active} results in a persistent directed motion at low temperatures, with larger fluctuations erasing the persistent motion at high temperatures. In a temperature gradient, this results in a preferred direction of movement from high to low temperatures.

Multiple simulated worms can aggregate into a blob, held together by attractive forces as governed by the attachment strength ε_{blob}. We show that the simulated blob can collectively navigate along a temperature gradient provided that the tangential force and attachment strength are balanced. In a parameter sweep over the attachment strength ε_{blob} and the magnitude of the tangential force F_{active}, we observe a tradeoff between the worm velocity and the cohesiveness of the blob. Higher attachment reduces the speed of the blob and hinders collective motion in extreme cases, while a higher force increases the individual worm speed but can result in worms detaching from the blob. We identify the regime where blob movement is "optimal" from a biological perspective–i.e., where the blob quickly moves toward cooler, less dangerous temperatures, while remaining largely cohesive, as worms are less likely to survive on their own outside of the blob–quantified by a score that combines the blob velocity, blob size, and fraction of worms successfully reaching the cold side of the gradient.

We note that a similar tradeoff, between the fraction of successful worms and the blob speed, was observed in experiments, as illustrated in **Supplementary Figure S12** of [17]. For experiments at four different worm blob sizes (N = 10, 20, 40, and 80), it was observed that as the number of worms in a blob increased, the fraction of worms successfully reaching the cold side of the gradient increased as well. However, larger blobs were slower at reaching the cold side. While we have focused on a single blob size in this paper, our model can be expanded to other system sizes and can be used to make experimentally testable predictions of how the number of worms affects collective locomotion. Moreover, future experiments can involve altering the activity of individual worms (e.g. by adding alcohol to the water) and/or their attachment strength (e.g., by manipulating light conditions as observed in [17]) in order to test our predictions on these parameters' effect on blob motility.

Currently, the parameters of our model are chosen such that there is qualitative agreement between the behavior of the simulated worm and observed *L. variegatus*. However, we expect that our model should be broadly generalizable to describe other long, slender, flexible organisms including annelids and nematodes. Future work will investigate the effect of the aspect ratio of individual worms on their collective behavior in temperature gradients. For instance, *T. tubifex* are a similar length to blackworms but are about a quarter as thick, though collective locomotion in *T. tubifex* has not been observed. Blob formation was also observed in terrestrial worms such as common earthworms (*Lumbricus terrestris*) and red wigglers (*Eisenia fetida*) [17], but collective locomotion in such worms remains to be investigated. Moreover, in the limit of an aspect ratio of 1, the polymer picture reduces to that of a single round particle. Such a model can be useful to describe aggregations of organisms that more closely resemble particles rather than filaments, such as ants and bees; future research can work toward a unified model that captures collective behavior along the gradient between active particles and filaments.

A primary limitation of our current model is its two-dimensionality. While we are able to capture collective behavior of active worm-like polymers, in reality, blackworms form blobs that are three-dimensional in nature. In sufficiently deep water, small blackworm blobs are hemispherical (**Figure 4A**). Future work will generalize the current model to three dimensions, which will also allow us to explicitly model the physical entanglement of polymers. Entanglement and reptation in polymer melts and solutions has been extensively examined for decades (e.g., by de Gennes [45]). More recently, non-equilibrium polymeric fluids containing active polymers have come under focus, as these systems cannot be explained by statistical-mechanical theories [24, 35, 46]. For instance, Manna and Kumar showed that in a confined volume, contractile active polymers spontaneously entangled, and moreover that this entangled state was stable for any volume fraction of polymers [46]. Meanwhile, for extensile active polymers, they observed a phase transition between disentanglement and entanglement governed by the activity and volume fraction.

In our current model, for simplicity, we have implemented self-propulsion of worms as a tangential force with constant magnitude, without consideration of the medium through which the worms are moving. In reality, worms harness friction to propel themselves, employing a combination of peristaltic elongation and contraction, undulatory strokes, and helical movements to crawl on surfaces, burrow through sediments, or swim through water [18, 47]. While our goal in this paper is to develop a parsimonious and generalizable description of worm behavior, accounting for hydrodynamics and friction can provide a more complete analysis of a specific biological system. As such, we expect that while a model with hydrodynamics can allow for a more accurate depiction of worm dynamics at smaller time and length scales, our current model nevertheless captures observed collective worm behavior.

By simulating entangled active polymers, we can more closely examine the mechanisms by which blackworm blobs collectively locomote: the differentiation of activity whereby worms at the front are elongated and pull the clump of coiled worms at the back. In particular, we can examine the role of trailing "wiggler" worms that lift themselves off the surface, potentially to reduce friction, which cannot be probed currently with our 2-D model. In experiments, differentiation of activity has only been explicitly observed in small blobs containing on the order of tens of worms, where such differentiation of activity can be seen by eye [17]. These observations were validated by force cantilever experiments, which demonstrated that a few worms were able to exert a force strong enough to pull the blob, and by robophysical experiments, in which a blob of entangled "smarticles" could only move as a unit if the group was divided into a few robots that use a "crawl" or "wiggle" gait while the rest remain inactive, as opposed to all crawling or all wiggling [17]. In future simulations, we aim to simulate 3-D entangled worm blobs in order to elucidate whether this collective motion mechanism remains valid as blob size increases.

Here, we have examined the collective dynamics in a general system of active filament-like worms, focusing on a section of parameter space chosen to reflect blackworm behavior. However, real three-dimensional blackworm blobs also exhibit properties that are not captured in our model. For instance, in a surface in air, blackworms form a hemispherical blob to maximize moisture retention; they will also spread out in long "arms" in order to search for moisture and shrink back into a hemisphere if no moisture is found [17]. To describe this particular biological system, our current model could be expanded to explicitly incorporate rules that describe worms' sensing of their local environments. Indeed, the interplay between individual sensing and interaction with the environment, coupled with interactions between worms in close proximity, leads to fascinating emergent collective phenomena such as this cooperative searching behavior.

In conclusion, we have developed a model that examines active polymers in the context of entangled living systems much larger than the scale of cytoskeletal, cellular, and other biological systems typically described within similar frameworks. We subsequently identified a regime wherein effective collective locomotion emerges as a result of balancing the tradeoff

between directed activity and attachment of individuals. While the experimental observations of the California blackworm in particular have driven our current work, our research opens up avenues for new experiments and theoretical investigations of the collective behavior of long, slender organisms at the meso- and macroscales.

DATA AVAILABILITY STATEMENT

The simulation code developed for this study can be found at https://github.com/peleg-lab/active-polymer-worm.

AUTHOR CONTRIBUTIONS

All authors designed the study. YO-A and HT conducted the experiments; CN and YO-A analyzed the experiments; and CN and OP constructed the model and wrote the code for the simulations. CN wrote the paper and all authors revised the final manuscript.

FUNDING

DG acknowledges funding support from ARO MURI award (W911NF-19-1-023) and NSF Physics of Living Systems Grant (PHY-1205878). MB. acknowledges funding support from NSF Grants CAREER 1941933 and 1817334.

SUPPLEMENTARY MATERIAL

The Supplementary Material for this article can be found online at: https://www.frontiersin.org/articles/10.3389/fphy.2021.734499/full#supplementary-material

REFERENCES

1. Friedl P, and Gilmour D. Collective Cell Migration in Morphogenesis, Regeneration and Cancer. *Nat Rev Mol Cel Biol.* (2009) 10:445–57. doi:10.1038/nrm2720
2. Giardina I. Collective Behavior in Animal Groups: Theoretical Models and Empirical Studies. *HFSP J* (2008) 2:205–19. PMID: 19404431. doi:10.2976/1.2961038
3. Farkas I, Helbing D, and Vicsek T. Mexican Waves in an Excitable Medium. *Nature* (2002) 419:131–2. doi:10.1038/419131a
4. Silverberg JL, Bierbaum M, Sethna JP, and Cohen I. Collective Motion of Humans in Mosh and circle Pits at Heavy Metal Concerts. *Phys Rev Lett* (2013) 110:228701. doi:10.1103/PhysRevLett.110.228701
5. Camazine S, Deneubourg JL, Franks NR, Sneyd J, Theraulaz G, and Bonabeau E.*Self-Organization in Biological Systems*. Princeton, NJ: Princeton University Press (2001).
6. Anderson C, Theraulaz G, and Deneubourg J-L. Self-assemblages in Insect Societies. *Insectes Sociaux* (2002) 49:99–110. doi:10.1007/s00040-002-8286-y
7. Hu DL, Phonekeo S, Altshuler E, and Brochard-Wyart F. Entangled Active Matter: From Cells to Ants. *Eur Phys J Spec Top* (2016) 225:629–49. doi:10.1140/epjst/e2015-50264-4
8. Mlot NJ, Tovey CA, and Hu DL. Fire Ants Self-Assemble into waterproof Rafts to Survive Floods. *Proc Natl Acad Sci* (2011) 108:7669–73. doi:10.1073/pnas.1016658108
9. Reid CR, Lutz MJ, Powell S, Kao AB, Couzin ID, and Garnier S. Army Ants Dynamically Adjust Living Bridges in Response to a Cost-Benefit Trade-Off. *Proc Natl Acad Sci USA* (2015) 112:15113–8. doi:10.1073/pnas.1512241112
10. Peleg O, Peters JM, Salcedo MK, and Mahadevan L. Collective Mechanical Adaptation of Honeybee Swarms. *Nat Phys* (2018) 14:1193–8. doi:10.1038/s41567-018-0262-1
11. Brinkhurst RO, and Gelder SR.*Annelida: Oligochaeta and Branchiobdellida*. San Diego, CA: Academic Press (1991). p. 431–64. chap. 12.
12. Ramaswamy S. The Mechanics and Statistics of Active Matter. *Annu Rev Condens Matter Phys* (2010) 1:323–45. doi:10.1146/annurev-conmatphys-070909-104101
13. Marchetti MC, Joanny JF, Ramaswamy S, Liverpool TB, Prost J, Rao M, et al. Hydrodynamics of Soft Active Matter. *Rev Mod Phys* (2013) 85:1143–89. doi:10.1103/RevModPhys.85.1143
14. Bechinger C, Di Leonardo R, Löwen H, Reichhardt C, Volpe G, and Volpe G. Active Particles in Complex and Crowded Environments. *Rev Mod Phys* (2016) 88:045006. doi:10.1103/RevModPhys.88.045006
15. Zirbes L, Brostaux Y, Mescher M, Jason M, Haubruge E, and Deneubourg J-L. Self-assemblage and Quorum in the Earthworm eisenia Fetida (Oligochaete, Lumbricidae). *PLOS ONE* (2012) 7:e32564. doi:10.1371/journal.pone.0032564
16. Deblais A, Maggs AC, Bonn D, and Woutersen S. Phase Separation by Entanglement of Active Polymerlike Worms. *Phys Rev Lett* (2020) 124:208006. doi:10.1103/PhysRevLett.124.208006
17. Ozkan-Aydin Y, Goldman DI, and Bhamla MS. Collective Dynamics in Entangled Worm and Robot Blobs. *Proc Natl Acad Sci USA* (2021) 118:e2010542118. doi:10.1073/pnas.2010542118
18. Drewes CD. Helical Swimming and Body Reversal Behaviors in Lumbriculus Variegatus (Annelida: Clitellata: Lumbriculidae). *Hydrobiologia* (1999) 406:263–9. doi:10.1007/978-94-011-4207-6_26
19. Lesiuk NM, and Drewes CD. Behavioral Plasticity and central Regeneration of Locomotor Reflexes in the Freshwater Oligochaete, Lumbriculus Variegatus. I: Transection Studies. *Invertebrate Biol* (2001) 120:248–58. doi:10.1111/j.1744-7410.2001.tb00035.x
20. Lesiuk NM, and Drewes CD. Behavioral Plasticity and central Regeneration of Locomotor Reflexes in the Freshwater Oligochaete, Lumbriculus Variegatus. II: Ablation Studies. *Invertebrate Biol* (2001) 120:259–68. doi:10.1111/j.1744-7410.2001.tb00036.x
21. Brues CT. A Migrating Army of Sciarid Larvae in the philippines. *Psyche: A J Entomol* (1951) 58:73–6. doi:10.1155/1951/36389
22. Zirbes L, Deneubourg J-L, Brostaux Y, and Haubruge E. A New Case of Consensual Decision: Collective Movement in Earthworms. *Ethology* (2010) 116:546–53. doi:10.1111/j.1439-0310.2010.01768.x
23. Deblais A, Woutersen S, and Bonn D. Rheology of Entangled Active Polymer-like T. Tubifex Worms. *Phys Rev Lett* (2020) 124:188002. doi:10.1103/PhysRevLett.124.188002
24. Winkler RG, Elgeti J, and Gompper G. Active Polymers - Emergent Conformational and Dynamical Properties: A Brief Review. *J Phys Soc Jpn* (2017) 86:101014. doi:10.7566/JPSJ.86.101014
25. Winkler RG, and Gompper G. The Physics of Active Polymers and Filaments. *J Chem Phys* (2020) 153:040901. doi:10.1063/5.0011466
26. Ghosh A, and Gov NS. Dynamics of Active Semiflexible Polymers. *Biophysical J* (2014) 107:1065–73. doi:10.1016/j.bpj.2014.07.034
27. Isele-Holder RE, Elgeti J, and Gompper G. Self-propelled Worm-like Filaments: Spontaneous Spiral Formation, Structure, and Dynamics. *Soft Matter* (2015) 11:7181–90. doi:10.1039/C5SM01683E
28. Duman Ö, Isele-Holder RE, Elgeti J, and Gompper G. Collective Dynamics of Self-Propelled Semiflexible Filaments. *Soft Matter* (2018) 14:4483–94. doi:10.1039/C8SM00282G
29. Martín-Gómez A, Eisenstecken T, Gompper G, and Winkler RG. Active Brownian Filaments with Hydrodynamic Interactions: Conformations and Dynamics. *Soft Matter* (2019) 15:3957–69. doi:10.1039/C9SM00391F
30. Samanta N, and Chakrabarti R. Chain Reconfiguration in Active Noise. *J Phys A: Math Theor* (2016) 49:195601. doi:10.1088/1751-8113/49/19/195601
31. Chaki S, and Chakrabarti R. Enhanced Diffusion, Swelling, and Slow Reconfiguration of a Single Chain in Non-gaussian Active bath. *J Chem Phys* (2019) 150:094902. doi:10.1063/1.5086152

32. Martin-Gomez A, Eisenstecken T, Gompper G, and Winkler RG. Hydrodynamics of Polymers in an Active bath. *Phys Rev E* (2020) 101: 052612. doi:10.1103/PhysRevE.101.052612
33. Bianco V, Locatelli E, and Malgaretti P. Globulelike Conformation and Enhanced Diffusion of Active Polymers. *Phys Rev Lett* (2018) 121:217802. doi:10.1103/PhysRevLett.121.217802
34. Huber F, Schnauß J, Rönicke S, Rauch P, Müller K, Fütterer C, et al. Emergent Complexity of the Cytoskeleton: from Single Filaments to Tissue. *Adv Phys* (2013) 62:1–112. PMID: 24748680. doi:10.1080/00018732.2013.771509
35. Kruse K, Joanny JF, Jülicher F, Prost J, and Sekimoto K. Asters, Vortices, and Rotating Spirals in Active Gels of Polar Filaments. *Phys Rev Lett* (2004) 92: 078101. doi:10.1103/PhysRevLett.92.078101
36. Lin S-N, Lo W-C, and Lo C-J. Dynamics of Self-Organized Rotating Spiral-Coils in Bacterial Swarms. *Soft Matter* (2014) 10:760–6. doi:10.1039/C3SM52120F
37. Chelakkot R, Gopinath A, Mahadevan L, and Hagan MF. Flagellar Dynamics of a Connected Chain of Active, Polar, Brownian Particles. *J R Soc Interf* (2014) 11:20130884. doi:10.1098/rsif.2013.0884
38. Ding SS, Schumacher LJ, Javer AE, Endres RG, and Brown AE. Shared Behavioral Mechanisms Underlie *C. elegans* Aggregation and Swarming. *eLife* (2019) 8:e43318. doi:10.7554/eLife.43318
39. Rubinstein M, and Colby RH.*Polymer Physics*. Oxford, UK: Oxford University Press (2003).
40. Allen MP, and Tildesley DJ.*Computer Simulation of Liquids*. 2 edn. Oxford, UK: Oxford University Press (2017).
41. Fillafer C, and Schneider MF. On the Temperature Behavior of Pulse Propagation and Relaxation in Worms, Nerves and Gels. *PLOS ONE* (2013) 8:e66773–7. doi:10.1371/journal.pone.0066773
42. Ester M, Kriegel HP, Sander J, and Xu X. A Density-Based Algorithm for Discovering Clusters in Large Spatial Databases with Noise. In: Proceedings of the Second International Conference on Knowledge Discovery and Data Mining (KDD-96). AAAI Press (1996). p. 226–31.
43. Kriegel HP, Kröger P, Sander J, and Zimek A. Density-based Clustering. *Wires Data Mining Knowl Discov* (2011) 1:231–40. doi:10.1002/widm.30
44. Li H-J, Bu Z, Wang Z, and Cao J. Dynamical Clustering in Electronic Commerce Systems *via* Optimization and Leadership Expansion. *IEEE Trans Ind Inf* (2020) 16:5327–34. doi:10.1109/TII.2019.2960835
45. de Gennes PG. Reptation of a Polymer Chain in the Presence of Fixed Obstacles. *J Chem Phys* (1971) 55:572–9. doi:10.1063/1.1675789
46. Manna RK, and Kumar PBS. Emergent Topological Phenomena in Active Polymeric Fluids. *Soft Matter* (2019) 15:477–86. doi:10.1039/C8SM01981A
47. Kudrolli A, and Ramirez B. Burrowing Dynamics of Aquatic Worms in Soft Sediments. *Proc Natl Acad Sci USA* (2019) 116:25569–74. doi:10.1073/pnas.1911317116

Conflict of Interest: The authors declare that the research was conducted in the absence of any commercial or financial relationships that could be construed as a potential conflict of interest.

Publisher's Note: All claims expressed in this article are solely those of the authors and do not necessarily represent those of their affiliated organizations, or those of the publisher, the editors and the reviewers. Any product that may be evaluated in this article, or claim that may be made by its manufacturer, is not guaranteed or endorsed by the publisher.

frontiers in Physics

ORIGINAL RESEARCH
published: 22 October 2021
doi: 10.3389/fphy.2021.716576

Spatial Structure and Information Transfer in Visual Networks

Winnie Poel[1,2]*, *Claudia Winklmayr*[1,2] *and Pawel Romanczuk*[1,2]*

[1]*Department of Biology, Institute for Theoretical Biology, Humboldt Universität zu Berlin, Berlin, Germany,* [2]*Bernstein Center for Computational Neuroscience Berlin, Berlin, Germany*

In human and animal groups, social interactions often rely on the transmission of information via visual observation of the behavior of others. These visual interactions are governed by the laws of physics and sensory limits. Individuals appear smaller when far away and thus become harder to detect visually, while close by neighbors tend to occlude large areas of the visual field and block out interactions with individuals behind them. Here, we systematically study the effect of a group's spatial structure, its density as well as polarization and aspect ratio of the physical bodies, on the properties of static visual interaction networks. In such a network individuals are connected if they can see each other as opposed to other interaction models such as metric or topological networks that omit these limitations due to the individual's physical bodies. We find that structural parameters of the visual networks and especially their dependence on spatial group density are fundamentally different from the two other types. This results in characteristic deviations in information spreading which we study via the dynamics of two generic SIR-type models of social contagion on static visual and metric networks. We expect our work to have implications for the study of animal groups, where it could inform the study of functional benefits of different macroscopic states. It may also be applicable to the construction of robotic swarms communicating via vision or for understanding the spread of panics in human crowds.

Keywords: spatial networks, collective behavior, social contagion, complex systems, visual interactions, network topology

OPEN ACCESS

Edited by:
Natasha Mhatre,
Western University, Canada

Reviewed by:
Vishwesha Guttal,
Indian Institute of Science (IISc), India
William H. Warren,
Brown University, United States

***Correspondence:**
Winnie Poel
winnie.poel@gmail.com
Pawel Romanczuk
pawel.romanczuk@hu-berlin.de

Specialty section:
This article was submitted to Social Physics, a section of the journal Frontiers in Physics

Received: *28 May 2021*
Accepted: *01 October 2021*
Published: *22 October 2021*

Citation:
Poel W, Winklmayr C and Romanczuk P (2021) Spatial Structure and Information Transfer in Visual Networks. Front. Phys. 9:716576. doi: 10.3389/fphy.2021.716576

1 INTRODUCTION

The emergent collective behavior of animal groups, or more generally multi-agent systems, is decisively shaped by the underlying networks of social interactions [1–3]. These networks may strongly differ in their spatio-temporal embedding and topology depending on the type of interaction or the behavior of interest. For example in humans, online social networks have no, or only very weak, relation to physical space and interactions typically do not depend on instantaneous communication [4,5]. On the other hand, contact networks governing the (direct) spread of pathogens between individuals [6,7] or interaction networks governing the collective movement of human crowds [8–10], represent examples of spatial networks with a tight correlation between spatial and temporal distance of individuals and the probability (or strength) of corresponding interaction links. In non-human animals a similar variety of networks can be observed ranging from mating and hierarchy networks [11] to strongly spatio-temporally constrained interaction networks underlying the collective movement of fish schools [2,12], bird flocks [1,13] or insect swarms and colonies [14,15]. Especially in large animal collectives many inter-individual interactions forming the

basis for coordinated collective movements [16], collective decision making [17], or spread of information [12] are directly governed by spatio-temporal proximity.

Typically, spatially embedded interaction networks between biological agents are modelled either via *metric* network models [17], where the probability of a link (or its strength) depends only on the inter-individual distance, or by *topological* models [3,18] where a focal agent is connected to a set of spatial neighbors based on their distance rank in comparison to all others, as e.g., in the *k*-nearest neighbor network model [1,3], but where the actual link probability (or strength) does not dependent on the absolute physical distance. In the past, most agent-based models assumed metric interaction networks, but after evidence for topological interaction in starling flocks has been presented by Ballerini et al. [1], corresponding topological interaction networks have received increased attention in the context of collective animal behavior.

However, the discussion of these two idealized models of interaction networks largely ignores the constraints set by different sensory and cognitive mechanisms underlying social interactions (see e.g., [19]). Vision mediated interactions play an important role for a wide range of social phenomena [2,8,20,21]. In particular, visual interaction networks accounting for visual occlusions have been shown to outperform both metric and topological interaction networks in describing collective behavior of fish [2]. Acoustic communication, on the other hand, which shapes social behavior of many animals [22,23], is not affected by the same constraints as vision (e.g., occlusion at high densities) but depends mainly on sensory limits and properties of the medium. Here, metric interaction networks may provide a simple model for acoustic social interactions. Finally, topological interaction networks with a limited number of nearest neighbors have been recently discussed in the context of cognitive constraints regarding the number of neighbors (or objects) a focal individual can pay attention to [3].

Although the importance of visual interactions has been highlighted in recent research [2,12], there is a lack of systematic investigations of the structure of visual networks, in particular with respect to their ability to transmit information and behavior. Here, we address this gap by comparing static visual networks with the established metric and topological models which, as discussed above, may represent different sensory and/or cognitive constraints.

Comparing different types of networks quantitatively is challenging and even more so when networks represent social interactions based on different sensory limits which will be unique for a given biological agent and environment and can not generally be related to each other (i.e., some species may be able to hear further than they can see while for others the opposite may be true). While a common approach is to quantitatively compare networks of similar average degree (i.e., average number of interaction partners per individual) this may not yield the most relevant insights into biological systems where sensory limits may be fixed and tuning them to achieve a certain number of interactions may not be possible. It is known though that animal groups can quickly modify their spatial density of individuals in response to changes in the environment, e.g., related to predation risk [20,24] which in turn influences network structure. Thus besides the common approach of quantitatively comparing networks of similar degree, we also especially focus on a qualitative comparison of the networks dependence on the spatial density of individuals.

First, we study structural differences between the three network types using static network measures that have been used to classify and compare different types of networks [25,26]. We then move beyond pure structural network analysis and compare the dynamics of a simple and a complex SIR-type contagion process spreading on the static visual and metric networks. This approach is motivated by observed collective behaviors for which a time-scale separation exists, where the spread of information is much faster than any changes in the interaction network, as e.g., in the escape response in fish [12] or flight initiation in birds [27]. Through the general and simple framework of the two contagion types it also provides first insights into the potential impact of network structure on information transfer more generally. While simple contagion may be viewed as a minimal model for information diffusion in animal interaction networks, complex contagion describes the spread of behaviors or emotions where simultaneous, non-linear reinforcement by multiple neighbors is at play, as observed e.g., in escape waves in schooling fish [12] and various quorum responses [28].

Our work demonstrate the fundamental difference of visual networks in terms of structural parameters in comparison to metric and topological interaction networks. In particular, visual networks exhibit qualitatively different behavior in response to density modulation. Second, we demonstrate that these structural differences result in characteristic deviations in the dynamics of the two contagion processes on visual and metric networks.

2 METHODS

In order to investigate and compare the influence of spatial structure on properties of and dynamics on visual networks we will construct visual, metric and topological networks in two dimensional space. Here, we first discuss how we generate and characterize the spatial distribution of individuals, i.e., the network nodes. We then move on to explain the construction of the different spatially-embedded networks and the network measures we will use to characterize them, before introducing the two contagion models that we use to investigate the transfer of information or behaviors on these networks.

2.1 Network Construction: Spatial Distribution and Shape of Nodes

We initially place $N = n^2$ nodes on an n by n two dimensional square grid with distance g (measured in body length) between nearest neighbors. This setup creates a homogeneous density controlled via the parameter g. To yield more realistic distributions we add positional noise, $\eta_x, \eta_y \sim \mathcal{U}(-\eta_{pos}, \eta_{pos})$, drawn from the uniform random distribution between $\pm\ \eta_{pos}$ which we also scale by a factor g. Thus, node positions are given by

$$\vec{r}_i = \begin{pmatrix} x_i \\ y_i \end{pmatrix} = g\begin{pmatrix} n_x + \eta_x \\ n_y + \eta_y \end{pmatrix} \quad (1)$$

where $n_x, n_y \in (0, 1, \ldots, n-1)$ with $i = nn_x + n_y$. Here, we only consider values of η_{pos} up to 0.5 to ensure that the density stays relatively homogeneous which allows us to systematically study its effect on the networks by varying g. Note that in the limit of large noise η_{pos}, the random placement of agents will correspond to the simple two-dimensional spatial Poisson process.

Throughout this work we mainly characterize spatial distribution of nodes by density and polarization. We estimate spatial density, ρ, via the average third nearest neighbor distance, $\bar{r}_{3nnd}$, a measure which describes the average radius of a disk containing four individuals (the focal individual and its three nearest neighbors, for a sketch see SI). An estimate of the local density which is relatively robust with respect to positional noise is thus given by

$$\rho = \frac{4}{\pi \bar{r}_{3nnd}^2} \quad . \quad (2)$$

Inspired by the elongated body shape of fish, single agents are represented by identical ellipses of length 1 and width w with orientations ϕ_i that are drawn from a von Mises distribution

$$f(\phi|\mu, \kappa) = \frac{e^{\kappa \cos(\phi - \mu)}}{2\pi I_0(\kappa)} \quad (3)$$

where $\mu = 0$ is the average, $I_0(\kappa)$ is the modified Bessel function of order 0 and κ a parameter that defines the width of the distribution (here we use $\kappa = 0.1, 1.7, 31.6$). Note that because ellipses are of length one, density is measured in inverse squared body length (BL). We characterize the group's *polarization* (degree of orientational order) by the absolute value of the normalized sum of all orientation unit vectors $\vec{\phi}_i = (\cos(\phi_i), \sin(\phi_i))^T$

$$\Phi = \frac{1}{N}\left|\sum_{i=1}^{N} \vec{\phi}_i\right| \quad . \quad (4)$$

To eliminate overlap of the ellipses (to keep the group strictly two dimensional) we use simulations of ellipse shaped particles based on the code provided by [29]. These particles repel each other with a force proportional to their overlap area and we let them settle into a non-overlapping configuration (see SI). Thus there is a upper limit to density given by the physical bodies of the nodes. An example of a spatial configuration generated using $g = 1.4$, $\eta_{pos} = 0.5$, $N = 36$, $\kappa = 0.9$, $w = 0.3$ is shown in **Figure 1B**.

2.2 Network Construction: Edges

The three network types considered in this work are distinguished exclusively via the rules for the construction of links based on spatial positions of the ellipse shaped bodies, i.e., the network nodes. We limit ourselves to binary networks with the adjacency matrix given by

$$A_{ij} = \begin{cases} 1 & \text{if there is a link from } i \text{ to } j \\ 0 & \text{otherwise} \end{cases} \quad . \quad (5)$$

The decision rule determining if a link from i to j exists depends on the type of network and is explained in the following paragraphs. An illustration of the connection rules can be seen in **Figure 1A**. **Figure 1B** provides an example of each network type for $N = 36$, where the same positions and orientations of ellipses are underlying each network and respective thresholds are chosen such that the total number of links is identical between networks.

2.2.1 Visual Networks

In a visual network a link from node i to node j exists if i is visible to j. To account for sensory and/or cognitive limitations an individual i must have an angular area (defined below) in the visual field of j that is above a certain threshold, θ_{visual}, in order to be visible to j. This threshold parameterizes our visual network model

$$A_{ij}^{\text{visual}} = \begin{cases} 1 & \text{if } \alpha_{ij} \geq \theta_{\text{visual}} \\ 0 & \text{otherwise} \end{cases} \quad . \quad (6)$$

The angular area, α_{ij}, is the angle that the *visible part* of an ellipse i occupies in the visual field of j. Thus if i is partially occluded by other ellipses k then the visual threshold applies to the partially visible portion of i. We determine the angular area through a combination of analytical calculation of the unobstructed (occlusion-free) visual angle of i in the visual field of j, $\alpha_{ij}^{\text{free}}$, with a numerical casting of rays at angles specified by the analytics to determine occlusions (for details refer to the SI and Leblanc [30]). As a result of partial occlusions the angular area, α_{ij} is thus smaller than that of the unobstructed ellipse, $\alpha_{ij} \leq \alpha_{ij}^{\text{free}}$. **Figure 1A** illustrates the visual field of a central ellipse as shaded areas. Here, angular areas larger than the visual threshold, $\theta_{\text{visual}} = 0.43$, are illustrated by the angles of the purple shaded areas while those smaller than the visual threshold are shaded light grey. The effect of a partial occlusion on the angular area can be seen for the bottom left ellipse and a more detailed illustration of angular areas including other cases of partial occlusions can be found in **Supplementary Figure S3** of the SI. Correspondingly, it can be seen in **Figure 1A** that the central individual only has incoming links from those individuals with $\alpha_{ij} \geq \theta_{\text{visual}}$. Because visibility is not necessarily reciprocal, visual networks are generally directed. Note that for simplicity, we assume each ellipse has 360° vision from a single eye located at the center of the ellipse.

2.2.2 Metric Networks

In a metric network two nodes are connected if their Euclidian distance, $r_{ij} = |\vec{r_i} - \vec{r_j}|$, is smaller than the metric threshold, θ_{metric} [31]

$$A_{ij}^{\text{metric}} = \begin{cases} 1 & \text{if } r_{ij} \leq \theta_{\text{metric}} \\ 0 & \text{otherwise} \end{cases} \quad . \quad (7)$$

This rule is illustrated in **Figure 1A**, where a focal individual (white) has incoming links from all individuals within a radius of θ_{metric} (marked by a shaded circle). Because $r_{ij} = r_{ji}$ metric networks are undirected. Note that, when not considering occlusion, visual networks can also be understood as having a metric interaction range because the visual threshold sets an

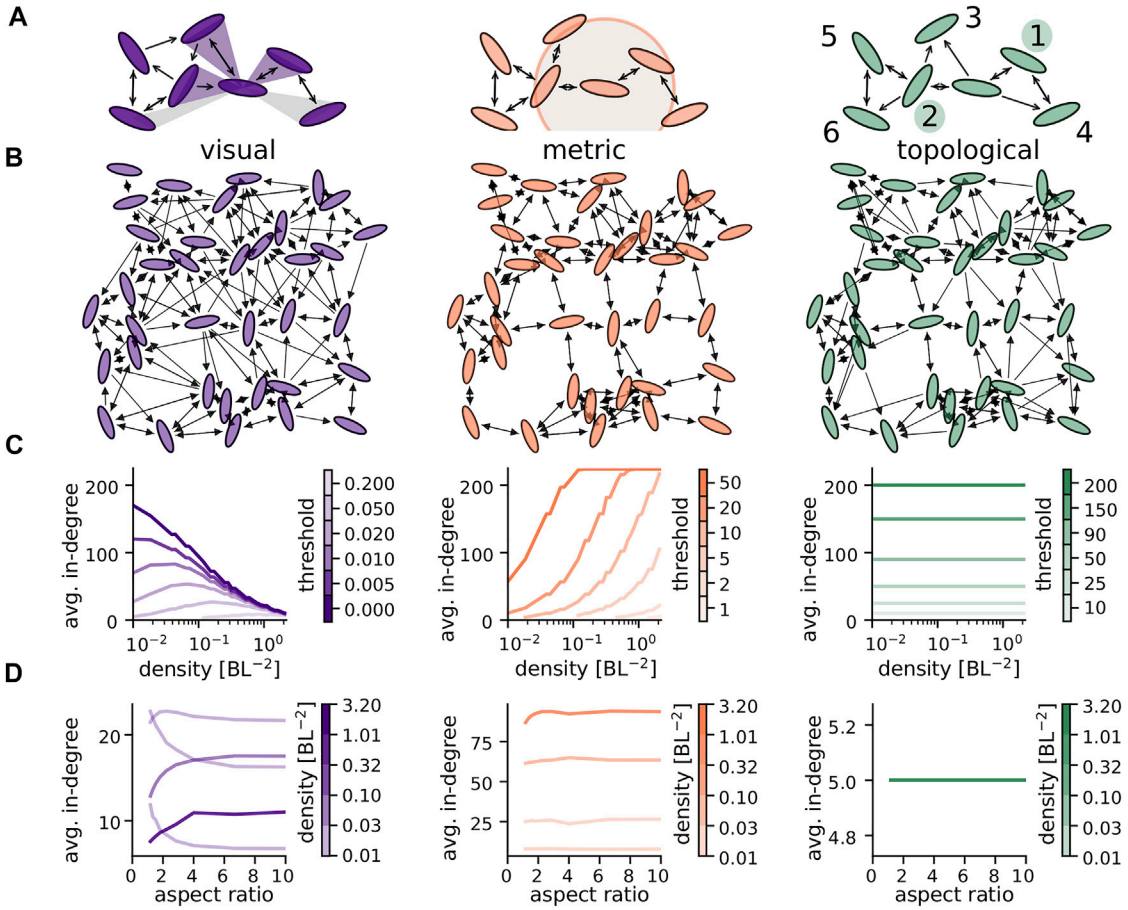

FIGURE 1 | The different network types: **(A)** illustration of rules determining incoming network links of the central individual (white). Left: visual angles needs to be larger than a threshold value, θ_{visual} =0.43, (purple shaded areas indicate visual angles that fulfill this requirement, light grey ones do not, threshold chosen very high for the purpose of illustration). Center: metric distance between individuals needs to be below a certain threshold (indicated by a circle). Right: incoming links are coming from fixed number of nearest neighbors (here 2) for the topological model. Numbers indicate closeness rank. **(B)** Examples of the different networks for $g = 1.4$, $\eta_{pos} = 0.5$, $N = 36$, $\kappa = 0.5$, $w = 0.3$ using the same positions, orientations and total number of links (thresholds: $\theta_{\text{visual}} = 0.254$, $\theta_{\text{metric}} = 2.1035$, $\theta_{\text{topo}} = 5$, yielding 180 directed links). **(C)** Average in-degree as a function of density for different threshold values indicated by line color. The average in-degree of the different network types show a very distinct dependence on density. **(D)** Influence of ellipses, aspect ratio on avg. in-degree for different density regimes indicated by line color for fixed thresholds, $\theta_{\text{visual}} = 0.05$, $\theta_{\text{metric}} = 8$, $\theta_{\text{topo}} = 5$. At low density circles (aspect 1) are visible over larger distances leading to an increase in average in-degree. At high densities, elongated ellipses (high aspect ratio) cause fewer occlusions which in turn increases the average in-degree. $N = 225$ in (C) and (D).

upper limit for the interaction distance. The exact distance at which the angular area of an ellipse drops below the visual threshold, will of course depend on its orientation and width (see SI). When needing to construct the visual threshold resulting in an equivalent effective cutoff distance for visual networks as in a certain metric network, we therefore averaged over all possible relative orientations for a specific value of w (see SI).

2.2.3 Topological Networks

In a topological network node i has incoming links from its θ_{topo} nearest neighbors, chosen successively by increasing Euclidian distance. If we assign each individual j a closeness rank, k_{ij}, with respect to individual i as $k_{ij} = |\{m | r_{im} < r_{ij}\}| + 1$ where $\|$ denotes the set's cardinality (number of elements in the set) we can write the construction rule as

$$A_{ij}^{\text{topo}} = \begin{cases} 1 & \text{if } k_{ij} \leq \theta_{\text{topo}} \\ 0 & \text{otherwise} \end{cases} . \tag{8}$$

The connection rule is illustrated in **Figure 1A**, where individuals close to a focal individual (white) are labeled according to their closeness rank and the focal individual has incoming links from those with a closeness rank up to $\theta_{\text{topo}} = 2$. Because closeness rank is not necessarily reciprocal, topological networks are generally directed as can been seen in the example in **Figure 1B**.

2.3 Network Measures

To assess and compare the structural properties of the different networks we use three well-established measures, the average in-degree, the average clustering coefficient and average shortest

path length. These measures have been used widely to classify and compare different types of networks (see e.g., Newman [25]; Barthélemy [31]) and are known to influence contagion processes, with shorter paths enabling a faster spreading of a simple contagion process and a higher clustering leading to a more robust spreading of a complex contagion process [32]. We calculate the latter two quantities using the methods implemented in Python's `networkx` library [33].

2.3.1 In-Degree and Out-Degree

The in-degree d_i^{in} of a node i is defined as the number of its incoming links, $d_i^{in} = \sum_{j\neq i} A_{ji}$. The average in-degree is given by $\bar{d}^{in} = \frac{1}{N}\sum_{i=1}^{N} d_i^{in}$. The out-degree is analogously defined as $d_i^{out} = \sum_{j\neq i} A_{ij}$.

2.3.2 Clustering Coefficient

In an undirected, unweighted network the clustering coefficient of node i describes the probability that two neighbors, j and k of node i are also linked among each other. This is calculated by dividing the number t_i of all triangles of actual links formed by i by the number T_i of all possible triangles that could be formed by i. Here, we use the following simple extension of this measure to directed graphs from Fagiolo [34]:

$$c_i = \frac{t_i}{T_i} = \frac{\frac{1}{2}\sum_{j\neq i}\sum_{k\neq(i,j)}\left(A_{ij}+A_{ji}\right)\left(A_{ik}+A_{ki}\right)\left(A_{jk}+A_{kj}\right)}{d_i^{tot}\left(d_i^{tot}-1\right)-2d_i^{\leftrightarrow}} \qquad (9)$$
$$d_i^{tot} = d_i^{in} + d_i^{out}, \quad d_i^{\leftrightarrow} = \sum_{i\neq j} A_{ij}A_{ji}\ .$$

The average clustering coefficient of a network is then given by $\frac{1}{N}\sum_{i=1}^{N} c_i$.

2.3.3 Average Shortest Path Length

The average shortest path length describes the average minimum number of steps on the network needed to get from a node i to a node j. It is defined as

$$a = \frac{1}{N(N-1)}\sum_{i,j} d(i,j) \qquad (10)$$

where $d(i, j)$ is the length of the shortest path between nodes i and j. We use `networkx`'s implemented algorithm `average_shortest_path_length` to determine the value for a where possible (networks need to be weakly connected).

2.3.4 Relative Link Length

While the shortest path measures the topological distance between nodes in spatial networks the link length, $l_{ij} = r_{ij}$ if $A_{ij} = 1$, measures the Euclidean distance between two connected agents. In order to make link length comparable across densities, we measure link length in units of the longest possible link, $l^{\max}$, in the group. For the grid configuration used in this paper this *relative link length* is given by

$$l_{ij}^{\mathrm{rel}} = \frac{l_{ij}}{l^{\max}} = \frac{r_{ij}}{g\sqrt{2}\left(\sqrt{N}-1\right)}\ . \qquad (11)$$

2.4 Contagion Models

We investigate two models, one of simple and one of complex contagion, to demonstrate the differential impact of the network topology on these processes. In simple contagion, the probability of an infection in a time interval Δt can be decomposed into the superposition of independent pair-wise interactions between a non-infected (susceptible) individual and its infected (network) neighbors. In complex contagion such a decomposition is not possible as the infection probability is a non-linear function of the number or fraction of infected neighbors. We emphasize that "infection" does not refer here to disease spread, but to spreading of information or behavior. Thus, throughout this work, becoming infected refers to an individual becoming informed or activated (see e.g., [20]). Both types of contagion models are studied via discrete time approximation of the continuous time stochastic infection and recovery processes using a (small) numerical time step $\Delta t = 0.05$. In what follows we describe the respective processes.

2.4.1 Simple Contagion Model

Each agent within the network can be in one of three states: susceptible S, infected I or recovered R. A susceptible agent in contact with a single infected neighbor can become infected with a constant probability rate β. Thus, the infection probability for such a pair-wise contact during a short time interval Δt is $p_{\Delta t} = \beta\Delta t$. The total infection probability of a susceptible individual connected to n_{inf} neighbors during the small time interval Δt for such a simple contagion can be calculated to:

$$P_{sc,\Delta t}(n_{\mathrm{inf}}) = 1 - \left(1 - p_{\Delta t}\right)^{n_{\mathrm{inf}}}. \qquad (12)$$

Infected individuals transition to the recovered state with a finite, constant recovery rate γ. Thus, the average infection duration is $\tau_{\mathrm{inf}} = \gamma^{-1}$. For simplicity, we assume that the recovered state is an absorbing state, i.e., once recovered an agent does not change its state anymore. Starting from an initial state of mostly susceptible agents and a small number of infected the epidemic spread will terminate once there are no more infected agents in the network.

2.4.2 Complex Contagion Model

The complex contagion model is analogous to the simple contagion model described above, with exception of the infection probability. Here, we assume a complex contagion process with an overall infection rate of a susceptible individual β_{cc} given by a sigmoidal function $\mathcal{S}(r_{\mathrm{inf}})$ of the fraction of its infected network neighbors $r_{\mathrm{inf}} = n_{\mathrm{inf}}/d^{\mathrm{in}}$ with d^{in} being the in-degree of the susceptible individual:

$$\beta_{cc}(r_{\mathrm{inf}}) = \beta_{\max}\mathcal{S}(r_{\mathrm{inf}}, r_0) = \beta_{\max}\frac{1+\tanh\left(\sigma\left(r_{\mathrm{inf}}-r_0\right)\right)}{2} \qquad (13)$$

Here, $\beta_{\max}$ sets the maximal possible infection rate, σ controls the steepness of the sigmoidal function, whereas r_0 sets the inflection point of the sigmoid with $\mathcal{S}(r_0) = 1/2$. For large $\sigma \gg 1$, **Eq. 13** yields a sharp, step-like function with $\beta_{cc}(0) \approx 0$ and $\beta_{cc}(1) \approx \beta_{\max}$. For $\sigma \approx 1$, $\beta_{cc}(r_{\mathrm{inf}})$ is approximately linear with $\beta_{cc}(0) = \beta_{\max}[1 - \tanh(\sigma r_0)]/2$ and

$\beta_{cc}(1) = \beta_{\max}[1 + \tanh\sigma(1 - r_0)]/2$. For $\sigma = 0$, the infection rate becomes independent on $r_{\inf}$ with $\beta_c = \beta_{\max}/2$. The overall probability of an susceptible agent to get infected in a short time interval Δt is thus simply:

$$P_{cc,\Delta t}(r_{\inf}) = \beta_{cc}(r_{\inf})\Delta t. \tag{14}$$

As the infection probability depends on the fraction of infected individuals and not on the absolute number of infected neighbors, this model describes a fractional, complex contagion process.

3 RESULTS

In a first step we study how different network properties such as average in-degree, clustering coefficient, shortest path length and the distribution of link length depend on network density. We use networks of $N = 225$ individuals unless stated differently. In the case of visual networks we find that all these measures exhibit an interesting non-monotonic relationship with density. The choice of density as an independent parameter is reasonable when studying social behavior because while animals might not be able to change individual perceptual thresholds they can usually adapt their distance to neighboring individuals. For example fish schools have been shown to move closer together under the threat of predation [20].

Given that the average in-degree is modified by network density and the in-degree in turn affects both the clustering coefficient and the average shortest path length we then explicitly investigate the relationship between in-degree and clustering coefficient as well as shortest path length. Here we still find that visual networks differ qualitatively from both metric and topological networks.

In a second step we study how these static properties affect information propagation by comparing the speed and reach of simple and complex contagion processes through visual and metric networks. Finally, we use the contagion processes to show examples of anisotropy in contagious spreading that can be observed in visual networks for certain combinations of density and sensory limits and are absent in metric networks. For the study of anisotropy we use larger networks of $N = 400$ individuals.

3.1 Density Dependence of Network Properties

3.1.1 In-Degree

Figure 1C shows the average in-degree as a function of spatial density of individuals for all three network types and various sensory thresholds. In the case of topological networks the in-degree is not affected by density due to the constraint that an individual can only interact with a fixed number of neighbors independent of their distance. For metric networks average in-degree increases with density. This is explained by the networks, construction where every individual is connect to all other individuals within a fixed range and naturally, the number of individuals within this fixed interaction radius increases with density.

Visual networks, on the other hand, exhibit a different relationship between density and average in-degree: depending on the visual threshold the average in-degree either monotonically decreases with density (very small visual thresholds) or exhibits a maximum at intermediate densities (higher visual thresholds), the exact position of which depends on the value of the visual threshold. The decrease at high densities is due to occlusions in the visual field that become more prominent at high packing fractions and constrain visual interactions. The decrease at low densities is the result of the non-zero visual threshold. Individuals need to occupy a certain angular area in the visual field of a focal individual before they become connected and this requires them to be within a certain distance to it. This behavior is similar to that of the metric network with the maximal interaction radius being determined by the visual threshold and the projected body size of the individual. Since this projected body size heavily depends on the ellipses aspect ratio, **Figure 1D** takes a closer look at the variation of average in-degree with aspect ratio, which is $\frac{10}{3} \approx 3.3$ in **Figures 1A–C** and throughout the rest of this paper.

In topological and metric networks the average in-degree does generally not depend on the ellipse shape. An exception is the case of metric networks at high density, where for elongated ellipses (high aspect ratio) the average in-degree increases because ellipses can move closer together with a high aspect ratio and thus slightly increases the average in-degree by increasing the number of individuals that can fit within a fixed interaction radius. For visual networks one observes a strong dependence of in-degree on aspect ratio at all ranges of density. For high densities elongated ellipses (high aspect ratio) lead to less occlusions and thus a higher average in-degree. For low densities, circles (aspect ratio 1) remain visible best at large distances, leading to a higher average in-degree for small aspect ratio. At intermediate densities these two opposing effects can lead to a maximum of the average in-degree at intermediate aspect ratios.

Note that throughout this study we vary density and network thresholds only within limits that result in at least weakly connected networks. This yields to a lower limit on density for each threshold which becomes apparent in our results, i.e., in the line corresponding to a 2 BL in **Figure 1C** ending at a density of roughly 0.1 BL^{-2}. Where possible, we consider densities from 0.01 to 2 BL^{-2}. This covers a range of densities we can roughly estimate from reported nearest neighbor distances and body length for different animal species.

Juvenile golden shiners, schooling freshwater fish with an average body length of 5.5 cm, exhibit median (first) nearest neighbor distances of roughly $\bar{r}_{1nnd} = 3$ to 7 cm [20]. Using $\rho = 2/(\pi\bar{r}^2_{1nnd})$ in analogy to **Eq. 2** this results in a density of roughly 0.4 to 2.1 BL^{-2}. Buhl et al. [35] states the density of marching desert locust as ranging from 20 to 120 with an average of 50 locusts/m^2. Assuming an average body length of 7.5 cm [36] this corresponds to a density of roughly 0.1 to 0.7 with an average of 0.3 locusts/BL^2. Lower densities are observed for starling flocks where the average nearest neighbor distance lies between 0.68 and 1.51 m [1]. Common starlings have a body length of roughly 20 cm and a wingspan of roughly 35 cm [37]. For the sake of comparability we calculate a two-dimensional density using the reported nearest neighbor distance in three dimensions (which is likely lower than that in two dimensions)

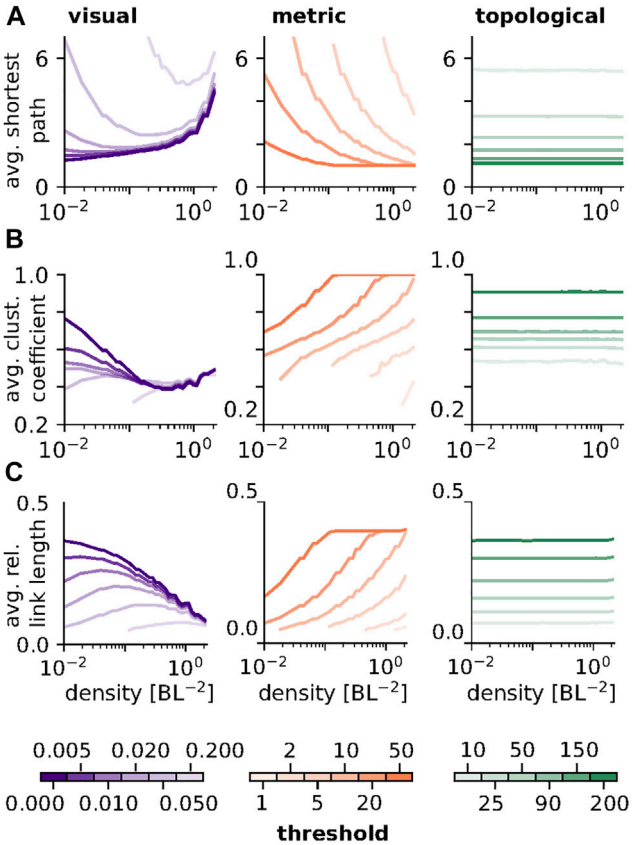

FIGURE 2 | Density dependence of network measures: **(A)** Average shortest path length as a function of density for all three network types. In visual networks the shortest path length assumes a threshold dependent minimum. In metric networks shortest path length decreases with density. In topological networks no density dependence is observed. **(B)** Average clustering coefficient as a function of density for all three network types. In visual networks the average clustering coefficient assumes a minimum at intermediate to high densities. The average clustering coefficient increases with density in metric networks and shows no density dependence in topological networks. **(C)** Average relative link length as a function of density. Visual networks exhibit a threshold dependent maximum while for metric networks link length increases with density. Again, topological networks show no dependence on density. $N = 225$ was used for all subplots.

and 20 cm as body length, yielding an estimated range of density from 0.01 to 0.06 starlings/BL^2. We want to stress that these are only very crude estimates of density to give the reader an qualitative impression of where different animal species are located in the considered density range. They do not constitute a rigorous scientific measurement of density.

3.1.2 Other Network Measures

We study the effect of network density on the average clustering coefficient, the average shortest path length and the distribution of relative link lengths, measures that have proven useful in characterizing types of spatial networks [26] and thus allow us to contextualize visual networks in the broader landscape of spatial networks.

Figure 2A summarizes the effect of spatial density of individuals on the average shortest path length for all three network types and the same sets of thresholds as in **Figure 1**. For topological networks the length of the shortest path is unaffected by network density. In metric networks the average length of the shortest path decreases monotonically with increasing density, which can be explained by the simultaneous increase in in-degree (see **Figure 1C**). In visual networks the average shortest path can exhibit a minimum, the position of which depends on the visual threshold and roughly matches with the maximum in the average in-degree (**Figure 1C**).

Figure 2B shows the effect of density on the average clustering coefficient. For topological networks the clustering coefficient depends only on the threshold, θ_{topo}, and shows no density dependence. For metric networks the clustering coefficient increases monotonically with density. This can again be explained by network construction: since every node is connected to all nodes within a radius prescribed by the threshold, two neighbors of the same node are also likely to be close to each other and thus share a connection. In the case of visual networks, the clustering coefficient exhibits a non-monotonic relationship with density. In particular, for some threshold values we find a maximum at low densities followed by a (threshold independent) minimum at intermediate density values.

Average relative link length, depicted in **Figure 2C**, varies with density similarly to the average in-degree, shown in **Figure 1C**. Qualitative differences between the link length distributions of the different network types, which are not adequately captured by the average, can be seen in an example in **Figure 3C** and the SI.

3.2 Quantitative Comparison of Network Types

While we have observed a variety of changes in networks measures with density, we have also found that they can to a large degree be explained by changes in the average in-degree. It is thus important to discern how much of this difference between network types persists when the average in-degree is kept fixed. The results, shown in **Figure 3**, represent averages over all densities.

Figure 3A depicts the average shortest path, which decreases as networks become more densely connected with little difference between metric and topological networks. In visual networks, however, shortest paths tend to be shorter, especially at low to intermediate in-degrees. This decreased average shortest path length can most likely be explained by the presence of long links allowing shortcuts between spatially distant nodes (see **Figure 3C**).

Figure 3B shows that for all three network types the average clustering coefficient increases with the number of incoming links per node. Again, there is little difference between metric and topological networks, whereas over a wide range of in-degrees the clustering of visual networks is substantially lower. This phenomenon can be partly explained by the presence of long-range connections breaking local clusters (cf. [38]). Additionally, local clustering structure is disrupted by the visual blocking of neighbors on either side of an individual. At very high average in-

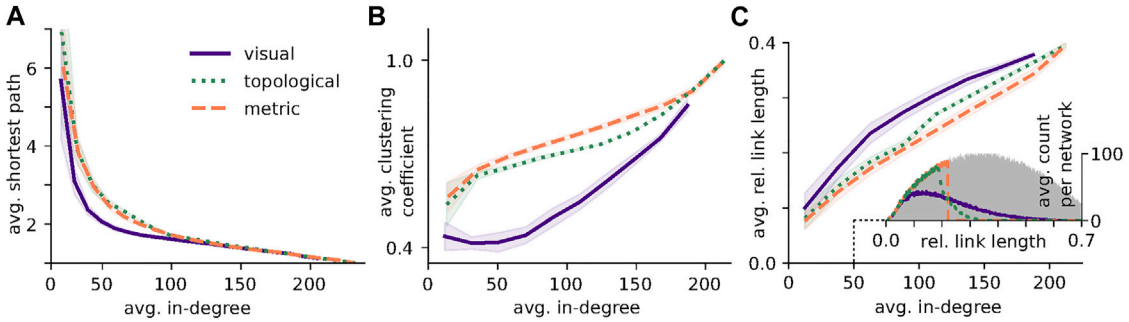

FIGURE 3 | Degree dependence of network measures**.** All Figures were created using networks of $N = 225$ averaged over all densities and thresholds. **(A)** Average shortest path length as a function of average in-degree. At low in-degrees visual networks exhibit shorter shortest-path lengths than both metric and topological networks. **(B)** Average clustering coefficient as a function of average in-degree. Consistent with the results in Figure 2 visual network display substantially lower clustering across a wide range of in-degrees than both metric and topological networks. **(C)** Average relative link length as a function of average in-degree. For intermediate in-degree, visual networks exhibit considerable longer links than both metric and topological networks. Inset: Example of the average distribution of relative link length for networks of average in-degree 50. The grey shaded area indicates the link length distribution for a fully connected network. Parameters: $g = 2.0$, $\theta_{vis} = 0.00505$, $\theta_{metric} = 9.2944$, $\theta_{topo} = 50$, averaged over 40 networks.

degree, when the networks become essentially all-to-all connected, clustering approaches one. Visual networks however, do not reach such high degrees due to occlusions.

Finally, **Figure 3C**, shows the average relative link length of the different network types. While visual networks have a slightly higher average relative link length, the difference between the networks becomes more apparent when looking at the full distributions, shown as an inset for an average in-degree of 50. For comparison the distribution of the fully connected network is added in grey. In metric networks all links up to the threshold value are realized, where the distribution shows a sharp cutoff. For our spatial distribution of relatively homogeneous density, topological networks include all links up to a certain length and then show a fast decay in the distribution. The distribution of visual networks shows a much slower decay for higher link length, confirming the existence of substantially longer links in visual networks and underpinning our attribution of differences in the other two network measures to a difference in link length and shortcuts via a few very long links.

3.3 Density Dependence of Contagion Processes

In *Density Dependence of Network Properties* we showed that the density dependence of the visual networks structural properties is very distinct from that of the other two network types. In order to understand their implications for dynamic processes, we compare the evolution of simple and complex contagion dynamics on visual to that on metric networks. We omit topological networks because of the independence of their topological properties from density and their similarity to metric networks in their dependence on average in-degree (see **Figures 2**, **3**).

3.3.1 Simple Contagion

For a connected network and a sufficiently low recovery rate a simple contagion process will always spread through the entire network activating all nodes eventually. In order to compare the two network types we study the speed of the spread measured by the inverse of the time it takes for the activation to spread from a single individual to 75% of the network, $1/t_{75}$. The probability of a node becoming infected is proportional to its number of infected neighbors (see **Eq. 12**). Therefore we can expect the infection to spread faster in networks with high average in-degree.

Figures 4A,B show examples of the time course of infection for low and high densities respectively (for parameter sets refer to the figure caption). For the parameters used, at low densities (A) the infection spreads faster on visual networks, at high densities (B) the metric networks have a speed advantage. The solid lines in **Figure 4C** summarize the effect of density on speed for both network types and confirms the observation that for lower densities a simple contagion process will spread substantially faster through a visual than through a metric network while at higher densities this effect is reversed. The speed maximum of visual networks in the low to mid density regime correlates nicely with the shortest path length as shown in **Figure 2** (for the threshold value 0.05) and can be explained by the presence of long-range connections.

However, the above examples are for one specific choice of metric and visual thresholds, $\theta_{metric} = 5$ BL and $\theta_{visual} = 0.05$ rad. As illustrated in **Figure 4G**, this choice allows visual links of (on average) up to 13 BL and thus longer-ranged visual than metric interactions (5 BL). For a full picture of the possible quantitative differences between the two network types, we include two more parameter values of the metric network. For $\theta_{metric} = 13$ BL the maximal link length of metric and visual networks is similar (dashed line) and the two networks have a comparable contagion speed at low density, only diverging at higher densities when occlusions in the visual network lead to a decrease in average in-degree compared to the metric networks. For $\theta_{metric} = 25$ BL metric interactions can be longer than visual ones (dotted line) and the simple contagion process spreads faster on the metric networks at all densities because of their higher average in-degree.

Considering metric networks as a simple model of acoustic interactions, the different choices of thresholds could describe

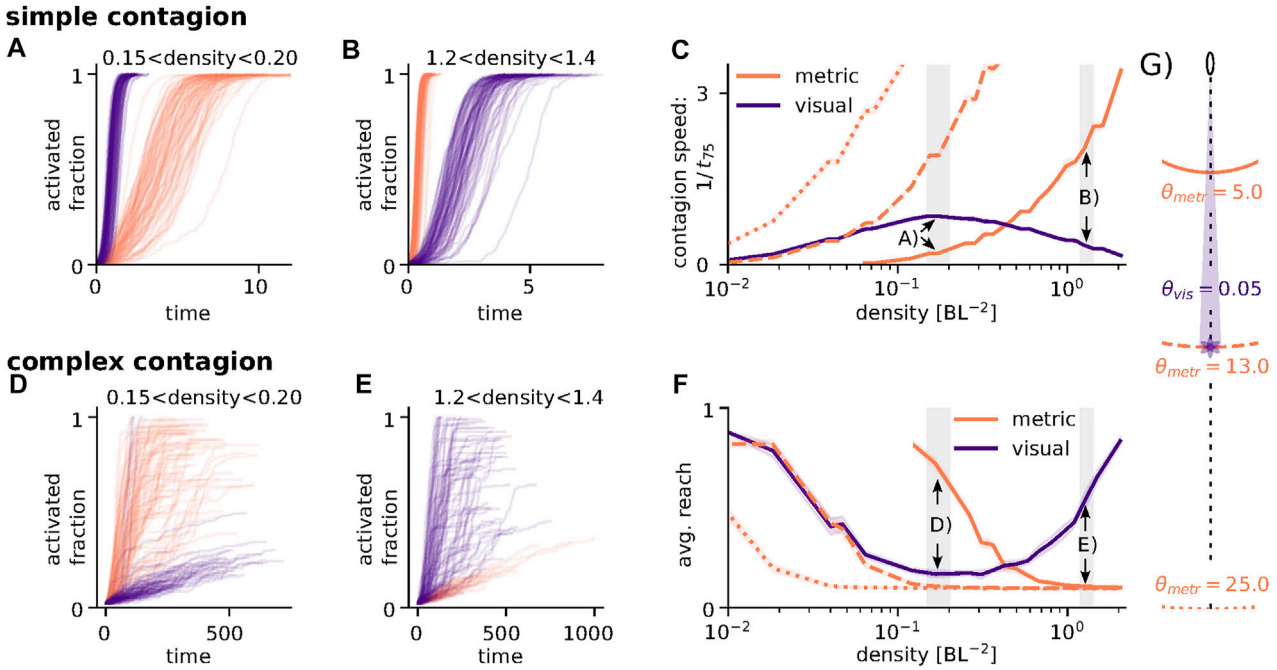

FIGURE 4 | Simple and complex contagion on visual and metric networks. **(A)** Example trajectories for a simple contagion process at low densities for visual (purple) and metric (orange) networks showing faster spread in metric networks. **(B)** same as (A) but for high densities showing faster spread for visual networks. **(C)** Comparison of visual and metric network with respect to the speed of infection via simple contagion. In metric networks the speed of spread increases monotonically with density. In visual networks the contagion speed assumes a maximum at intermediate densities. Line-styles correspond to different thresholds of the metric network as illustrated in (G). Shaded grey areas correspond to the density ranges in (A) and (B) respectively. **(D)** Example trajectories for a complex contagion process at low densities showing faster spread in metric networks. Note, that most trials do not reach full activation in either network type. **(E)** Same as (D) for high densities, showing faster spread in visual networks. Again, most trials do not reach full activation. **(F)** Comparison of average reach (i.e., final fraction of activated individuals) as a function of density for both network types. In metric networks average reach decreases with density, while visual networks show a minimum at intermediate densities. As in (C) line-styles correspond to different metric thresholds and shaded areas correspond to the examples in (D) and (E) respectively. **(G)** Illustration of different thresholds. Parameters: $N = 225$, $\Phi \in [0, 0.3]$, $\gamma = 0.03$, $\beta = 0.3$, $r_0 = 0.35$, $\sigma = 10$. Lines in (C) and (F) are averages over 100 networks and 100 runs per network, starting the contagion process with one (simple contagion) or five (complex contagion) randomly chosen individuals.

animals that can see further/equally far/shorter than they can hear which will strongly depend on the animals physiology but also on the properties of the surrounding medium. While in those cases where metric interactions can be longer than visual ones acoustic interactions can be understood to provide a faster transfer of information across the group at all densities (dotted line), for the opposite case (solid line), the fastest mode of information transfer strongly depends on density.

3.3.2 Complex Contagion

In the complex contagion model considered here, the probability of getting infected is a sigmoidal function of the fraction of infected neighbors. Thus individuals only have a high infection probability if their fraction of infected neighbors, r_{inf}, exceeds the threshold r_0. A fractional contagion process is not guaranteed to spread through the entire network. If no node has a fraction of infected neighbors $\geq r_0$, the remaining infection rates of the individuals may drop far below the recovery rate and the process can come to a halt. To account for the possibility of incomplete spread we compare the network types with respect to the fraction of the network that gets infected before the process stops, instead of the contagion speed for the complex contagion. We refer to this as the *reach* of the contagion.

Where in the case of simple contagion having a high in-degree increases a node's rate of infection, because it increases its probability to have infected neighbors, the contrary is true for fractional contagion in the case of a low overall prevalence of the "infected" state. Assuming a fixed number of infected neighbors (as we use to initiate the processes in **Figures 4D–F**), an increase in in-degree will only lower a node's fraction of infected neighbors and thus decrease infection probability.

Figure 4D and **E** show the time course of infection for the same density regimes as in A and B. Compared to the simple contagion process the roles of the networks appear reversed: at low densities the fractional contagion process spreads faster and further in metric than in visual networks, while at high densities visual networks are faster and become infected to a larger fraction. It is also clear, that most networks do not get fully infected for this choice of parameters. **Figure 4F** compares the fraction of infected nodes in both network types as a function of density for the same set of thresholds as in **Figure 4C**. The effect of density is clearly reversed between the complex and the simple contagion process which can be attributed to the opposing effect of an increase in in-degree on the infection probability of a node as discussed above.

Coming back to the interpretation of the two network types as based on two different senses (vision and hearing), we can now

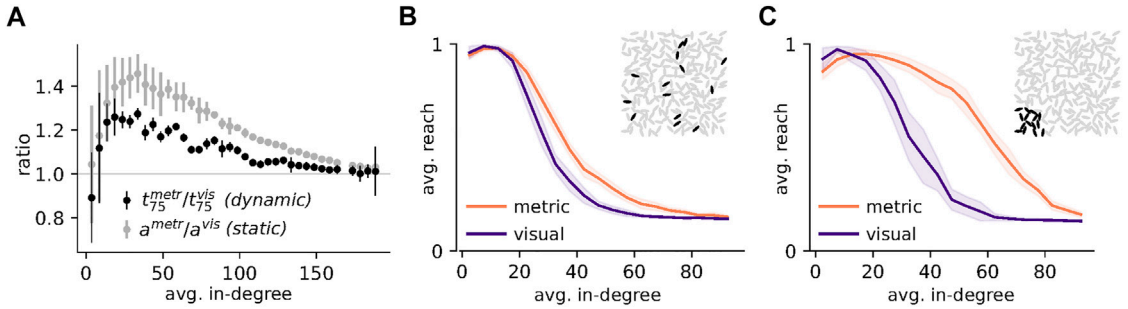

FIGURE 5 | Structural differences influence dynamics on networks: **(A)** The ratio of contagion speeds (time to 75% infected or recovered, $t_{75}^{metr}/t_{75}^{vis}$) shows a similar dependence on average in-degree as the ratio of average shortest path lengths (a^{metr}/a^{vis}, grey). Dots represent averages and errorbars one standard deviation over 100 networks (static) or 100 runs on 100 networks (dynamic). **(B)** and **(C)** Effect of clustering coefficient on fractional contagion. (B) Initial activation by 15 randomly selected individuals (see black ellipses in inset for an example). (C) Initial activation by 15 individuals in one corner of the group (inset). Lines represent averages over 100 networks with 100 runs of the fractional contagion dynamic each, shaded areas represent one standard deviation of the networks, average reach. A higher clustering coefficient (as in metric networks, compare Figure 3) is beneficial for a spatially clustered initial activation, (C). Parameters: $N = 225$, $\Phi \in [0.0, 0.3]$, $\gamma = 0.01$, $\beta = 0.3$, $r_0 = 0.4$, $\sigma = 10$.

see that in addition to the group density the optimal mode of transmission (acoustic or visual) does also depend on the type of contagion process. A combination of both interaction types may allow robust communication independent of group density.

Another notable feature that distinguishes visual from metric networks here is their consistency and robustness over a wide range of densities. While contagion speed for metric networks quickly increases with density (for all threshold values), visual networks provide comparable speeds at high and low densities. Similarly, for each metric threshold there is an upper density limit for the transmission of a complex contagion, but we can find visual thresholds that allow a complex contagion to (partially) pass at all densities.

3.4 Quantitative Comparison of Contagion Processes on Visual and Metric Networks

In *Quantitative Comparison of Network Types* a degree-controlled comparison of the different network types revealed that for intermediate average in-degrees visual networks on average have a lower shortest path length, a lower average clustering coefficient and links that span larger distances than their metric and topological counterparts (**Figure 3**). In order to illustrate the effect that these differences can have on dynamic processes, we again compare the evolution of simple and complex contagion dynamics on visual to that on metric networks for an exemplary set of parameters, see caption of **Figure 5**.

Figure 5A depicts the spreading speed of a simple contagion on visual networks in units of the spreading speed on degree-matched metric networks, $t_{75}^{\mathrm{metr}}/t_{75}^{\mathrm{vis}}$, as a function of average in-degree (black dots). Spreading on visual networks is faster (indicated by values larger than 1) for a wide range of intermediate average in-degrees. The ratio of average shortest path lengths, $a^{\mathrm{metric}}/a^{\mathrm{visual}}$, (grey dots) mirrors the qualitative shape of the speed ratio indicating that the increased speed of the simple contagion process on visual networks can be attributed to their shorter average shortest paths (compare **Figure 3A**).

Figures 5B,C illustrate the effect of the lower clustering coefficient of visual networks on the reach of the complex fractional contagion. As already discussed in *Density Dependence of Contagion Processes* in the context of **Figure 4F**, as long as the number of infected individuals in the network is low and infections are randomly distributed (illustrated in the inset of **Figure 5B**), each additional link is most likely decreasing the focal node's infection probability in the fractional contagion process (because it is more likely to a susceptible than to an infected individual). This is the case in **Figure 5B** for both network types and explains the decrease of the average reach with increasing average in-degree. A spatial clustering of infections (as in the initial conditions of **Figure 5C**, illustrated in the inset) increases the fraction of infected individuals in the neighborhood of nodes with a high local clustering and close to the "wave front" of the infection (the border between susceptible and infected individuals). Therefore, the average reach of the fractional contagion remains substantially larger on metric than on visual networks with increasing average in-degree for a spatially correlated initial activation (**Figure 5C**).

Put differently, visual networks have a longer average link length for a comparable average in-degree, which results in a lower clustering and in nodes receiving inputs from many, possibly far away and not spatially correlated neighbors. This makes it difficult for any node to reach the required fraction of infected neighbors in case of a very spatially confined spreading (i.e., a single wave front passing throught the group). The long range connections lead to a diffusion of information and an overall decrease in the local fraction of infections. Thus the same mechanisms that have proven helpful in the case of simple contagion (i.e., the long links, providing short cuts), hinder the spread of information for complex contagion. The hampering effect of long range connections has also been described in the sociological literature where its is known as the "weakness of long ties" [32].

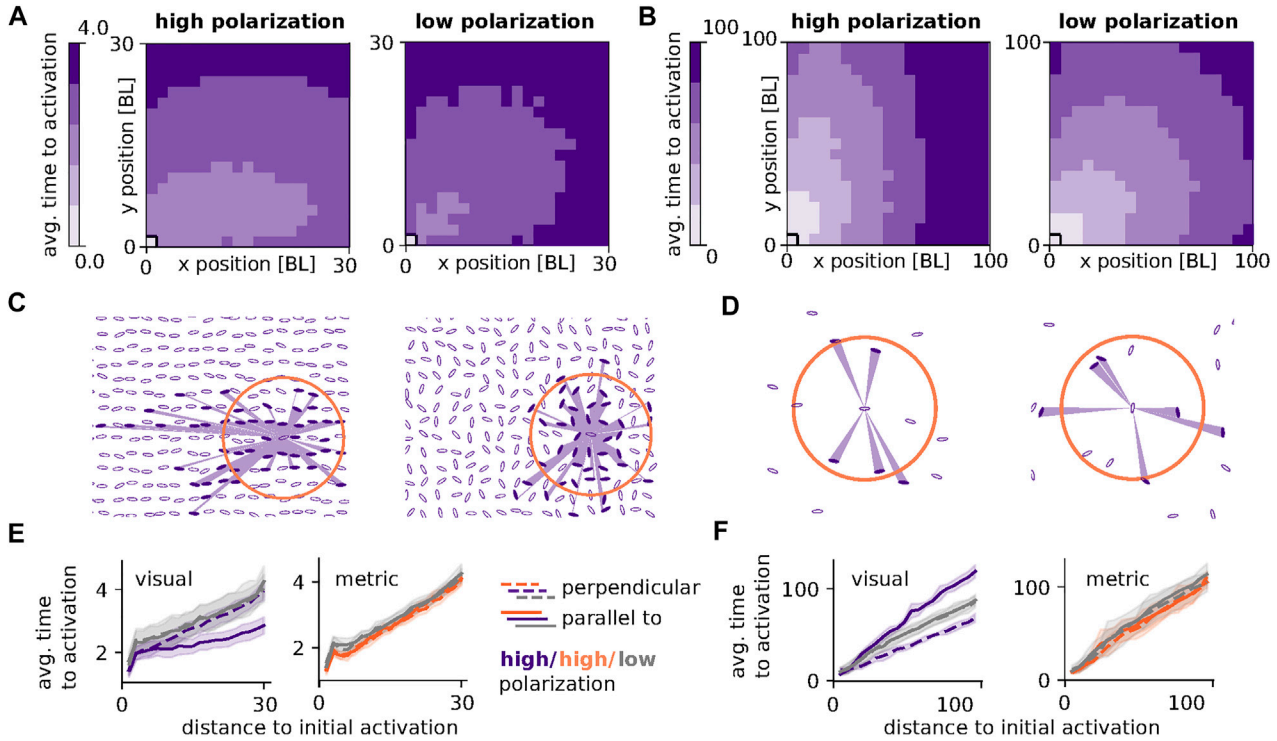

FIGURE 6 | Anisotropic spreading of simple contagion for high group polarization: **(A)** Propagation time of a simple contagion process initiated at $t = 0$ by one individual in the bottom left corner of a 20 × 20 grid with $g = 1.5$ BL and high (**left**, $\Phi \in [0.8, 1.0]$) and low (**right**,$\Phi \in [0.0, 0.2]$) polarization along the x-axis. Average time to activation (time, $t > 0$, at which an individual at position (x,y) is infected) is obtained as an average over 30 visual networks with 50 runs each and $\theta_{visual} = 0.01$. **(B)** Like (A), but for $g = 5.0$ and $\theta_{visual} = 0.1$. **(C)** and **(D)** Illustrations of the spatial configurations and visual fields used in the contruction of networks underlying the results of (A) and (B) respectively. Visual angles $\alpha_{ij} > \theta_{visual}$ are shown as shaded purple areas for one exemplary focal individual. Orange circles indicate the metric thresholds used in the construction of (E), $\theta_{metric} = 6$, and **(F)** $\theta_{metric} = 7$. **(E)** Average time to activation averaged over 3 outer rows in x (solid lines) and y (dashed lines) direction for high (purple, orange) and low (grey) polarization. The contagion spreads faster parallel than perpendicular to the polarization for the visual networks **(left)**. For metric networks **(right)** polarization has no effect on activation time. Parameters as in (A) and (C). (F) As in (E) but with parameters as in (B) and (D). For this combination of density and visual threshold the contagion spreads faster perpendicular to the polarization. Metric thresholds were chosen to yield similar contagion speeds as low polarization visual networks. Parameters: $N = 400$, $\gamma = 0.03$, $\beta = 0.1$.

3.5 Polarization

While so far we have studied the effect of density and degree on the structural properties of and contagion processes on the different network types, we have not considered the influence of the group's polarization which we have kept between 0 and 0.3. While under natural conditions polarization may correlate with density and thus indirectly influence network structure, for our grid-like positioning of ellipses, metric and topological network links are not influenced by the orientation of individuals because of their sole dependence on the Euclidean distance between individuals. For visual networks, however, the orientation of an ellipse may crucially influence its visibility and thus its social interactions. A high polarization may therefore lead to an anisotropy in spreading only on visual networks, i.e., a difference in speed of propagation in direction of the polarization to that perpendicular to it. **Figure 6** illustrates this effect with two examples of a combination of group density and visual threshold that leads to an anisotropy at high polarization, which is notable in the speed of a simple contagion process on visual networks.

Figures 6A,B depict the average propagation of a simple contagion process through a group of 400 individuals in a square 20x20 grid with average distance of 1.5 BL and 5.0 BL respectively between grid neighbors ($g = 1.5$ and $g = 5.0$). The contagion process is initiated by one individual in the lower left corner at $t = 0$ for high ($\Phi \in [0.0, 0.2]$, left) and low ($\Phi \in [0.8, 1.0]$, right) polarization along the x-axis. The average time it takes the infection to spread from the initial position at (0,0) to any other point in the group (given by an x and y position in body length) is indicated by color intensity (averages over 30 networks with 50 runs each). For low polarization the contagion process spreads evenly in all directions (circular equitemporal regions) while for high polarization spreading speed is enhanced either along (A) or perpendicular (B) to the direction of polarization (elliptic equitemporal regions).

Panels C and D show examples of the underlying spatial group configurations. They include examples of the visual field of one focal individual. Angular areas that exceed the visual threshold used for the construction of networks for A and B ($\theta_{visual} = 0.01$ BL in A,C,E and $\theta_{visual} = 0.1$ BL in B, D, F), are shown as shaded purple areas and corresponding visual network neighbors are filled in purple. For the low visual threshold and high density used in C, at high polarization links can span longer distances and are

more numerous in direction of the polarization as occlusions are less prominent in this direction because of the smaller visual angles. For the high visual threshold and low density used in D, at high polarization links are more likely to exist perpendicular to the polarization because of the larger angular areas of ellipses when seen from the side. These unevenly distributed links increase spreading speed in the direction of higher link density and length. In Panel E and F we summarize the above results by averaging over the outer three rows of individuals in x (solid lines) and y (dashed lines) direction for high (purple) and low (grey) polarization. For low polarization perpendicular and parallel propagation times are similar, while for high polarization propagation time is reduced either parallel (E) or perpendicular (F) to the polarization. Metric networks with a threshold of $\theta_{\text{metric}} = 6$ BL (illustrated by orange circle in C) and $\theta_{\text{metric}} = 7$ BL (D) show no difference in propagation times for high and low polarization (E,F). Metric threshold values were chosen to yield similar contagion speeds as the visual counterparts.

4 DISCUSSION

Animal groups represent examples of spatially-embedded interaction networks, where the spatial density of individuals does not only vary due to external factors but can be actively modulated by the group members based on environmental context [20]. We have shown, that when describing such systems with highly variable density by considering fixed interaction thresholds, potentially related to sensory or cognitive limitations, the fundamental properties of the resulting interaction network, their qualitative dependence on density and their emergent collective dynamics will crucially depend on the type of the network used. In particular, each network type shows a characteristic qualitative dependence of the average degree on density, which influences the density dependence of other network measures as well as the speed and reach of two classes of contagion processes (**Figures 1**, **2**, **4**). We characterized visual networks as a distinct class of interaction networks and highlighted the often neglected dependence of collective behavior on density and network type.

When modelling the collective behavior of animal groups with variable densities and fixed thresholds, intermediate-threshold visual networks display several key advantages. In contrast to metric networks, the average degree does not monotonically increase with density and thus avoids unrealistically high values at high densities. In contrast to topological networks they show a non-trivial dependence of the (in-) degree on density, and more crucially the finite visual threshold introduces a maximal interaction distance, which makes their behavior more realistic at low densities. In addition, they exhibit a maximum in the average (in-) degree at intermediate spatial densities of individuals which could explain preferred group densities.

Our results further demonstrate that for wide ranges of group densities visual networks are characterized by the existence of long-ranged links, absent in metric or topological interaction networks with comparable in-degrees which are accompanied by a lower average shortest path and clustering coefficient (**Figure 3**). The role of such long-range links in facilitating simple contagion processes such as information diffusion, has been studied extensively in network science and is known as the "strength of weak ties" or the "small-world" phenomenon [39,40]. Here we observe their influence in an increased spreading speed of the simple contagion on visual networks as compared to metric ones of similar degree (**Figure 5**). On the other hand, visual networks have in general smaller clustering coefficients in comparison to metric and topological networks, which is disadvantageous for the spread of fractional, complex contagion processes, assumed to be involved in spreading of behaviors [12] and known as the "weakness of long ties" [32]. We can observe this effect in our simulations of a complex fractional contagion process on visual and metric networks of the same degree. Here, the contagion process spreads to a larger fraction of the metric than the visual network and this effect becomes even more apparent when the initial activation is spatially correlated (**Figure 5**).

In summary, how fast and how far a behavior or information will spread, is dependent upon the network density, the agent's sensory limits and the type of contagion process. The use of multiple types of interactions (like visual or acoustic) may enable organisms to compensate the shortcomings of one type of sensory interaction and thus enable reliable collective response across a range of densities or sensory limits varying under changing environmental conditions.

Finally, we show that only visual networks have a strong dependence on the aspect ratio and orientation of individuals. More specifically, the breaking of a group's orientational symmetry due to alignment of individuals induces a symmetry breaking in the interaction network and consequently spatial anisotropy of social interactions. For two exemplary combinations of density and visual threshold we found anisotropy in the spreading of a simple contagion process on visual networks of polarized groups. More detailed studies of this dependence could reveal advantages or disadvantages of different spatial configurations of animal collectives observed in nature, especially when studied together with their visual detection ability [41].

Overall, our work provides compelling arguments for the consideration of visual networks in the study of social behavior. Nevertheless, it marks only a first step towards a full understanding of their role in collective animal behavior. While our results for artificially generated, static networks based on a square grid allow us to systematically study the effect of density, they do not capture the temporal nature and full range of structures observed in animal groups. Luckily, recent improvements in tracking software promise faster and more convenient access to realistic animal network data, including visual networks [42]. Using networks constructed from animal tracking would provide information about naturally occurring group sizes, densities and polarization as well as spatio-temporal fluctuations within these measures and thus allow to study their effects within a naturally occurring parameter range. Additional knowledge about the sensory limits specific to the studied organism (including the addition of a visual blind angle) will further improve the interaction networks and may enable a direct comparison between networks based on different senses like sound perception and vision.

A next step could then be to move on to non-static networks and to study the effect of different macroscopic states such as milling or swarming on network structure and spreading dynamics. Here, one could also use movement models that simulate the trajectories of all individuals based on the different types of social interactions. This approach could then go beyond the SIR-type spreading of information and investigate how movement information, e.g., a preferred direction of a few informed individuals, can spread and influence the group when using different interaction modes (visual, metric, topological).

Such an approach could also take into account the interactions of a group with the environment, asking, for example, how the detection of visual cues and the trade-off between private (external) and social information depends on group structure. It has been shown that predator detection based on sensory limits is dependent on density and group size and varies between different macroscopic states of fish schools [41] whereas interactions with the environment may induce density fluctuations. We hypothesize that visual networks are more robust to such spatial perturbations (i.e., a local increase or decrease in density).

Finally, let us note that, by starting with the most basic approach and considering binary connections (1 or 0 for presence or absence of links), we laid out the fundamental effects of the different networks dependency on density and threshold. A natural extension to weighted networks in the visual model would be to use relative angular area (angular area divided by the total field of view) as a link weight. Such an approach would entail an additional dependence of average link strength on density, which would in turn affect the weighted counterparts of the network measures. For the purpose of this paper, i.e., to establish visual networks as fundamentally different from other spatial networks by making direct comparisons between network types, the introduction of link weights would have been impractical as it would have introduced additional and arbitrary dependencies on density by the choice of link weights for each network type. Observed differences between the weighted networks would be heavily influenced by the choice of link weights and could therefore be less clearly attributed to sensory limits and the different rules establishing links. A comparisons between weighted networks will thus be most informative when studying a specific biological system which justifies the choice of link weights. Nevertheless, we expect essential features of the visual network, i.e., the existence of an upper bound on the degree at high densities, a lower clustering, the existence of longer links and the anisotropy of visual interaction networks due to orientational symmetry breaking, to also hold for weighted networks.

In conclusion, our work proposes experimentally testable hypothesis, e.g., in the context of behavioral contagion in animal groups [12,43], as well as a theoretical foundation for future investigation on how collective information processing could be dynamically tuned by individual-level behavioral adaptations affecting local density [20]. We highlighted several important qualities of visual networks, including their unique dependence on density and polarization, which encourages further research in this area. Overall, visual networks provide a promising and necessary addition to the established toolkit for the study of social interactions and collective behaviour and emphasize the need to include system-specific sensory limits.

DATA AVAILABILITY STATEMENT

The original contributions presented in the study are included in the article/**Supplementary Material**, further inquiries can be directed to the corresponding authors. The networks analyzed for this study were created using the code provided in https://doi.org/10.5281/zenodo.4983257.

AUTHOR CONTRIBUTIONS

WP and PR conceived the idea and designed the study. WP and CW performed the research. All authors discussed the results and wrote the manuscript. All authors contributed to manuscript revision, read, and approved the submitted version.

FUNDING

WP and PR were funded by the Deutsche Forschungsgemeinschaft (DFG) (German Research Foundation), Grant RO47766/2-1. PR acknowledges funding by the DFG under Germany's Excellence Strategy–EXC 2002/1 "Science of Intelligence"–Project 390523135.

ACKNOWLEDGMENTS

We acknowledge the support by Luke Longreen with exploratory simulations of visual networks as part of his lab rotation.

SUPPLEMENTARY MATERIAL

The Supplementary Material for this article can be found online at: https://www.frontiersin.org/articles/10.3389/fphy.2021.716576/full#supplementary-material

REFERENCES

1. Ballerini M, Cabibbo N, Candelier R, Cavagna A, Cisbani E, Giardina I, et al. Interaction Ruling Animal Collective Behavior Depends on Topological rather Than Metric Distance: Evidence from a Field Study. *Proc Natl Acad Sci* (2008) 105:1232–7. doi:10.1073/pnas.0711437105
2. Strandburg-Peshkin A, Twomey CR, Bode NW, Kao AB, Katz Y, Ioannou CC, et al. Visual Sensory Networks and Effective Information Transfer in Animal Groups. *Curr Biol* (2013) 23:R709–R711. doi:10.1016/j.cub.2013.07.059
3. Rahmani P, Peruani F, and Romanczuk P. Flocking in Complex Environments—Attention Trade-Offs in Collective Information Processing. *PLoS Comput Biol* (2020) 16:e1007697. doi:10.1371/journal.pcbi.1007697

4. Kumar R, Novak J, and Tomkins A. Structure and Evolution of Online Social Networks. In: *Link Mining: Models, Algorithms, and Applications*. New York, NY: Springer (2010). p. 337–57.
5. Mislove A, Marcon M, Gummadi KP, Druschel P, and Bhattacharjee B. Measurement and Analysis of Online Social Networks. In: Proceedings of the 7th ACM SIGCOMM conference on Internet measurement; 2007 October 24–26; San Diego, CA (2007). p. 29–42.
6. Balcan D, Colizza V, Gonçalves B, Hu H, Ramasco JJ, and Vespignani A. Multiscale Mobility Networks and the Spatial Spreading of Infectious Diseases. *Proc Natl Acad Sci* (2009) 106:21484–9. doi:10.1073/pnas.0906910106
7. Isella L, Stehlé J, Barrat A, Cattuto C, Pinton JF, and Van den Broeck W. What's in a Crowd? Analysis of Face-To-Face Behavioral Networks. *J Theor Biol* (2011) 271:166–80. doi:10.1016/j.jtbi.2010.11.033
8. Moussaïd M, Helbing D, and Theraulaz G. How Simple Rules Determine Pedestrian Behavior and Crowd Disasters. *Proc Natl Acad Sci* (2011) 108: 6884–8. doi:10.1073/pnas.1016507108
9. Moussaïd M, Kapadia M, Thrash T, Sumner RW, Gross M, Helbing D, et al. Crowd Behaviour during High-Stress Evacuations in an Immersive Virtual Environment. *J R Soc Interf* (2016) 13:20160414. doi:10.1098/rsif.2016.0414
10. Wirth T, and Warren W. The Visual Neighborhood in Human Crowds: Metric vs. Topological Hypotheses. *J Vis* (2016) 16:982. doi:10.1167/16.12.982
11. Krause J, James R, Franks DW, and Croft DP. *Animal Social Networks*. USA: Oxford University Press (2015).
12. Rosenthal SB, Twomey CR, Hartnett AT, Wu HS, and Couzin ID. Revealing the Hidden Networks of Interaction in mobile Animal Groups Allows Prediction of Complex Behavioral Contagion. *Proc Natl Acad Sci* (2015) 112:4690–5. doi:10.1073/pnas.1420068112
13. Ling H, Mclvor GE, Westley J, van der Vaart K, Vaughan RT, Thornton A, et al. Behavioural Plasticity and the Transition to Order in Jackdaw Flocks. *Nat Commun* (2019) 10:1–7. doi:10.1038/s41467-019-13281-4
14. Sarfati R, Hayes JC, Sarfati É, and Peleg O. Spatio-temporal Reconstruction of Emergent Flash Synchronization in Firefly Swarms via Stereoscopic 360-degree Cameras. *J R Soc Interf* (2020) 17: 20200179. doi:10.1098/rsif.2020.0179
15. Wild B, Dormagen DM, Zachariae A, Smith ML, Traynor KS, Brockmann D, et al. Social Networks Predict the Life and Death of Honey Bees. *Nat Commun* (2021) 12:1–12.
16. Vicsek T, and Zafeiris A. Collective Motion. *Phys Rep* (2012) 517:71–140. doi:10.1016/j.physrep.2012.03.004
17. Couzin ID, Krause J, Franks NR, and Levin SA. Effective Leadership and Decision-Making in Animal Groups on the Move. *Nature* (2005) 433:513–6. doi:10.1038/nature03236
18. Camperi M, Cavagna A, Giardina I, Parisi G, and Silvestri E. Spatially Balanced Topological Interaction grants Optimal Cohesion in Flocking Models. *Interf Focus* (2012) 2:715–25. doi:10.1098/rsfs.2012.0026
19. Lemasson BH, Anderson JJ, and Goodwin RA. Collective Motion in Animal Groups from a Neurobiological Perspective: the Adaptive Benefits of Dynamic Sensory Loads and Selective Attention. *J Theor Biol* (2009) 261:501–10. doi:10.1016/j.jtbi.2009.08.013
20. Sosna MMG, Twomey CR, Bak-Coleman J, Poel W, Daniels BC, Romanczuk P, et al. Individual and Collective Encoding of Risk in Animal Groups. *Proc Natl Acad Sci* (2019) 116:20556–61. doi:10.1073/pnas.1905585116
21. Bastien R, and Romanczuk P. A Model of Collective Behavior Based Purely on Vision. *Sci Adv* (2020) 6:eaay0792. doi:10.1126/sciadv.aay0792
22. Fichtel C, and Manser M. Vocal Communication in Social Groups. In: *Animal Behaviour: Evolution and Mechanisms*. Springer (2010). p. 29–54.
23. Demartsev V, Strandburg-Peshkin A, Ruffner M, and Manser M. Vocal Turn-Taking in Meerkat Group Calling Sessions. *Curr Biol* (2018) 28:3661–6. doi:10.1016/j.cub.2018.09.065
24. Romenskyy M, Herbert-Read JE, Ioannou CC, Szorkovszky A, Ward AJ, and Sumpter DJ. Quantifying the Structure and Dynamics of Fish shoals under Predation Threat in Three Dimensions. *Behav Ecol* (2020) 31:311–21. doi:10.1093/beheco/arz197
25. Newman ME. The Structure and Function of Complex Networks. *SIAM Rev* (2003) 45:167–256. doi:10.1137/S003614450342480
26. Barthélemy M. Transitions in Spatial Networks. *Comptes Rendus Physique* (2018) 19:205–32. doi:10.1016/j.crhy.2018.10.006
27. Lima SL. Collective Detection of Predatory Attack by Birds in the Absence of Alarm Signals. *J Avian Biol* (1994) 25:319–26.
28. Ward A, and Webster M. *Sociality: The Behavior of Group-Living Animals*. Springer Nature (2016).
29. Palachanis D, Szabó A, and Merks RMH. Particle-based Simulation of Ellipse-Shaped Particle Aggregation as a Model for Vascular Network Formation. *Comput Part Mech* (2015) 2:371–9. doi:10.1007/s40571-015-0064-56
30. Leblanc S. *Information Flow on Interaction Networks*. Princeton University (2018) Ph.D. thesis.
31. Barthélemy M. Spatial Networks. *Phys Rep* (2011) 499:1–101. doi:10.1016/j.physrep.2010.11.002
32. Centola D, and Macy M. Complex Contagions and the Weakness of Long Ties. *Am J Sociol* (2007) 113:702–34. doi:10.1086/521848
33. Hagberg AA, Schult DA, and Swart PJ. Exploring Network Structure, Dynamics, and Function Using Networkx. In: G Varoquaux, T Vaught, and J Millman, editors. *Proceedings of the 7th Python in Science Conference*. Los Alamos, NM: Los Alamos National Lab. (LANL) (2008) p. 11–5.
34. Fagiolo G. Clustering in Complex Directed Networks. *Phys Rev E* (2007) 76: 026107. doi:10.1103/PhysRevE.76.026107
35. Buhl J, Sumpter DJT, Couzin ID, Hale JJ, Despland E, Miller ER, et al. From Disorder to Order in Marching Locusts. *Science* (2006) 312:1402–6. doi:10.1126/science.1125142
36. Showler AT. *Desert Locust,* Schistocerca gregaria *Forskål (Orthoptera: Acrididae) Plagues*. Dordrecht: Springer Netherlands (2008) p. 1181–6. doi:10.1007/978-1-4020-6359-6_885
37. Craig A, and Feare C. *Starlings and Mynas*. London, GB: A&C Black (2010).
38. Brockmann D, and Helbing D. The Hidden Geometry of Complex, Network-Driven Contagion Phenomena. *Science* (2013) 342:1337–42. doi:10.1126/science.1245200
39. Granovetter MS. The Strength of Weak Ties. *Am J Sociol* (1973) 78:1360–80.
40. Watts DJ, and Strogatz SH. Collective Dynamics of 'small-World'networks. *nature* (1998) 393:440–2. doi:10.1038/30918
41. Davidson JD, Sosna MMG, Twomey CR, Sridhar VH, Leblanc SP, and Couzin ID. Collective Detection Based on Visual Information in Animal Groups. *J R Soc Interface* (2021) 18:20210142. doi:10.1098/rsif.2021.0142
42. Walter T, and Couzin ID. Trex, a Fast Multi-Animal Tracking System with Markerless Identification, and 2d Estimation of Posture and Visual fields. *Elife* (2021) 10:e64000.
43. Herbert-Read JE, Buhl J, Hu F, Ward AJW, and Sumpter DJT. Initiation and Spread of Escape Waves within Animal Groups. *R Soc Open Sci* (2015) 2: 140355. doi:10.1098/rsos.140355

Conflict of Interest: The authors declare that the research was conducted in the absence of any commercial or financial relationships that could be construed as a potential conflict of interest.

frontiers in Physics

ORIGINAL RESEARCH
published: 29 October 2021
doi: 10.3389/fphy.2021.670317

Simple Physical Interactions Yield Social Self-Organization in Honeybees

Martina Szopek, Valerin Stokanic, Gerald Radspieler and Thomas Schmickl*

Artificial Life Laboratory, Institute of Biology, University of Graz, Graz, Austria

Social insect colonies show all characteristics of complex adaptive systems (CAS). Their complex behavioral patterns arise from social interactions that are based on the individuals' reactions to and interactions with environmental stimuli. We study here how social and environmental factors modulate and bias the collective thermotaxis of young honeybees. Therefore, we record their collective decision-making in a series of laboratory experiments and derived a mathematical model of the collective decision-making in young bees from our empirical observations. This model uses only one free parameter that combines the ultimate effects of several aspects of the microscopic individual behavioral mechanisms, such as motion behavior, sensory range, or contact detection, into one single coefficient. We call this coefficient the "social factor." Our model is capable of capturing the observed aggregation patterns from our empiric experiments with static environments and of predicting the emergent swarm-intelligent behavior of the system in dynamic environments. Besides the fundamental research aspect in studying CAS, our model enables us to predict the effects of a physical stimulus onto the macroscopic collective decision-making that affects several crucial prerequisites for efficient and effective brood production and population growth in honeybee colonies.

Keywords: collective decision-making, self-organization, complex adaptive systems (CAS), honeybees, social interactions, swarm intelligence

OPEN ACCESS

Edited by:
Alex Jordan,
Max Planck Institute of Animal Behaviour, Germany

Reviewed by:
Xiao Han,
Beijing Jiaotong University, China
Chengyi Xia,
Tianjin University of Technology, China
Jitesh Jhawar,
Max Planck Institute of Animal Behaviour, Germany
Amir Haluts,
Weizmann Institute of Science, Israel

****Correspondence:***
Martina Szopek
martina.szopek@uni-graz.at

Specialty section:
This article was submitted to Social Physics, a section of the journal Frontiers in Physics

Received: *21 February 2021*
Accepted: *16 September 2021*
Published: *29 October 2021*

Citation:
Szopek M, Stokanic V, Radspieler G and Schmickl T (2021) Simple Physical Interactions Yield Social Self-Organization in Honeybees. Front. Phys. 9:670317. doi: 10.3389/fphy.2021.670317

1 INTRODUCTION

Complex adaptive systems (CAS) are ubiquitous. They include diverse systems such as social networks, Earth's climate, or its ecosystems [1, 2], but all CAS have specific properties and features in common: They are comprised of many independent agents whose loosely coupled and local interactions on the microscopic system level lead to emergent outcomes that are observable on the macroscopic system level. These macroscopic outcomes often happen surprisingly suddenly, e.g., phase transitions, which can profoundly alter the overall system's properties. These system changes are not sufficiently predictable by looking only at the microscopic individual behavior [3]. Similar phenomena can be observed in eusocial insect colonies, which possess all the typical characteristics of CAS [4]. The abilities of honeybee colonies (such as the western honeybee *Apis mellifera* L.) allow colony adaptation on various levels by altering or modulating the interaction network that emerges between the individuals. These properties involve many nonlinear feedback loops with significant time constants (delays). These properties of system ingredients are textbook examples of prerequisites for complex behavior arising from very simple interaction patterns [5, 6]. While these functional components may easily lead to chaotic behaviors, the existence of balancing feedback loops within social insect colony systems yields homeostasis and resilience through mechanisms of social self-regulation and self-organization [7]. Ultimately, these colonies can be seen as super-organisms: as a collective, they manage to navigate the delicate balance between

complexity-induced chaos and homeostatic self-regulation, a property that is seen as a characteristic of organisms and of life itself [8]. This residing on the edge between chaos and order makes social insect colonies in general, and honeybee colonies specifically, an excellent model system for complex but not chaotic CAS.

We examined the CAS of honeybees by a set of down-scaled laboratory experiments to keep the complexity of the study system within tractable bounds but still large enough to show interesting phenomena, such as collective decision-making, symmetry breaking, and biasing effects through informed leadership within the collective. We focused on how group size, environmental conditions, environmental dynamics, and local availability of information affect the individual and collective decision-making within this CAS.

Therefore, we studied groups of young honeybees, which already show complex social behaviors, e.g., in the collective thermotaxis where bees are able to collectively distinguish local from global thermal optima in complex thermal environments [9], based on simple individual processes [10]. The temperature-based self-localization behavior and the collective decision-making of young bees in complex and dynamic temperature fields of the brood nest are crucial components of the self-regulatory feedback loops of the colony. These mechanisms are governed by physical environmental stimuli that are capable of modulating the microscopic behaviors of the bees, e.g., their motion speed or their ability to preferably stay longer at places with specific environmental conditions.

Our focal research question in the presented work is as follows: Can we explain naturally observed examples of complex group-level behavior (e.g., collective thermotaxis) in complex adaptive systems (e.g., honeybees) as an emergent phenomenon arising from simple microscopic individual motion principles and simple interaction mechanisms? We here restrict ourselves to study the simplest set of mechanisms to allow us the building and parametrization of a simple but complex-enough model that is able to predict a rich set of empirical data that are collected on these CAS. This model is able to predict the emergence of collective taxis, and also the arising collective decision-making and symmetry breaking phenomena with respect to specific environmental configurations and dynamics. We further consider the social context in these processes, because it may be modulated by group members that have additional information or follow specifically different roles than our modeled agents. These predictions are made by a simple difference equation model that we develop here based on our empirical data. We used two different methods to solve the model: a mechanistic top-down approach using the forward Euler method and a bottom-up approach using an individual-based Monte Carlo simulation.

To understand the complex link between the individual microscopic behavioral repertoire of young bees and the emerging macroscopic patterns of aggregation that emerges from a collective decision-making process and the physical environment, we first conducted a set of experiments as a macroscopic evaluation of the system. We observed groups of young honey bees in static and dynamic temperature fields showing either a) one global, b) one global and one local, or c) two global optima and observed the aggregation behavior of the bees in these environments. By considering the most relevant underlying microscopic mechanisms that are the individual behaviors of young bees in such temperature fields, we ultimately developed a mathematical model that connects these two system levels. The first difference equation model is fitted to the observed empirical data collected in static temperature fields. This way the only "free parameter" our model contains, the social factor X_{bee}, is parametrized based on empirical data on living honeybees. Based on this parametrized difference equation model, a set of predictions is made regarding how this CAS will behave in dynamically changing environments. These predictions are then compared to empirical data for further validation of the model. Finally, we extend the model to incorporating social context and again predict the effect of biases that may arise by special actors in the collective that either pursue other goals have different limitations or possess alternative pieces of information.

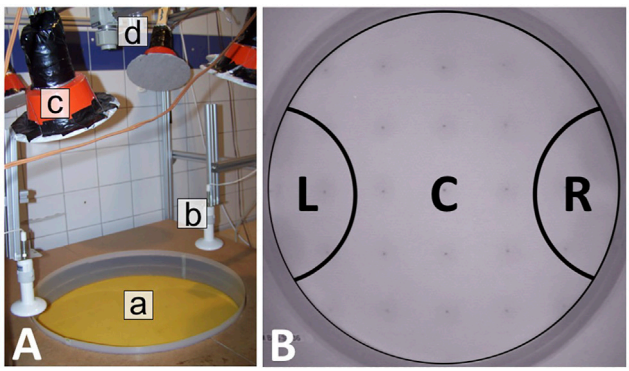

FIGURE 1 | Circular temperature arena setup and evaluation zones. **(A)** The setup consists of a circular arena (a) with temperature sensors that are embedded in the acrylic glass floor underneath the wax foundations, surrounded by a plastic barrier. The two thermal optima are generated with ceramic heating lamps mounted above the arena (b). The setup is illuminated with lamps that are covered with filters so that only infrared light is emitted (c), and the experiments are recorded with an IR-sensitive camera (d). Furthermore, technical details can be found in **Section 2.1.2** and [9]. **(B)** Evaluation zones: The arena was divided into three zones, with the left zone (L) and the right zone (R) representing the area under each heat lamp and the center (C) representing the area outside of these zones. For collecting the empirical data, the number of bees in each zone was determined from video recordings in either 1-minute intervals (Exp. 1–4) or at the end of each experimental run in minute 30 (Exp. 5).

2 MATERIALS AND METHODS

2.1 Experiments With Honeybees

2.1.1 Animals

All experiments were conducted with young honeybees (*Apis mellifera* L.) aged between 1 and 30 h after hatching from their brood cells. Honeybees at this age are still ectothermic, i.e., they are not able to produce heat on their own with their wing muscles

yet [11] and are therefore dependent on the appropriate thermal environment, in which they navigate actively. To collect bees with this defined age, a set of brood combs with many sealed pupae was gathered from colonies and incubated at 35°C and at a relative humidity of 60%. After hatching, the freshly emerged bees were removed from the combs and transferred to ventilated plastic containers with access to honey *ad libitum* to support their health and development. Each individual bee was participating only once in an experiment, and no individual with a visible handicap was used. After participating in an experiment, all bees were transferred to an identical separate container, and all bees were re-introduced into full colonies after the experiments each day.

2.1.2 Experimental Setup

Our basic experimentation setup consisted of a circular arena (with a diameter of 60 cm) that was surrounded by a plastic wall (**Figure 1A**). To prevent the bees from climbing the boundary, the plastic wall was coated with Teflon spray. The thermal environments were generated with either one or two ceramic heat lamps that were mounted above the arena (**Figure 1B**). To actively regulate the thermal environment in our setup, an array of temperature sensors was built into the acrylic glass arena floor (based on the methods described in [12]). The arena floor was covered with wax foundations that were replaced after each trial to remove any possible scent traces left behind by the bees. A standard PC controlled two digital dimmers that regulate the ceramic heat lamps by using the data from the temperature sensors. Three additional sensors were used to measure the ambient room temperature. The room temperature was kept around 29 ± 1°C by either heating with a radiator or by cooling with a portable air conditioning unit before starting each experiment. All experiments were performed under infrared light (**Figure 1C**), at a wavelength that is invisible for bees [13] so that we could exclude that the bees use any visual cues but were required to rely purely on their thermal sensory system and on their haptic sensory inputs when touching other bees or obstacles. Such conditions exist also in the brood area deep in the colony's hive, where young bees usually locate themselves [14]. All experiments were recorded with an IR-sensitive camera (**Figure 1D**). For technical details of the individual components and the setup, see [9, 15].

2.1.3 Experiments

We carried out five different sets of experiments to gather empirical data on the honeybees' behavioral repertoire: Three sets of experiments were conducted with groups of bees in static thermal environments to examine the influence of a static, thermally heterogeneous environment on the collective behavior. Another set of experiments was conducted with groups of bees in a dynamic environment to examine the flexibility of the collective behavior in response to sudden changes in the environmental conditions. Finally, another set of experiments was conducted with a static thermal environment and an additional social stimulus. The optimum temperature of 36°C was chosen in all experiments as it corresponds to the preferred temperature (thermal optimum) of freshly emerged, still ectothermic, honeybees [16]. To minimize the time the animals have to spend in the experimental setup, we set the runtime of experiments in stable thermal environments to 30 min to ensure enough time for the bees to explore their environment and form stable aggregations and to 105 min in dynamic thermal environments to additionally take into account the thermal inertia and the time the bees need to react to the changes in the thermal environment.

Static Thermal Environments—Experiments 1, 2, and 3

We conducted three different sets of experiments with this setting, each one with groups of 64 bees, in different configurations of static thermal environments. The bees were introduced (released from their cup) in the center of the arena, and each experimental run lasted for 30 min. In Experiment 1, we generated a thermal environment with one global optimum at 36 ± 1°C on one arena side and with a pessimum of 30 ± 1°C on the other arena side, as depicted in **Figure 2A** (n = 9 repetitions). In Experiment 2, we generated a more complex environment with, again, a global optimum at 36 ± 1°C on one arena side, but this time also with a local optimum at 32 ± 1°C on the opposite side of the arena as depicted in **Figure 2B** (n = 8 repetitions). In Experiment 3, we generated a thermal environment with two equally optimal spots at 36 ± 1°C on two opposite sides of the arena as depicted in **Figure 2C** (n = 6 repetitions).

Dynamic Thermal Environment—Experiment 4

The experimental runs with a dynamic thermal environment were also performed with groups of 64 bees. The bees were introduced in the center of the arena, and each experimental run lasted for 105 min (n = 17 repetitions). For this experimental setup, we generated an initial environment with a global optimum at 36 ± 1°C and a local optimum at 32 ± 1°C on the opposite side of the arena, equal to the second set of experiments with a static thermal environment. Thirty minutes after introducing the bees, the heat lamp providing the 36 ± 1°C optimum was shut off while the heat lamp generating the 32 ± 1°C optimum remained at the initial setting, leading to a change in the thermal environment as depicted in **Figure 2D**.

Static Thermal Environment With Social Stimulus—Experiment 5

In the experimental runs with a social stimulus, we used groups of 24–25 bees that could run freely in the arena. The thermal environment was equivalent to the one used in experiment 2 with one global optimum at 36 ± 1°C and a local optimum at 32 ± 1°C on the opposite side of the arena (as depicted in **Figure 2B**). To provide a local social stimulus, we introduced additional bees as a local "social stimulus" that was confined to a specific location. To confine these "social stimulus" bees, we used circular cages that were built from wire mesh and covered with an acrylic glass Petri dish (3B). We put two cages in the arena, one under each heat lamp (3A), whereby the cage in the local optimum contained the five stimulus bees. The cage in the global optimum remained empty and acted as a control against effects such as the wire cage itself hypothetically acting as an attractant for the bees. The test bees were introduced in the center of the arena and could run

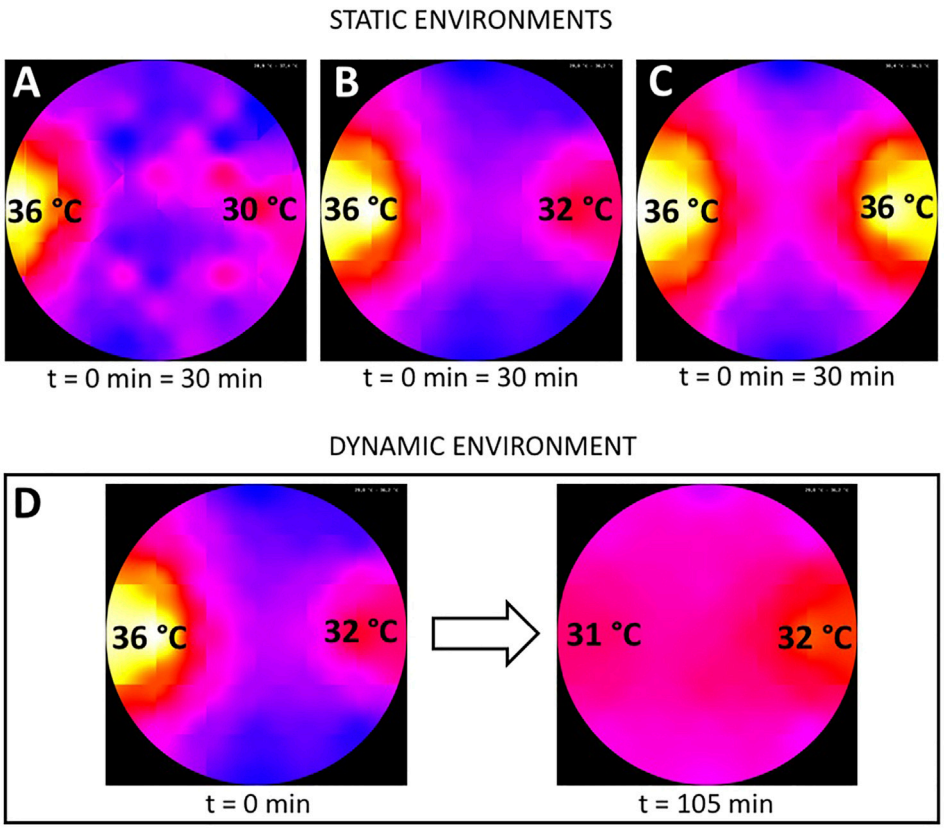

FIGURE 2 | Graphical representation of the used static and dynamic thermal environments in the different experiments. **(A)** static environment with one global optimum of 36±1°C on the left side (used in Experiment 1), **(B)** static thermal environment with a global (36±1°C) optimum on the left and a local optimum (32±1°C) on the right side (used in Experiments 2 and 5), **(C)** static environment with two global 36±1°C optima on opposing sides of the arena (used in experiment 3) and **(D)** dynamic environment used in Experiment 4 with an initial configuration equal to **(B)** and the resulting thermal environment at the end of the experiment after switching off the heat lamp on the left side at minute 30 with the new global optimum of 32±1°C on the right side. The run-time of the experiments with static environments was 30 minutes and 105 minutes in the experiments with the dynamic environment.

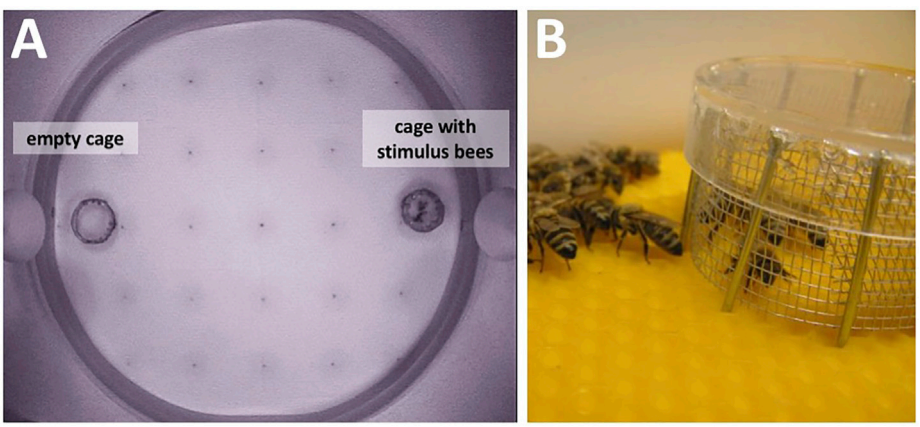

FIGURE 3 | Setup for experiment 5. **(A)** A wire cage with a transparent top was placed under each heat lamp. The cage placed under the right heat lamp that produced the local optimum contained 5 stimulus bees while the cage on the left in the global optimum remained empty and acted as a control. **(B)** Close-up of the caged bees with aggregated bees around.

freely in the arena, except for the space covered by the cages. Each experimental run lasted for 30 min (n = 10 repetitions).

2.1.4 Data Collection and Evaluation

The experiments were evaluated by assessing the location of the bees in specific time intervals throughout the experimental runtime. To collect the data, the area of the circular arena was subdivided into three zones: L (zone under left heat lamp), R (zone under right heat lamp), and C (remaining area; center) as depicted in **Figure 1B**. The left and right zones cover 11.2% of the total arena size each, corresponding to the area heated by the heat lamps. We manually counted the bees in each evaluation zone in 1-min intervals on still images from the recordings for experiments 1–4 to acquire a sufficient amount of data points for the model fitting (experiments 1–3) and to capture the dynamics in experiment 4. For experiment 5, we evaluated the number of bees in the respective zones at the end of the experimental runs (after 30 min). Each bee was attributed to the zone where most of its body was located. If a bee happened to be exactly on the evaluation line between two zones, it was attributed to the zone its thorax was located in. If a bee's thorax was directly on the line, it was attributed to the zone it was headed to. We evaluated a total of 50 runs with this method.

To visually depict the influence of the physical stimulus (temperature) on the macroscopic distribution pattern of the bees, we indicate the expected occupancy of the different zones, assuming that the bees ignore other bees and the local temperature (uniform distribution as a null model, see also [9]), in the result graphs for the empirical data. The expected occupancy is indicated as a dotted horizontal line for the respective evaluation zone, with an expected fraction of bees of 0.112 for the right and the left zones, respectively, and 0.776 for the center, corresponding to the size ratios of the evaluation zones.

All statistical comparisons were performed using the MannWhitney *U* test with a significance level of 0.05, and the *p* values are given in parentheses where results are reported.

2.2 Method of Parameterization and Fitting of the Developed Difference Equation Model

2.2.1 Implementation of the Temperature-Dependent Waiting Time

Bees are known to often rest (wait) for some time after a bee-to-bee contact, and it is known that this behavior is affected by the local temperature [9, 17]. To represent this important mechanism in the difference equation model, we generated a waiting-time function that maps a given time-dependent temperature $T(t)$ to a predicted waiting period duration.

This waiting time of a bee $W(T(t))$ is derived from empirical data collected in observations of young honeybees [18] and is described through the sigmoidal function

$$W(T(t)) = a \cdot tanh\left(\frac{T(t)}{b} - d\right) + e \tag{1}$$

with the parameters $a = 12$, $b = 1.2$, $d = 27$, and $e = 13$. This yields a curve that returns 1 s at 28°C and 25 s at 36°C as depicted in **Figure 4A**. Restricted through the lower boundary of the waiting time, we chose a time step of $\Delta t = 1$ s for our model.

Our model needs also to be able to depict a dynamic thermal environment, i.e., the temperature decay over time that is a significant aspect in experiment 4 after the heating lamp is turned off. Thus, we used the mean temperature sensor data for the left temperature field zone from the runs of experiment 4 and fitted a temperature decay curve to the values that lie on the mean of the deviation (see **Figure 4B**).

2.2.2 Model Fitting

To fit our model's difference equations, we used the proven method of least squared residuals. Here, we looked at the difference between the model's prediction and the empirically observed mean value at equally spaced given points in time and minimized the sum of all squared residuals by numerically solving the equations while adjusting our social parameter X_{bee}. To find the one parameter value that suits all the conducted experiments 1, 2, and 3, we fitted the equations to the mean empirical data of all zones and experiments at once.

2.2.3 Noise Implementation

The basic behavior exhibited by most bees in a thermal field is forms of correlated random walks [10, 17, 19, 20]. To reflect this randomness in the underlying microscopic behaviors, we implemented a noise-affected term in our model. This noise is introduced to the system by multiplicative application of a time-discrete, uncorrelated, and Gaussian distributed random value (see **Eq. 2**) on the free parameter, the social factor X_{bee}, with the mean $\mu = 1$ and a standard deviation $\sigma = 0.25$ restricting the possible values to the interval [0; 2], which is necessary to guarantee non-negativity and symmetry around the mean.

$$\epsilon(t) = \frac{1}{\sigma\sqrt{2\pi}} e^{-\frac{1}{2}\left(\frac{t-\mu}{\sigma}\right)^2} \tag{2}$$

3 RESULTS

3.1 Groups of Bees in Static Thermal Environments

To examine the macroscopically observable patterns of aggregation, we conducted experiments with different static thermal environments. In experiment 1, with only one global optimum at 36°C, the majority of bees are found in the left evaluation zone at the end of the experimental runs. This zone corresponds to the global thermal optimum, and most bees are located there within 15 min. The median fraction of bees in the left zone is significantly higher than in the center zone and the right zone after 15 and after 30 min ($p < 0.001$, compare **Figure 5A** left, center, and right). Similarly, in experiment 2, with a global optimum on the left and a local optimum on the right side of the arena, the median fraction of bees at the global optimum on the left was significantly higher than the median

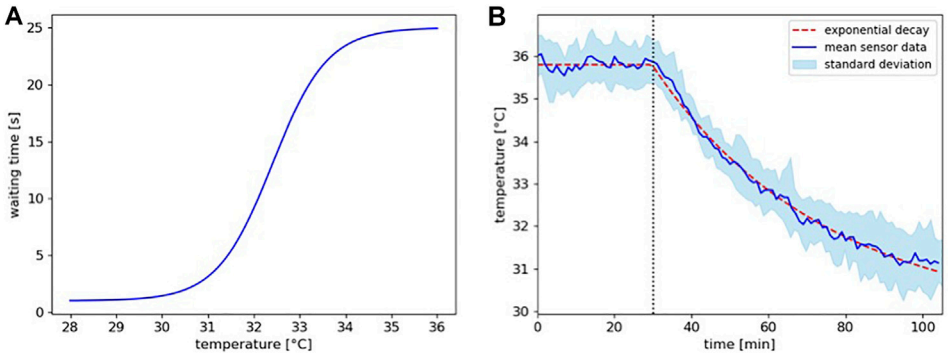

FIGURE 4 | (A) Function of the implemented waiting time in dependence of the locally experienced temperature according to equation 1. **(B)** Temperature decay model. Shown are the mean temperature sensor data with standard deviation from the left zone overtime for the runs of experiment 4 (blue line and band) and the implemented temperature profile for the model (dashed red line). The decrease in temperature after the lamp was switched off at minute 30 (dotted vertical line) follows the characteristics of an exponential decay.

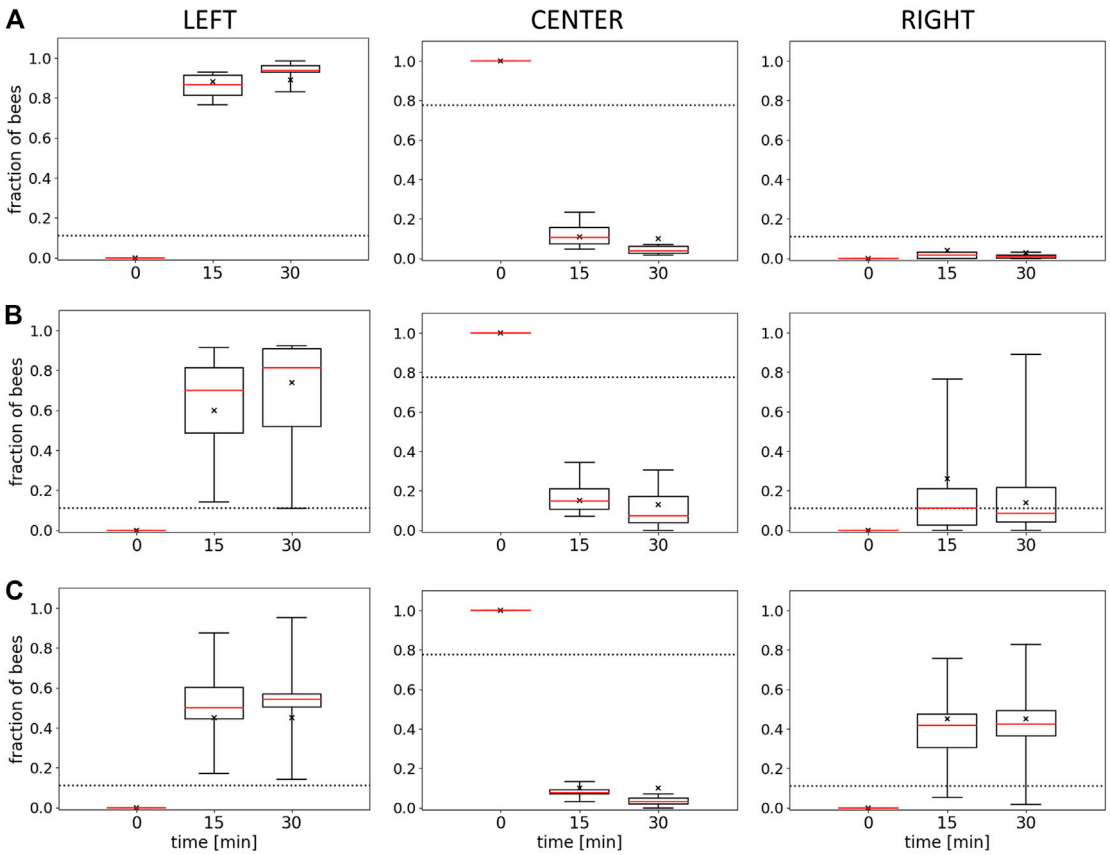

FIGURE 5 | Results of Experiments 1, 2, and 3. Shown is the median fraction of bees (with Q1, Q3, minimum, and maximum) at minutes 0, 15, and 30 in the left evaluation zone (L), the center (C), and the right evaluation zone (R) for **(A)** Experiment 1 (L: 36±1°C, R: 30±1°C), *n*=9 repetitions, **(B)** Experiment 2 (L: 36±1°C, R: 32±1°C), *n*=8 repetitions, and **(C)** Experiment 3 (L: 36±1°C, R: 36±1°C), *n*=6 repetitions. The crosses indicate the model fits for each data series for the model described in the discussion section. Dotted horizontal lines indicate the expected occupancy if the bees ignored other bees and the local temperature (uniform distribution model).

fraction of bees in the center ($p = 0.003$) and at the local optimum on the right ($p = 0.012$) (**Figure 5B** left, center, and right) after 30 min. In experiment 3, with a thermal environment containing two equally warm global optima, the results in **Figure 5C** show no statistical difference in the median fraction of bees between the right and the left zones ($p = 0.261$). For this experiment, we also

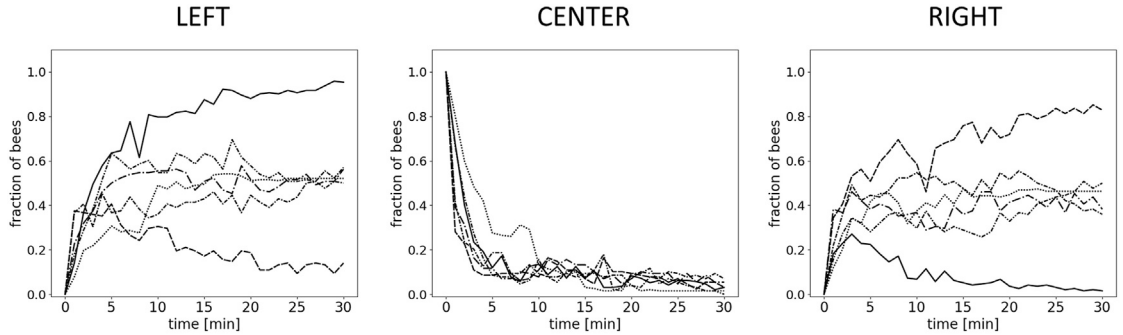

FIGURE 6 | Results for Experiment 3–individual runs. Shown is the fraction of bees in 1-minute wide intervals over the whole experimental run-time (30 minutes) for each individual run (n=6 repetitions) in the left zone (36±1°C), the center, and the right zone (36±1°C).

TABLE 1 | Model variables and parameters.

Model variables				
Symbol	**Description**	**Value**	**Units**	**Source**
$L(t)$, $C(t)$, $R(t)$	Number of bees in the left, center, and right zones (at time t)	-	*bees*	-
$T_l(t)$, $T_r(t)$	Temperature in the left and right zones (at a time t)	-	$^{\circ}C$	empirical data
$W_l(T)$, $W_r(T)$	Waiting time in the left and right zones (at a temperature T)	-	s	[18]
$\epsilon_1(t)$, $\epsilon_2(t)$, $\epsilon_3(t)$	Gaussian distributed noise (at a time t)	[0; 2]	dmnl	first principles
X_{bee}	Social factor	0.0056	$(s \cdot bees)^{-1}$	fitting
X_{seed}	Weight parameter for stimulus bees	1	dmnl	free parameter
$P_{c,l}$	Probability for bee switching from center to left zone	-	dmnl	-
$P_{c,c}$	Probability for bee staying in center zone	-	dmnl	-
$P_{c,r}$	Probability for bee switching from center to right zone	-	dmnl	-
$P_{l,l}$	Probability for bee staying in left zone	-	dmnl	-
$P_{l,c}$	Probability for bee switching from left to center zone	-	dmnl	-
$P_{r,r}$	Probability for bee staying in right zone	-	dmnl	-
$P_{r,c}$	Probability for bee switching from right to center zone	-	dmnl	-
Model parameters				
Symbol	**Description**	**Value**	**Units**	**Source**
L (0), C (0), R (0)	Initial number of bees in the left, center and right zone (at t = 0)	$L(0) = 0$ $C(0) = 64$ $R(0) = 0$	*bees*	empirical data
N	Total number of bees	$64\,(exp.1-4)$ $24, 25\,(exp.5)$	*bees*	empirical data
S_l, S_r	Number of stimulus bees in the left and right zones	$S_l = 0$ $S_r = 5$	*bees*	empirical data

looked at the individual trials that show that while the groups split up approx. 50:50 in most of the trials, in 20% of the trials a strong symmetry breaking occurred, i.e. the majority of the bees aggregated on one side of the arena (see **Figure 6**).

3.2 Building a Difference Equation Model of the Observed System

Based on the empirical results we described in the previous section, we here develop a simple difference equation model in which we break down the social stimulus-based self-localization behavior into basic principles. We aim at constructing a parsimonious model with a limited set of parameters that describe the observed complex behaviors in a simple way. An overview of all model variables and parameters is given in **Table 1**. The model tracks the bees with conservation of mass and describes their rates of change between the three compartments that were used and are thus suggested by the empirical experiments' analysis method: The state variable $L(t)$ models all bees located in the left zone, the state variable $R(t)$ models all bees located in the right zone, and the state variable $C(t)$ models all other bees. The total number of bees is $N = L(t) + C(t) + R(t)$, guaranteeing respect for mass conservation in the model. For the sake of simplicity, we do not explicitly model the area of the zones (and, respectively, the proportions of its boundaries) or the area a bee or a group of bees would occupy.

The changes of the three state variables are then described as a system of coupled ordinary difference equations, whereby

$$\frac{\Delta L}{\Delta t} = meet_l(t) + join_l(t) - leave_l(t) \quad (3)$$

models the change in the number of bees in the left zone,

$$\frac{\Delta R}{\Delta t} = meet_r(t) + join_r(t) - leave_r(t) \quad (4)$$

models the change in the number of bees in the right zone, and

$$C(t) = N - L(t) - R(t) \quad (5)$$

models the number of bees in the center simply by subtracting the number of bees that are in the left and right zones from the total number of bees.

These three equations are modeled following the standard mass action law, as it expresses the expected interactions of entities based on their mean densities, as it is also used in the mathematical modeling of predator-prey and host-parasite systems [21, 22], intraspecific competition [23], interspecific competition [24], the spreading of infectious diseases [25], or chemical, e.g., enzyme-substrate interactions [26].

As we aim for the simplest version of this model, we combined all individual microscopic parameters—motion behavior, sensory range, contact detection—into one single parameter that we named "social factor" X_{bee}. Another microscopic system-level aspect that needs to be modeled is the individual behavioral response to the locally perceived temperature and how this affects the social interaction. Young honeybees tend to stop after encountering another bee and rest for some time after such collisions, whereby the resting time is positively correlated with the local temperature [9, 17]. This temperature-dependent waiting time is represented by $W(T)$. For the model, we assume that the bees move randomly and stop when encountering another bee with a probability determined by X_{bee} and that the waiting time of those individuals depends on the locally prevalent temperature [9]. The implemented waiting-time function is depicted in **Figure 4A**. The terms on the RHS of our equations are functions of time in our model. They express specific processes that affect the rate of change of the specific system variable on the LHS of the equation.

The functions $meet_l(t)$ and $meet_r(t)$ represent half of the initial center zone bees that, after interacting with each other in dependence of our social factor X_{bee}, form a cluster in the left and right zones equally likely and are described as

$$meet_l(t) = meet_r(t) = \frac{1}{2} \cdot X_{bee} \cdot C(t)^2 \quad (6)$$

The functions $join_l(t)$ and $join_r(t)$ represent initial center zone bees that join already present bees in the left and right zones and are described as

$$join_l(t) = X_{bee} \cdot L(t) \cdot C(t) \quad (7)$$

for the left zone and

$$join_r(t) = X_{bee} \cdot R(t) \cdot C(t) \quad (8)$$

for the right zone.

Finally, the functions $leave_l(t)$ and $leave_r(t)$ represent the bees in either zone that transition back to the center zone after their temperature-dependent waiting time has expired and are described as

$$leave_l(t) = \frac{L(t)}{W_l(T_l(t))} \quad (9)$$

for the left zone and

$$leave_r(t) = \frac{R(t)}{W_r(T_r(t))} \quad (10)$$

for the right zone.

In our empirical experiments with bees, the number of bees was kept constant in experiments 1 to 3. For the simulation runs of our model, we thus set N to a value of 64, and equivalent to the experiments, all bees were starting in the center region, therefore $C(0) = N$ bees and $L(0) = R(0) = 0$ bees. The variables that represent the mean temperatures within the left and right area are set $T_l(t) = 36$°C and $T_r(t) = 30$°C, respectively, for comparison with experiment 1, to $T_l(t) = 36$°C on the right and $T_r(t) = 32$°C on the left for comparison with experiment 2 and to $T_l(t) = T_r(t) = 36$°C on both sides for comparison with experiment 3.

The functions that involve the waiting times $W_l(T(t))$ and $W_r(T(t))$ in the modeling of specific rates of change represent the number of bees that leave their zone of resting (**Eq.(3)** and (**4**) and transition back into the center zone (**Eq.5**), which can be assumed to be equal to the mean time a bee spends in this zone. This waiting duration is not directly a function of time, but a function of the local temperature, as was expressed by $W(T(t))$ in **Eq. 1**. However, the mean temperatures and thus the waiting times within the two zones are able to change in time in our experiments.

Finally, our system of coupled difference equations is numerically solved through the forward Euler method with a step size of $\Delta t = 1$.

In our model building approach, we aim at a "one fits all" model; thus, we fitted our free parameter X_{bee} to the empirical data set from all our experiments in static environments (experiments 1–3), aiming for a value with which the model can qualitatively (and partially even quantitatively) represent the results from all three experiments sufficiently.

Using the method described in **subsection 2.2.2**, we found the best fit for our free parameter with a value of $X_{bee} = 0.0056 \frac{1}{s \cdot bee}$. The results of this fitting are shown in **Figure 7**, where the empirical data (median fraction of bees, IQR, minimum, and maximum) that were used for fitting are plotted over time for experiments 1 (**Figure 7A**), 2 (**Figure 7B**), and 3 (**Figure 7C**) with the respective fitted model results (dashed lines).

3.3 Predicting Macroscopic Aggregation Patterns in Complex Environments

To test the predictive ability of the model when applied to new data, we simulated our model in resembling to the two experimental settings that were not previously used to fit the model's parameters: experiment 4 with a dynamic thermal environment and experiment 5 with an additional social stimulus. The model predictions of these experiments can then

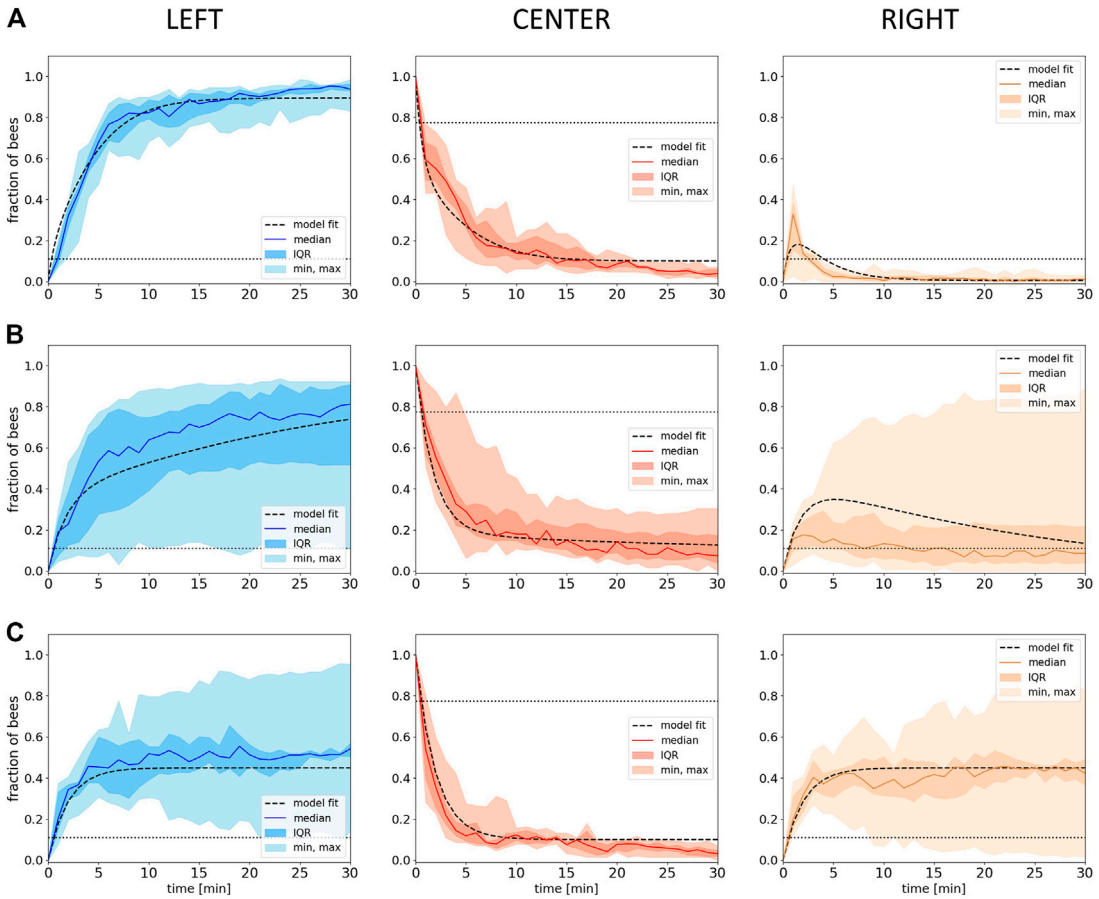

FIGURE 7 | Model fitting. Shown is the fraction of bees in the different evaluation zones **(Left, Center, Right)** from empirical data (median with IQR, minimum and maximum) over time with the respective fitted model data (dashed lines) with the social factor X_{bee} of $0.0056\frac{1}{s \cdot bee}$ for **(A)** experiment 1 (L: 36±1°C, R: 30±1°C), n=9 repetitions **(B)** experiment 2 (L: 36±1°C, R: 32±1°C), n=8 repetitions and **(C)** experiment 3 (L: 36±1°C, R: 36±1°C), n=6 repetitions. Dotted horizontal lines indicate the expected occupancy if the bees ignored other bees and the local temperature (uniform distribution model).

be compared to the empirical observations for validation purposes.

3.3.1 Aggregation Patterns in a Dynamic Thermal Environment (Model Solved With the Forward Euler Method)

The empiric results from experiment 4 show that the median fraction of bees in the left zone at the optimal temperature rises in the initial phase, when this side holds a global optimum of 36°C. As soon as the heat lamp on the left is switched off in minute 30, the median fraction of bees in the left zone starts to decrease. In parallel, we find an increase in the right zone (32°C) while the median fraction of bees in the center rises only slightly (8A). As soon as the left zone starts to cool down, the unchanged right zone becomes the global optimum in the system, and the bees collectively start to aggregate in this zone. Statistical analysis of our data indicates a median fraction of bees in the left zone that is significantly higher than in the right zone at minute 30 ($p < 0.001$). When comparing the median fraction of bees in the left zone at minute 30 with the median fraction of bees in the right zone at the end of the experiment (minute 105), no statistical difference was found ($p = 0.97$). The same was found when comparing the median fraction of bees in the left zone at minute 105 and the right zone at minute 30 ($p = 0.63$).

To model the dynamic thermal environment from experiment 4, we implemented the time dependency *via* the temporal progression of the temperature $T = T(t)$, as detailed in **Section 2.2.1**. Besides adding the required exponential decay of temperature in the left zone and applying noise to the system's free parameter (see **Section 2.2.3**), no changes were made to the model for simulating experiment 4. As the system has three distinct possibilities for the interaction of bees (C^2, $C \cdot L$, and $C \cdot R$), we implemented three uncorrelated noise factors $\epsilon_1(t)$, $\epsilon_2(t)$, and $\epsilon_3(t)$, corresponding to **Eq. 2**, and with one factor for each of the three possibilities. As the bees that leave the center split up 50:50 (**Eq. 6**), the noise that is applied to one side needs to be reflected in the other by subtracting it from the maximum possible value that the noise can deliver, forming the term $(2 - \epsilon_1(t))$.

After introducing the noise, the resulting cluster functions (**Eqs. 6–8**) are being restated as following:

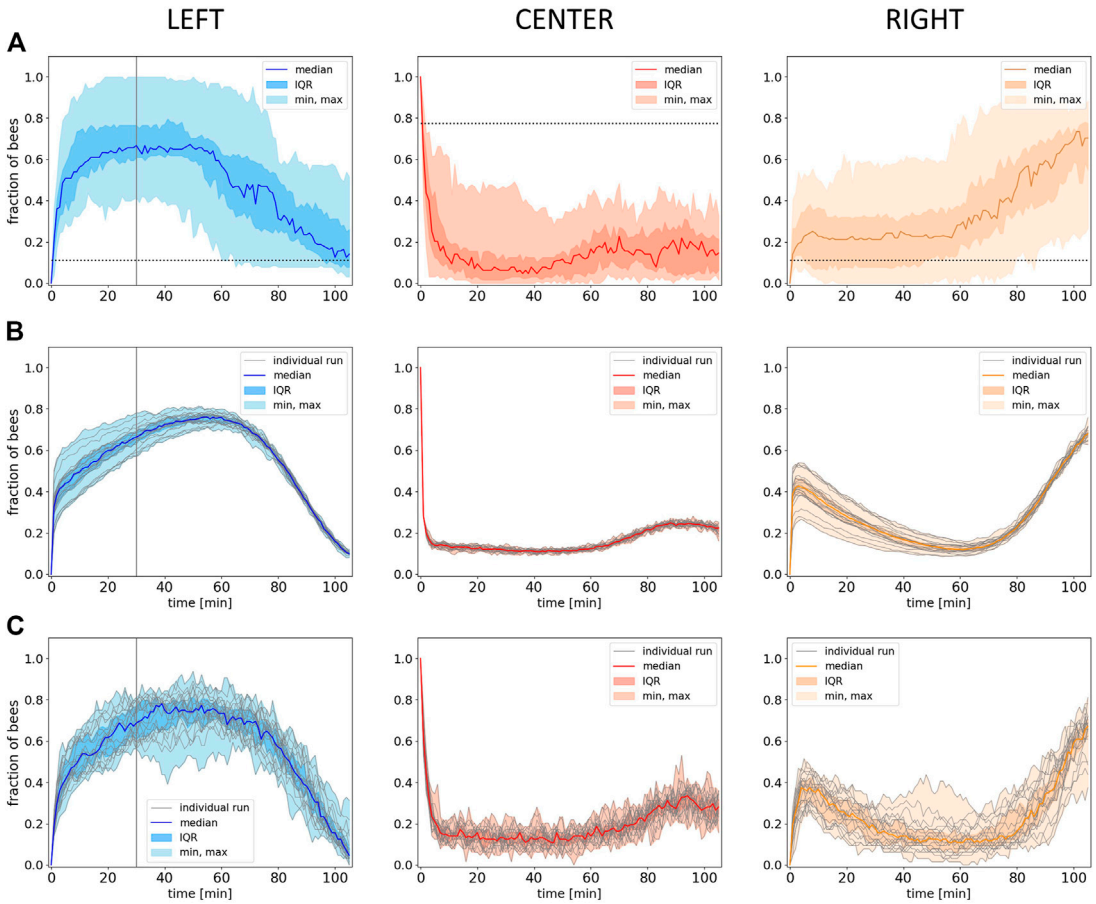

FIGURE 8 | Empirical and model results from experiment 4. **(A)** Empirical data: Shown is the median fraction of bees (with IQR, minimum and maximum) in the different evaluation zones **(Left, Center, Right)** over 105 minutes experimental runtime (data collected in 1-minute intervals), n=17 repetitions. Dotted horizontal lines indicate the expected occupancy if the bees ignored other bees and the local temperature (uniform distribution). **(B)** Predictions of the model solved with the forward Euler method: Shown is the median fraction of bees (with IQR, minimum and maximum) in the different evaluation zones **(Left, Center, Right)** over an equivalent of 105 minutes experimental runtime, grey lines represent the individual model runs, n=20 repetitions. **(C)** Individual-based Monte Carlo simulation predictions: Shown is the median fraction of bees (with IQR, minimum and maximum) in the different evaluation zones over the experimental runtime, grey lines represent the individual model runs, n=20 repetitions. The solid vertical lines in the graphs for the left zone in **(A)**, **(B)** and **(C)** indicate the point in time where the lamp in this zone was switched off at minute 30.

$$meet_l(t) = \epsilon_1(t) \cdot \frac{1}{2} \cdot X_{bee} \cdot C(t)^2 \tag{11}$$

$$meet_r(t) = (2 - \epsilon_1(t)) \cdot \frac{1}{2} \cdot X_{bee} \cdot C(t)^2 \tag{12}$$

$$join_l(t) = \epsilon_2(t) \cdot X_{bee} \cdot L(t) \cdot C(t) \tag{13}$$

$$join_r(t) = \epsilon_3(t) \cdot X_{bee} \cdot R(t) \cdot C(t) \tag{14}$$

For the prediction of the empirical data, we performed 20 individual runs with the model, with settings that match the experimental conditions: An initial static thermal environment with 36°C on the left side and 32°C on the right side, with the temperature on the left side decreasing according to the exponential decay and groups of 64 bees. For X_{bee}, we used the value $0.0056\frac{1}{s \cdot bee}$ as it was determined by the initial fit to data from static thermal environments.

The resulting simulation data are shown in **Figure 8B**: Our model generates a lower variance but predicts the dynamics in all zones quantitatively well when compared to the empirical data. The model also qualitatively captures the delay between the switching off of the heat lamp in the left zone and the decrease in the median fraction of bees, but compared to the empirical data, the delay is longer and even shows an initial increase (compare **Figure 8A** left and B left). Similarly to the empirical data, also in the model, the median fraction of bees is comparably low and increases slightly in the later half of the experimental runtime during the transition of bees from the left to the right side (**Figure 8B**). The model also qualitatively captures the increase in the number of bees in the right zone at about the point in time when the median fraction of bees on the other side starts to decrease, what also fits qualitatively well to the empirical data (**Figure 8B**). The median fraction of bees in the right zone after the transition at minute 105 does not significantly differ from the median fraction of bees in the left zone at minute 30 before the transition in the model data (p =

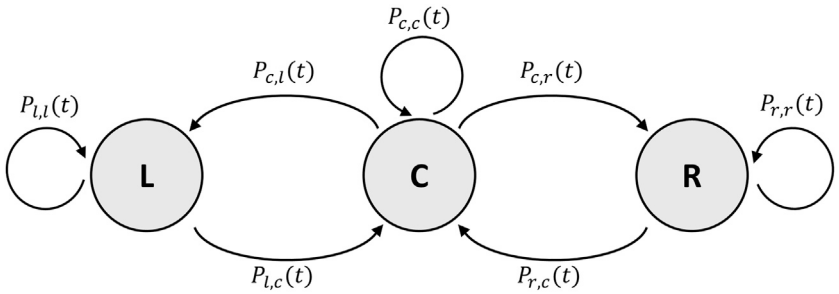

FIGURE 9 | Finite state machine of the individual-based Monte Carlo simulation. States and transitions as described in **Section 3.3.2**.

0.253). While the empirical data show no statistical significant differences when comparing the median fraction of bees in the left zone at minute 105 and in the right zone at minute 30, the model results show a significant difference for the same comparison ($p < 0.001$).

The quantitative comparison between the empirical data and the model data shows that there is no significant difference between the median fraction of bees in the experimental left zone and in the simulated left zone ($p = 0.843$) and also no significant difference when comparing the median fraction of bees in the experimental and in the simulated right zone ($p = 0.96$) at minute 30. The same was found when comparing the median fraction of bees of the experimental and of the model data in the left zone ($p = 0.165$) and in the right zone ($p = 0.353$) at minute 105.

The noise in the model that is solved with the forward Euler method produces a lower variance compared to the empirical data. We therefore simulated the same experiment with an individual-based sequential Monte Carlo method as described in the next section.

3.3.2 Aggregation Patterns in a Dynamic Thermal Environment (Individual-Based Monte Carlo Simulation)

To represent the higher variance that is shown in the experimental data, we introduce a sequential and individual-based Monte Carlo simulation, in which the difference equations are described by the probabilities for each bee to transition into a neighboring zone (see **Figure 9**).

The probability P for a bee to transition from the center C to the left zone L is defined as $P_{c,l}(t) = X_{bee} \cdot (L(t) + 0.5 \cdot C(t))$ and, respectively, to the right zone R as $P_{c,r}(t) = X_{bee} \cdot (R(t) + 0.5 \cdot C(t))$. The probability for a bee to leave the left zone is defined as $P_{l,c}(t) = 1/W_l(t)$ and as $P_{r,c}(t) = 1/W_r(t)$ to leave the right zone. The probabilities $P_{l,l}(t)$, $P_{r,r}(t)$, and $P_{c,c}(t)$ are the counter-probabilities and are defined as $P_{l,l}(t) = 1 - P_{l,c}(t)$ for the left zone, $P_{r,r}(t) = 1 - P_{r,c}(t)$ for the right zone, and $P_{c,c}(t) = 1 - P_{c,l}(t) - P_{c,r}(t)$ for the center zone.

The results are depicted in **Figure 8C** and show that the variance produced by the individual-based Monte Carlo simulation is greater than the variance produced by the model solved with the forward Euler method (**Figure 8B**) and more similar to the empirical data shown in**Figure 8A**.

Similarly to the predictions made by the model solved with the forward Euler method, the median fraction of simulated bees in the right zone after the transition at minute 105 does not significantly differ from the median fraction of bees in the left zone at minute 30 before the transition ($p = 0.291$). As it is the case for the results of the model solved with the forward Euler method, and in contrast to the empirical results, the results from the individual-based Monte Carlo simulation also show a significant difference when comparing the median fraction of bees in the left zone at minute 105 and in the right zone at minute 30 ($p < 0.001$).

The quantitative comparison between the empirical data and the model data shows that there is no significant difference between the median fraction of bees in the experimental left zone and in the simulated left zone ($p = 0.772$) and also no significant difference when comparing the median fraction of bees in the experimental and in the simulated right zone ($p = 0.437$) at minute 30. The same was found when comparing the median fraction of bees of the experimental and of the model data in the right zone at minute 105 ($p = 0.279$), while there is a significant difference between the median fraction of bees of the experimental data and the model data in the left zone at minute 105 ($p = 0.002$).

3.3.3 Aggregation Patterns in a Static Environment With an Added Social Stimulus

The results from experiment 2 reported in **Section 3.1** show that the bees are collectively able to distinguish the global from the local optimum with the majority of the bees found in the right zone at 36°C after 30 min (**Figure 5B**). Based on these findings, we studied whether or not this collective decision-making process can be biased by a social stimulus in the local optimum in the same thermal environment used for experiment 2. Therefore, we tested groups of 24–25 bees and additionally introduced five bees that were confined in the local optimum. The empirical results for this experiment are shown in **Figure 10A** (blue data set). To show the effect of the social stimulus on the macroscopic behavior, we compare it with data from comparable experiments without a social stimulus, redrawn from [9] (red data set), where experiments with groups of 24 bees in the same static thermal environment were reported.

These results show that the median fraction of bees in the global optimum is significantly lower in experiments with a social

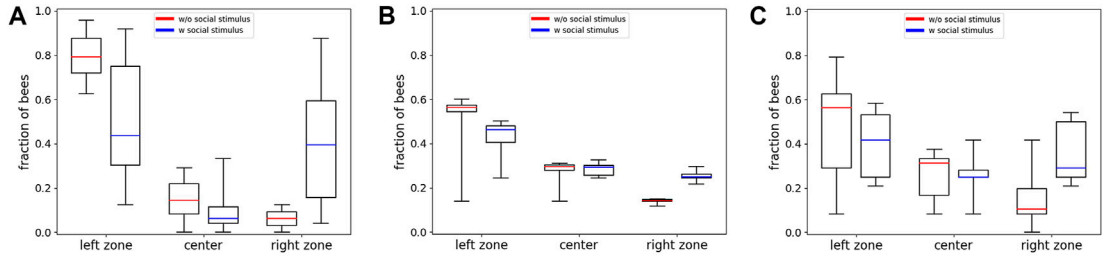

FIGURE 10 | Empirical and model results from experiment 5. **(A)** Empirical data: Shown is the comparison of the median fraction of bees (with Q1, Q3, minimum and maximum) in the different evaluation zones **(Left, Center, Right)** at minute 30 between experiments with an added social stimulus in the local optimum (blue, n=10 repetitions) and experiments without this social stimulus (red, data redrawn from [9], n=8 repetitions). **(B)** Predictions of the model solved with the forward Euler method: Comparison of the median fraction of bees (with Q1, Q3, minimum, and maximum) in the different zones **(Left, Center, Right)** at minute 30 between runs with an added social stimulus in the local optimum (blue, n=10 repetitions) and experiments without this social stimulus (red, n=10 repetitions). **(C)** Predictions of the individual-based Monte Carlo simulation: Comparison of the median fraction of bees (with Q1, Q3, minimum, and maximum) in the different zones **(Left, Center, Right)** at minute 30 between runs with an added social stimulus in the local optimum (blue, n=10 repetitions) and experiments without this social stimulus (red, n=10 repetitions).

stimulus compared to experiments without a social stimulus (p = 0.036, compare boxplots in **Figure 10A** left zone), while the median fraction of bees is significantly higher in the local optimum in experiments with a social stimulus (caged bees) compared to the experiments without caged bees (p = 0.009, compare boxplots in **Figure 10A** right zone); thus, the data show that a social stimulus has an influence on the overall macroscopic aggregation pattern of the bees.

To be able to predict the results of the empirical experiment with a social stimulus with our model, we had to implement an equivalent for these "caged bees." We did this by modifying our difference equation system and included an additional term that takes into account the number of stimulus bees S_l and S_r and another parameter different from X_{bee}, the "social seed" parameter X_{seed}, that acts as a weighting value for S_l and S_r. We can see these bees as being "informed agents" or acting as social "influencers" in the collective decision-making process. We assume that a stimulus bee weighs as much as a free bee in the calculations, thus X_{seed} = 1.0. The three difference equations for the three zones are being extended by introducing the following functions to the left and right zones, respectively:

$$social_l(t) = \epsilon_2(t) \cdot X_{bee} \cdot C(t) \cdot X_{seed} \cdot S_l \quad (15)$$

$$social_r(t) = \epsilon_3(t) \cdot X_{bee} \cdot C(t) \cdot X_{seed} \cdot S_r \quad (16)$$

Furthermore, while all other empirical data are based on experiments with groups of 64 bees, the experiments with caged bees were performed with groups of 24–25 bees plus five bees in the cage at the local optimum. The model was previously fitted to a group size of 64 bees and was not refitted to adapt for the smaller group size, and thus the lower population density, in the same setup.

The simulation results with the extended model solved with the forward Euler method are depicted in **Figure 10B**. To show the effect of the implemented social stimulus, we compare the results with simulations using groups of 24 bees without the social stimulus term. The median fraction of bees in the global optimum is predicted to be significantly lower in runs with a social stimulus acting at the zone with the local optimum on the opposite arena side, compared to runs without a social stimulus acting on the other side (p < 0.001, compare boxplots in **Figure 10B** left zone). The median fraction of bees is predicted to be significantly higher in the local optimum zone in runs with the social stimulus presents compared to the runs without the social stimulus (p < 0.001, compare boxplots in **Figure 10B** right zone).

The statistical analysis shows that there is no significant difference between the empirical and the model data with social stimulus in the median fraction of bees in the left zone (p = 0.734) as well as in the right zone (p = 0.273, compare **Figures 10A,B** blue data series in left zone and A and B blue data series in right zone). The prediction of the model solved with the forward Euler method is therefore quantitatively comparable to the empirical data.

The resulting distributions of 10 exemplary runs of the individual-based Monte Carlo simulation are shown in **Figure 10C**. The comparison between the results from the model solved with the forward Euler method and the individual-based Monte Carlo simulation shows that there is no significant difference between the median fraction of bees in the left zones (p = 0.623, compare boxplots of left zone in **Figures 10B,C**) or the right zones (p = 0.053, compare boxplots of right zones in **Figures 10B,C**).

4 DISCUSSION AND CONCLUSIONS

This study shows that groups of young bees, in contrast to the highly variable individual thermotactic behavior of young bees [10], reliably manage to aggregate at a global thermal optimum amongst the accessible set of options. It provides novel empirical findings about symmetry-breaking events and shows the flexibility and dynamics of the bees' collective thermotactic behavior in dynamic environments and the influence of social cues on the collective decision-making. The simple model of this collective thermotactic behavior, which was step-wise developed here (**Figure 11**), uses only one free parameter that combines all microscopic individual parameters. Despite its simplicity, the model is able to capture the bees' aggregation patterns of all

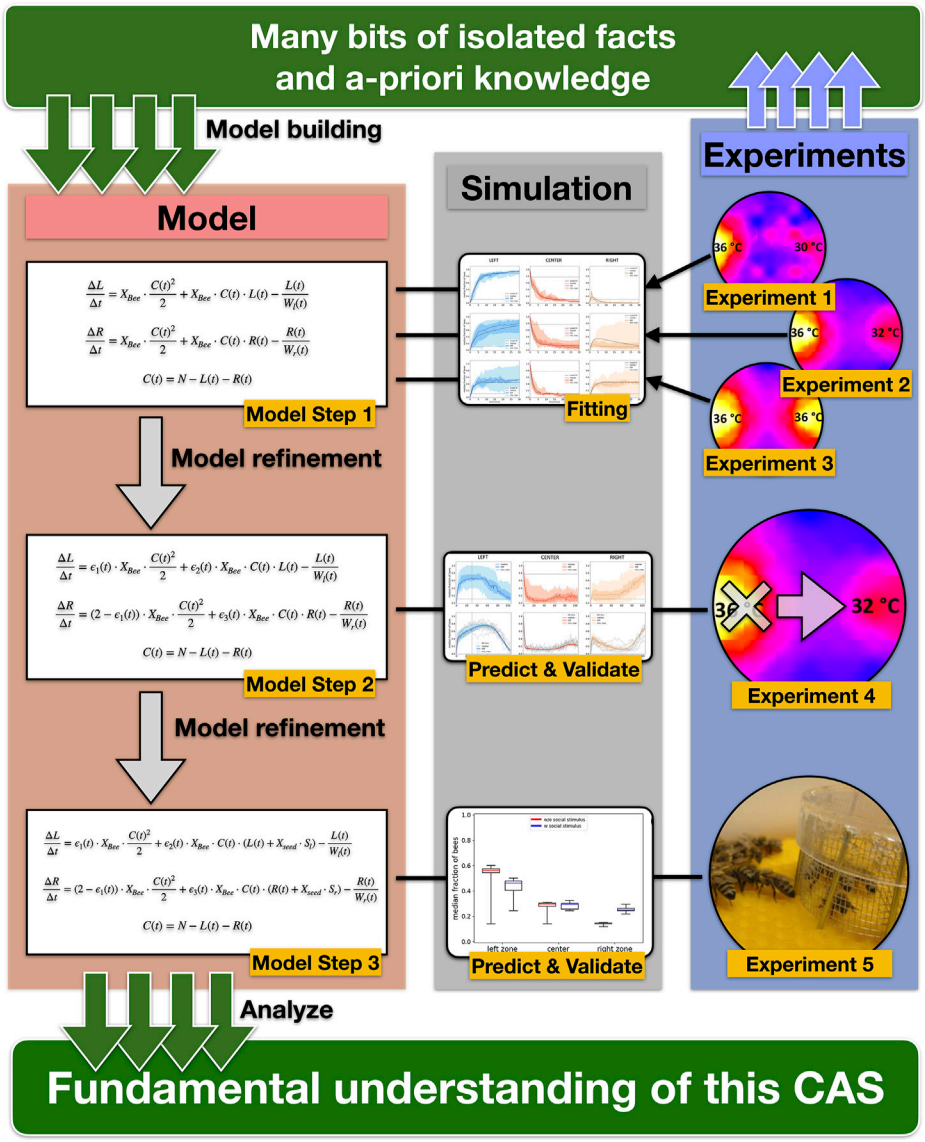

FIGURE 11 | Graphic representation of our scientific workflow and concept. Based on empiric results from laboratory experiments and a-priory knowledge (e.g., temperature-dependent waiting time), we built a simple model of the collective thermotaxis in honeybees that describe the change of the number of bees in the three zones with three coupled difference equations and combined all individual microscopic parameters into the free parameter X_{bee} in Model Step 1. We then fitted the model to data from 3 different laboratory experiments to determine a single value for the free parameter X_{bee}. After this fitting, the model was further refined by adding noise to the free parameter X_{bee} (Model Step 2). To test the predictive ability and validate the model, we compared the simulation results to a laboratory experiment with a dynamic gradient (Experiment 4) using the previously fitted value for X_{bee}. In Model Step 3, we introduced the "social seed" parameter X_{bee} to simulate caged bees equivalent to Experiment 5. Starting with single empirical facts, we gained a fundamental understanding of the CAS by gradually developing our model and using subsequent empirical experiments to validate previous model building steps.

tested scenarios. The model shows that the prerequisites for explaining the abilities of the bee collective by means of social interactions are much smaller than an equally well-performing individual problem-solving would require. Thus, the observed behavior is a clear candidate for a phenomenon known as "swarm intelligence" [5, 27–29]. This phenomenon has aspects of emergence and exhibits interesting micromacro bridging at its core, a simple model to describe such systems is therefore of great value.

The empirical data show that local optima do not trap a significant amount of bees; thus, we can reject that the bees simply perform an individual uphill walk in the temperature gradient. In addition, we deduce from our experiments with two equal optima in the environment an informative result: The analysis of the individual runs shows that the bees sometimes exhibit strong symmetry breaking and collectively choose one of the two equally favorable options. Such symmetry breaking is, for example, known to happen in choice experiments with ants, where

small random variations in trail laying are amplified and lead to a collective choice for one of two identical shelter options [6]. We assume a similar effect in our focal honeybee system: Whenever more bees randomly move to one side of the arena, more small initial aggregations may emerge faster on this side than on the other and increase the probability of additional bees joining there. Furthermore, empirical research on the individual motion behavior in this experimental setting (e.g., tracking individual trajectories) will be necessary to learn more about the prerequisites for symmetry breaking in this system.

We further showed the adaptability of the collective thermotaxis in honeybees in dynamic environments as the bees were capable of selecting a previously neglected less warm place when the environment changed. This shows that bees are not exclusively searching for their thermal optimum of 36°C, but instead dynamically and adaptively choose the best available option in their environment at a given time collectively, while they simultaneously try to stay together as a group. This is demonstrated by introducing a "social seed" to bias the group decision: Although the bees usually would choose the warmest area in the environment, an additional social stimulus unfolds a significant influence onto the overall collective behavior and ultimately has a tendency of drawing the bees to a comparably suboptimal temperature zone. The caged bees can exert some sort of direct physical influence, e.g., *via* olfactory or ground-vibrational cues. Additionally, they also exert some indirect influence *via* the system's behavioral feedback loops, e.g., by increasing the stopping probability. Such effects have also been observed in swarms of robots that perform similar behavioral programs [19]. Analogous to our experiments, some immobile robots are placed at a local optimum. These immobile robots simply increase the stopping probability there, what induces a similar change in the macroscopic swarm behavior without the need of emitting any additional cues. This indicates that no direct influence from the caged bees is necessary, just their plain local presence was sufficient to emphasize local behavioral feedback loops to draw the group to the local temperature optimum. Although the robot swarm example shows that communication *via* direct signal exchange is not necessary to achieve such effects, the bees could still exchange signals, e.g., to achieve a faster or more stable effect. Also, more indirect density-dependent amplifiers are possible. The temperature-dependent waiting time could be additionally modulated by cluster size, as it was shown for the aggregation behavior of cockroaches [30]. A bee could wait increasingly longer the more bees it is surrounded by, what would further stabilize aggregations as soon as a certain number of bees are aggregated.

The results of our experiments suggest that the ability to solve the given sets of problems cannot be explained by simple individual behavioral programs such as a simple gradient ascent, probabilistic choosing, or a specific temperature threshold. Thus, solving the problem on an individual level would require a sophisticated behavior, assuming several sophisticated (cognitive) abilities: good sensor discrimination, memory, self-localization in the environment (map making), and the ability to choose individually from multiple options.

Rejecting complex individual behaviors and looking into simple collective behaviors are the core motivation of the model that we have built and have, based on empirical validation experiments, refined here in several steps (see **Figure 10**). Our simulations show that a simple model of interactions amongst the bees is sufficient to capture the observed collective macroscopic behavior through a few simple assumptions about the mechanisms operating on the microscopic system level. Under the assumption of social interaction, purely random motion and modulating the resting behavior after a bee-to-bee contact suffice to explain all the observed collective behavioral patterns in all tested environments, which are a significant step in the understanding of a natural complex adaptive system, such as a honeybee colony. With only one free parameter, which we call the "social factor" (X_{bee}), both modeling approaches, the mean-field approach of the model solved with the forward Euler method and the individual-based Monte Carlo simulation, were capable of qualitatively and for the most part also quantitatively predicting the emerging flexible group-level behavior of the bees in a complex dynamic environment. The free parameter was exclusively fitted with data from static environments, and both modeling approaches used the same parameter value, what shows an interesting generality of our model. The only addition that was necessary to model the dynamic environmental setting was not in the model of the bees but in the model of the environment: It was required to develop an additional temperature decay function. While the individual-based Monte Carlo simulation better captured the variance in the empirical data, the model solved with the forward Euler method more accurately predicted the overall macroscopic behavior when compared to the empirical data.

Quantitative differences between the results from empirical and simulation experiments, especially in the variance can be attributed to the following factors: While the empirical data show some fluctuations in the set temperatures in our setup (±1°C, as shown in [9], **Figure 2**), we used idealized temperature gradient fields in the model. With no noise acting on the waiting time, all bees joining a zone in the same time step will therefore have the exact same waiting time, making the idealized system more reactive. In experiment 5, the differences can additionally be attributed to the different group sizes used in the experiments and the model. As the free parameter, X_{bee} integrates several microscopic individual parameters that have an influence on density-dependent processes in the system (e.g., stopping probability after contact with another bee), changes in the initial setting of the model runs, like the group size, can lead to quantitatively different outcomes. Another important difference between the empirical system and the difference equation model is the fact that in the model, the bees are considered to be volumeless points in space. Thus, in the model, an infinite number of bees can squeeze themselves into an infinitely small amount of space, while in reality, target spots can get saturated. In addition, in reality, clusters can form everywhere in the arena and block the path of bees towards better places. Furthermore, physiological aspects, like depleting energy reserves of individual bees that could lead to increased

resting times, especially in dynamic environments, are not taken into account in the model. It can therefore be the case that special, more complex collective behaviors cannot be represented with these simple models' abstraction of the bee behavior and mean-filed approximation. We show with our implementation of an individual-based Monte Carlo simulation a better representation of the variance and diversity concerning the macroscopic collective behavior. Thus, a multi-agent model with complex state machines [31, 32] or neural networks [33] to control the agent's behaviors could be the better approach for depicting more complex situations. This would however require a full reversal of the model-building strategy. Additionally, environmental factors and beehive physics, such as acoustics and chemical and thermal interactions with older bees, would then have to be implemented, what may increase the degree of complexity by several orders of magnitude.

Besides the fundamental basic research aspect, studying such systems is of additional importance: Honeybees are under severe ecological stress today, and this is endangering their wide-spread role as ecosystem-service providers (pollination). Our model enables us to predict the effects of a physical stimulus onto the macroscopic collective decision-making such as the process of preparing cells for the egg-laying of the queen, which is performed by young bees at the same age as our experimental bees. We found that the local abundance of such cell-preparing bees is affected by the local temperature conditions. In the brood nest, the local temperature conditions are actively regulated (again collectively) by older bees, and this collective thermoregulation is also influenced by the temperatures outside of the hive. Ultimately, understanding how temperature fields can affect the self-localization of young bees is a crucial aspect of understanding brood production and colony population growth in times of climate change. There is also an application aspect to be considered here: Understanding the complex adaptive system at the core of honeybee colonies can help in designing novel smart beehives, in which technological devices are capable of producing exactly these physical stimuli and may thus exert a regulatory support for colonies in distress, e.g., by motivating them to keep up brood production in adverse environments or colony situations. We see this as a potential cornerstone in developing modern "smart beehives" that go beyond mere sensing by actively promoting the stability and robustness of the colony [34, 35].

DATA AVAILABILITY STATEMENT

The raw data supporting the conclusions of this article will be made available by the authors, without undue reservation.

AUTHOR CONTRIBUTIONS

TS implemented the first version of the difference equation model and contributed significantly to the planning of this study. He also advised and mentored the other authors in the course of the research and the paper writing. The mathematical models were further elaborated by VS and MS. MS, TS, VS, and GR wrote the article together in a collaborative effort. Experiment 1: conducted by GR and analyzed by GR and MS; Experiments 2, 3, and 4: conducted and analyzed by MS; Experiment 5: analyzed by MS. Statistical analyses were made by MS. Model data were analyzed by VS. **Figures 1–3** were conceived and implemented by MS. **Figures 4–10** were conceived and implemented by VS and MS. **Figure 11** was conceived and implemented by TS.

FUNDING

This work was supported by the Field of Excellence Complexity of Life in Basic Research and Innovation (COLIBRI) at the University of Graz, the Austrian Science Fund research grant P19478-B16, the EU H2020 FET-Proactive project HIVEOPOLIS (no. 824069), and the EU ICT project ASSISIbf (no. 601074).

REFERENCES

1. Gell-Mann M. Complex Adaptive Systems. In: G Cowan, D Pines, and D Metzer, editors. *Complexity: Metaphors, Models, and Reality*. Reading, MA: Addison-Wesley (1994). p. 17–45.
2. Levin SA. Ecosystems and the Biosphere as Complex Adaptive Systems. *Ecosystems* (1998) 1:431–6. doi:10.1007/s100219900037
3. Holland JH. Complex Adaptive Systems. *Daedalus* (1992) 121:17–30.
4. Bonabeau E. Social Insect Colonies as Complex Adaptive Systems. *Ecosystems* (1998) 1:437–43. doi:10.1007/s100219900038
5. Bonabeau E, Dorigo M, and Théraulaz G. *Swarm Intelligence: From Natural to Artificial Systems*. Oxford University Press (1999).
6. Camazine S, Franks NR, Sneyd J, Bonabeau E, Deneubourg JL, and Theraula G. *Self-Organization in Biological Systems*. Princeton University Press (2001).
7. Moritz RFA, and Fuchs S. Organization of Honeybee Colonies: Characteristics and Consequences of a Superorganism Concept. *Apidologie* (1998) 29:7–21. doi:10.1051/apido:19980101
8. Lewin R. *Complexity: Life at the Edge of Chaos*. University of Chicago Press (1999).
9. Szopek M, Schmickl T, Thenius R, Radspieler G, and Crailsheim K. Dynamics of Collective Decision Making of Honeybees in Complex Temperature fields. *PLoS One* (2013) 8:e76250. doi:10.1371/journal.pone.0076250
10. Kengyel D, Hamann H, Zahadat P, Radspieler G, Wotawa F, and Schmickl T. Potential of Heterogeneity in Collective Behaviors: A Case Study on Heterogeneous Swarms. In: International Conference on Principles and Practice of Multi-Agent Systems Proceedings; Bertinoro, Italy; October 26–30, 2015 Springer (2015). p. 201–17. doi:10.1007/978-3-319-25524-8_13
11. Stabentheiner A, Kovac H, and Brodschneider R. Honeybee Colony Thermoregulation - Regulatory Mechanisms and Contribution of Individuals in Dependence on Age, Location and Thermal Stress. *PLoS one* (2010) 5:e8967. doi:10.1371/journal.pone.0008967
12. Becher MA, and Moritz RFA. A New Device for Continuous Temperature Measurement in Brood Cells of Honeybees (apis Mellifera). *Apidologie* (2009) 40:577–84. doi:10.1051/apido/2009031
13. Menzel R, and Backhaus W. Color Vision Honey Bees: Phenomena and Physiological Mechanisms. In: DG Stavenga and RC Hardie, editors. *Facets of Vision*. Berlin Heidelberg: Springer (1989). p. 281–97. doi:10.1007/978-3-642-74082-4_14
14. Seeley TD. Adaptive Significance of the Age Polyethism Schedule in Honeybee Colonies. *Behav Ecol Sociobiol* (1982) 11:287–93. doi:10.1007/bf00299306

15. Scheiner R, Abramson CI, Brodschneider R, Crailsheim K, Farina WM, Fuchs S, et al. Standard Methods for Behavioural Studies ofApis Mellifera. *J Apicultural Res* (2013) 52:1–58. doi:10.3896/IBRA.1.52.4.04
16. Heran H. Untersuchungen über den Temperatursinn der Honigbiene (Apis mellifica) unter besonderer Berücksichtigung der Wahrnehmung strahlender Wärme. *Z für vergleichende Physiologie* (1952) 34:179–206.
17. Kernbach S, Thenius R, Kernbach O, and Schmickl T. Re-embodiment of Honeybee Aggregation Behavior in an Artificial Micro-robotic System. *Adaptive Behav* (2009) 17:237–59. doi:10.1177/1059712309104966
18. Mills R, Zahadat P, Zahadat P, Silva F, Mlikic D, Mariano P, Schmickl T, and Correia L. Coordination of Collective Behaviours in Spatially Separated Agents. In: Proceedings of the ECAL 2015: the 13th European Conference on Artificial Life; York, United Kingdom; July 20–24, 2015 MIT Press (2015). p. 579–86. doi:10.7551/978-0-262-33027-5-ch101
19. Schmickl T, and Hamann H. Beeclust: A Swarm Algorithm Derived from Honeybees. In: Y Xiao and F Hu, editors. *Bio-inspired Computing and Communication Networks*. Boca Raton, London, New York: CRC Press (2011). p. 95–137.
20. Schmickl T, Thenius R, Moeslinger C, Radspieler G, Kernbach S, Szymanski M, et al. Get in Touch: Cooperative Decision Making Based on Robot-To-Robot Collisions. *Auton Agent Multi-agent Syst* (2009) 18:133–55. doi:10.1007/s10458-008-9058-5
21. Lotka AJ. *Elements of Physical Biology*. Baltimore: Williams & Wilkins (1925).
22. Volterra V. Fluctuations in the Abundance of a Species Considered Mathematically1. *Nature* (1926) 118:558–60. doi:10.1038/118558a0
23. Verhulst PF. Recherches mathématiques sur la loi d'accroissement de la population. *J des Économistes* (1845) 12:276.
24. Smale S. On the Differential Equations of Species in Competition. *J Math Biol* (1976) 3:5–7. doi:10.1007/BF00307854
25. Kermack WO, and McKendrick AG. A Contribution to the Mathematical Theory of Epidemics. *Proc R Soc Lond A* (1927) 115:700–21. doi:10.1098/rspa.1927.0118
26. Palsson BO, and Lightfoot EN. Mathematical Modelling of Dynamics and Control in Metabolic Networks. I. On Michaelis-Menten Kinetics. *J Theor Biol* (1984) 111:273–302. doi:10.1016/S0022-5193(84)80211-8
27. Millonas MM. Swarms, Phase Transitions, and Collective Intelligence. In: C Langton, editor. *Swarms, Phase Transitions, and Collective Intelligence*. Reading, MA: Addison-Wesley (1993).
28. Eberhart RC, Shi Y, and Kennedy J. *Swarm Intelligence*. Elsevier (2001).
29. Schranz M, Di Caro GA, Schmickl T, Elmenreich W, Arvin F, Şekercioğlu A, et al. Swarm Intelligence and Cyber-Physical Systems: Concepts, Challenges and Future Trends. *Swarm Evol Comput* (2021) 60:100762. doi:10.1016/j.swevo.2020.100762
30. Jeanson R, Rivault C, Deneubourg J-L, Blanco S, Fournier R, Jost C, et al. Self-organized Aggregation in Cockroaches. *Anim Behav* (2005) 69:169–80. doi:10.1016/j.anbehav.2004.02.009
31. Schmickl T, Thenius R, and Crailsheim K. Swarm-intelligent Foraging in Honeybees: Benefits and Costs of Task-Partitioning and Environmental Fluctuations. *Neural Comput Applic* (2012) 21:251–68. doi:10.1007/s00521-010-0357-9
32. Schmickl T, and Crailsheim K. Costs of Environmental Fluctuations and Benefits of Dynamic Decentralized Foraging Decisions in Honey Bees. *Adaptive Behav* (2004) 12:263–77. doi:10.1177/105971230401200311
33. Schmickl T, Zahadat P, and Hamann H. Wankelmut: A Simple Benchmark for the Evolvability of Behavioral Complexity. *Appl Sci* (2021) 11:1994. doi:10.3390/app11051994
34. Schmickl T, Szopek M, Mondada F, Mills R, Stefanec M, Hofstadler DN, et al. Social Integrating Robots Suggest Mitigation Strategies for Ecosystem Decay. *Front Bioeng Biotechnol* (2021) 9:612605. doi:10.3389/fbioe.2021.612605
35. Ilgün A, Angelov K, Stefanec M, Schönwetter-Fuchs S, Stokanic V, Vollmann J, et al. Bio-hybrid Systems for Ecosystem Level Effects. In: Artificial Life Conference 2021 Proceedings; Virtual (formerly Prague, Czech Republic); July 19–23, 2021 MIT Press (2021).

Conflict of Interest: The authors declare that the research was conducted in the absence of any commercial or financial relationships that could be construed as a potential conflict of interest.

Publisher's Note: All claims expressed in this article are solely those of the authors and do not necessarily represent those of their affiliated organizations, or those of the publisher, the editors and the reviewers. Any product that may be evaluated in this article, or claim that may be made by its manufacturer, is not guaranteed or endorsed by the publisher.

frontiers in Physics

ORIGINAL RESEARCH
published: 01 November 2021
doi: 10.3389/fphy.2021.735438

A Computational Study of Hydrodynamic Interactions Between Pairs of Sperm With Planar and Quasi-Planar Beat Forms

Lucia Carichino[1]*, *Derek Drumm*[2] *and Sarah D. Olson*[2]

[1]School of Mathematical Sciences, Rochester Institute of Technology, Rochester, NY, United States, [2]Department of Mathematical Sciences, Worcester Polytechnic Institute, Worcester, MA, United States

Although hydrodynamic interactions and cooperative swimming of mammalian sperm are observed, the key factors that lead to attraction or repulsion in different confined geometries are not well understood. In this study, we simulate the 3-dimensional fluid-structure interaction of pairs of swimmers utilizing the Method of Regularized Stokeslets, accounting for a nearby wall via a regularized image system. To investigate emergent trajectories of swimmers, we look at different preferred beat forms, planar or quasi-planar (helical with unequal radii). We also explored different initializations of swimmers in either the same plane (co-planar) or with centerlines in parallel planes. In free space, swimmers with quasi-planar beat forms and those with planar beat forms that are co-planar exhibit stable attraction. The swimmers reach a maintained minimum distance apart that is smaller than their initial distance apart. In contrast, for swimmers initialized in parallel beat planes with a planar beat form, we observe alternating periods of attraction and repulsion. When the pairs of swimmers are perpendicular to a nearby wall, for all cases considered, they approach the wall and reach a constant distance between swimmers. Interestingly, we observe sperm rolling in the case of swimmers with preferred planar beat forms that are initialized in parallel beat planes and near a wall.

Keywords: method of regularized stokeslets, sperm motility, hydrodynamic interactions, image systems, quasi-planar beatforms, collective motion

OPEN ACCESS

Edited by:
Laura Ann Miller,
University of Arizona, United States

Reviewed by:
Charles Wolgemuth,
University of Arizona, United States
Wanda Strychalski,
Case Western Reserve University, United States

***Correspondence:**
Lucia Carichino
lcsma1@rit.edu

Specialty section:
This article was submitted to Social Physics, a section of the journal Frontiers in Physics

Received: *02 July 2021*
Accepted: *27 September 2021*
Published: *01 November 2021*

Citation:
Carichino L, Drumm D and Olson SD (2021) A Computational Study of Hydrodynamic Interactions Between Pairs of Sperm With Planar and Quasi-Planar Beat Forms. Front. Phys. 9:735438. doi: 10.3389/fphy.2021.735438

1 INTRODUCTION

The tumultuous journey of the mammalian sperm involves navigating the female reproductive tract. Even though millions of sperm are deposited at the beginning of the tract, only a select few are able to traverse the long distances and overcome all of the hurdles to make it to the egg [1, 2]. Using a single flagellum, sperm progress through a wide range of environments and their motility patterns must change in response to various chemical and physical cues; this could act to group sperm together or separate them [3–5]. A sperm senses other nearby sperm and surfaces via hydrodynamic interactions, which results in a wide range of collective motion, from alignment in trains and vortices to synchronization and attraction [6–8].

Sperm are able to propel themselves through different fluid environments by bending their elastic and flexible flagellum or tail. Within the flagellum, dynein is the molecular motor that actively generates force along the length of the flagellum, which results in a bending wave [2, 9–11]. The emergent beat form and trajectory will depend on the local fluid environment and the particular

species of sperm. In experiments, emergent planar, helical, and quasi-planar flagellar beat forms have been observed, with planar beat forms more likely in higher viscosity fluids [10, 11]. Similarly, tracking of sperm trajectories has shown linear trajectories as well as helical trajectories [12, 13].

Surface interactions play an important role of many micro-organisms, including sperm swimming in the reproductive tract [6, 14]. Once sperm reach the oviduct, they generally bind to the epithelial cell wall and remain in this sperm reservoir until the time of ovulation [15]. At ovulation, signaling molecules such as heparin or progesterone will increase in concentration and will aid in the release of the sperm from the oviductal wall [15–17]. Likely, these signaling molecules will either act to break bonds of the cell body with the wall or bind to the flagellum and initiate a different beat form that will aid in generating increased force to break away from the wall [18, 19]. There are many interesting and unanswered questions as to how sperm get to the walls, how long they stay at the walls, as well as how the sperm reservoir could act as a filter to sort out healthy sperm [20, 21]. Investigations with microfluidic channels have revealed that sperm guidance can be achieved with surface topography and microchannels [22, 23].

There are many different modeling approaches that can be taken to model sperm motility, but one of the key ingredients is how the sperm cell itself is being represented. Simplified approaches neglect the head or cell body [24–26]; headless sperm can still swim and previous analysis has shown that neglecting the cell body results in similar dynamics [27, 28]. Other studies have focused on capturing accurate cell body geometries to investigate the role on swimming and interactions [29–31]. Similarly, when accounting for the bending of the flagellum, there are a few options. One can actuate or drive the dynamics of the flagellum with forces or torques corresponding to a curvature wave [24, 32], prescribe a preferred curvature that is utilized in an energy functional that determines forces [25, 26, 33], or exactly prescribe the beat form [29–31]. When the beat form is prescribed exactly, the swimmer may rotate, but the flagellum will always have its entire centerline in the same plane and it will always have the same beat form parameters (e.g., amplitude and beat frequency). Preferred beat forms will have emergent beat forms based on interactions with other swimmers and/or surfaces.

To date, there have been many studies that have investigated the 3-dimensional (3D) dynamics of a single sperm near a wall [10, 19, 34]. Wall attraction was observed when approaching at specific angles, including perpendicular to the wall. Similarly, there have been studies of pairs of swimmers in free space to study the dynamics of attraction since biologically, most sperm are not swimming in isolation [24–26, 31]. Since there has not been a detailed study of the interactions of pairs of swimmers near a wall, our goal is to further investigate and characterize how pairwise interactions vary from free space to the case where the sperm are swimming in close proximity and perpendicular to a planar wall. Using the method of regularized Stokeslets with an image system to account for the wall, we study swimmers propagating both preferred planar and quasi-planar beat forms. The dynamics of attraction and repulsion of swimmers is explored through different configurations; we vary both the initial distance between the sperm as well as the planes in which the swimmers are initialized. Our results show that sperm will attract to and stay near the wall while phenomenon such as sperm rolling will occur for a subset of sperm configurations. Our results further contextualize divergent results for pairs of swimmers in previous studies and provides insight into relevant interactions that can be utilized in the development of artificial micro-swimmers [35–37].

2 MATERIALS AND METHODS

2.1 Mathematical Model

We utilize a fluid-structure interaction framework where the sperm is assumed to be neutrally buoyant and immersed in the fluid. Since sperm swim in viscosity dominated environments and are often in close proximity to a wall or boundary [2, 38], we will consider the 3-dimensional (3D) incompressible Stokes equations for the fluid velocity $\boldsymbol{u}$ above a planar wall at $x = \mathcal{W}$:

$$\mu\Delta\boldsymbol{u}(\boldsymbol{x}) = \nabla p - \boldsymbol{f}_b(\boldsymbol{x}), \qquad \nabla\cdot\boldsymbol{u} = 0, \qquad \{\boldsymbol{x}|x > \mathcal{W}\}, \tag{1}$$

subject to the boundary condition $\boldsymbol{u}(\boldsymbol{x})|_{x=\mathcal{W}} = \boldsymbol{0}$. Here, μ is the viscosity, p is the pressure, and $\boldsymbol{f}_b$ is the sperm body force density exerted on the fluid as the flagellum actively bends. That is, the hydrodynamic stresses are coupled to the bending of the flagella; the fluid "feels" the swimmers through $\boldsymbol{f}_b$ and the swimmers "feel" each other through the fluid.

To determine the body forces, we will study a simplified representation of a sperm cell where we neglect the cell body, similar to previous studies of [32, 39]. Additionally, we assume the sperm flagellum is isotropic and homogeneous with constant radius much smaller than length L so that we can represent it using the Kirchhoff Rod (KR) model. This allows for each cylindrical elastic flagellum ι to be represented via a space curve $\boldsymbol{X}_\iota(t, q)$ for arc length parameter q $(0 \le q \le L)$. Local twisting is accounted for via a right-handed orthonormal triad, $\boldsymbol{D}_\iota(t, q) = \{\boldsymbol{D}_\iota^1, \boldsymbol{D}_\iota^2, \boldsymbol{D}_\iota^3\}$. We briefly summarize the model here and refer the reader to [39–42] for additional details.

In the KR model, through a variational energy argument, we can define the internal force $\boldsymbol{F}_\iota$ and torque $\boldsymbol{M}_\iota$ on a cross section of flagellum ι as $\boldsymbol{F}_\iota = \sum_{i=1}^3 F_\iota^i \boldsymbol{D}_\iota^i$ and $\boldsymbol{M}_\iota = \sum_{i=1}^3 M_\iota^i \boldsymbol{D}_\iota^i$, respectively. The scalar components of the force and torque in the Darboux frame are defined as:

$$F_\iota^i = b_i\left(\boldsymbol{D}_\iota^i \cdot \frac{\partial \boldsymbol{X}_\iota}{\partial q} - \delta_{3i}\right),\ M_\iota^i = a_i\left(\frac{\partial \boldsymbol{D}_\iota^j}{\partial q}\cdot \boldsymbol{D}_\iota^k - \hat{\kappa}_i\right),\ i = 1, 2, 3, \tag{2}$$

where δ_{3i} is the Kronecker delta and F_ι^i, M_ι^i are defined for any cyclic permutation of (i, j, k). The physical properties of the flagellum determine the moduli (a_1, a_2-bending, a_3-twisting, b_1, b_2-shearing, b_3-stretching); the stiffness of sperm flagella can be measured experimentally and related to these moduli [43, 44]. The preferred kinematics can be described by the preferred twist $\hat{\kappa}_3$, normal curvature $\hat{\kappa}_1$, and geodesic curvature $\hat{\kappa}_2$ [45, 46]. In

this formulation, there will be no torque when the flagellum is in its preferred shape, which we will now define.

Sperm propagate bending along the length of the flagellum due to the coordinated action of molecular motors inside the flagellum [2, 47]. We can capture a range of beat forms representative of experimental observations [9, 10] by assuming that the flagella have the preferred configuration of

$$\hat{\boldsymbol{X}}(q,t) = (x(q,t), \alpha \sin(\eta x(q,t) - \omega t), \beta \cos(\eta x(q,t) - \omega t)), \tag{3}$$

with beat frequency $f = \omega/2\pi$, wavelength $2\pi/\eta$, and beat amplitudes α and β. Planar bending of the flagellum occurs when either α or β are zero whereas quasi-planar bending occurs when $\alpha, \beta \neq 0$ and either $\alpha < \beta$ or $\beta < \alpha$. We note that we are not prescribing a rotation of the flagellum; we simply actuate or drive it to beat (and bend) in this preferred planar or quasi-planar configuration that is a function of arc length parameter q and time t. Similarly, these are the initialized and preferred configurations that can deviate later in the simulation due to interactions with other swimmers and/or the wall. Utilizing this preferred configuration, we can calculate the preferred orthonormal triad $\hat{\boldsymbol{D}}(t,q)$ by setting $\hat{\boldsymbol{D}}^3$ as the tangent to $\hat{\boldsymbol{X}}$, and choosing $\hat{\boldsymbol{D}}^1$ as the normal and $\hat{\boldsymbol{D}}^2$ as the binormal vector. Then, the preferred curvature and twist can be calculated as

$$\hat{\kappa}_i(q,t) = \left(\frac{\partial \hat{\boldsymbol{D}}^j}{\partial q}\right) \cdot \hat{\boldsymbol{D}}^k, \tag{4}$$

which is a spatiotemporal function based on $\hat{\mathbf{X}}(q,t)$ in **Eq. 3**.

For this configuration, we impose force and torque balance along the length of the flagellum. That is, the fluid feels the sperm through a force per unit length $\boldsymbol{f}_\iota$ and torque per unit length $\boldsymbol{m}_\iota$ [only defined on $\boldsymbol{X}_\iota(q,t)$],

$$\mathbf{0} = \boldsymbol{f}_\iota + \frac{\partial \boldsymbol{F}_\iota}{\partial q}, \qquad \mathbf{0} = \boldsymbol{m}_\iota + \frac{\partial \boldsymbol{M}_\iota}{\partial q} + \left(\frac{\partial \boldsymbol{X}_\iota}{\partial q} \times \boldsymbol{F}_\iota\right). \tag{5}$$

The body force $\boldsymbol{f}_{b_\iota}$ in **Eq. 1** will be equal and opposite to the internal forces of the flagellum and will also need to be a smooth force field on the fluid domain with finite velocities on $\boldsymbol{X}$. Hence, we will set

$$\boldsymbol{f}_{b_\iota}(\boldsymbol{x}) = -\int_{\Gamma_\iota} \left(\boldsymbol{f}_\iota \psi_\varepsilon(r) + \frac{1}{2}(\nabla \times \boldsymbol{m}_\iota)\phi_\varepsilon(r)\right) dq, \tag{6}$$

where $\Gamma_\iota = \boldsymbol{X}_\iota(q,t)$, $\boldsymbol{x}$ is any point in the 3D domain with $x > \mathcal{W}$ and $r = \|\boldsymbol{x} - \boldsymbol{X}\|$. The regularization functions ψ_ε and ϕ_ε are radially symmetric, satisfying $\int_{\mathbb{R}^3} \psi_\varepsilon(r) d\boldsymbol{x} = \int_{\mathbb{R}^3} \phi_\varepsilon(r) d\boldsymbol{x} = 1$, and smooth the singular force field with parameter ε governing the region where most of the force is spread [48, 49]. In this model, each sperm flagellum will have a preferred configuration $\hat{\boldsymbol{X}}$ and $\hat{\boldsymbol{D}}(q,t)$, but its ability to achieve that configuration will depend on the local fluid flow through a no-slip condition,

$$\frac{\partial \boldsymbol{X}_\iota(q,t)}{\partial t} = \boldsymbol{u}(t, \boldsymbol{X}_\iota(q,t)),$$
$$\frac{\partial \boldsymbol{D}_\iota^i(q,t)}{\partial t} = \boldsymbol{w}(t, \boldsymbol{X}_\iota(q,t)) \times \boldsymbol{D}_\iota^i(q,t), \qquad i = 1,2,3, \tag{7}$$

where $\boldsymbol{w} = \frac{1}{2}\nabla \times \boldsymbol{u}$ is the angular velocity.

2.2 Numerical Method

We discretize each of the $\mathfrak{m}$ flagella into $\mathfrak{p}$ points and use standard second order central finite difference approximations to determine forces and torques in **Eqs 2**, **5**. The body force in **Eq. 6** is approximated using the trapezoidal rule. In free-space, utilizing the linearity of **Eq. 1**, the flow can be written as a superposition of regularized fundamental solutions (regularized due to the smoothing of the body force in **Eq. 6**). Since we are interested in the flow above a wall at $x = \mathcal{W}$, we utilize a regularized image system that first accounts for the resulting flow in $\mathbb{R}^3$ (no wall) and then cancels the flow at the wall $x = \mathcal{W}$ through combinations of fundamental solutions at additional image points on the other side of the wall (outside of the half space of interest). Let $\boldsymbol{X}_{\ell_\iota} = (x_{\ell_\iota}, y_{\ell_\iota}, z_{\ell_\iota})$ be the ℓ-th discretized point on the ι-th flagellum, $h_{\ell_\iota} = x_{\ell_\iota} - \mathcal{W}$ the height above the wall, and $\boldsymbol{X}_{\ell_\iota}^{im} = (-h_{\ell_\iota}, y_{\ell_\iota}, z_{\ell_\iota})$ the image point of $\boldsymbol{X}_{\ell_\iota}$. The linear velocity $\boldsymbol{u}$ is

$$\boldsymbol{u}(\boldsymbol{x}) = \frac{1}{\mu} \sum_{\iota=1}^{\mathfrak{m}} \sum_{\ell=1}^{\mathfrak{p}} \left(S_{\psi_\varepsilon}\left[\boldsymbol{\xi}_{f,\ell_\iota}, r_{\ell_\iota}\right] + R_{\phi_\varepsilon}\left[\boldsymbol{\xi}_{n,\ell_\iota}, r_{\ell_\iota}\right] + S^{im}_{\psi_\varepsilon,\phi_\varepsilon}\left[\boldsymbol{\xi}_{f,\ell_\iota}, r_{\ell_\iota}, r^{im}_{\ell_\iota}\right] + R^{im}_{\psi_\varepsilon,\phi_\varepsilon}\left[\boldsymbol{\xi}_{n,\ell_\iota} \boldsymbol{X}^{im}_{\ell_\iota}\right] \right), \tag{8}$$

where $r_{\ell_\iota} = \|\boldsymbol{x} - \boldsymbol{X}_{\ell_\iota}\|$, $r^{im}_{\ell_\iota} = \|\boldsymbol{x} - \boldsymbol{X}^{im}_{\ell_\iota}\|$, $\boldsymbol{\xi}_{n,\ell_\iota} = -\xi \boldsymbol{m}_{\ell_\iota}$, $\boldsymbol{\xi}_{f,\ell_\iota} = -\xi \boldsymbol{f}_{\ell_\iota}$, and ξ is the quadrature weight. S and R denote the fundamental solutions for a point force and point torque, corresponding to the Stokeslet and Rotlet, respectively, and the subindex refers to the particular regularization function that is being utilized to smoothly spread the force or torque in **Eq. 6**. $S^{im}_{\psi_\varepsilon,\phi_\varepsilon}$ and $R^{im}_{\psi_\varepsilon,\phi_\varepsilon}$ are the regularized image systems for the Stokeslet and Rotlet. Via a direct calculation, $\boldsymbol{w} = \frac{1}{2}\nabla \times \boldsymbol{u}$ for $\boldsymbol{u}$ in **Eq. 8**. As detailed previously in [50, 51]; [34], we set the regularization functions as

$$\psi_\varepsilon(r) = \frac{15\varepsilon^4}{8\pi(r^2+\varepsilon^2)^{7/2}}, \qquad \phi_\varepsilon = \frac{3\varepsilon^2}{4\pi(r^2+\varepsilon^2)^{5/2}}, \tag{9}$$

which ensures that the boundary condition at the wall is satisfied, $\boldsymbol{u}|_{x=\mathcal{W}} = \mathbf{0}$. Additionally, this ensures that the regularized image system in **Eq. 8** satisfies the property that in the limit as $\varepsilon \to 0$, the singular image system is recovered.

To solve this coupled fluid-structure interaction, at each time point t, we complete the above steps to determine the resulting linear and angular velocity due to a given flagellar configuration (assuming the preferred configuration in **Eqs 3**, **4**). Once the velocity of the flagellum, $\boldsymbol{u}$ ($\boldsymbol{X}_\iota$), and angular velocity of the triads, $\boldsymbol{w}$ ($\boldsymbol{D}_\iota$), are known, we determine the new flagellar location and triads at time $t + \tau$ by solving the no-slip equations in **Eq. 7** with the forward Euler method. This process is repeated, solving for the new instantaneous flow due to each time-dependent force balance equation, which depends on the emergent flagellar configurations. We emphasize that this is a Lagrangian method; only the flagella are discretized. Through the regularized image system in **Eq. 8**, we automatically satisfy that the wall at $x = \mathcal{W}$ has zero velocity. Additionally, we can evaluate **Eq. 8** at any point of interest in the fluid domain.

2.3 Quantifying Interactions of Swimmers

The actual beat form, swimming speed, and trajectory that the sperm achieves is an emergent property of the coupled system that depends

TABLE 1 | Computational parameters for preferred planar (P) and quasi-planar (Q) beat forms.

Parameter	Value for P and Q
Arc length, L (μm)	60 for P, Q
Points on flagellum, $\mathfrak{p}$	301 for P, Q (equispaced)
Regularization parameter, ε (μm)	5 △ q for P, Q
Amplitude, α (μm)	3 for P, Q
Amplitude, β (μm)	0 for P, 1 for Q
Wavelength, $2\pi/\eta$ (μm)	30 for P, Q
Beat frequency, $f = \omega/2\pi$ (Hz)	20 for P, Q
Bending modulus, $a_1 = a_2$ (g μm^3 s^{-2})	1 for P, Q
Twisting modulus, a_3 (g μm^3 s^{-2})	1 for P, Q
Shear modulus, $b_1 = b_2$ (g μm s^{-2})	0.6 for P, Q
Stretch modulus, b_3 (g μm s^{-2})	0.6 for P, Q
Time step, τ (s)	10^{-6} for P, Q
Viscosity, μ (g μm^{-1} s^{-1})	10^{-6} for P, Q

on both the geometry of the swimmers and the wall, fluid parameters such as viscosity, beat form parameters, as well as stiffness or moduli of the flagella. We will explore these dynamic and nonlinear relations through simulations. Here we highlight some of the metrics and different parameters that are studied.

The sperm number is a non-dimensional number that characterizes the ratio of viscous fluid effects to elastic effects of the bending flagellum, computed as

$$S_p = \left(\frac{f\chi L^4}{a_1}\right)^{1/4}, \quad \chi = \frac{4\pi\mu}{\ln(2L/\varepsilon)}. \tag{10}$$

Here, L is the flagellum length, f is the beat frequency (inverse time), ε is the regularization parameter that approximates the flagellum radius, μ is fluid viscosity, and a_1 is the bending modulus. To compare to previous studies, we utilize the resistive force theory coefficient χ to capture viscous effects, similar to [32]. For mammalian sperm, previous estimates have had S_p in the range of 2–17 [2]. Using the values reported in **Table 1**, the baseline sperm number for our simulations is $S_p = 5.11$. We explore increasing S_p to a value of 7.64 by increasing μ to 5μ and increasing S_p to 9.08 by increasing μ to 10μ. Similarly, we also explore increasing S_p by setting a_i to $a_i/5$ or $a_i/10$ for $i = 1, 2, 3$. Even though this leads to the same sperm number, we explore the differences since a change in μ changes the magnitude of all terms in **Eq. 8** whereas a change in a_i only changes the magnitude of the terms involving the torque, which can be seen from **Eq. 2**.

Through interactions, the beating planes of swimmers may continue to deviate from the plane they were initialized in. A diagram of the directions of pitching and/or rolling out of the beating plane is given in **Figure 1**. The beating plane is calculated as the plane that passes through the center of mass $\bar{\boldsymbol{X}} = \frac{1}{\mathfrak{p}}\sum_{\ell=1}^{\mathfrak{p}} \boldsymbol{X}_\ell$ of the swimmer and minimizes the orthogonal distances between the points on the flagellum and the plane [26, 52]. The pitching angle θ of the swimmer's beating plane is the angle between the plane and the unitary vector in the x-direction $\mathbf{e}_x$,

$$\theta = 90^\circ - \arccos\left(\frac{\mathbf{n}\cdot\mathbf{e}_x}{|\mathbf{n}|}\right), \tag{11}$$

where $\mathbf{n}$ is the normal vector to the beating plane. The pitching angle θ is in the range $[-90^\circ, 90^\circ]$ and $\theta > 0$ ($\theta < 0$) corresponds to the plane pitching upward (downward). The rolling angle γ of the swimmer's beating plane is the angle between the plane and the unitary vector in the y-direction $\mathbf{e}_y$,

$$\gamma = 90^\circ - \arccos\left(\frac{\mathbf{n}\cdot\mathbf{e}_y}{\|\mathbf{n}\|}\right). \tag{12}$$

The rolling angle γ is also in the range $[-90^\circ, 90^\circ]$ and $\gamma > 0$ ($\gamma < 0$) corresponds to the plane rolling right (left) with respect to the direction of motion.

3 RESULTS AND DISCUSSION

The aim of this study is to further quantify and understand the hydrodynamic interactions of pairs of swimmers close to or far away from a wall. To do this, we will consider a few different scenarios that include planar or quasi-planar beat forms initialized a distance d apart. For the case of planar beat forms, we also consider the case of flagellar beating with centerlines initialized in parallel planes or the same plane (co-planar). The wall is either initialized at $x = -5$ (near a wall) or at $x = -10{,}000$, which we denote as the free space solution since the wall has negligible effects on swimming at this location. The baseline parameters used for the numerical methods and preferred beat form are given in **Table 1**; we assume that in a given simulation, all sperm flagella have the same preferred configuration given by **Eqs 3**, **4**, with values in the range of mammalian sperm [10]. Swimmers are separated by a distance d in either the y or z-directions. We explore distances d in the range of 3–30 μm, i.e., distances where there is non-negligible flow effects from the nearby swimmer. Here, 30 μm is half the length of the swimmer (L = 60 μm) and 3 μm is equal to the beat amplitude α.

3.1 Co-Planar Swimmers

This case involves two planar swimmers ($\alpha = 3$ and $\beta = 0$ in **Eq. 3**) initialized such that their initial beating planes are in the plane $z = 0$, shifted a distance d apart in the y-direction. That is, the average y-value, $\bar{y}$, is set at $\bar{y} = 0$ for the bottom swimmer and $\bar{y} = d$ for the top swimmer.

3.1.1 Free Space

Figure 2A shows the configuration of two co-planar sperm cells at time $t = 0$ (gray dashed lines) and at time $t = 0.6$ s (gray solid lines) for swimmers initialized $d = 6$ μm apart. The first point is represented by a solid gray circle and denotes the cell body and swimming direction. The trajectories of the first point during this time frame (blue and black solid lines) show the hydrodynamic attraction of the two sperm cells; the top sperm starts to go down and attract to the bottom sperm, which is swimming with an upward trajectory. We classify this movement as yaw since these motions remain within the plane $z = 0$, which has been observed in other modeling work for a single swimmer [29, 30, 34]. A solo swimmer has an upward yaw [34], but attraction dominates and

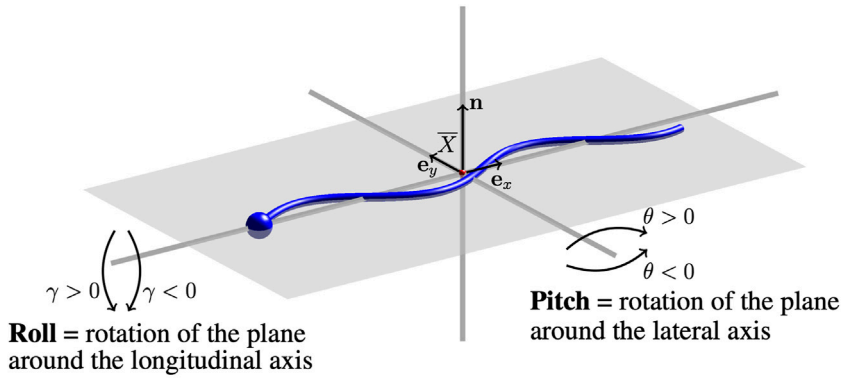

FIGURE 1 | Pitching and Rolling of Flagellar Beating Planes. A sketch of the swimmer (blue) and the beating plane (gray). Changes in the initial beating plane are characterized by a pitching angle θ and rolling angle γ. The center of mass of the swimmer $\bar{X}$ is represented by a small red sphere at the origin. The normal vector to the beating plane is $\mathbf{n}$, and $\mathbf{e}_x$ and $\mathbf{e}_y$ are the unitary vectors in the x and y direction, respectively. In this sketch, $\theta = \gamma = 0$ since the beating plane is in the plane $z = 0$.

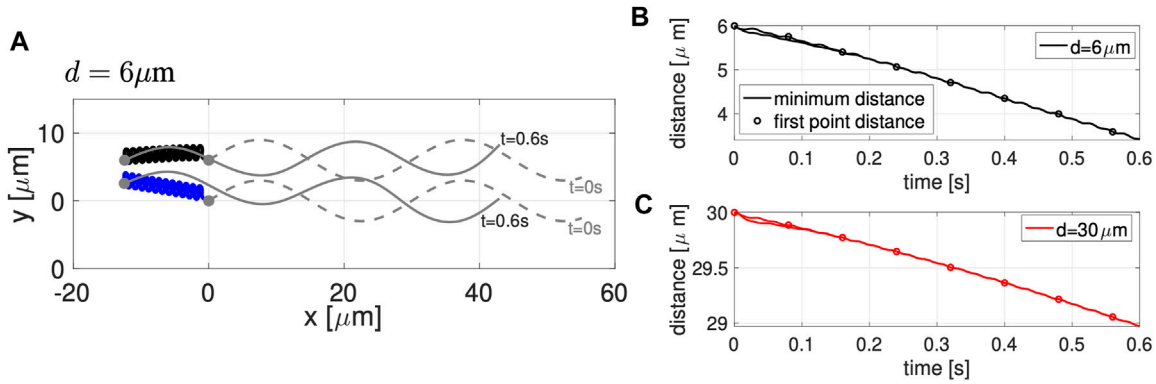

FIGURE 2 | Co-Planar Sperm in Free Space. **(A)** Swimmer configurations with planar preferred beat forms at $t = 0$ s (dashed gray lines) and $t = 0.6$ s (solid gray lines), and traces of the first point on the swimmer in time (blue and black solid lines) for the initial separation distance of $d = 6$ μm. Minimum distance between the two sperm (solid lines) and distance between the first points of the two swimmers (circles) in time, for initial distances $d = 6$ μm **(B)** and $d = 30$ μm **(C)**. Distances reported are the average over a beat period.

allows the top swimmer to have a downward yaw and attract to the bottom swimmer. This attraction is also in agreement with previously published theoretical and experimental studies [24–26, 31, 33, 53].

Figures 2B,C track the minimum distance between the two sperm (solid lines) and the distance between the first points of the two sperm (circles) as a function of time, for the initial distances d considered. In both cases, for $d = 6$ and $d = 30$ μm, we observe a monotonic decrease in the distance between the sperm for this initial time period of attraction, similar to results of [26]. Even though the sperm are initialized at the same distance d apart along the entire flagellum, the minimum distance between the sperm cells occurs at the head (first point). For longer time simulations, we continue to observe attraction, reaching a steady configuration of flagella that are a very small distance apart. We do not show simulations or report this distance since a repulsion term is required to keep the filaments from occupying the same space and hence, the steady state distance between the flagella will depend on the strength and form of the repulsion term.

We also varied the sperm number S_p (given in **Eq. 10**); similar dynamics of attraction were observed but on a slower time scale (results not shown). As previously noted in [32], for a solo swimmer, increasing S_p results in a decreased swimming speed. We observe a similar decrease for a pair of swimmers with increased S_p, which leads to the increased time scale for attraction to occur.

Previous studies with planar beat forms required to stay in the plane have reported an increase in swimming speeds for pairs of swimmers relative to the case of a solo swimmer when filaments propagate planar beat forms, are co-planar, and the flagella are sufficiently stiff [25]. Other studies that allow beat forms to deviate from the plane have reported a slowdown of swimming speed while swimmers attract [26]. For the parameters utilized in **Figure 2** (reported in **Table 1**), we observe a decrease in swimming speed for a pair of swimmers initialized $d = 6$ μm apart and a small increase in swimming speed for a pair of swimmers initialized $d = 30$ μm. The speeds reported in **Table 2** are looking at the magnitude of velocity of the first

point on the flagellum by utilizing locations at time $t = 0$ and $t = 0.6$ s; for two swimmers, the speed is the average over both swimmers. We do not observe a significant increase in swimming speed during the attraction phase for a range of initial separation distances. However, on longer time intervals after attraction has occurred, we do observe an increase in swimming speed (results not shown).

TABLE 2 | Swimming speeds in free-space for the preferred planar (*P*) beatform in co-planar or parallel beating planes and quasi-planar (*Q*) beat forms, comparing the two sperm configuration initialized d apart to the solo sperm.

Configuration	Two sperm		Solo sperm
	Initial distance	Speed [μm/s]	Speed [μm/s]
Co-planar (*P*)	d = 6 μm	20.95	28.04
	d = 30 μm	28.85	
Parallel planes (*P*)	d = 5 μm	28.82	28.04
	d = 30 μm	28.01	
Quasi-planar (Q)	d = 6 μm	20.70	23.60
	d = 30 μm	23.61	

3.1.2 Near a Wall

We have shown that our model can capture a range of known phenomena for a pair of swimmers in free space, but sperm are not swimming in isolation and they are swimming in close proximity to walls as they navigate the female reproductive tract [2, 5]. Hence, we wish to go beyond previous studies of a pair of swimmers in free space or a solo swimmer near a wall to understand whether the wall will help or hinder attraction of swimmers. For a solo swimmer, simulations have shown attraction to a wall is immediate but no yawing motion or vertical translation (up or down with respect to the centerline of the flagellum) is observed [34]. We note that for a solo swimmer initialized perpendicular to the wall, it will always attract to the wall regardless of whether it starts 2 μm or 50 μm away (the wall does not cause the swimmer to tilt and escape the wall). The questions are now 1) will additional sperm change the dynamics of attraction to a wall; 2) will swimmers near a wall still be able to attract to each other; 3) if attraction occurs,

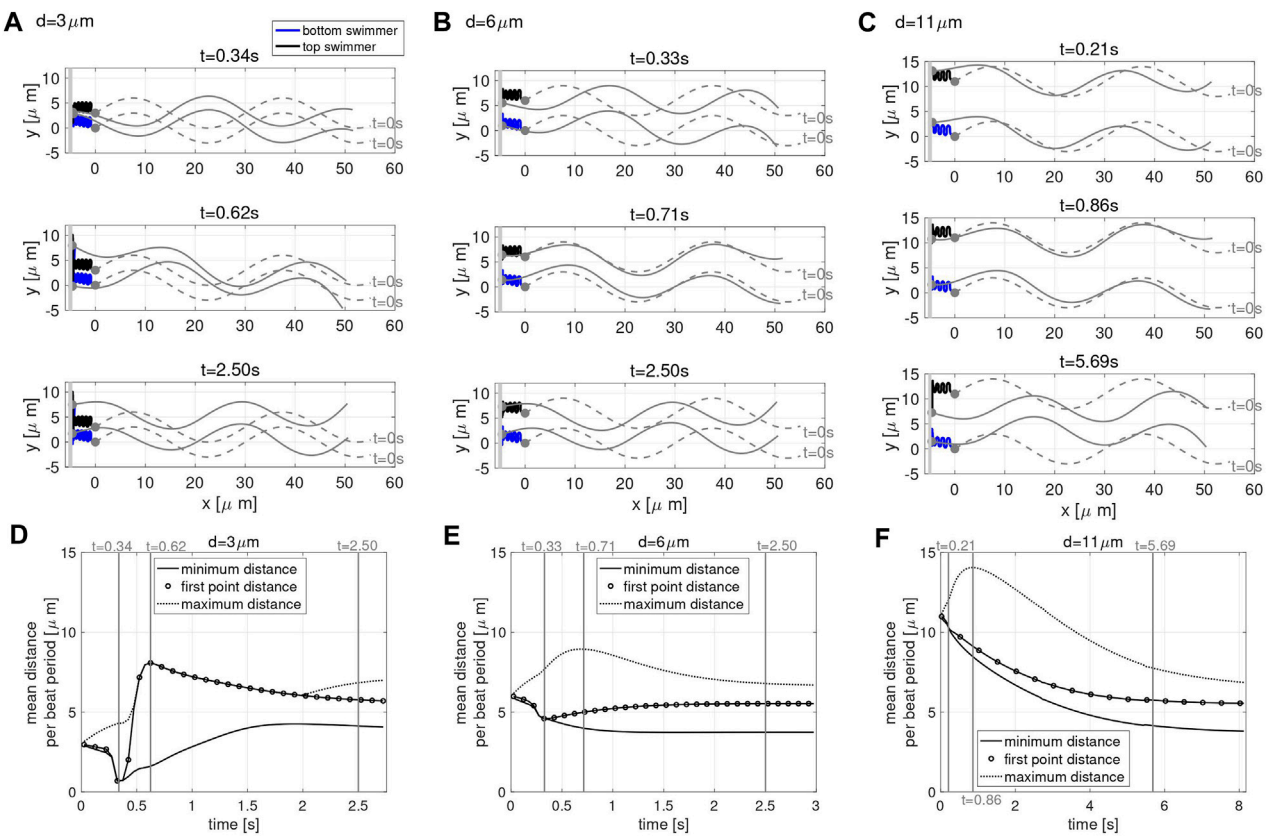

FIGURE 3 | Co-Planar Sperm Near a Wall. Swimmer configurations with planar preferred beat forms at $t = 0$ s (dashed gray lines) and at three snapshots in time (solid gray lines) for the initial distance $d = 3$ μm **(A)**, $d = 6$ μm **(B)** and $d = 11$ μm **(C)** with a planar wall at $x = -5$ μm. The traces of the first point on the swimmer are shown (blue and black solid lines). The time-dependent distance between swimmers is characterized in **(D)**–**(F)**. For initial swimmer distances of $d = 3$ μm **(D)**, $d = 6$ μm **(E)** and $d = 11$ μm **(F)**, the minimum (solid line), maximum (dashed line), and first point distance (circles) are reported as averages over each beat period. The times chosen to report the swimmer configurations for each value of d **(A–C)** are identified with vertical gray lines in the corresponding distance graphs **(D–F)**. The thick gray vertical line in **(A–C)** represents the wall.

will it happen with heads decreasing their distance apart at a faster rate (similar to **Figures 2B,C**)?

To study these questions, we consider the case of two co-planar swimmers initialized at a distance d apart and perpendicular to a planar wall at $x = -5$ μm. **Figure 3** shows the configurations of the swimmers at time $t = 0$ (gray dashed lines) and at three snapshots in time (gray solid lines), for the initial distance of $d = 3$ μm in **A**, $d = 6$ μm in **B**, and $d = 11$ μm in **C**. The first point of the swimmer is represented by a solid gray circle and the trace of this point (from $t = 0$ until the time point given in that panel) is shown with the solid lines. For all values of d considered, the swimmers start with the head 5 μm away from the wall and rapidly attract to the wall, remaining close to the wall for the full time of the simulation (over 2.5 s).

In order to explore the rich dynamics of swimmers near a wall, we also report the minimum (solid line) and maximum (dotted line) distance between the two swimmers, along with the average distance between the first points of the two swimmers (circles) in **Figure 3**, for initial distance $d = 3$ μm in **D**, $d = 6$ μm in **E** and $d = 11$ μm in **F**. The snapshots in time in **A–C** are identified with vertical gray lines in the corresponding distance graphs in **D–F**, and were chosen to highlight specific points of interest. The top panel in **Figures 3A–C** is the last time point for which the distance between the first points equals the minimum distance between the swimmers, i.e., the end of the first attraction period between the two swimmers where the heads are moving closer. The middle panel in **Figures 3A–C** is where the maximum distance between the swimmers is at a maximum. The stable configuration achieved by the swimmers is shown in the bottom panel in **Figures 3A–C**. Here, we are defining stable as attaining an average distance between points on the swimmer that persists in time. The same preferred beat form is given for all swimmers in all of these simulations; the presence of the wall and the initial separation distance is what causes the different beat forms to emerge. We note that two swimmers in free space attract, with the top swimmer yawing down and the bottom swimmer yawing up (**Figure 2B**). The dynamics of the nearby wall prevent the swimmers to attract with equal yawing due to the emergent flagellar beat forms.

For all the values of d considered, the stable configuration achieved toward the end of the simulation (third snapshot) consists of an average first point distance of approximately 5.5 μm, in between the maximum and minimum average distance between the swimmers. As shown in **Figures 3A,D**, for an initial distance d smaller than 6 μm, the swimmer's first points initially attract, reaching a minimum distance on the order of 1 μm at $t = 0.34$ s, then repulse reaching the maximum average distance of approximately 8 μm at $t = 0.62$ s (with the top swimmer moving up). Due to hydrodynamic interactions of the swimmer and the close wall, even though the swimmers have centerlines that are parallel, we observe a dramatic yaw in the top swimmer as the head of the top swimmer is pushed up. Later, the swimmers reach a stable configuration after 2.50 s where flagellar centerlines are again parallel. For an initial distance d equal to 6 μm, shown in **Figures 3B,E**, the head of the swimmers (first point) attract up until $t = 0.33$ s, reaching a distance of approximately 4.5 μm. After this initial attraction, the heads of the swimmer then repulse, reaching a maximum distance 9 μm apart at $t = 0.71$ s, and reach the stable configuration after 2.50 s. For an initial distance d greater than 6 μm, **Figures 3C,F**, the maximum distance of 14 μm between the swimmers is reached at $t = 0.86$ s and the distance between the first points show a continuous decrease in time until reaching a plateau and the stable configuration after 5.69 s. In this last scenario, the top swimmer, after reaching the wall, is moving downward to get closer to the bottom swimmer, clearly visible in **Figure 3C** at $t = 5.69$ s. The asymmetry between the swimmer's behavior is due to the direction of motion chosen. When the direction of motion is reversed (wall at $x = 5$, swimmers reflected about the y-axis, and preferred beat form propagating a wave in the opposite direction with $-\omega$), we observe the bottom swimmer moving upward to get closer to the top swimmer (results not shown).

To explore competing effects of wall attraction and swimmer dynamics, we vary the sperm number S_p in **Eq. 10**. **Figure 4** shows the swimmer configurations obtained for the different values of S_p considered in the case of two co-planar swimmers near a wall, varying μ in **A**,**B**,**E** and varying a_i in **C**,**D**,**F**. Increasing S_p means that the viscous effects are increasing relative to the elastic effect. As a result, in both **Figures 4A–D**, increasing S_p exhibits a beat form with decreased achieved amplitude. In **A**,**B**, this is due to the increased viscosity of the fluid creating additional drag on the bending flagellum whereas in **C**,**D**, this is due to the decrease in the bending moduli making the flagellum less stiff and less able to propagate bending at the preferred amplitude. Even though the achieved amplitude of the flagellar beat form decreases, this does not prevent or slow down attraction to the wall (shown in zoomed views in **B** and **D**). Through a close examination of the distance between the swimmers at different time points, we can see the subtle differences between increasing S_p via increasing μ in **Figure 4E** and decreasing a_i in **Figure 4F**. The baseline value of $S_p = 5.11$ exhibits attraction and then repulsion with the heads being further apart than the rest of the flagellum at later time points (**Figures 4E,F**) and reaching a steady state configuration by $t = 2$ s. In contrast, if an increase in S_p to 7.64 or 9.08 is obtained by increasing μ by a factor 5 or 10, the swimmers do not maintain a stable configuration near the wall, but they continue to attract with the heads being the closest points at later time points (**Figure 4E**). Increased S_p in **Figure 4E** results in continued attraction whereas increased S_p in **Figure 4F** results in a quasi steady state configuration at $t = 2$ s.

We emphasize that for all simulations presented here for co-planar swimmers near a wall, the swimmers had a preferred planar configuration. With swimmer interactions and the presence of the wall, there was some out of plane motion, but on average, the swimmers tended to maintain a beat form in the same plane (due to torques in **Eq. 2** that penalize deviations from the preferred motion). Additionally, for all simulations, the head or first point of the swimmers attract to the wall and maintains a small distance away from the wall. This occurs for a range of parameters in the case of two swimmers and also occurs on a similar time scale to that of a solo swimmer [34]. For a sperm number of $S_p = 5.11$, in the range for mammalian sperm, we observe swimmers reaching a somewhat steady state distance of

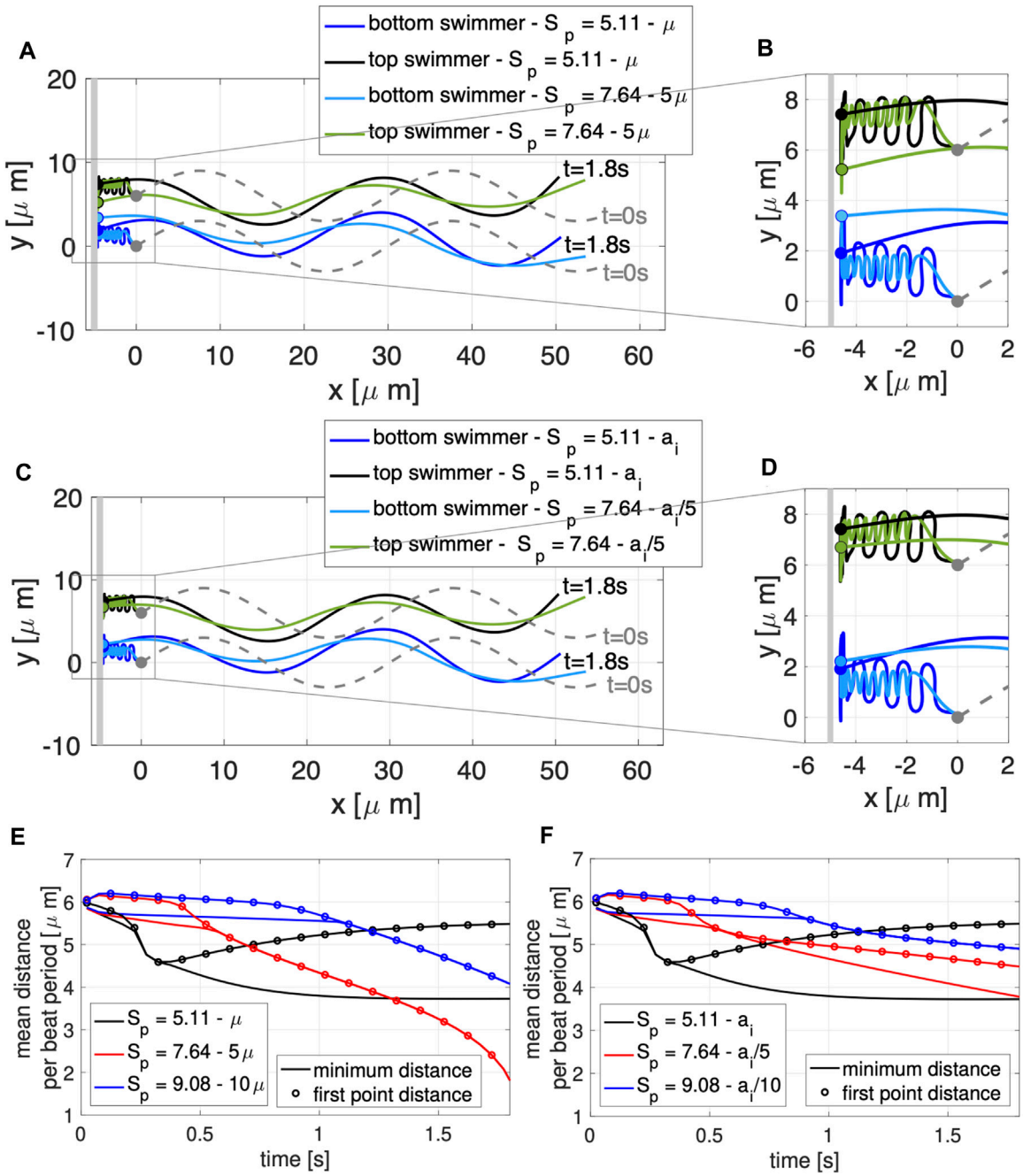

FIGURE 4 | Varying Sperm Number: Co-Planar Sperm Near a Wall. Swimmers with planar preferred beat forms are initialized a distance d = 6 μm apart with a planar wall at x = –5 μm. Configurations at t = 0 s (gray dashed lines) and t = 1.8 s (colored solid lines) are shown along with traces of the first point on the flagellum for varying fluid viscosity in **(A)**, with zoomed in view in **(B)**, and varying flagellar material parameters a_i in **(C)**, with zoomed in view in **(D)**. The thick gray vertical line in **(A)**–**(D)** represents the wall. The minimum distance between the two swimmers (solid lines) and distance between the first points of the two swimmers (circles) are shown as averages over a beat period, varying μ in **(E)** and a_i in **(F)**.

~5.5 μm within a few seconds when starting in the same plane at a distance of 3–11 μm apart. Since the beat frequency of the swimmers is set to f = 20 Hz; attraction on the order of seconds near the wall requires hundreds of beats of the flagellum. The dynamics of attraction will depend on the sperm number and increased S_p (increased viscous forces) results in sperm being able to attract closer at the first point or cell body. This is important to consider since the epithelial cells on the oviductal walls may be secreting proteins and/or fluids that will change the viscosity near the walls [54] and potentially control or dominate emergent interactions and motility of sperm [55].

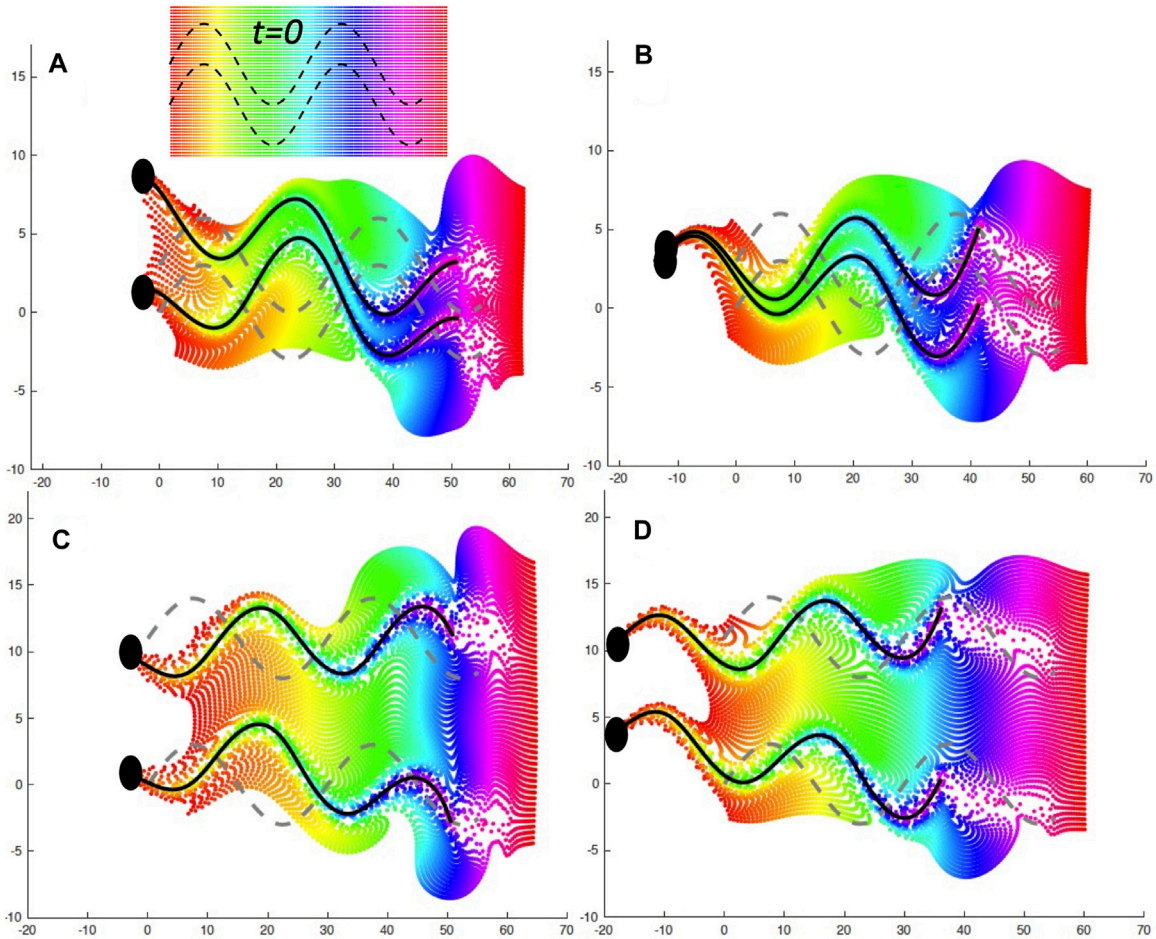

FIGURE 5 | Fluid Mixing by Co-Planar Swimmers. A plane of fluid markers was initialized at $t = 0$ with $x \in [0, 60]$ and either $y \in [-4, 7]$ when $d = 3$ μm or $y \in [-4, 16]$ when $d = 11$ μm, as shown on the inset in **(A)**; fluid markers are colored by initial x-value. The fluid markers are advected by the flow and are shown at later time points with the same color as at $t = 0$. **(A)**: $d = 3$ μm and a nearby wall at $x = -5$ at $t = 0.882$ s, **(B)**: $d = 3$ μm and free space at $t = 0.804$ s, **(C)**: $d = 11$ μm and a nearby wall at $x = -5$ at $t = 0.882$ s, **(D)**: $d = 11$ μm and free space at $t = 0.804$ s. The gray dashed lines correspond to the initial location at $t = 0$ and the solid black lines correspond to the flagellar configurations at the specified time point.

3.1.3 Fluid Mixing

It is well known that as mammalian sperm navigate through the female reproductive tract, their motility patterns change in response to different signaling molecules, which may be released from the wall or be present in the entire fluid [2, 3, 5]. When sperm are trapped on the oviductal walls, signaling molecules such as heparin or progesterone initiate changes in motility by binding to the cell body or the flagellum [15, 16]. In turn, changes to asymmetrical beating occur, which aids in the release of these trapped sperm [15–17, 19]. The ability for these molecules to reach the sperm and bind to receptors is highly dependent on the local fluid flows. In **Figure 5**, we look at the mixing of the fluid by the swimmers in the case of an initial separation of $d = 3$ μm in **A**,**B** and a separation of $d = 11$ μm in **C**,**D**. The left hand side (**A**,**C**) is the case of the wall at $x = -5$ μm where as the right hand side is the free space case (**B**,**D**). For each plot, the initialization is a plane of passive fluid markers (in the plane of the swimmers at $t = 0$), similar to the inset in **A**. We initialize these locations and track their movement by solving **Eq. 8** for their velocity due to the moving swimmers and update the fluid marker locations using **Eq. 7**. Similar to the swimmers in **Figures 2**, **3**, the fluid particles initialized in this plane remain mostly in the plane. In all of the cases in **Figure 5**, we observe a region at the end of the flagella that is empty. These fluid particles have traveled with the swimmer and can be seen along the flagella. Due to the beat form of the flagella, we observe fluid markers that were originally a vertical stripe that have moved and now taken on a range of x-values. For example, the yellow fluid particles were initialized at $x \sim 9$–10 μm and are now in the approximate range of $x = -5$ to 20 μm in **D**. We observe significant movement in both directions for this x − location; this means that signaling molecules can get close to the flagella if being passively advected by the flow that the flagella are generating.

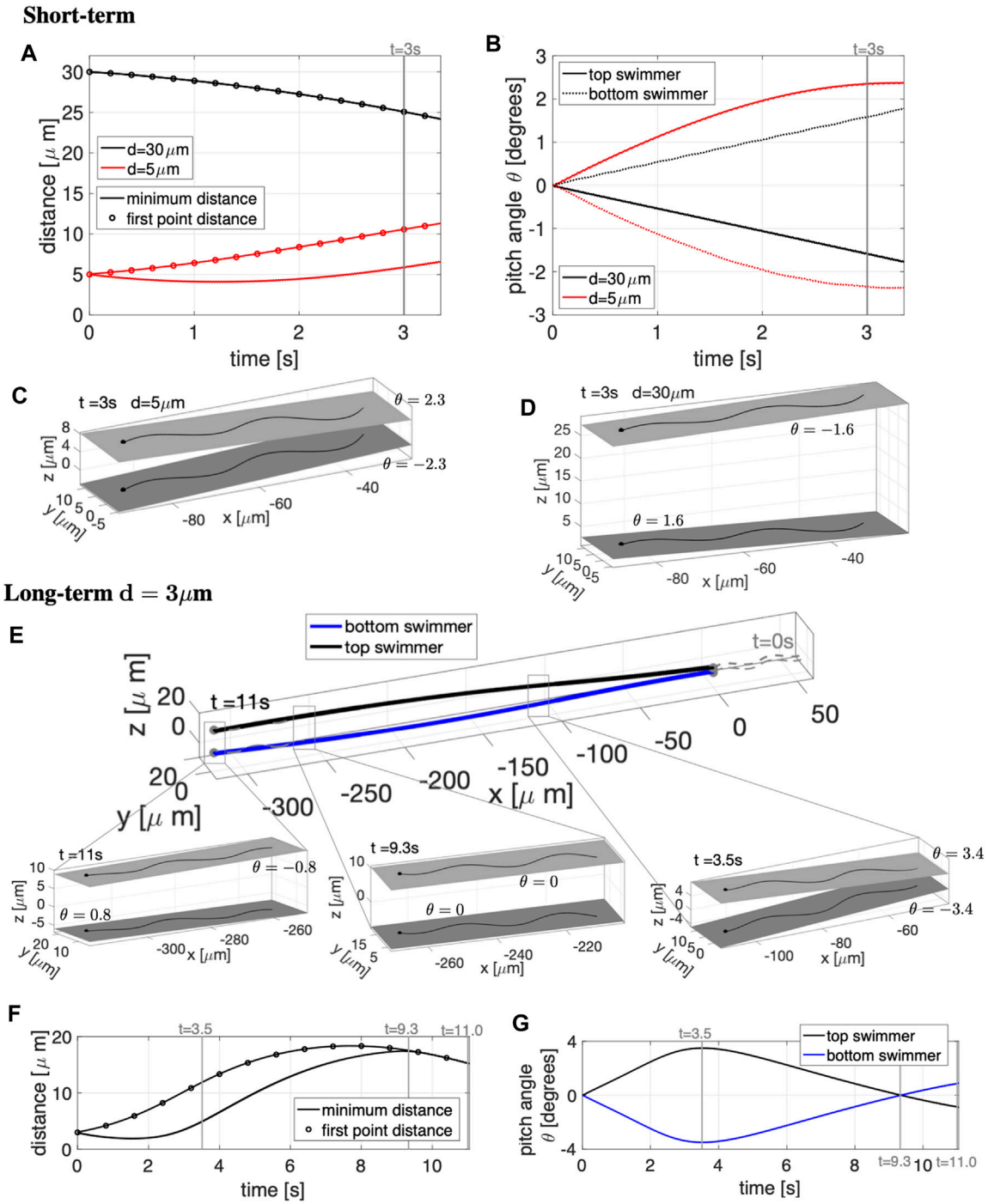

FIGURE 6 | Parallel Sperm in Free Space. Short-term behavior for initial distances d = 5, 30 μm **(A–D)** and long-term behavior for d = 3 μm **(E–G)** for swimmers initialized in parallel beating planes. Minimum distance between the two swimmers (solid lines) and distance between the first points of the two swimmers (circles) in time, for initial distances d = 5, 30 μm in **(A)** and d = 3 μm in **(F)**. Pitching angle θ of the beating planes of the **top and bottom** swimmers in time, for initial distances d = 5, 30 μm in **(B)** and d = 3 μm in **(G)**. **Top** and **bottom** swimmer's beating planes and pitching angles θ for d = 5 μm in **(C)** and d = 30 μm in **(D)** at time t = 3 s. **(E)** Swimmer configurations at t = 0 s (gray dashed lines) and traces of the swimmers initial points in time (colored solid lines). **Top** and **bottom** swimmer's beating planes and pitching angles θ for three snapshots in time are reported in the corresponding zoomed portions. The times chosen for the zoomed portions of **(E)** are identified with vertical gray lines in **(F,G)**. In **(C,D,E)**, a filled in sphere is used to denote the swimmer first point in the direction of motion.

3.2 Parallel Swimmers

We continue to consider the case of two planar swimmers ($\alpha = 3$ and $\beta = 0$ in **Eq. 3**), but now these swimmers are initialized with parallel beating planes. The distance d between the swimmers is initialized by placing the bottom swimmer in the plane $z = 0$ and the top swimmer in the plane $z = d$. However, the emergent beat plane may pitch upward or downward in the z-direction and/or roll left or right around the lateral axis (refer to **Figure 1** for a schematic). Similar to the co-planar case, we wish to first benchmark our model and further explore the case of swimmers far away (free space) or close to a wall to understand how these dynamics change.

3.2.1 Free Space

The results in the case of free space are reported in **Figure 6**. The short-term simulations, up to $t = 3.25$ s, are shown in **Figures 6A–D**. A non-monotonic behavior depending on the initial distance d between the swimmer's beating planes is observed. For $d = 5$ μm, the distance between the first points of the two swimmers increases in time (**Figure 6A**) while the rest of the swimmers slightly attract and then slowly increase their distance. The beating plane of the bottom swimmer pitches downward while the top swimmer pitches upward by angles of $\pm 2.3^{\circ}$ at $t = 3$ s (**Figures 6B,C**), corresponding to the swimmers pushing away from each other. In contrast, for $d = 30$ μm, the distance between the first points of the two swimmers decrease in time (**Figure 6A**), attracting with the beating plane of the bottom swimmer pitching upward and the top swimmer pitching downward with angles of $\pm 1.6^{\circ}$ (**Figures 6B,D**). In the shorter time simulations (**Figures 6A–D**), the beating plane of both swimmers have a minimal rolling motion, alternating between left and right rolling with $-0.26^{\circ} \leq \gamma \leq 0.26^{\circ}$ for $d = 5$ μm and $-0.14^{\circ} \leq \gamma \leq 0.14^{\circ}$ for $d = 30$ μm.

In terms of the swimming speeds for these shorter term dynamics over 3 s, the swimming speed of two parallel swimmers was similar to the corresponding solo swimmer (**Table 2**). This is similar to previous results for pairs of swimmers separated by a distance of at least half their length, swimming speeds are similar to that of a solo swimmer [24, 26, 31]. However, we observe marked differences between swimmers that are co-planar and those that are in parallel planes. At an initial separation distance of $d = 6$ μm, the swimmers in parallel planes are significantly faster (~28 μm/s) than the case of the co-planar swimmers (~20 μm/s).

To investigate the long-term dynamics, we look at an initial separation of $d = 3$ μm for $t = 0$–11 s in **Figures 6E–G**. The zoomed in portions of **Figure 6E** show the top and bottom swimmer's beating planes and corresponding pitching angles θ for the three snapshots in time, delineating the switches among near-field, mid-field and far-field dynamics. The times of the snapshot are identified with vertical gray lines in **Figures 6F,G**. The swimmers show near-field repulsion until $t = 3.5$ s, i.e., with heads or first points increasing in separation (**Figure 6F**) and beating planes pitching away from each other (**Figure 6G** and right-most zoomed portion of **Figure 6E**). The top and bottom swimmer's beating planes obtain their maximum pitching angle at $t = 3.5$ s and after $t = 3.5$ s, the swimmers enter the mid-field regime where they will continue to repel each other (**Figure 6F**) but the pitching angles will decrease in magnitude (**Figure 6G**) and reach $\theta \simeq 0$ at $t = 9.3$ s (central zoomed portion of **Figure 6E**). After $t = 9.3$ s, the swimmers show far-field attraction, i.e., decreasing distance between the swimmers (**Figure 6F**) with beating planes pitching toward each other (**Figure 6G** and leftmost zoomed portion of **Figure 6E**). In the long-term simulations, the rolling of the beating planes is also minimal, with $-0.38^{\circ} \leq \gamma \leq 0.38^{\circ}$ over 11 s.

In summary, swimmers that are close to each other will initially show near-field repulsion and then eventually, after reaching a significant distance between each other, will transition to far-field attraction (**Figure 6E**). Conversely, if the swimmers are initialized relatively far away from each other, the swimmers will initially show far-field attraction and then eventually, when getting too close to each other, will transition to near-field repulsion (results not shown for $d = 14$ μm). Hence, dynamics of swimmers with planar beat forms in initially parallel beating planes will not reach a stable configuration of attraction and will continue to oscillate between attraction and repulsion. Our far-field attraction results differ from previous results of [26] where only repulsion was observed and [31] where only attraction is observed; this is likely due to different modeling assumptions with regards to the preferred planar beat form, how out of plane beating is penalized, and geometry of the cell body. We note that rotations of swimmers with respect to θ and γ are also on par with previous studies [24].

3.2.2 Near a Wall

Similar to the previous cases, we wish to understand whether pairs of swimmers initialized in parallel planes will attract or repulse when near a wall. Results for the case of a wall at $x = -5$ μm are highlighted in **Figure 7**. For all the values of d considered, the swimmers also attract to the wall (similar to the case of initially co-planar swimmers in **Figures 3**, **4**). When the swimmers are initialized $d = 3$ μm apart, they push apart and then quickly reach a constant distance apart (**Figure 7A**) whereas in free space, they continued to push apart initially (**Figure 6A**) and then oscillate between attraction and repulsion in the long term (**Figure 6E**). With the wall, the beating plane of the bottom swimmer pitches downward while the top swimmer pitches upward, but at a very small angle (**Figures 7B,C**). For the full ~ 4 s simulation, the beating planes show minimal rolling behavior with $-0.91^{\circ} \leq \gamma \leq 0.91^{\circ}$. For the case of an initial distance of $d = 30$ μm, we observe constant attraction in **Figure 7A**, similar to the free space case in **Figure 6A**. In **Figure 7A**, the average distance between the two swimmers decreases monotonically in time for $t \geq 2.5$ s. To understand why the first point or head distance is in between the minimum and maximum distance, we can see in **Figure 7D** that the entire length of the flagellum is not remaining in the same plane. The beating plane of the bottom swimmer pitches upward while the top swimmer pitches downward (i.e., toward each other), with a more preeminent rolling motion of the swimmer's beating planes (**Figures 7B,D**), with $-3.29^{\circ} \leq \gamma \leq 3.29^{\circ}$ for $d = 30$ μm.

To investigate the long-term behavior, we report in **Figures 7E–I** the results for $d = 11$ μm for ~ 10 s. **Figure 7E** shows the

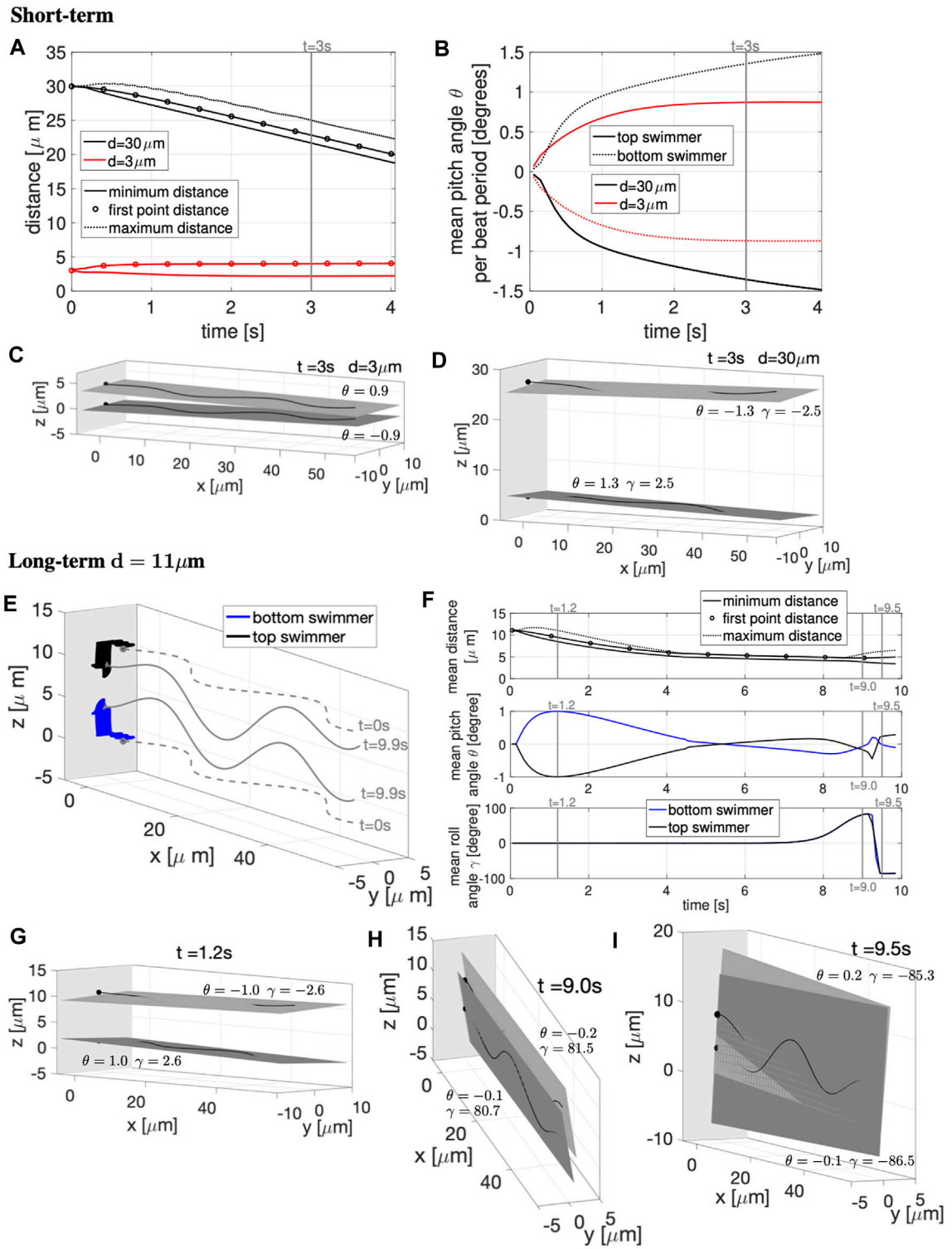

FIGURE 7 | Parallel Sperm Near a Wall. Sperm with planar beat forms initialized in parallel planes ($z = 0$ and $z = d$) near a wall at $x = -5$ μm. **(A–D)**: Short-term behavior for initial distances $d = 3$, 30 μm. **(A)** Minimum (solid lines) and maximum (dotted lines) distance between the two swimmers and distance between the first points of the two swimmers (circles). **(B)** Pitching angle θ of the **top and bottom** swimmers in time. The **top and bottom** swimmers beating planes for $d = 3$ μm is in **(C)** and $d = 30$ μm is in **(D)**, both at time $t = 3$ s. **(E–I)**: Long-term behavior for $d = 11$ μm. **(E)** Swimmer configurations at $t = 0$ s (gray dashed lines) and traces of the first point in time (colored solid lines). Corresponding beating planes of the swimmers for three snapshots are in **(G–I)**. The times chosen for the snapshots are identified with vertical gray lines in **(F)**, which has distance between the swimmers in the **top panel,** pitching angle θ in the middle panel, and rolling angle γ in the **bottom panel.** In **(C–E,G–I)**, a filled in sphere is used to denote the swimmer first point in the direction of motion. The light gray plane in **(C–E,G–I)** represents the wall (and the darker gray planes are the beating planes).

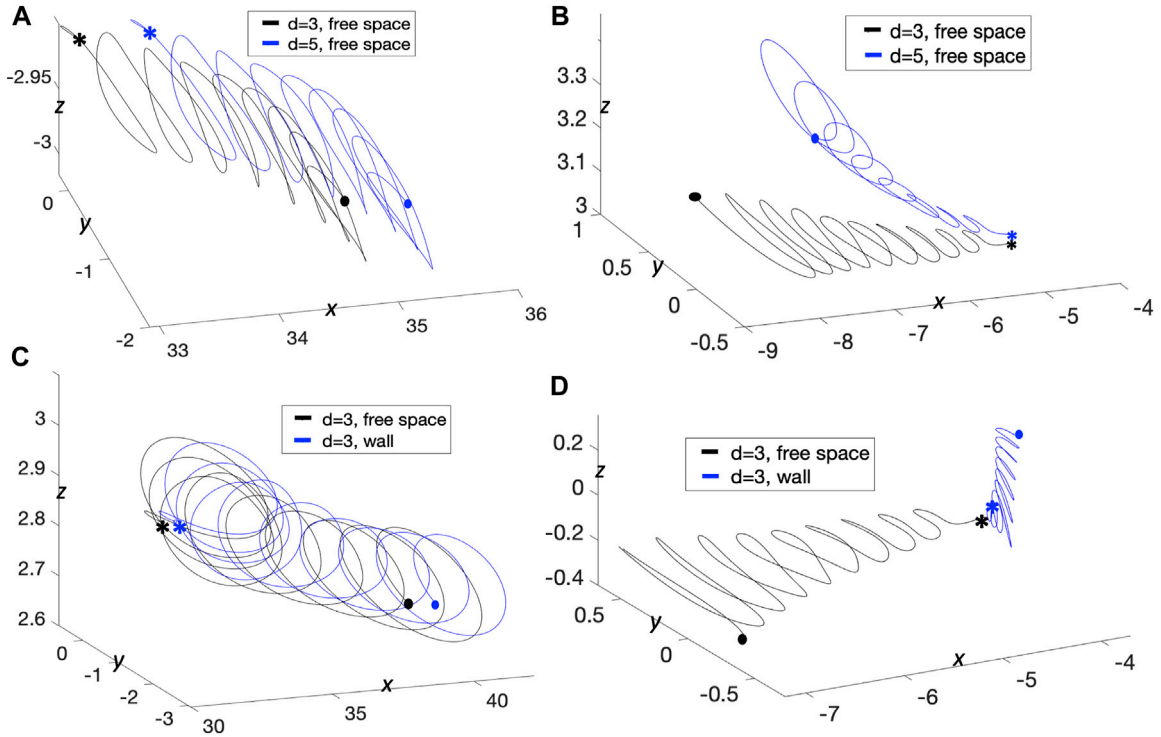

FIGURE 8 | Trajectories with Parallel Sperm. Resulting trajectories for passive fluid markers as a result of the motion of sperm initialized in parallel planes with preferred planar beat forms. **(A,B)** Free space case with swimmers initialized $d = 3, 5$ μm apart. Initial locations of fluid markers in **(A)** are (33, 0, −2.9) and (33.6, 0, −2.9) and initialized at (−4.8, 0, 3.02) and (−4.8, 0, 3.04) in **(B)**, for $t = 0$–0.4775 s. **(C,D)** Comparing trajectories with and without a wall with swimmers initialized $d = 3$ μm apart. Initial locations of fluid markers in **(C)** are (32.84, 0, 2.82) and (33.28, 0, 2.82) and initialized at (−4.2, 0, −0.1) and (−4.12, 0, −0.04) in **(D)**, for $t = 0$–0.4325 s. Starting locations are denoted with * and ending locations are denoted with ●.

swimmer configurations at t = 0 s (gray dashed lines) and traces of the first point or head in time (colored solid lines). **Figures 7G–I** shows the top and bottom swimmer's beating planes and corresponding pitching and rolling angles (θ and γ) for three snapshots in time. The times coincide with the vertical gray lines in **Figure 7F**. When initialized at $d = 11$ μm, the swimmers show far-field attraction until $t \simeq 4$ s, reaching an average distance apart of ~5 μm (**Figure 7F** top panel). The top and bottom swimmer's beating planes obtain their maximum average pitching angle at $t = 1.2$ s (**Figure 7G**) and after $t \simeq 4$ s, the swimmers enter in the near-field stability regime with the swimmer's beating planes pitching away from each other (**Figure 7F** mid panel). However, after $t \simeq 8$ s, the swimmer's dynamics change drastically since the average rolling angle γ, for both swimmers, increases and reaches the maximum value of ~84° (**Figure 7F** bottom panel), i.e., both swimmer's beating planes roll to the right and the beating planes become almost perpendicular to the $z = 0$ plane (**Figure 7H**). Then, both swimmer's beating planes roll to the left with an almost 180° motion (**Figure 7I**), the average rolling angle γ decreases and reaches the minimum value of ~ −86° (**Figure 7F** bottom panel). After this second rotation, the swimmers reach a configuration similar to the one obtained in the two co-planar swimmers case in **Figures 3C,G** for the same initial distance $d = 11$ μm.

In summary, if the swimmers are initialized close to a wall and relatively far away from each other, the swimmers will initially attract and then eventually, when getting too close to each other, will transition to a short-term near-field stability. After a certain period of time, the stability is broken by variations in the rolling angle γ that cause the swimmer's planes to rotate (twice) and reach a final configuration in which the swimmers are almost co-planar, with beating planes almost perpendicular to the $z = 0$ plane.

The rolling of sperm has been observed in experiments where the frequency of rolling is correlated with the beat frequency of the flagellum [10, 56]. In this longer term simulation, we observe two rotations in ~10 s with a beat frequency of 20 Hz (**Table 2**), so this is at a higher rate than the beat frequency. Simulations observe rolling with a very low frequency but we hypothesize that additional perturbations to the flow from additional swimmers would increase the rolling rate; this is backed up by a recent study that showed a nonplanar component of the beat form is necessary to see rolling [57]. Indeed, rolling was previously observed in free space with a pair of swimmers when they were initialized as a perturbation to the coplanar configuration [26]. This will be important to further investigate as it has been proposed that sperm rolling plays an important role in selection of sperm as well as in the organization of sperm in the female reproductive tract [56]. In our simulations, the rolling episode is what enables the swimmers to fully align, allowing for cooperative movement of sperm swimming in close proximity and near a wall.

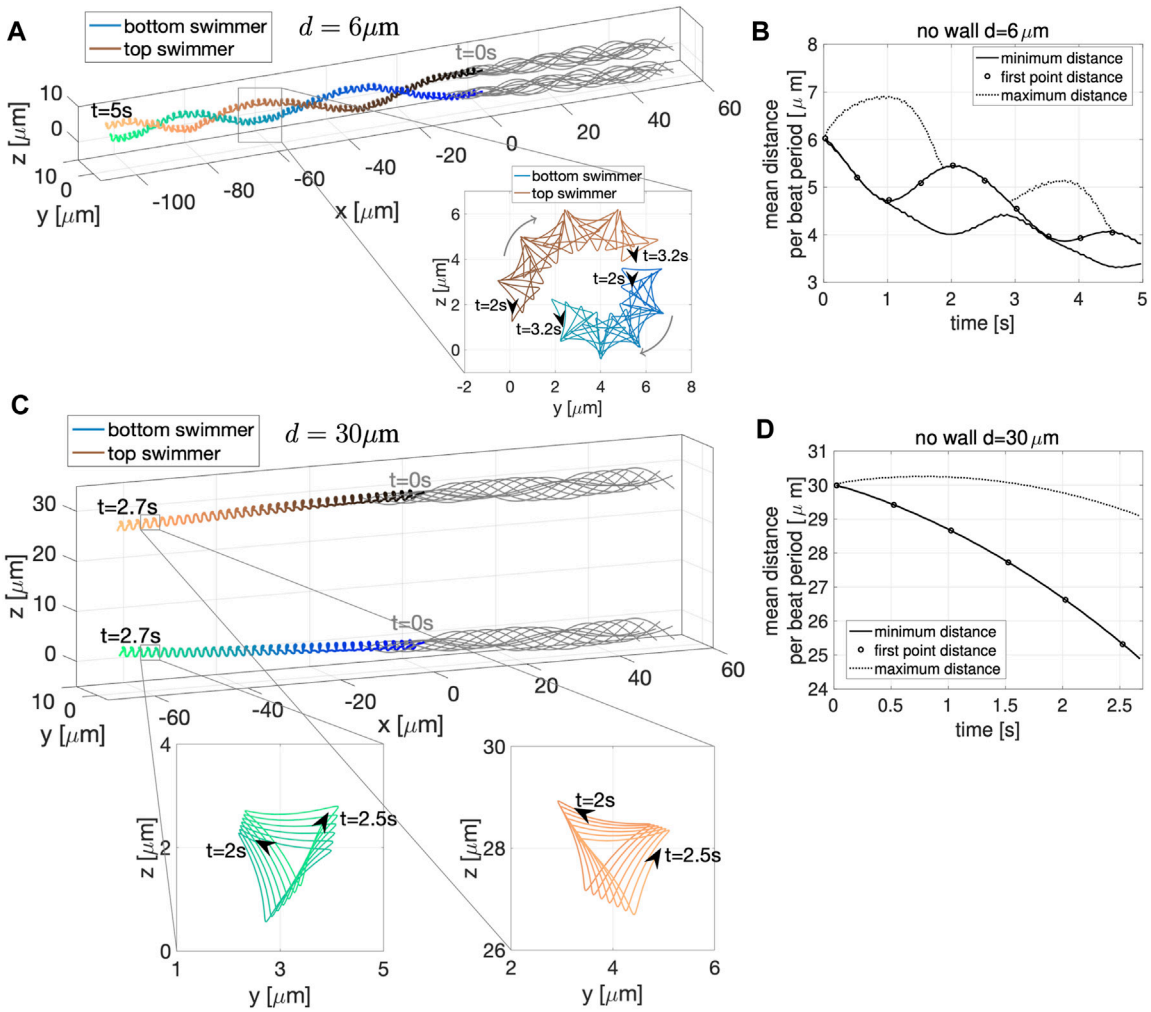

FIGURE 9 | Quasi-Planar Swimmers in Free Space. 3D flagellar configurations for the first beat period (gray lines) and the trajectory of the first point in the direction of swimming (colored lines with respect to time) over the specified time interval for the two swimmers, initialized at a distance $d = 6$ μm apart in **(A)** and $d = 30$ μm apart in **(C)**. The curves traced by the first point of the two swimmers on the *yz*-plane over the specified time interval are shown in the corresponding zoomed-in portions. Minimum (solid line) and maximum (dotted line) distance between the two swimmers and distance between the first points (circles) with respect to time for initial distance $d = 6$ μm in **(B)** and $d = 30$ μm in **(D)** (averages over a beat period).

3.2.3 Particle Trajectories

We also investigated trajectories of passive fluid markers to further understand how signaling molecules near or around the swimmer would be advected by the flow. In **Figures 8A,B**, we look at particles initialized at different x-locations with swimmers separated by distances of $d = 3, 5$ μm. For reference, even though the swimmer is not shown, it is similar to that of **Figure 6** where the swimmers are 60 μm in length and the top swimmer is in the plane $z = d$ and the bottom swimmer is in the plane $z = 0$. In **Figure 8A**, the fluid particles start below the bottom swimmer ($z = -2.9$) and mid-way along the swimmer in the x-direction. We observe that for both cases, trajectories below the bottom swimmer are the same at this location and that particles are being pushed down and further back, similar to the pitching angles of the swimmers. Signaling molecules initialized in this region will not be able to reach and bind to the flagellum. When looking at a particle trajectory initialized slightly above the plane $z = 3$ (**Figure 8B**), we observe that the particles are moving in an upward trajectory and are being advected in the negative x-direction, corresponding to the direction of swimming. At these time points, the fluid particle is also pitching at a similar angle to that of the top swimmer, while attracting to the swimmer. The movement of these particles is also interesting in that the amplitude of their movement is growing in time in the y-direction. In comparison, we look at fluid particles with a wall at $x = -5$ and compare it to the free space case for an initial separation distance of $d = 3$ μm in **Figures 8C,D**. Mid-way along the swimmer in **Figure 8C**, at these early time points, we observe that trajectories of fluid markers behave in the same way, being pushed down in the $z-$ direction regardless of whether the

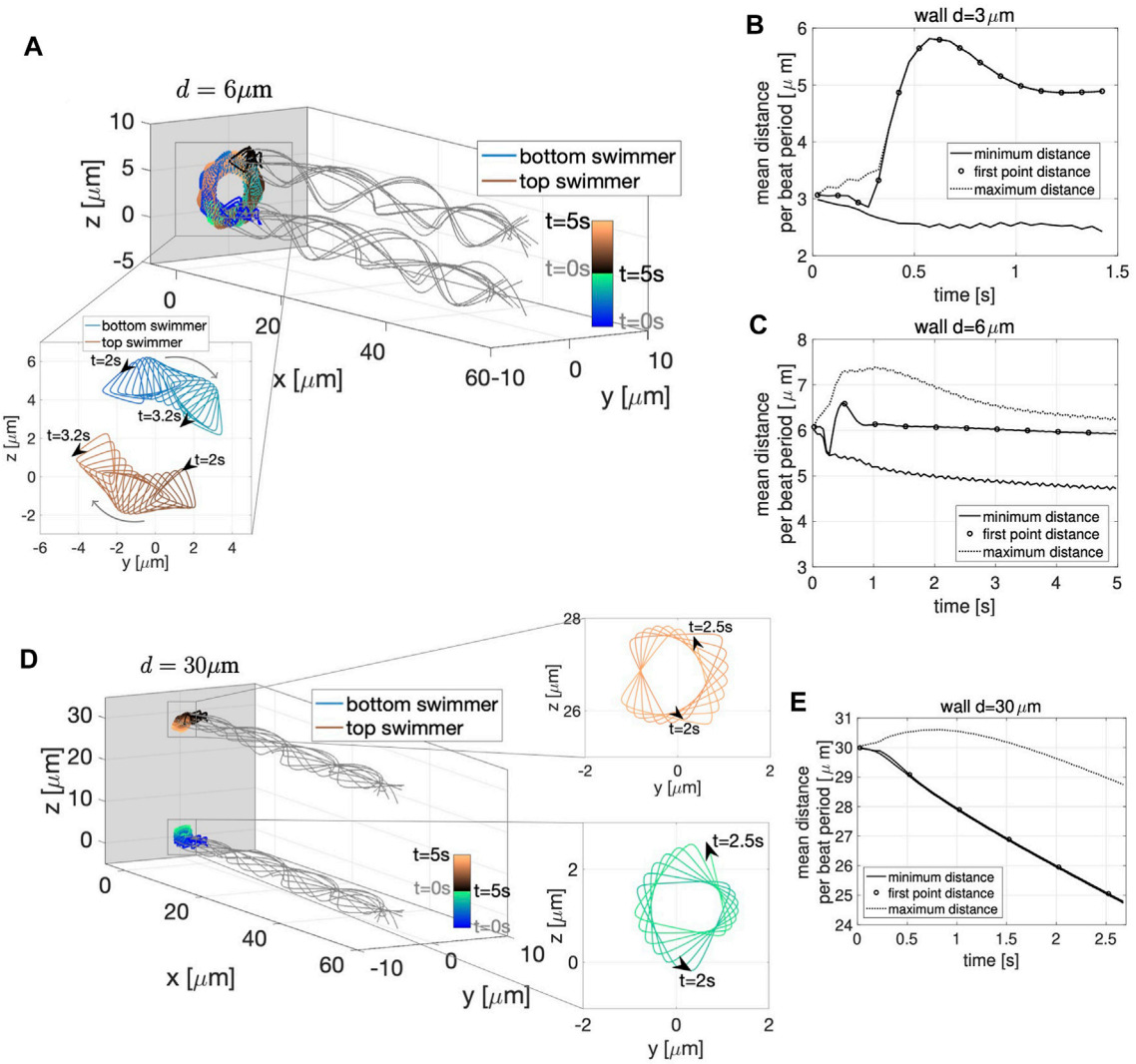

FIGURE 10 | Quasi-Planar Swimmers Near a Wall. 3D flagellar configurations for the first beat period (gray lines) and the trajectory of the first point in the direction of swimming (colored lines with respect to time) over the time interval from 0 to 5 s for the two swimmers, initialized at a distance d = 6 μm in **(A)** and d = 30 μm in **(D)** near a wall at x = −5 μm. The curves traced by the first point of the two swimmers on the yz-plane over the specified time interval are shown in the corresponding zoomed-in portions. Minimum (solid line) and maximum (dotted line) distance between the two swimmers and distance between the first points of the two swimmers (circles) with respect to time for initial distance d = 3 μm in **(B)**, d = 6 μm in **(C)**, and d = 30 μm in **(E)** (distances averaged over a beat period). The gray panel in **(A,D)** represents the wall.

wall is present close by. This fluid particle is initialized close to but below the top swimmer and it is being pushed downward in the direction of the bottom swimmer. In contrast, we observe the effects of the wall in **Figure 8D** when initializing a fluid particle close to the wall and directly below the swimmer. In the case of the wall, the particle trajectory is following and getting close to the swimmer, increasing in the z-direction with hardly any progression in the x –direction due to the wall. The free space case shows the extensive movement in the x-direction, but little movement in the z-direction.

3.3 Quasi-Planar Swimmers

Everything presented thus far has been for swimmers with a planar preferred beat form. Due to interactions with a swimmer or the wall, nonplanar beat forms have emerged (e.g., **Figure 7D**). Since different species of sperm exhibit a variety of nonplanar beat forms [2, 9], we now consider here the case of two quasi-planar swimmers where α = 3 μm and β = 1 μm in the preferred beat form in **Eq. 3**. The bottom swimmer is initialized with its centerline lying on the plane z = 0 and the top swimmer's centerline is on the plane $z = d$.

3.3.1 Free Space

We now wish to further characterize interactions of two swimmers with quasi-planar beat forms and understand how they are similar or different to swimmers with planar beat forms. In **Figure 9**, for an initial distance d = 6 μm apart, the two

swimmer's trajectories rotate around each other creating a bundle formed by the two flagella. At the same time, the two swimmers are attracting to each other, as shown in **Figure 9B**, where all distance metrics considered are oscillating and decreasing in time. Here, there are no signs of repulsion between the swimmers as they reach a minimum distance between the swimmers on the order of 3–4 μm for $t \in [4, 5]$s, similar to the swimmers with planar beat forms that were initialized as co-planar in **Figure 2B** and in contrast to those initialized in parallel planes in **Figures 6A,E** where repulsion was observed when starting $d = 3, 5$ μm apart. For the quasi-planar case, as expected, the trace of the first point shown in the zoomed portions of **Figure 9A** exhibit a more complicated trajectory, known as the flagelloid curve (or f-curve), as previously recorded in experiments and simulations for a single sperm [32, 39, 58, 59]. The flagelloid curve is shown in the *yz*-plane over the time interval from 2 to 3.2 s, where the curvature is higher at the bottom of the bundle and lower at the top of the bundle; this trend in curvature is consistent for the full time of the simulation.

We have also considered the case of two quasi-planar swimmers initialized at a distance of $d = 30$ μm in **Figure 9C**. In this case, the swimmer's trajectories show clear attraction between the swimmers. That is, the minimum distance between the swimmers in **Figure 9D** is monotonically decreasing. Here, the average minimum distance and the average distance between the first points coincide for the full simulation. The flagelloid curves for $d = 30$ μm are also reported in the zoomed in portions of **Figure 9C** and exhibit a similar pattern to those in the zoomed in portions of **Figure 9A**.

The results reported in **Figure 9** suggest that the fundamental dynamics in free space of two quasi-planar swimmers, in terms of attraction and repulsion, is similar to the dynamics of two co-planar swimmers reported in **Section 3.1.1** and **Figure 2**. We also quantified the swimming speeds of a solo quasi-planar swimmer as well as a pair of quasi-planar swimmers (**Table 2**). Again, similar to the dynamics of attraction, the swimming speed trends were similar to that of the co-planar swimmers. Relative to the swimming speed of a solo swimmer, a pair of swimmers 5 μm apart had a decrease in swimming speed whereas swimmers initially 30 μm apart had a very small increase in swimming speed (at earlier time points). For the preferred configurations studied, the quasi-planar swimmers were slower than the planar swimmers (by a few μm/s). We also emphasize that no difference in the results are obtained if the second swimmer was initialized with a centerline lying on the plane $y = d$, instead of $z = d$, i.e., translating on the *y*-axis instead of the *z*-axis.

3.3.2 Near a Planar Wall

Figure 10A shows the dynamics near a planar wall for a pair of swimmers initialized a distance $d = 6$ μm apart; the two swimmers attract to the wall and start rotating around each other. Similar to the free space case in **Figure 9A**, the swimmers continue to circle each other. However, with the wall in **Figure 10A**, they do not progress forward but stay a constant distance away from the wall, remaining perpendicular to the wall. The zoomed portion of **Figure 10A** shows the flagelloid curves traced by the first point on the swimmers. The curvature is approximately the same whether the swimmer is at the top or at the bottom of the bundle. This trend in curvature is consistent for the full time of the simulation and in contrast to quasi-planar swimmers in free space (**Figures 9A,C**). In terms of the dynamics of attraction, after an initial transient period of approximately 1 s where the first points of the swimmer attract and then repulse, the swimmers reach an almost-constant average distance between the heads at ~6 μm apart (**Figure 10C**). Similarly, swimmers initialized 3 μm apart reach a constant distance apart around 1 s, but the heads repulse initially and level off at a distance ~5 μm apart (**Figure 10B**).

The case of two quasi-planar swimmers initialized at a distance of 30 μm apart and also near the wall at $x = -5$ is shown in **Figure 10D**. In this case, the swimmer's trajectories show clear attraction, i.e., monotonic decrease of the average minimum distance between the swimmers (**Figure 10E**). The results reported in **Figure 10** suggest that the fundamental dynamics near a wall of two quasi-planar swimmers, in terms of attraction and repulsion, is similar to the dynamics of two co-planar swimmers near a wall reported in **Section 3.1.1** and **Figure 3**. In particular, we point out the strong similarity between **Figures 3D–F** and **Figures 10B,C,E**. We also emphasize that no difference in the results were obtained if the second swimmer was initialized with a centerline lying on the plane $y = d$, instead of $z = d$.

4 CONCLUSION

The ability of mammalian sperm to reach and fertilize the egg is aided by a multitude of dynamic interactions between swimmers, signaling molecules in the fluid, and walls of the female reproductive tract. In this work, we provide a detailed look at pairs of swimmers to characterize conditions that lead to emergent phenomena such as attraction or repulsion of swimmers. In free space, we observe long-term attraction of two swimmers in the case of initially co-planar sperm with preferred planar beat forms and sperm initially with centerlines in parallel planes with preferred quasi-planar beat forms. In contrast, sperm initially with centerlines in parallel planes and preferred planar beat forms exhibit oscillatory dynamics, alternating between periods of attraction and repulsion. For both of these, we emphasize that these classifications are for separation distances on a length scale smaller than the length of the flagella and greater than or equal to the beat amplitude. When sperm are swimming in close proximity to a wall, we observe attraction to the wall for planar and quasi-planar beat forms, i.e., even if swimmers are in close proximity when near the wall, they are still trapped at the wall. For sperm initialized in parallel planes with a planar preferred beat form and near a wall, due to the instability in the angle of the attracted swimmers, we observe significant rolling episodes that allow the swimmers to attain a beat form and distance apart that can then be maintained. The observation of this rolling behavior is important as it is proposed to be an important mechanism in sperm selection [56].

The results presented in this work further clarify and contextualize divergent results in the literature. For

example, in the case of parallel sperm in free space, our far-field attraction results differ from previous results of [26] where only repulsion was observed and [31] where only attraction is observed. We are able to show that the swimmers in this configuration will not reach a stable configuration of attraction and will continue to oscillate between attraction and repulsion. Zooming in on a particular time frame and/or different parameter choice leads to these divergent behaviors. Understanding the complex interactions of beat form and elasticity of the flagella can also be utilized to design artificial micro-swimmers that navigate in complex environments [35–37].

The modeling framework used did not account for background fluid flows and limited the study to the case of two swimmers initialized in the same plane or with centerlines in parallel planes. In all of the cases where attraction is observed, we emphasize that perturbations to the flow would likely cause additional rolling and pitching. Similarly, we focused on the case of a purely homogeneous fluid with a constant viscosity. It is well known that the viscosity of the fluid in the female reproductive tract varies and will often exhibit nonlinear properties with respect to stress and strain [2, 10]. We observed changes in the dynamics of attraction with increases in the viscosity and hence, we expect that nonhomogeneous or nonlinear fluid contributions will also act to change the frequency of rolling and the degree of pitching in the swimmers. This will be the focus of future studies.

DATA AVAILABILITY STATEMENT

The raw data supporting the conclusions of this article will be made available by the authors, without undue reservation.

AUTHOR CONTRIBUTIONS

LC and SO conceptualized this research and completed the writing. LC and DD completed simulations and created figures. All authors have contributed to this article and have given approval for this submission.

FUNDING

The work of SDO and DD was supported, in part, by NSF DMS 1455270. SDO was also supported, in part, by the Fulbright Research Scholar Program. Simulations were run on a cluster at WPI acquired through NSF grant 1337943 and on a cluster provided by Research Computing at the Rochester Institute of Technology (60).

REFERENCES

1. Dcunha R, Hussein R, Ananda H, Kumari S, Adiga S, Kannan N, et al. Current Insights and Latest Updates in Sperm Motility and Associated Applications in Assisted Reproduction. *Reprod Sci* (2020) [Epub ahead of print] 1–19. doi:10.1007/s43032-020-00408-y
2. Gaffney EA, Gadêlha H, Smith DJ, Blake JR, and Kirkman-Brown JC. Mammalian Sperm Motility: Observation and Theory. *Annu Rev Fluid Mech* (2011) 43:501–28. doi:10.1146/annurev-fluid-121108-145442
3. Alavi S, and Cosson J. Sperm Motility in Fishes. (II) Effects of Ions and Osmolality: a Review. *Cel Biol Int* (2006) 30:1–14. doi:10.1016/j.cellbi.2005.06.004
4. Suarez SS, and Pacey AA. Sperm Transport in the Female Reproductive Tract. *Hum Reprod Update* (2006) 12:23–37. doi:10.1093/humupd/dmi047
5. Suarez SS. Regulation of Sperm Storage and Movement in the Mammalian Oviduct. *Int J Dev Biol* (2008) 52:455–62. doi:10.1387/ijdb.072527ss
6. Elgeti J, Winkler RG, and Gompper G. Physics of Microswimmers-Single Particle Motion and Collective Behavior: a Review. *Rep Prog Phys* (2015) 78: 056601. doi:10.1088/0034-4885/78/5/056601
7. Schoeller SF, and Keaveny EE. From Flagellar Undulations to Collective Motion: Predicting the Dynamics of Sperm Suspensions. *J R Soc Interf* (2018) 15:20170834. doi:10.1098/rsif.2017.0834
8. Schoeller SF, Holt WV, and Keaveny EE. Collective Dynamics of Sperm Cells. *Phil Trans R Soc B* (2020) 375:20190384. doi:10.1098/rstb.2019.0384
9. Guerrero A, Carneiro J, Pimentel A, Wood CD, Corkidi G, and Darszon A. Strategies for Locating the Female Gamete: the Importance of Measuring Sperm Trajectories in Three Spatial Dimensions. *Mol Hum Reprod* (2011) 17: 511–23. doi:10.1093/molehr/gar042
10. Smith DJ, Gaffney EA, Gadêlha H, Kapur N, and Kirkman-Brown JC. Bend Propagation in the Flagella of Migrating Human Sperm, and its Modulation by Viscosity. *Cell Motil. Cytoskeleton* (2009) 66:220–36. doi:10.1002/cm.20345
11. Woolley DM, and Vernon GG. A Study of Helical and Planar Waves on Sea Urchin Sperm Flagella, with a Theory of How They Are Generated. *J Exp Biol* (2001) 204:1333–45. doi:10.1242/jeb.204.7.1333
12. Su TW, Xue L, and Ozcan A. High-throughput Lensfree 3D Tracking of Human Sperms Reveals Rare Statistics of Helical Trajectories. *Proc Natl Acad Sci U S A* (2012) 109:16018–22. doi:10.1073/pnas.1212506109
13. Su T-W, Choi I, Feng J, Huang K, McLeod E, and Ozcan A. Sperm Trajectories Form Chiral Ribbons. *Sci Rep* (2013) 3:1664. doi:10.1038/srep01664
14. Lauga E, and Powers TR. The Hydrodynamics of Swimming Microorganisms. *Rep Prog Phys* (2009) 72:096601. doi:10.1088/0034-4885/72/9/096601
15. Ardon F, Markello RD, Hu L, Deutsch ZI, Tung CK, Wu M, et al. Dynamics of Bovine Sperm Interaction with Epithelium Differ between Oviductal Isthmus and Ampulla. *Biol Reprod* (2016) 95:90–7. doi:10.1095/biolreprod.116.140632
16. Lamy J, Corbin E, Blache M-C, Garanina AS, Uzbekov R, Mermillod P, et al. Steroid Hormones Regulate Sperm-Oviduct Interactions in the Bovine. *Reprod* (2017) 154:497–508. doi:10.1530/rep-17-0328
17. Ramal-Sanchez M, Bernabo N, Tsikis G, Blache M-C, Labas V, Druart X, et al. Progesterone Induces Sperm Release from Oviductal Epithelial Cells by Modifying Sperm Proteomics, Lipidomics and Membrane Fluidity. *Mol Cell Endocrinol* (2020) 504:110723. doi:10.1016/j.mce.2020.110723
18. Curtis MP, Kirkman-Brown JC, Connolly TJ, and Gaffney EA. Modelling a Tethered Mammalian Sperm Cell Undergoing Hyperactivation. *J Theor Biol* (2012) 309:1–10. doi:10.1016/j.jtbi.2012.05.035
19. Simons J, Olson S, Cortez R, and Fauci L. The Dynamics of Sperm Detachment from Epithelium in a Coupled Fluid-Biochemical Model of Hyperactivated Motility. *J Theor Biol* (2014) 354:81–94. doi:10.1016/j.jtbi.2014.03.024
20. Wang S, and Larina IV. *In Vivo* three-dimensional Tracking of Sperm Behaviors in the Mouse Oviduct. *Development* (2018) 145:dev157685. doi:10.1242/dev.157685
21. Camara Pirez M, Steele H, Reese S, and Kölle S. Bovine Sperm-Oviduct Interactions Are Characterized by Specific Sperm Behaviour, Ultrastructure and Tubal Reactions Which Are Impacted by Sex Sorting. *Sci Rep* (2020) 10: 16522. doi:10.1038/s41598-020-73592-1
22. Denissenko P, Kantsler V, Smith DJ, and Kirkman-Brown J. Human Spermatozoa Migration in Microchannels Reveals Boundary-Following Navigation. *Proc Natl Acad Sci U S A* (2012) 109:8007–10. doi:10.1073/pnas.1202934109
23. Tung C-k., Ardon F, Fiore AG, Suarez SS, and Wu M. Cooperative Roles of Biological Flow and Surface Topography in Guiding Sperm Migration

Revealed by a Microfluidic Model. *Lab Chip* (2014) 14:1348–56. doi:10.1039/c3lc51297e
24. Llopis I, Pagonabarraga I, Lagomarsino MC, and Lowe C. Cooperative Motion of Intrinsic and Actuated Semiflexible Swimmers. *Phys Rev E* (2013) 87: 032720. doi:10.1103/physreve.87.032720
25. Olson SD, and Fauci LJ. Hydrodynamic Interactions of Sheets vs Filaments: Synchronization, Attraction, and Alignment. *Phys Fluids* (2015) 27:121901. doi:10.1063/1.4936967
26. Simons J, Fauci L, and Cortez R. A Fully Three-Dimensional Model of the Interaction of Driven Elastic Filaments in a Stokes Flow with Applications to Sperm Motility. *J Biomech* (2015) 48:1639–51. doi:10.1016/j.jbiomech.2015.01.050
27. Miki K, and Clapham DE. Rheotaxis Guides Mammalian Sperm. *Curr Biol* (2013) 23:443–52. doi:10.1016/j.cub.2013.02.007
28. Ishimoto K, and Gaffney EA. Fluid Flow and Sperm Guidance: a Simulation Study of Hydrodynamic Sperm Rheotaxis. *J R Soc Interf* (2015) 12:20150172. doi:10.1098/rsif.2015.0172
29. Gillies EA, Cannon RM, Green RB, and Pacey AA. Hydrodynamic Propulsion of Human Sperm. *J Fluid Mech* (2009) 625:445–74. doi:10.1017/s0022112008005685
30. Smith DJ, Gaffney EA, Blake JR, and Kirkman-Brown JC. Human Sperm Accumulation Near Surfaces: a Simulation Study. *J Fluid Mech* (2009) 621: 289–320. doi:10.1017/s0022112008004953
31. Walker B, Ishimoto K, and Gaffney E. Pairwise Hydrodynamic Interactions of Synchronized Spermatozoa. *Phys Rev Fluids* (2019) 4:093101. doi:10.1103/physrevfluids.4.093101
32. Ishimoto K, and Gaffney EA. An Elastohydrodynamical Simulation Study of Filament and Spermatozoan Swimming Driven by Internal Couples. *IMA J Appl Math* (2018) 83:655–79. doi:10.1093/imamat/hxy025
33. Yang Y, Elgeti J, and Gompper G. Cooperation of Sperm in Two Dimensions: Synchronization, Attraction, and Aggregation through Hydrodynamic Interactions. *Phys Rev E Stat Nonlin Soft Matter Phys* (2008) 78:061903. doi:10.1103/PhysRevE.78.061903
34. Huang J, Carichino L, and Olson SD. Hydrodynamic Interactions of Actuated Elastic Filaments Near a Planar wall with Applications to Sperm Motility. *J Coupled Syst Multiscale Dyn* (2018) 6:163–75. doi:10.1166/jcsmd.2018.1166
35. Gao W, and Wang J. Synthetic Micro/nanomotors in Drug Delivery. *Nanoscale* (2014) 6:10486–94. doi:10.1039/c4nr03124e
36. Nelson BJ, Kaliakatsos IK, and Abbott JJ. Microrobots for Minimally Invasive Medicine. *Annu Rev Biomed Eng* (2010) 12:55–85. doi:10.1146/annurev-bioeng-010510-103409
37. Sanders L. Microswimmers Make a Splash: Tiny Travelers Take on a Viscous World. *Sci News* (2009) 176:22–5. doi:10.1002/scin.5591760124
38. Fauci LJ, and Dillon R. Biofluidmechanics of Reproduction. *Annu Rev Fluid Mech* (2006) 38:371–94. doi:10.1146/annurev.fluid.37.061903.175725
39. Carichino L, and Olson SD. Emergent Three-Dimensional Sperm Motility: Coupling Calcium Dynamics and Preferred Curvature in a Kirchhoff Rod Model. *Math Med Biol* (2019) 36:439–69. doi:10.1093/imammb/dqy015
40. Lim S, Ferent A, Wang XS, and Peskin CS. Dynamics of a Closed Rod with Twist and bend in Fluid. *SIAM J Sci Comput* (2008) 31:273–302. doi:10.1137/070699780
41. Lim S. Dynamics of an Open Elastic Rod with Intrinsic Curvature and Twist in a Viscous Fluid. *Phys Fluids* (2010) 22:024104. doi:10.1063/1.3326075
42. Olson SD, Lim S, and Cortez R. Modeling the Dynamics of an Elastic Rod with Intrinsic Curvature and Twist Using a Regularized Stokes Formulation. *J Comput Phys* (2013) 238:169–87. doi:10.1016/j.jcp.2012.12.026
43. Schmitz-Lesich KA, and Lindemann CB. Direct Measurement of the Passive Stiffness of Rat Sperm and Implications to the Mechanism of the Calcium Response. *Cel Motil. Cytoskeleton* (2004) 59:169–79. doi:10.1002/cm.20033
44. Olson SD, Suarez SS, and Fauci LJ. Coupling Biochemistry and Hydrodynamics Captures Hyperactivated Sperm Motility in a Simple Flagellar Model. *J Theor Biol* (2011) 283:203–16. doi:10.1016/j.jtbi.2011.05.036
45. Chouaieb N, and Maddocks JH. Kirchhoff's Problem of Helical Equilibria of Uniform Rods. *J Elasticity* (2004) 77:221–47. doi:10.1007/s10659-005-0931-z
46. Chouaieb N, Goriely A, and Maddocks JH. Helices. *Proc Natl Acad Sci* (2006) 103:9398–403. doi:10.1073/pnas.0508370103
47. Woolley DM. Flagellar Oscillation: a Commentary on Proposed Mechanisms. *Biol Rev Camb Philos Soc* (2010) 85:453–70. doi:10.1111/j.1469-185X.2009.00110.x
48. Cortez R. The Method of Regularized Stokeslets. *SIAM J Sci Comput* (2001) 23: 1204–25. doi:10.1137/s106482750038146x
49. Cortez R, Fauci L, and Medovikov A. The Method of Regularized Stokeslets in Three Dimensions: Analysis, Validation, and Application to Helical Swimming. *Phys Fluids* (2005) 17:0315041. doi:10.1063/1.1830486
50. Ainley J, Durkin S, Embid R, Boindala P, and Cortez R. The Method of Images for Regularized Stokeslets. *J Comput Phys* (2008) 227:4600–16. doi:10.1016/j.jcp.2008.01.032
51. Cortez R, and Varela D. A General System of Images for Regularized Stokeslets and Other Elements Near a Plane wall. *J Comput Phys* (2015) 285:41–54. doi:10.1016/j.jcp.2015.01.019
52. Eberly D. *Least Squares Fitting of Data (Version February 14, 2019)*. Chapel Hill, NC: Magic Software (2000).
53. Woolley DM, Crockett RF, Groom WDI, and Revell SG. A Study of Synchronisation between the Flagella of Bull Spermatozoa, with Related Observations. *J Exp Biol* (2009) 212:2215–23. doi:10.1242/jeb.028266
54. Hunter RHF, Coy P, Gadea J, and Rath D. Considerations of Viscosity in the Preliminaries to Mammalian Fertilisation. *J Assist Reprod Genet* (2011) 28: 191–7. doi:10.1007/s10815-010-9531-3
55. Kirkman-Brown JC, and Smith DJ. Sperm Motility: Is Viscosity Fundamental to Progress? *Mol Hum Reprod* (2011) 17:539–44. doi:10.1093/molehr/gar043
56. Babcock DF, Wandernoth PM, and Wennemuth G. Episodic Rolling and Transient Attachments Create Diversity in Sperm Swimming Behavior. *BMC Biol* (2014) 12:67. doi:10.1186/s12915-014-0067-3
57. Gadêlha H, Hernández-Herrera P, Montoya F, Darszon A, and Corkidi G. Human Sperm Uses Asymmetric and Anisotropic Flagellar Controls to Regulate Swimming Symmetry and Cell Steering. *Sci Adv* (2020) 6: eaba5168. doi:10.1126/sciadv.aba5168
58. Woolley D. Motility of Spermatozoa at Surfaces. *Reprod* (2003) 126:259–70. doi:10.1530/rep.0.1260259
59. Woolley DM. Studies on the Eel Sperm Flagellum. 2. The Kinematics of normal Motility. *Cel Motil. Cytoskeleton* (1998) 39:233–45. doi:10.1002/(sici)1097-0169(1998)39:3<233::aid-cm6>3.0.co;2-5
60. Rochester Institute of Technology. *Research Computing Services* (2019). [Dataset]. doi:10.34788/0S3G-QD15

Conflict of Interest: The authors declare that the research was conducted in the absence of any commercial or financial relationships that could be construed as a potential conflict of interest.

Publisher's Note: All claims expressed in this article are solely those of the authors and do not necessarily represent those of their affiliated organizations, or those of the publisher, the editors and the reviewers. Any product that may be evaluated in this article, or claim that may be made by its manufacturer, is not guaranteed or endorsed by the publisher.

frontiers in Physics

ORIGINAL RESEARCH
published: 02 December 2021
doi: 10.3389/fphy.2021.734447

Air-Fluidized Aggregates of Black Soldier fly Larvae

Hungtang Ko[1], Grace J. Cassidy[2], Olga Shishkov[3], Enes Aydin[4], David L. Hu[1,5] and Daniel I. Goldman[4]**

[1]School of Mechanical Engineering, Georgia Institute of Technology, Atlanta, GA, United States, [2]School of Chemical Engineering, Georgia Institute of Technology, Atlanta, GA, United States, [3]Biofrontiers Institute, University of Colorado Boulder, Boulder, CO, United States, [4]School of Physics, Georgia Institute of Technology, Atlanta, GA, United States, [5]School of Biology, Georgia Institute of Technology, Atlanta, GA, United States

Black soldier fly larvae are a sustainable protein source and play a vital role in the emerging food-waste recycling industry. One of the challenges of raising larvae in dense aggregations is their rise in temperature during feeding, which, if not mitigated, can become lethal to the larvae. We propose applying air-fluidization to circumvent such overheating. However, the behavior of such a system involves complex air-larva interactions and is poorly understood. In this combined experimental and numerical study, we show that the larval activity changes the behavior of the ensemble when compared to passive particles such as dead larvae. Over a cycle of increasing and then decreasing airflow, the states (pressure and height) of the live larva aggregates are single-value functions of the flow speed. In contrast, dead larva aggregates exhibit hysteresis characteristic of traditional fluidized beds, becoming more porous during the ramp down of airflow. This history-dependence for passive particles is supported by simulations that couple agent-based dynamics and computational fluid dynamics. We show that the hysteresis in height and pressure of the aggregates decreases as the activity of simulated larvae increases. To test if air fluidization can increase larval food intake, we performed feeding trials in a fluidization chamber and visualized the food consumption via x-ray imaging. Although the food mixes more rapidly in faster airflow, the consumption rate decreases. Our findings suggest that providing moderate airflow to larval aggregations may alleviate overheating of larval aggregations and evenly distribute the food without reducing feeding rates.

Keywords: black soldier fly larvae, fluidization, living matter, collective behavior, activity, Gaussian force, CFD, agent-based simulation

OPEN ACCESS

Edited by:
Tim Landgraf,
Freie Universität Berlin, Germany

Reviewed by:
Louwrens Hoffman,
The University of Queensland, Australia
Shih-Yuan Chen,
North Carolina State University, United States

****Correspondence:***
Daniel I. Goldman
daniel.goldman@physics.gatech.edu
David L. Hu
hu@me.gatech.edu

Specialty section:
This article was submitted to Social Physics, a section of the journal Frontiers in Physics

Received: *01 July 2021*
Accepted: *20 October 2021*
Published: *02 December 2021*

Citation:
Ko H, Cassidy GJ, Shishkov O, Aydin E, Hu DL and Goldman DI (2021) Air-Fluidized Aggregates of Black Soldier fly Larvae. Front. Phys. 9:734447. doi: 10.3389/fphy.2021.734447

1 INTRODUCTION

Every year, humans waste over one billion tons of food, a third of all food production [1]. Such excessive food waste also creates management problems. When left unattended in traditional landfills, rotting food becomes an environmental hazard that can spread diseases and release greenhouse gases [2]. One solution to this issue involves feeding the food waste to insects, which subsequently can be rendered into livestock feed or biofuel [3–6]. Black soldier fly larvae (*Hermetia illucens*) have been used extensively for this process because they reduce the house fly population and have high nutritional value [7–9]. However, raising black soldier fly larvae in denser aggregations than those found in nature creates a number of new challenges, such as the distribution of food, the

removal of uneaten food, and the removal of solid and liquid waste produced by the larvae. Furthermore, larval metabolic heat dissipates slowly in dense aggregations, causing them to rise to temperatures lethal to larvae. As a result, it is recommended to grow larvae at area densities lower than five larvae per square centimeter, or equivalently, at heights lower than approximately three times the larval width [8, 10]. This factor limits efficient space utilization in the industry. To feed larvae in denser aggregations, it has been proposed to provide aeration during feeding [11–13].

Providing fluid flows through particle aggregations, a process called fluidization, is a common strategy used in industrial processes such as coal gasification, catalytic cracking, chemical synthesis, heat exchange, and coating [14–16]. During the procedure, air or other inert fluids are forced from below the particle beds. The external flow lifts the particles and allows them to behave like fluids themselves. Fluidization is a collective phenomenon: the flow velocity required for the aggregations to fluidize is insufficient to lift one particle. Fluidization is adopted in industrial applications mainly for three reasons: the increased surface area exposure to the fluid, even distribution of heating, and mixing of particles [14]. While aeration can indeed cool larval aggregations [12], it is unclear if fluidization can improve the mixing of food in the aggregates well. A better understanding of the interactions between airflow and larvae could help improve industrial practices.

Fluidization has also drawn much interest from physicists for generating interesting multiphase states of matter [15, 17, 18]. A fluidization-defluidization cycle is defined as a ramp up and then ramp down in flow rate. A critical feature of fluidized beds undergoing such cycles is that the particulate response to airflow is history-dependent due to granular-level interactions. Both state variables, the air pressure difference across the aggregation, and the aggregation height, show hysteresis effects. Particles pack together more loosely towards the end of the fluidization-defluidization cycle compared to the beginning [15, 17, 18]. Previous fluidization studies have mostly considered passive particles, but black soldier fly larvae have their own energy source and can deform their bodies, thus actively generating forces on their neighbors. This study will show how active matter behaves in a fluidized bed.

In this project, we used both experiments and simulations to examine the behavior of black soldier fly larvae under fluidization-defludization cycles and to develop a minimal model for how living aggregates interact with airflow. We subjected live and dead larvae to ramps in airflow and measured their height and air pressure. To study the effect of activity on fluidization, we developed simulations with actively propelling agents in fluidization-defluidization cycles. Using both approaches, we also explored how food mixes with the larvae under airflow.

2 MATERIALS AND METHODS

2.1 Experiment

We used the black soldier fly larvae from EVO Conversion Systems for our experiments. Larva sizes were affected by the environmental conditions during growth, including the conditions during shipment. Due to this challenge, we used one of three size classes of larvae (short, medium, and long) in each experiment. Larvae sizes were not mixed in any experiment. Long larvae were 20.1 ± 1.9 mm long, 6.2 ± 0.5 wide, and 4.2 ± 0.6 thick (N = 50). Medium larvae were 12.0 ± 1.4 mm long and 4.4 ± 0.5 mm wide. Short larvae were 9.7 ± 2.2 mm long, 4.0 ± 0.4 wide, and 2.1 ± 0.4 thick (N = 26). In the experiments with dead larvae, we euthanized the larvae by placing them in a freezer overnight and then thawing them to room temperature. We performed the fluidization experiments with larval aggregations with masses 300 and 600 g.

To estimate the larval propulsive force, we placed plastic spheres 6 mm in diameter and 0.11 g each in mass on the surface of the larva aggregates. We tracked the trajectories of the spheres using the circular Hough transform in MATLAB and obtained the acceleration by calculating the finite differences over 0.06-s intervals. The force on a sphere was obtained by multiplying the acceleration by the mass.

The fluidization chamber consisted of a 95 mm-diameter acrylic tube. Beneath the tube, we used a 0.635 cm-thick, porous plastic sheet with 50 μm-diameter pores to support the weight of the larval aggregation and to laminarize the flow. We supplied the airflow by connecting the setup to a Toro Ultra Leaf Blower Vac (51619), whose voltage was controlled manually by a voltage relay Staco 3PN1010. The system can provide a maximum air speed of approximately 2 m/s at the outlet of the fluidization chamber. We performed the fluidization experiments with a voltage ramp rate of 0–100% at 1% per second, as well as two and four times this rate. In a typical trial, airflow velocity increased linearly, was held at the maximum for 20 seconds, and then decreased linearly. In total, each trial took 220 s for the experiments at a 1x ramp rate. For experiments at greater ramp rates, 2x and 4x, all steps of the cycle were sped up accordingly. The duration of the constant velocity phase was halved for the 2x ramp rate and quartered for the 4x ramp rate. As a consequence, 2x trials and 4x trials took a half and a quarter of the time it took for 1x trials, respectively.

We measured air speed and pressure using an OMEGA FMA 1000 series anemometer and a Honeywell pressure sensor. The anemometer was positioned at the top of the setup, and the pressure sensor was placed at the bottom of the larval aggregates (**Figure 1E**). The data were digitized using an Arduino Uno and saved with MATLAB at a 5 Hz sampling rate.

For all trials, we captured side view videos using a webcam at 30 frames per second. We performed video processing using a custom MATLAB program which identified larvae based on the brightness difference and extracted the height of the larval columns as a function of time. In addition, we customized functions within PIVlab [19] to estimate the larval velocity field.

For the feeding trials, we used an x-ray machine (Orthoscan Mobile DI) to visualize the food within the larval aggregation (**Figure 6A**). In all feeding trials, medium size larvae were used. We prepared a food source composed of water, sugar, agar powder, and 20% contrast agent Omnipaque iohexol for x-ray imaging. We cut the "jelly" into cubes with sides 6.3 ± 0.7 mm long, roughly half the length of a larva. We performed the feeding experiments under three conditions: no flow, slow flow (1.4 m/s),

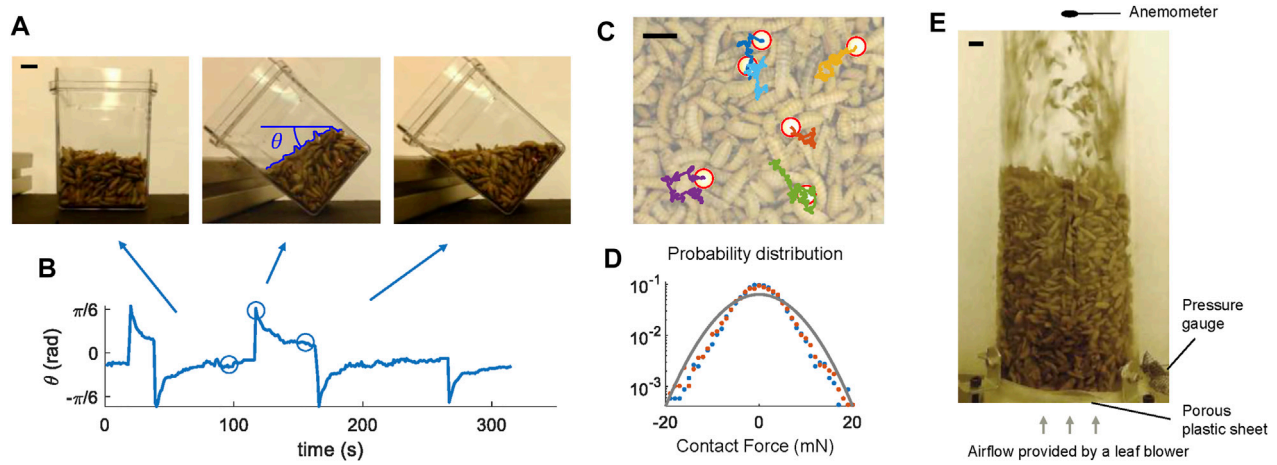

FIGURE 1 | Aggregates of live black soldier fly larvae show fluid-like behaviors. **(A)** Larva aggregates flow and level with the horizon as the container is tilted. **(B)** The orientation of the larva aggregate surface with respect to the horizon. The circles represent the snapshots in **(A)**. **(C)** Plastic spheres in the larva aggregates undergo Brownian motion. Red circles mark the locations of the plastic spheres, and colored lines show their tracked trajectories. **(D)** The probability distribution of translational forces on the plastic spheres. Blue dots and red dots show the force component in the *x* and *y* direction, respectively. The gray line shows a Gaussian distribution with a standard deviation of 6.3 mN. **(E)** Side view of the fluidization chamber. Scale bars are 1 cm long in all subfigures.

and fast flow (2 m/s). We conducted two trials for each condition. In each trial, we placed four jelly cubes onto the top surface of 150 g larval aggregations before recording x-ray images every 10 s.

2.2 Simulation

We simulated fly larvae in two dimensions as circular discs capable of actively propelling themselves. "Dead" larvae in simulations were the same shape but did not actively apply any forces. We wrote the simulation in the computational fluid dynamics package Basilisk, open-source software based in C [20]. Basilisk solves moving boundary problems using an adaptive Cartesian mesh and the volume of fluid (VOF) technique. The fidelity of this package has been verified in various benchmark tests [20]. We modified the solver to incorporate agent-based rules. The geometry and the dimensionless parameters of the simulation are comparable to those of the experiment, as detailed in the following subsection. Here, we highlight some key aspects of the simulations.

All agents moved following Newton's second law. Dead larvae were driven by three forces: 1. fluid viscous and pressure forces; 2. gravity; 3. viscoelastic collision forces with other agents and the container walls (**Figure 4A**). For live larvae, an additional active force F_{active} was applied. Based on our experimental measurements of the Brownian motion of plastic spheres at the bed surface, we model F_{active} as Gaussian white noise. The activity intensity is isotropic and homogeneous in the simulations.

In our simulations, the thickness of the virtual shell t_{shell} accounted for 30% of the diameter. The collision force $F_{collision}$ was applied when the virtual shells (gray in **Figure 4A**) overlapped. The virtual shells did not obstruct fluid flows. The collision force consisted of an elastic and a viscous component. $F_{collision} = k_s d + c\dot{d}$, where $k_s = 1.6 \times 10^6$ N/m is the spring constant and $c = 0.45$ N·s/m is the damping coefficient, d and $\dot{d}$ are the distance and relative velocity between the centers of two colliding discs. These values were chosen to prevent the core of the discs from overlapping without using thicker shells.

At each time step, the program updated the location and velocity of each agent. Their translational and rotational velocities became the boundary conditions for the fluid field at the next time step. At the inlet, a turbulent velocity profile was assumed. The velocity followed a 1/7 power-law increased from zero at the side walls to a maximum value at the center [21]. At the outlet, we set the Neumann boundary conditions for velocity and the Dirichlet boundary condition for the pressure. At each time step, the average velocity and pressure across the outlet were measured. The height of the aggregates was calculated by averaging the vertical locations of the 19 highest simulated larvae, which typically represent the top layer of the aggregation.

We simulated larval feeding using circular food with twice the radius of the larvae, which exceeded the size ratio in the experiment. Simulating food elements smaller than the larvae would require finer meshes and more computational time. Here instead of seeking quantitative agreement we sought to discover if our minimal model could capture features of feeding observed in the experiments. At each time step, the area of the food decreased by the product of the number of contacting larvae and a fixed feeding rate. Simulations were performed with fixed flow speeds of 0, 1.4, or 1.8 m/s.

The simulations required high resolution in space and time to resolve the fluid field. The mesh sizes adapt to the local fluid fields at each time step, becoming 0.74 mm wide at their finest. The size of the time step also varied according to the Courant–Friedrichs–Lewy condition requirement for the fluid field calculation [22]. Agents were updated at a fixed time step of 0.12 ms. The flow ramp rate and the feeding rate were sped up in the simulation to reduce the computation time.

TABLE 1 | Dimensionless parameters in the experiments and simulations.

Dimensionless parameters	Experiment	Simulation
Re	10^5	5×10^4
Fr	4.2	5
K	0.17	0–2.5
ρ_s/ρ	500	500
w_{larva}/D	0.042	0.050

We performed the simulations on the Partnership for an Advanced Computing Environment (PACE) clusters at the Georgia Institute of Technology. Fluidization simulations took approximately 5.5 h when calculated on 24 CPU cores in parallel. The simulations with food took approximately 3.5 h. The fluid field and the agent information are saved throughout the simulation. Occasionally, the fluid field failed to converge due to the limited spatial and temporal resolution. In these cases, we restarted the simulation a few time steps before its termination.

2.3 Normalization

Our experiments and simulations are each characterized by five dimensionless groups, including the Reynolds number, Re, which represents the ratio between the fluid inertia to the viscous force; the Froude number Fr, which represents the ratio between gravity and inertia; the activity level k, which represents the ratio of the random force intensity to the air inertial force; the density ratio between larvae and air; the dimensionless size of the larvae, which is the ratio of the larva width to bed width. They are defined as:

$$\mathrm{Re} = \frac{\rho u_{max} D}{\mu} \qquad \mathrm{Fr} = \frac{u}{\sqrt{gD}} \tag{1}$$

$$k = \frac{\sqrt{\langle F_{random}^2 \rangle}}{\rho u_{max} D^2} \qquad \rho_s/\rho \qquad w_{larvae}/D \tag{2}$$

Here ρ and $u_{\max}$ are the air density and the maximum velocity of the airflow in the fluidization-defluidization cycle, D is the diameter of the fluidization chamber, g is the gravitational acceleration, $\sqrt{\langle F_{random}^2 \rangle}$ is the standard deviation of the active force, w_{larvae} is the width of the larvae in the experiments. Experiments are characterized by another dimensionless group, w_{larvae}/L_{larvae}, the aspect ratio of the larvae, which was not matched in the simulations, which assumed circular particles.

The values of the dimensionless parameters are shown in **Table 1**. The orders of magnitude of all dimensionless groups are matched, except for the Reynolds number. Re is 10^5 in the experiments and 5×10^4 in the simulations, indicating the fluid inertia dominates over viscous effects. We artificially increased the viscosity of air by a factor of 10 to ensure that the fluid field could be simulated without using finer meshes. For the feeding trials, $k = 0.25$ was used for simulating live larvae.

The response of the system is also presented using dimensionless variables. We normalized the three state variables, pressure p, air velocity u, and height of the larvae bed h. We define their dimensionless counterparts P^*, U^*, and H^* (**Figure 2A**) as:

$$P^* = \frac{p}{M_{larvae} g/A} \tag{3}$$

$$U^* = \frac{u}{u(P^* = 1)} \tag{4}$$

$$H^* = \frac{h}{V_{larvae}/A}, \tag{5}$$

where M_{larvae} and V_{larvae} are the total mass and volume of the larvae in the container, g the gravitational acceleration, and A the cross-sectional area of the chamber. Dimensionless pressure $P^* = 1$ signifies the fluidization condition, which arises when the total larvae weight equals the applied air pressure force (which develops as the flow is forced through the porous medium). In this condition, the container is fluidized such that particles enter a collisional regime and do not experience enduring contacts. For most experiments, $P^* = 1$ when the airflow velocity reached 1.6 m/s. Therefore, we used 1.6 m/s to normalize the velocity. H^* is normalized by the height of the larvae if they had filled all the gaps among them. H^* equals the inverse of the volume fraction.

3 RESULTS

3.1 Fluidization

Aggregations of black soldier fly larvae behave like fluids even without external fluid flows (**Supplementary Video S1** and **Figure 1A**). For example, as the container of larvae is tilted, the larvae rearrange themselves, creating a level interface. Their movement creates a new configuration minimizing the center of mass. **Figure 1B** and **Supplementary Video S1** shows the orientation of the surface θ due to a series of inclinations of the container. As we moved the container, the magnitude of θ initially increased but then θ converged to zero within tens of seconds. Similarly, after larvae were forced to separate and occupy more volume due to the fluidization process (**Figure 1E**), larvae returned to the original densely-packed state through a continuous movement of individuals. Plastic spheres within the top layers of the larva aggregates exhibit approximate Brownian motion as shown in **Figures 1C,D**. Through tracking the movement of the spheres, we fit the force acting on each sphere to a 2D Gaussian distribution and obtained a standard deviation of 6.3 mN. Since the spheres are similar in size to the larvae, this provides an estimate for the force a larva within the aggregate would experience due to their neighbors' activity. The propulsive force generated by the larva itself should also be on the same order of magnitude.

We performed 25 fluidization-defluidization cycles using both live and dead larvae (**Supplementary Video S2**). **Figure 2B** shows the dimensionless height H^* and air pressure P^* of the aggregation as functions of time, with dead larvae shown by the black curves and live larvae by the red curves (Source data provided in **Supplementary Table S1**). To highlight the magnitude of hysteresis, **Figure 2C** plots the state variables H^* and P^* against U^*. As the flow velocity increases and then

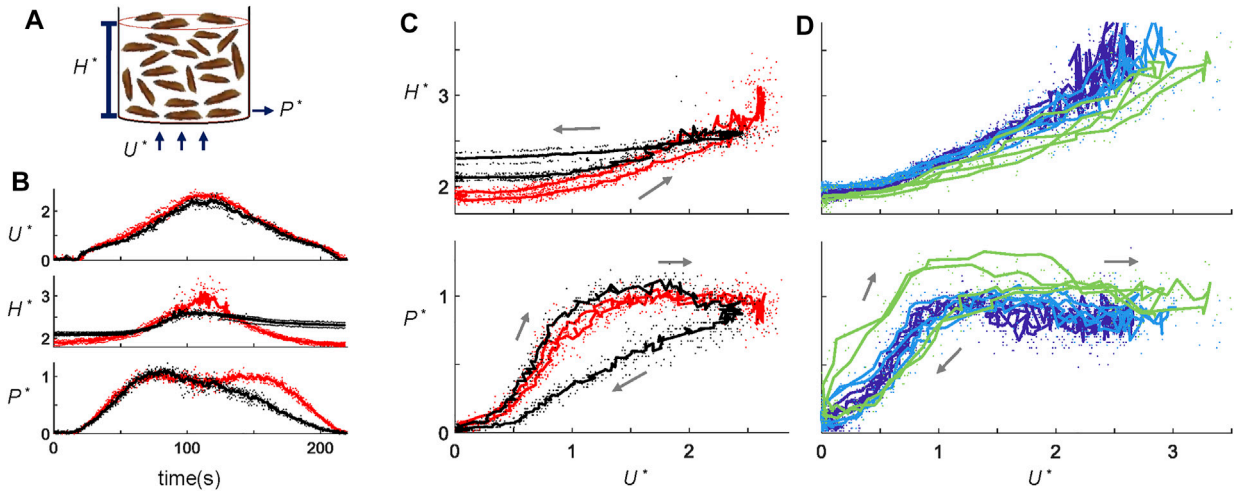

FIGURE 2 | Larva fluidization-defluidization experiments. **(A)** Schematic of the fluidization setup. **(B)** Time series of dimensionless variable U^*, H^*, and P^* in a fluidization cycle for 300 g "long" larvae at the 1x ramping rate. Red shows the live larva trials, and black shows the dead larva trials. **(C)** Hysteresis diagram plotting H^* and P^* as functions of U^*. Data and the color scheme are the same as **(B)**. **(D)** Hysteresis diagram for 300 g short larvae at ramping rates of 1x (dark blue), 2x (light blue), and 4x (green). Dots represent the raw data, whereas the solid lines show the average across trials.

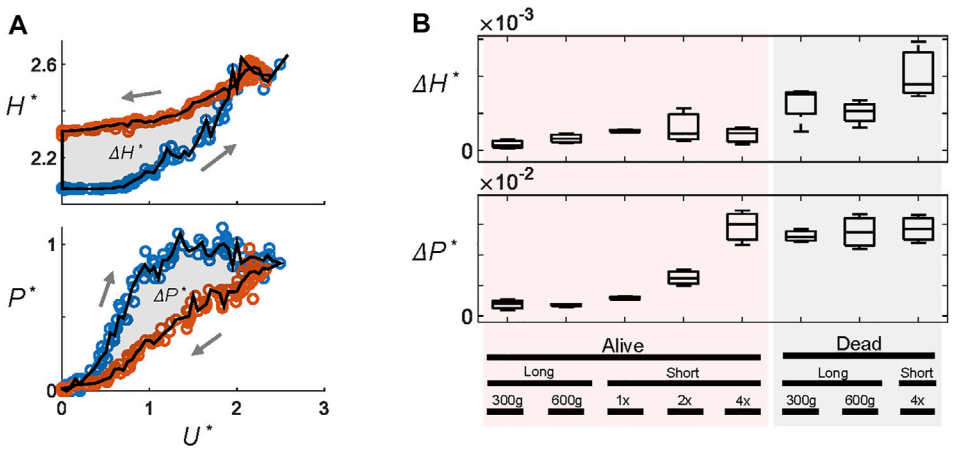

FIGURE 3 | The magnitude of hysteresis. **(A)** Hysteresis metrics ΔH^* and ΔP^* are defined as the area between the curves in the hysteresis diagrams such as **Figures 2C,D**. Here, blue and red circles represent ramping up and down, respectively. **(B)** ΔH^* and ΔP^* under different flow conditions. "Long" and "short" refer to the size of the larvae used. Other conditions include the total weight of larvae (300 g or 600 g) and the ramp rate (1x, 2x, and 4x). All long larva experiments are performed at 1x, and all short larvae experiments are 300 g.

decreases, dead larva aggregates expand and then contract. However, dead larvae do not return to their original height at the end of the fluidization-defluidization cycle. Instead, they form a more loosely packed configuration. This results in hysteresis, where the state of the system depends not only on the applied flow rate but also on its history. Such hysteresis is a characteristic of fluidized beds, as shown by numerous experiments with various granular systems, from sand to glass particles [18, 23]. The dimensionless pressure P^* also shows hysteresis, but a second mechanism becomes apparent. Similar to the fluidization of closely packed glass beads, during the airflow increase, pressure P^* of dead larvae exceeds 1 momentarily. At this moment, the air pressure force exceeds the gravity on the larvae since the aggregation cannot expand fast enough to fluidize. As U^* later decreases, dead larvae aggregates settle down to a more porous arrangement, allowing P^* to be lower than before.

In contrast to typical granular systems, live larvae do not show hysteresis. As shown by the red curves in **Figure 2C**, height H^* and pressure P^* are both single-valued functions of U^*. The larvae activity evidently erases the memory effect of the granular material, making the fluidization-defluidization cycles

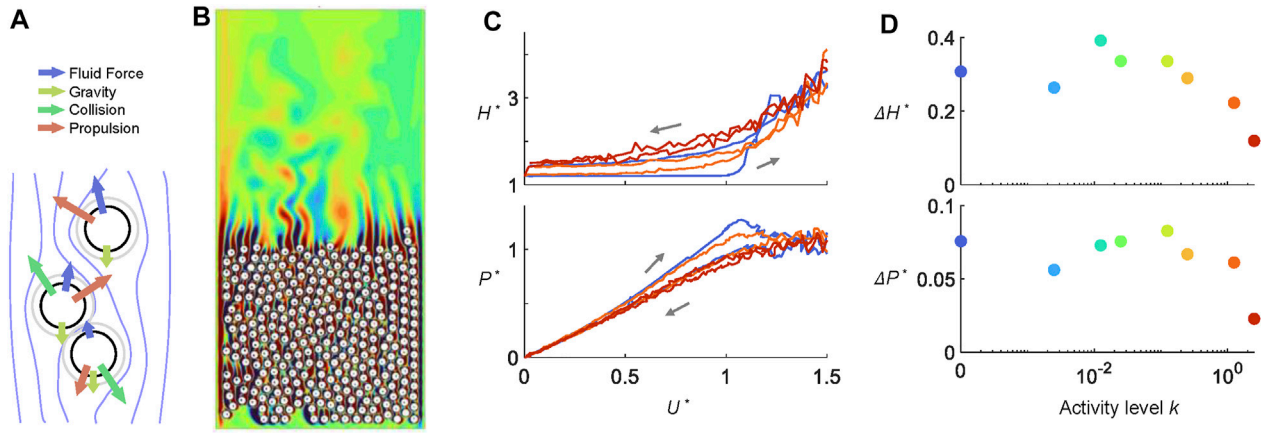

FIGURE 4 | Larva fluidization-defluidization simulations. **(A)** Agents move under fluid forces, collisional forces, and a random force that mimics larval activity. **(B)** A snapshot from the simulation of 396 active cylinders in ramping air flows. Contour colors represent the magnitude of the vorticity field. **(C)** Hysteresis diagram and **(D)** hysteresis metric ΔH^* and ΔP^* of cylinders at various activity level k. In both **(C–D)**, k = 2.5 is shown in red, k = 1.25 in orange, and k = 0 in blue.

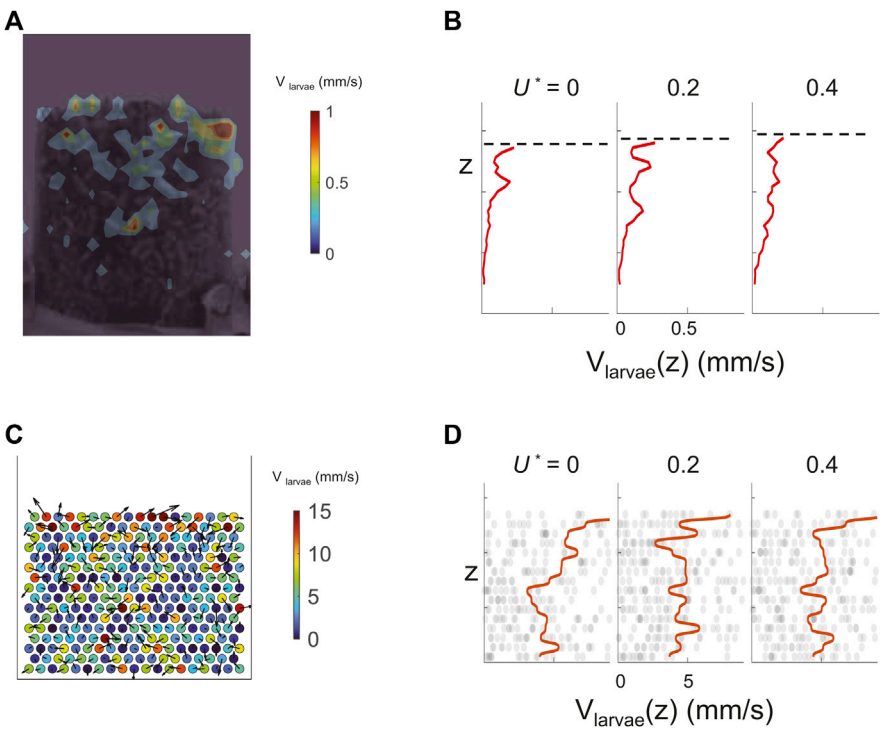

FIGURE 5 | Top layers of both live and simulated larvae move more rapidly. **(A)** Larval speed distribution at the boundary measured using Particle Image Velocimetry (PIV). The color bar shows the scale in mm/s. **(B)** Average larval speed (x-axis) at different elevation z (y-axis). Elevation level z corresponds to that in A. Dash lines mark the top surface of the larva aggregates in each snapshot. **(C)** Speed of active cylinders at the onset of fluidization is shown using colors and arrows. The color bar shows the scale in mm/s. **(D)** Average cylinder speed from simulation, the axes arrangement is the same as **(B)**.

independent of their history. We saw earlier that without flow, larvae rearranged to assume the lowest gravitational potential. Live larval aggregations expand earlier during increasing flow and pack themselves for a more extended period during decreasing airflow. We hypothesize that the rearrangement in live larval aggregates requires a specific time scale. If velocity U^* is varied at a rapid enough pace, larvae would not have enough time to rearrange, and pressure P^* and height H^* would show hysteresis.

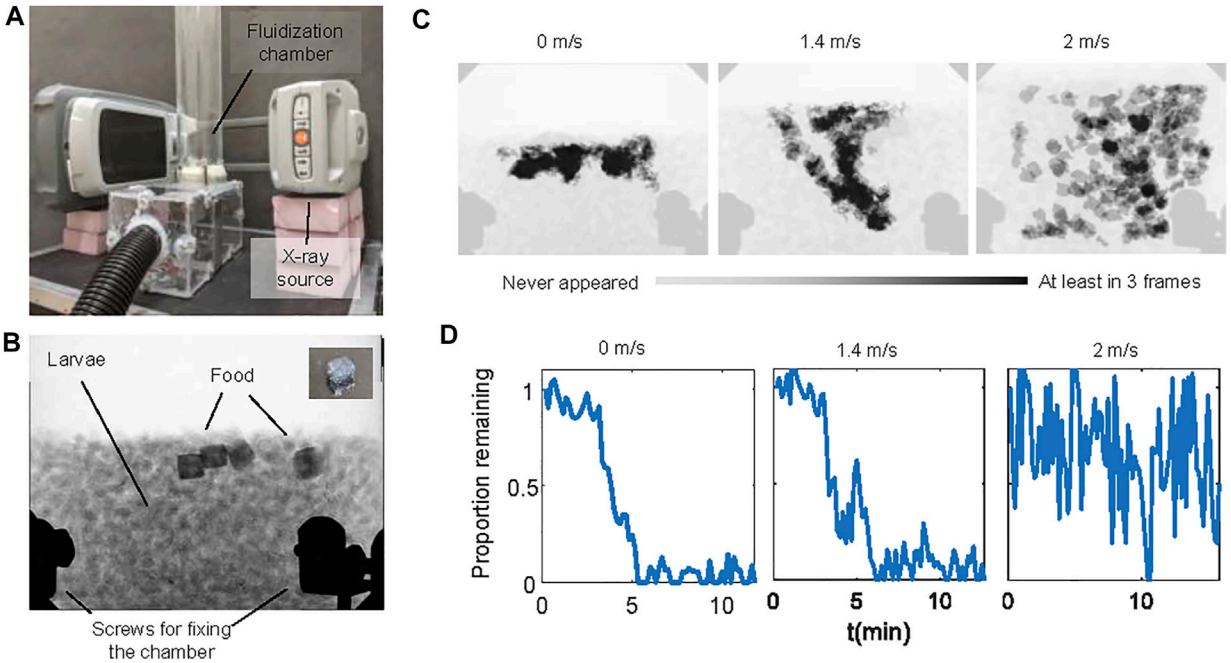

FIGURE 6 | Larva feeding experiments with cubic jellies. **(A)** The experimental setup for the feeding experiment consists of the fluidization chamber and a portable x-ray machine. **(B)** A representative X-ray image of the experiment. Darker regions near the top of the aggregations are food. The inset shows a picture of the cube-shaped jelly. The black shades near the bottom of the image are the screws of the chamber. **(C)** The spatial distribution of the food using time-lapse photography. Light gray shows that the food never appeared in the location throughout the video. Black shows that the food appeared at least in three video frames. **(D)** Time series of the proportion of food remaining in the chamber under no flow, slow flow, and fast flow conditions. Larvae used in here are medium size (see the *Materials and Methods* section).

To test this hypothesis, we performed experiments at various air ramp rates, from 2 cm/s^2 (1x) to 8 cm/s^2 (4x). Long larvae were used for **Figure 2D**. Short larvae in **Figure 2D** behave the same as the long larvae in **Figure 2C** at the 1x ramp rate. Nonetheless, **Figure 2D** shows that indeed, when the airflow increases at 8 cm/s^2, four times the original rate, even live larvae demonstrate hysteresis (bright green). Why do live larvae exhibit hysteresis at high ramp raptes? Larval aggregations respond similarly at all flow decelerations. However, at the highest accelerations, they do not have enough time to rearrange and adjust to the increasing flow, thus displaying hysteresis. The inability to cope with this time scale indicates that live larval aggregations in our system can be considered as fluids if the time scale of the disturbance is more than approximately 25 s, the duration of air acceleration at 4x ramp rate. This time scale is comparable to the time for a larva to crawl its body length, around 7 seconds ([24]).

We quantify the extent of hysteresis, ΔH^* and ΔP^*, as the area between the hysteresis diagrams (**Figure 3A**). **Figure 3B** summarizes the fluidization trials and shows that live larvae show hysteresis only at higher ramp rates. Dead larvae show hysteresis under all conditions.

The simulations recover the experimental measurements qualitatively through modeling larval activity with propulsive forces that act in random directions and magnitudes. We simulated 296 discs that move under physical forces as well as active propulsive forces [**Figures 4A,B** (**Supplementary Video S3**)]. **Figure 4C** shows as the dimensionless activity levels k increases from 0 to 2.5, the hysteresis in both height H^* and pressure P^* decreases. The ramp rate was 11.2 times the original speed, or 2.8 times the fastest ramp rate performed in experiments. The response during the ramp-up period is similar to those in **Figures 2C,D**. Active discs rise earlier and more smoothly. However, due to lack of friction and other simplifications made in the simulation, during the ramp down, H^* is lower, and P^* is higher compared to dead larvae (**Figures 2C,D**). **Figure 4D** demonstrates that ΔH^* and ΔP^* start to decrease when $k > 1$ or when the random propulsion is comparable with the scale of the air pressure force. Our simulation suggests that the hysteresis-free behavior of live larval aggregation does not require active strategies that involve sensory information. Instead, it can be achieved simply through larvae exerting random propulsive forces (achieved in their case via body self-deformation and locomotion).

3.2 Feeding and Mixing

Figure 5 shows that under low airflow, the larva motion is suppressed at positions deeper in the aggregation. In both experiments and simulations, with applied flow velocity from $U^* = 0$ to $U^* = 0.6$, larvae closer at the top surface move more rapidly than larvae in the bulk. This is because the contact forces among larvae are higher for the bottom layers due to the weight on top of them. The effect of self-propulsion is therefore negligible. In contrast, with little weight to support, larvae at

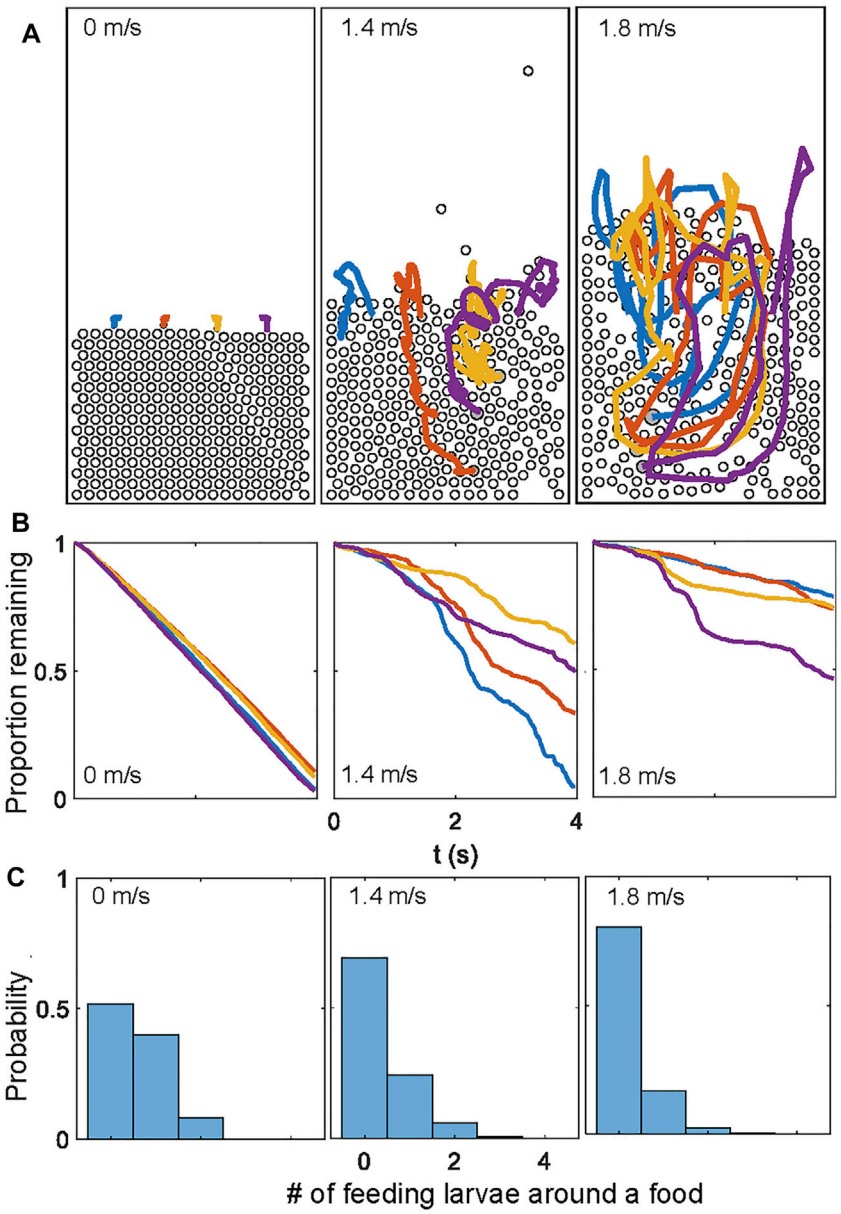

FIGURE 7 | Larva feeding simulations for different constant fluidization air speeds. **(A)** Trajectories of the four food particles. **(B)** Time series of the proportion of food remaining in the simulation over approximately 4 seconds. The feeding rates are significantly sped up in the simulations. **(C)** The histogram of numbers of "eating" larvae, defined as those contacting and consuming food in each time step.

the top layers "flow" freely. This points to the challenge of feeding in dense aggregations. Food may be mixed and consumed among the larvae close to the top surface, but larvae at the bottom layers remained unfed.

We confirmed the non-uniformity of motion using X-ray imaging experiments where we fed the larvae cubes of jelly. **Figures 6A–C** and **Supplementary Video S4** show that without flow, jelly cubes remain at the top of the aggregation. Under airflow, more layers of larvae can move, and the food can be distributed deeper into the aggregations. When the air speed is high (2 m/s), the larval aggregation is fully fluidized, and both food and larvae travel rapidly in the chamber. Surprisingly, despite a broader spatial distribution, jelly cubes were consumed at comparable or slower rates with respect to the no-flow condition (**Figure 6D**). Under fast flow, large pieces of food were still found after 15 min. However, jelly cubes fed to larvae without flow or with slow flow disappeared in approximately 5 min.

Similar conclusions were reached through simulating food particles that decreased in areas at a rate proportional to the number of neighbors (**Supplementary Video S5**). While a higher flow mixes the food more uniformly (**Figure 7A**), the feeding rate decreases (**Figure 7B**). The simulations also provide a potential reason for this observation: as food and larvae are agitated by rapid

flows, larvae are more likely to be suspended in mid-air without contacting the food (**Figure 7C**). This suggests that a moderate flow rate would be optimal for feeding dense aggregations of larvae. Such moderate flows prevent the larvae from being airborne for a prolonged period of time, while allowing food to travel deeper into the aggregation. The optimal flow rates for larval feeding remains to be determined in future research.

4 DISCUSSION

Mixing granular materials is critical to a wide range of industrial applications. Typically, it is achieved through applying external forces [25–28]. Common strategies require motions of the container, such as a rotating drum [29] or a manually tossed wok [30]. Air-fluidization provides another method to mix particulate matter since it does not require intrusion into or boundary-driven agitation of the particles, allowing nearly uniform particle motion. Black soldier fly larvae, on the other hand, can move like a fluid without airflow. Their activity propels them in random directions, which allows the aggregation to flow and minimize its gravitational potential. However, mixing through larval activity alone is limited since gravitational forces dominate their activity in deeper layers via the high contact forces due to increasing "lithostatic pressure". By carefully varying the airflow from below, black soldier fly farmers may optimize mixing, maximize larva feeding rates, and improve their use of space. Future research could help elucidate the optimal conditions for larva feeding, such as the flow rate and the food density.

Our work expands upon knowledge of biological aggregations, which have been shown to demonstrate fluid-like behaviors. These aggregations can be considered active granular fluids, where the animal movement prevails over the contact forces among individuals. As a result, live larva aggregates do not jam like grains in a fluidization-defluidization cycle. Active granular fluids span from the scale of plant cells [31] to that of fly larvae and can be realized with centimeter-scale robots [32]. It remains an open question how these active fluids consisting of millimeter-scale or micrometer-scale constituents behave differently from traditional fluids made up of nanometer-scale molecules. More intriguingly, how do fluids of different scales interact with each other? This paper presents one example of such interactions. More research is required to describe the behaviors of such systems.

The simulations presented in this paper are among the first to incorporate active particle dynamics into particle suspensions in fluids. Our simulations had several simplifications. To reduce running time, we used two-dimensional particles and decreased fluidization-defluidization cycle durations. We also used a rigid circular geometry for the larvae. Assuming frictionless particles may have reduced jamming effects during decreasing airflow. Lastly, larval activities were simplified as random body forces. Therefore, experimental observations such as larva squeezing through narrow gaps could not be simulated. Despite these shortcomings, our simulations successfully recovered features of fluidization, such as the plateauing of air pressure as airflow velocity increases, through capturing complex agent-environment interactions. The simplified form of activity in our simulation also caused the collectives to behave like fluids and reduced the magnitude of hysteresis, matching the behavior of live larval aggregates at least qualitatively. The relative success in these simulations paves the way for future studies that focus on animal collective behaviors in moving fluids.

DATA AVAILABILITY STATEMENT

The original contributions presented in the study are included in the article/**Supplementary Material**, further inquiries can be directed to the corresponding author.

AUTHOR CONTRIBUTIONS

HK, OS, DH, and DG contributed to the conception and design of the study. OS performed preliminary experiments. HK, GC, performed the experiments and collected data. EA prepared experimental materials. HK designed and performed the simulations. HK performed video processing. HK wrote the first draft of the manuscript. All authors contributed to manuscript revision, read, and approved the submitted version.

FUNDING

This study is supported by the Army research office (72989-EG and W911NF-12-R-001), ARO MURI award (W911NF-19-1-023), and NSF Physics of Living Systems Grant (PHY-1205878).

ACKNOWLEDGMENTS

This research was supported in part through research cyberinfrastructure resources and services provided by the Partnership for an Advanced Computing Environment (PACE) at the Georgia Institute of Technology, Atlanta, Georgia, United States. Black soldier fly larvae were provided by the generous support from EVO Conversion Systems LLC. We thank Andras Karsai for providing feedback on our manuscript.

SUPPLEMENTARY MATERIAL

The Supplementary Material for this article can be found online at: https://www.frontiersin.org/articles/10.3389/fphy.2021.734447/full#supplementary-material

Supplementary Video S1 | Fluid-like behavior of live larval aggregates in a container 10x.

Supplementary Video S2 | Air-fluidized aggregates of live and dead larvae 16x.

Supplementary Video S3 | Simulations of fluidized beds of active disks.

Supplementary Video S4 | Feeding larva aggregates under airflow 100x.

Supplementary Video S5 | Simulations of larvae feeding under airflow.

Supplementary Table S1 | An excel sheet of time series of U^*, H^*, P^* in fluidization experiments.

REFERENCES

1. Gustavsson J, Cederberg C, Sonesson U, Van Otterdijk R, Meybeck A. *Global Food Losses and Food Waste Section 3.2 (Study conducted for the International Congress "Save Food!" at Interpack2011, Düsseldorf, Germany) (FAO, Rural Infrastructure and Agro-Industries Division, 2011)*. Available at https://www.nature.com/articles/nature10452#Bib1 (2011).
2. Hall KD, Guo J, Dore M, Chow CC. The Progressive Increase of Food Waste in america and its Environmental Impact. *PloS One* (2009) 4:e7940. doi:10.1371/journal.pone.0007940
3. Diener S, Zurbrügg C, Tockner K. Conversion of Organic Material by Black Soldier Fly Larvae: Establishing Optimal Feeding Rates. *Waste Manag Res* (2009) 27:603–10. doi:10.1177/0734242x09103838
4. Hale O. Dried Hermetia Illucens Larvae (Diptera: Stratiomyidae) as a Feed Additive for Poultry. *Ga Entomol Soc J* (1973) 8:16–20.
5. Newton GL, Booram CV, Barker RW, Hale OM. Dried Hermetia Illucens Larvae Meal as a Supplement for Swine. *J Anim Sci* (1977) 44:395–400. doi:10.2527/jas1977.443395x
6. Li Q, Zheng L, Cai H, Garza E, Yu Z, Zhou S. From Organic Waste to Biodiesel: Black Soldier Fly, Hermetia Illucens, Makes it Feasible. *Fuel* (2011) 90:1545–8. doi:10.1016/j.fuel.2010.11.016
7. Diener S, Zurbrügg C, Gutiérrez FR, Nguyen DH, Morel A, Koottatep T, et al. Black Soldier Fly Larvae for Organic Waste Treatment Prospects and Constraints. *Proc WasteSafe* (2011) 2:13–5. doi:10.1007/s12649-011-9079-1
8. Sheppard DC, Tomberlin JK, Joyce JA, Kiser BC, Sumner SM. Rearing Methods for the Black Soldier Fly (Diptera: Stratiomyidae): Table 1. *J Med Entomol* (2002) 39:695–8. doi:10.1603/0022-2585-39.4.695
9. Sheppard C. House Fly and Lesser Fly Control Utilizing the Black Soldier Fly in Manure Management Systems for Caged Laying Hens. *Environ Entomol* (1983) 12:1439–42. doi:10.1093/ee/12.5.1439
10. Parra Paz AS, Carrejo NS, Gómez Rodríguez CH. Effects of Larval Density and Feeding Rates on the Bioconversion of Vegetable Waste Using Black Soldier Fly Larvae Hermetia Illucens (L.), (Diptera: Stratiomyidae). *Waste Biomass Valor* (2015) 6:1059–65. doi:10.1007/s12649-015-9418-8
11. Shishkov O, Hu M, Johnson C, Hu DL. *Systems and Methods for Cooling a Plurality of Containerized Animals*. WO 2017/106475 Al (2019).
12. Cheng JYK, Chiu SLH, Lo IMC. Effects of Moisture Content of Food Waste on Residue Separation, Larval Growth and Larval Survival in Black Soldier Fly Bioconversion. *Waste Manag* (2017) 67:315–23. doi:10.1016/j.wasman.2017.05.046
13. Palma L, Ceballos SJ, Johnson PC, Niemeier D, Pitesky M, VanderGheynst JS. Cultivation of Black Soldier Fly Larvae on almond Byproducts: Impacts of Aeration and Moisture on Larvae Growth and Composition. *J Sci Food Agric* (2018) 98:5893–900. doi:10.1002/jsfa.9252
14. Kunii D, Levenspiel O. *Fluidization Engineering*. Oxford, United Kingdom: Butterworth-Heinemann (1991).
15. Sundaresan S. Instabilities in Fluidized Beds. *Annu Rev Fluid Mech* (2003) 35:63–88. doi:10.1146/annurev.fluid.35.101101.161151
16. Jackson R. *The Dynamics of Fluidized Particles*. Cambridge, United Kingdom: Cambridge University Press (2000).
17. Ojha R, Menon N, Durian DJ. Hysteresis and Packing in Gas-Fluidized Beds. *Phys Rev E* (2000) 62:4442–5. doi:10.1103/physreve.62.4442
18. Goldman DI, Swinney HL. Signatures of Glass Formation in a Fluidized Bed of Hard Spheres. *Phys Rev Lett* (2006) 96:145702. doi:10.1103/physrevlett.96.145702
19. Thielicke W, Stamhuis E. Pivlab–towards User-Friendly, Affordable and Accurate Digital Particle Image Velocimetry in Matlab. *J Open Res Softw* (2014) 2:30. doi:10.5334/jors.bl
20. Popinet S. *Basilisk* (2014). Available from: http://basilisk.fr (Accessed December 2020).
21. Schlichting H, Gersten K. *Boundary-layer Theory*. New York, United States: Springer (2016).
22. Courant R, Friedrichs K, Lewy H. Uber die partiellen Differenzengleichungen der mathematischen Physik. *Math Ann* (1928) 100:32–74. doi:10.1007/bf01448839
23. Goldman DI. *Pattern Formation and Fluidization in Vibrated Granular Layers, and Grain Dynamics and Jamming in a Water Fluidized Bed*. Ph.D. Thesis. Ann Arbor, MI: The University of Texas at Austin; ProQuest Dissertations Publishing (2002).
24. Shishkov O, Hu M, Johnson C, Hu DL. Black Soldier Fly Larvae Feed by Forming a fountain Around Food. *J R Soc Interf* (2019) 16:20180735. doi:10.1098/rsif.2018.0735
25. Jaeger HM, Nagel SR, Behringer RP. Granular Solids, Liquids, and Gases. *Rev Mod Phys* (1996) 68:1259–73. doi:10.1103/revmodphys.68.1259
26. Goldhirsch I. Rapid Granular Flows. *Annu Rev Fluid Mech* (2003) 35:267–93. doi:10.1146/annurev.fluid.35.101101.161114
27. Jaeger HM, Nagel SR. Physics of the Granular State. *Science* (1992) 255:1523–31. doi:10.1126/science.255.5051.1523
28. Campbell CS. Rapid Granular Flows. *Annu Rev Fluid Mech* (1990) 22:57–90. doi:10.1146/annurev.fl.22.010190.000421
29. Schlick CP, Fan Y, Umbanhowar PB, Paul B, Ottino M, Lueptow RM. Granular Segregation In Circular Tumblers: Theoretical Model And Scaling Laws. *J Fluid Mech* (2015) 765:632–652.
30. Ko H, Hu DL. The Physics of Tossing Fried rice. *J R Soc Interf* (2020) 17:20190622. doi:10.1098/rsif.2019.0622
31. Bérut A, Chauvet H, Legué V, Moulia B, Pouliquen O, Forterre Y. Gravisensors in Plant Cells Behave like an Active Granular Liquid. *Proc Natl Acad Sci USA* (2018) 115:5123–8. doi:10.1073/pnas.1801895115
32. Li S, Dutta B, Cannon S, Daymude JJ, Avinery R, Aydin E, et al. Programming Active Cohesive Granular Matter with Mechanically Induced Phase Changes. *Sci Adv* (2021) 7(17):eabe8494. doi:10.1126/sciadv.abe8494

Conflict of Interest: The authors declare that the research was conducted in the absence of any commercial or financial relationships that could be construed as a potential conflict of interest.

frontiers in Physics

ORIGINAL RESEARCH
published: 06 December 2021
doi: 10.3389/fphy.2021.744428

Photogyrotactic Concentration of a Population of Swimming Microalgae Across a Porous Layer

Praneet Prakash[1] *and Ottavio A. Croze*[2]*

[1]*Department of Applied Mathematics and Theoretical Physics, Centre for Mathematical Sciences, University of Cambridge, Cambridge, United Kingdom,* [2]*School of Mathematics, Statistics and Physics, Newcastle University, Newcastle Upon Tyne, United Kingdom*

The light environment controls the swimming of microalgae through a light-seeking and avoiding behaviour, which is known as phototaxis. In this work, we exploit phototaxis to control the migration and concentration of populations of the soil microalga *Chlamydomonas reinhardtii*. By imaging a suspension of these microalgae in a cuvette illuminated from above by blue light, we study how phototaxis changes the stability of the suspension and demonstrate how a thin, porous layer at the top of the cuvette prevents phototaxing microalgae from sinking, leading to the up-concentration of the microalgae in the region above the porous layer. We discuss the potential implications of our findings for microalgae in biotechnological applications and the natural environment.

Keywords: microswimmers, microalgae, phototaxis, light environment, porous media, biotechnology

OPEN ACCESS

Edited by:
Natasha Mhatre,
Western University, Canada

Reviewed by:
Yongyun Hwang,
Imperial College London,
United Kingdom
Azusa Kage,
Gakushuin University, Japan

***Correspondence:**
Ottavio A. Croze
otti.croze@newcastle.ac.uk

Specialty section:
This article was submitted to Social Physics, a section of the journal Frontiers in Physics

Received: *20 July 2021*
Accepted: *11 October 2021*
Published: *06 December 2021*

Citation:
Prakash P and Croze OA (2021) Photogyrotactic Concentration of a Population of Swimming Microalgae Across a Porous Layer. Front. Phys. 9:744428. doi: 10.3389/fphy.2021.744428

1 INTRODUCTION

Environmental stimuli, such as chemical gradients, gravity, light and flow shear, bias the motion of swimming microorganisms [1–3]. At the level of a population, these biases cause the formation of spectacular, often macroscopic, patterns. Inasmuch as they cause cells to congregate and interact, these patterns can be considered a form of social behaviour. Paradigmatic examples of pattern formation in swimming microbes are the waves exhibited by bacteria [4, 5] and slime mold [6] sensing chemical gradients (chemotaxis), or the bioconvection patterns formed by ciliates and microalgae [7], responding to a combination of gravity and flow shear (gyrotaxis). More specifically, the latter is a bias resulting from the combination of a torque on a swimmer due to shear in the flow and one due to gravity, caused by asymmetry in body shape, mass distribution and/or between body and flagella [8].

Recent decades have seen a marked increase in the mechanistic understanding of how biases act at the individual swimmer level and how this affects macroscopic patterns. For example, mathematical models of flowing and dispersing gyrotactic suspensions of microalgae [9–12] have been compared with measurements of algae in an uniformly rotating flow [12], sheared bioconvection patterns [13], populations of microalgae dispersing in pipe flow [14], and laboratory versions of oceanic thin layers [15]. For comprehensive summaries of current work, we refer the reader to reviews covering recent progress in the physics of swimming microbes [16, 17] and bioconvection [7]. This area of research is also closely related to active matter [18] comprising biological swimmers, as we have just described, but also synthetic [19] and biohybrid ones [20–22].

In this study, we focus on how light can be used to control and concentrate a suspension of *Chlamydomonas reinhardtii* microalgae. The bias of swimming by light is known as phototaxis and is an adaptation that allows *C. reinhardtii* and other photosynthetic microorganisms to find optimal

levels of light needed to grow [23, 24]. Recent studies have demonstrated how exposing a suspension of microalgae to light can dramatically alter the patterns they form, and even generate new ones [25]. In the absence of phototactic stimulation, bioconvection patterns form in shallow layer suspensions, e.g., a thin layer of fluid in a Petri dish, as a result of the tendency of microalgae to swim upwards (gravitaxis) and form a dense layer of cells (denser than the fluid they are suspended in) at the top of the suspension [7]. This is unstable and results in sinking "plumes," which drive a bioconvective pattern, reinforced by the cells' response to the flow (gyrotaxis), which enhances the instability by driving cells towards downwelling plumes. Bees and Williams investigated how white light from above and below a suspension of the microalga *Chlamydomonas augustae* in a Petri dish alters the stability of bioconvection patterns, quantified by measuring the dominant initial pattern wavelength [26]. As well as changes to existing bioconvection patterns, recent investigations have also explored how shining light into a suspension can stimulate patterns that would not otherwise be there. For example, bioconvection patterns for the microalga *Euglena gracilis* were induced by illuminating a Hele-Shaw cell from below [27]. In the absence of light, the patterns vanished. A study by Arrieta *et al.* also demonstrated how quickly bioconvective structures can be created, and even reconfigured by light, using it to generate "blinking plumes"; the study also provided a model of this (ignoring gyrotactic effects), and reported good agreement with the experimental observations [28].

Aside from some of the studies above, several investigations in the literature have provided theoretical analyses of bioconvection in the presence of phototaxis. These have recently been reviewed comprehensively [7, 25]. We will discuss briefly here only the model by Williams and Bees [26], which includes phototactic and gyrotactic effects, and encompasses several simpler models that have been recently proposed. The model equations, summarized in Supplementary Appendix SA, describe the coupled dynamics of fluid flow, described by a Navier-Stokes equation, and a population of swimmers, described by a continuity equation. The probability density function (PDF) for the swimmer orientation obeys a Fokker-Planck equation, with a deterministic bias due to the combined action of flow, gravity and light. Taking moments of this PDF provides the mean swimming velocity and diffusivity in the continuity equation. Williams and Bees considered three alternative models to describe the effect of phototaxis on the swimmers [26]. In model A, the speed of the cells is dependent on light intensity (photokinesis), while gravitaxis and gyrotaxis are not affected. In model B, light causes a change in the bottom-heaviness of the cells, inducing an effective gravi/gyrotactic torque. In model C, cells respond directly to an effective torque due to light, dependent either of the light direction or the gradient of its intensity (the latter was also used by [23, 28]). Williams and Bees used their model to predict the stability of bioconvection patterns for a suspension illuminated from above and below, in qualitative agreement with the experiments with *C. augustae* microalgae in a Petri dish mentioned above [29].

Our study combines a photogyrotactic suspension with porous media, materials with voids through which microbes can swim. In the environment, these can occur as the spaces between particles in soils [30]; in the laboratory they can be patterned using microfluidics, or assembled using gels or beads. There has been much recent interest in the behaviour of swimming microorganisms, such as bacteria, in porous media [31]. A few recent studies have also considered how the transport of microalgae is altered in porous chambers [32] and microfluidic arrays [33], including the deflection of negatively phototactic swimmers through obstacle arrays [34].

Thus, it is known how porous media change the transport of microswimmers and it is well established that light perturbs, and drives instabilities in, suspensions of phototactic microalgae, visibly causing the concentration of cells. However, the systematic concentration of microalgae at a given location exploiting photogyrotaxis, which was suggested by Kessler as early as 1982 [35], has hitherto not been demonstrated. In this study, we aim to show that a unique combination of phototaxis and porous media permits the concentration of microalgae at a given location in a container. We report the first "milliliter-scale" experiments demonstrating how photogyrotactic microalgae can be concentrated above a porous layer of beads overlaid onto a metal mesh. We also observe interesting photogyrotactic instabilities and accumulations in the suspension, which have not been previously reported. An "essential" model to qualitatively account for the temporal evolution of the average concentration of cells above the porous layer and for their initial spatial distribution is also developed, leaving a full theoretical analysis of the photogyrotactic dynamics leading to this concentration for future work. Finally, we discuss how, a scaled-up version of our set-up could provide the basis for a new and efficient method to harvest swimming microalgae industrially. This is desirable since harvesting microalgae industrially is expensive (up to 20–30% of the total production costs [36]), and represents a bottleneck in the production of bioproducts from microalgae.

2 MATERIALS AND METHODS

2.1 Experimental Methods

We used the wild-type algal strain *Chlamydomonas reinhardtii* (CC125) for our studies. Single colonies of these algae were picked from slant cultures and inoculated into Tris-minimal growth media (Supplemental Material Section S1). These media are based on the standard TAP medium [37], but omit acetic acid and HCl is used to titrate to pH 7, and were chosen to ensure purely photosynthetic growth of cells so that they would be synchronised to light-dark cycles, following [38]. Indeed, liquid cultures of the microalgae were then grown in a 14:10 h light-dark cycle on a rotary shaker at 100 rpm and continuously bubbled with air, as in [38]. The shaking incubator (Infors Minitron) was maintained at a temperature of 25°C, and provided photosynthetically active radiation (PAR) at 315 – 325 μmol/m^{2}s, as measured with a PAR meter (Skye SKP200). It took around 7 – 10 days for a culture to reach a concentration of 1 – 2 million cells/mL. Thereafter, it was sub-cultured by mixing 10 mL of grown algae into 140 mL of fresh Tris-minimal media until the cell count, measured with a Z2

Coulter counter (Beckman Coulter, Brea, CA), reached 1.5 million/mL; this took about a week. Subsequently, algae were diluted everyday by replacing 50 ml of the culture with fresh media. This protocol maintains the algal count between 1.2 – 1.5 million/mL with mean diameter of 4.5 – 5 μm (estimated by using the Coulter counter); the subcultures can be used for 10 – 15 days. Care was taken to do experiments with microalgae harvested during the light phase of the growing cycle to avoid variations in the swimming parameters, and in particular the swimming speed, which have been observed at the onset the dark phase [38]. All the experiments were carried out in square plastic cuvettes of external dimensions $12.5 \times 12.5 \times 45$ mm^3 (Sigma-Aldrich, filling volume 2.5 ml) filled with 2 ml of algal suspension. The imaging was performed using a monochrome CMOS camera (Pointgrey, Grasshopper3 GS3-U3-23S6M) fitted with a macro lens (Sigma 17–70 mm f2.8-4). The cuvette was illuminated from the side by a red (660 nm) square 100 × 100 mm LED array (Advanced Illumination BL1960, Rochester, VT, United States), as shown in **Figure 1A**. This illumination was used as it allowed to image the suspension laterally without triggering a phototactic response [3]. The concentration of microalgae in the cuvette was estimated from the transmitted light intensity across the short dimension of the cuvette by applying the Lambert-Beer law: the intensity recorded by the camera (measured in arbitrary units, a. u.) can be converted into algal concentration (million/mL) from the calibration curve shown in Supplementary Figure S1. The intensity decays as $I = I_o \exp(-A.C)$, where $I_o = 179$ is the intensity in arbitrary units in the presence of cuvette containing just Tris-min medium, $A = 0.22$ is the attenuation coefficient and C is the algal concentration in million/mL. This exponential decay provides a mapping to concentration, with an excellent fit for intensity data higher than 50 a.u., and an R-squared value of 0.99 for a fit across the range of values (see Supplementary Figure S1). In the experiments described below, the swimmer concentration was then quantified from images by first measuring integrated pixel intensity in selected regions (see e.g., Supplementary Figure S2) of the cuvette using ImageJ, and then mapping to actual concentration values using the calibration curve just described.

For the phototaxis experiments, a blue LED (Thorlabs M470L2, nominal wavelength 470 nm) is mounted above the cuvette at a distance of 47 mm from its base. Using a PAR meter, the light intensity at the base of cuvette containing only the media was 16 – 18 μmol/m^{2}s, whereas the intensity immediately below the LED is 150 – 160 μmol/m^{2}s. The cuvette is separated into an upper "harvest" and a lower "reservoir" region by a porous layer of glass beads. The latter was achieved by folding a rectangular wire mesh so that it attaches to a cuvette, and overlaying it with glass beads of diameter 425 – 600 μm and various weights, as shown in **Figure 1B**. Glass beads of diameter 425 – 600 μm, provide a porous medium with spacings large (~50 – 200 μm) compared to the size of individual algae (< 10 μm), so that the latter could easily move through the pores. To initialize experiments, first an empty cuvette was filled with an algal suspension approximately up to the mesh height and thereafter the mesh was installed. To make a porous layer of various thicknesses, beads of appropriate weight were placed over the mesh. Finally, more algal suspension was poured from the top to create a harvest region of height ≈ 0.5 cm. The experiments reported below also considered the case of a bare mesh with no beads.

2.2 Essential Model of Concentration

We present here the details of a simplified model of the concentration of swimming microalgae into the upper "harvest" region by light. The model describes the case of a suspension of microalgae with a porous layer near the top (mesh + beads), as shown in **Figure 1**, and we shall also apply it below to

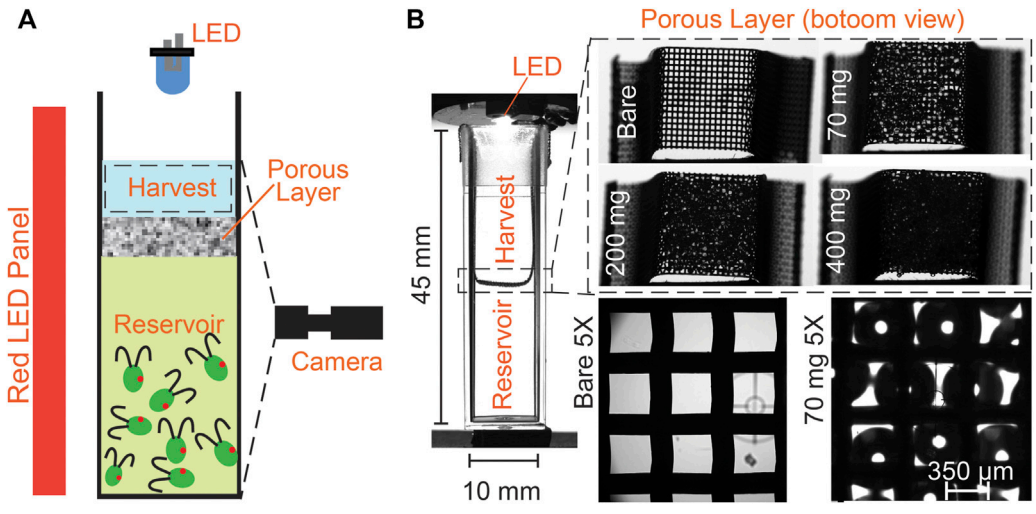

FIGURE 1 | Schematic showing lower reservoir and upper harvest regions, separated by a wire mesh overlaid with beads: the porous layer. **(A)** A blue LED is mounted on the top of the cuvette to create a phototactic bias. For imaging the suspension and concentration calibration, a deep red LED illuminates the cuvette from the side (deep red light does not elicit phototaxis [3]). **(B)** Glass beads of diameter 425 – 600 μm were used to create the porous layer. 70 mg of bead results in single layer, 200 mg–2 to 3 layers, and 400 mg–4 to 5 layers, respectively.

consider the case of a bare mesh. For the mesh + beads case, the suspension of microalgae is divided into three regions, an upper harvest region (u), a porous layer region (p) and a lower "reservoir" region (l). Photogyrotactic migration delivers microalgae to the upper region from the lower region through the porous region. As evident from our results and discussion (see **Section 3.4**, **4** below), the dynamics underpinning the concentration are complex; the challenge of describing them with a full photogyrotactic model is beyond the scope of this paper. Instead, we seek here to formulate a model to capture the essential features of the concentration process into the upper harvest region. We make the reasonable simplifying assumption that: 1) the average concentrations in the upper, porous and lower regions evolve slowly compared to the observed photogyrotactic dynamics; we consider here spatial and temporal variations separately, and assume a steady state for the fast dynamics in the upper region. We further assume that 2) phototactic migration is the dominant process and brings cells to from the lower region to the porous region, with swimmers migrating straight upwards toward the light (there is no dependence on light gradients, only light direction) at the maximum phototactic speed, equal to the mean swimming speed of the population, V_s. In the lower region, we assume that 3) the mean concentration is representative of the concentration of cells swimming into the porous layer. In the porous layer region, we assume that: 4) the speed of the swimmers is slowed down by collisions with the porous medium, but the swimming direction continues on average to be upwardly directed by phototaxis. In the upper harvest region, as well as the average concentration dynamics, we also consider a 0^{th} order spatial model of phototactic concentration. To set this up, as assumed above, we posit that there is a separation of timescales between the migration of cells from the lower region (slow) and the redistribution of cells in the upper region (fast). We further assume that: 5) the effect of flow is negligible prior to the formation of the plume from the upper surface (see **Figure 4B**); 6) upward phototactic swimming at the maximum speed V_s and diffusion dominate the fast suspension dynamics (gyrotactic effects are negligible); 7) diffusion is assumed approximately isotropic; 8) the meniscus at the top of the suspension is flat (any effects of curvature are neglected).

With the assumptions above, denoting by $\bar{c}_i$ the average concentrations in regions $i = u,\ p,\ l$ for the upper, porous and lower regions, respectively, and with A the cross-sectional area of the cuvette, the average cell numbers $\bar{N}_i$ in the three regions evolve according to the following balance equations:

$$\frac{d\bar{N}_l}{dt} = -A V_s \bar{c}_l, \tag{1a}$$

$$\frac{d\bar{N}_p}{dt} = A V_s \bar{c}_l - A V_{eff} \bar{c}_p, \tag{1b}$$

$$\frac{d\bar{N}_u}{dt} = A V_{eff} \bar{c}_p. \tag{1c}$$

Equation 1a describes the loss of cells from the lower region due to the phototactic flux of cells, of concentration $\bar{c}_l$, swimming into the porous region at speed V_s. Correspondingly, the porous region, as described by **Equation 1b**, gains an equal and opposite flux. This region also has a loss term due to cells, of concentration $\bar{c}_p$, swimming at a speed V_{eff} into the upper region. The upper harvest region, as shown in **Equation 1c**, has an equal and opposite gain. The speed V_{eff} is the effective swimming speed of the microalgae within the porous layer, which is given by [39].

$$V_{eff} = V_s \frac{\tau_c}{\tau} + \frac{l_{obs}}{\tau}, \tag{2}$$

where V_s is the "free" mean swimming speed of the microalgae, $\tau_c = \frac{\lambda}{V_s}$ is the time between collisions with the beads in the porous layer, and λ is the swimmer mean free path. The timescale $\tau = \tau_c + \tau_R$ is the total porous travel time, including the residence time τ_R that a swimmer spends at an obstacle. These parameters were recently measured experimentally for *C. reinhardtii* (see **Table 1**). To express system (1) in terms of concentrations only, we note that the mean number of cells in regions $i = u,\ p,\ l$ can be written as $\bar{N}_i = A h_i \bar{c}_i$, where, as above, A is the cross-sectional area of the cuvette, and h_i, $\bar{c}_i$ are the height and mean concentration in region i, respectively. Substituting into (1), we thus obtain, dividing both sides by the respective h_i,

$$\frac{d\bar{c}_l}{dt} = -\alpha \bar{c}_l, \tag{3a}$$

$$\frac{d\bar{c}_p}{dt} = \beta \bar{c}_l - \gamma \bar{c}_p, \tag{3b}$$

$$\frac{d\bar{c}_u}{dt} = \delta \bar{c}_p \tag{3c}$$

where we have defined the upswimming rate constants $\alpha = V_s/h_l$, $\beta = V_s/h_p$, $\gamma = V_{eff}/h_p$ and $\delta = V_{eff}/h_u$. **Equation 3a** has immediate solution $\bar{c}_l = k_0 e^{-\alpha t}$, where k_0 is a constant. The system of **Eq. 3** can then be solved analytically by substituting this solution into **(3b)**, and the resulting solution (e.g. by using the integrating factor $e^{\beta t}$) into **(3c)**. Applying the initial conditions $\bar{c}_l(0) = \bar{c}_l^0$, $\bar{c}_p(0) = \bar{c}_p^0$ and $\bar{c}_u(0) = \bar{c}_u^0$, where $\bar{c}_i^0$ represent the initial average concentrations in the three regions, we find:

$$\bar{c}_l(t) = \bar{c}_i^0 e^{-\alpha t}, \tag{4a}$$

$$\bar{c}_p(t) = \bar{c}_l^0 \frac{\beta}{\gamma - \alpha} e^{-\alpha t} + \left(\bar{c}_p^0 - \bar{c}_l^0 \frac{\beta}{\gamma - \alpha} \right) e^{-\gamma t}, \tag{4b}$$

$$\bar{c}_u(t) = \bar{c}_u^\infty - \bar{c}_l^0 \frac{\beta\delta}{\alpha(\gamma - \alpha)} e^{-\alpha t} - \left(\bar{c}_p^0 - \bar{c}_l^0 \frac{\beta}{\gamma - \alpha} \right) \frac{\delta}{\gamma} e^{-\gamma t}, \tag{4c}$$

where we have defined the long-time concentration in the upper region as

$$\bar{c}_u{}^\infty = \bar{c}_u{}^0 + \bar{c}_p{}^0 \frac{\delta}{\gamma} + \bar{c}_l{}^0 \frac{\beta\delta}{\alpha\gamma} = \bar{c}_u{}^0 + \bar{c}_p{}^0 \frac{h_p}{h_u} + \bar{c}_l{}^0 \frac{h_l}{h_u}, \tag{5}$$

and where, recalling the definitions of the constants α, β, γ and δ, we have re-written $\bar{c}_u^\alpha$ in terms of the heights of the regions. Thus, it is clear from **Equation 5** that, in this simple model, the long-time (maximum) concentration in the upper region occurs when all swimmers from the porous and lower regions have concentrated themselves into the upper region.

We also consider the "mesh-only" case (without a porous layer of beads). The derivation, shown in Supplementary Appendix SB,

TABLE 1 | Essential model parameters for the mesh + beads case. Values were obtained from direct measurements of our experimental system or literature values for the swimming parameter of *C. reinhardtii* grown under identical conditions.

Parameter	Symbol	Units	Value	References
Mean swimming speed of *C. reinhardtii*	V_s	*cm/s*	80×10^{-4}	[38]
Rotational diffusivity of *C. reinhardtii*	D_R	s^{-1}	0.4	[38]
Effective diffusivity of *C. reinhardtii*	$D = \frac{V_s^2}{D_R}$	cm^2/s	1.6×10^4	[38]
Mean free path in porous layer	λ	*cm*	125×10^{-4}	This work
Collision time in porous layer	$\tau_c = \frac{\lambda}{V_s}$	*s*	1.56	This work
Residence time at obstacle in porous layer	τ_R	*s*	1	[32]
Mean run time	$\tau = \tau_c + \tau_R$	*s*	2.56	[32]
Mean distance on obstacles	l_{obs}	*cm*	30×10^{-4}	[32]
Lower reservoir region height	h_l	*cm*	0.212	This work
Porous region height	h_p	*cm*	0.378	This work
Upper harvest region height	h_u	*cm*	0.422	This work
Initial mean concentration of suspension in the lower region	$\bar{c}_l^0$	*cells* cm^{-3}	1.20×10^6	This work
Initial mean concentration of suspension in the porous region	$\bar{c}_p^0$	*cells* cm^{-3}	1.18×10^6 ($\bar{c}_p^0 = \bar{c}_u^0$)	This work
Initial mean concentration of suspension in the upper region	$\bar{c}_u^0$	*cells* cm^{-3}	1.18×10^6	This work
Phototactic lengthscale	$l_p = \frac{D}{V_s}$	*cm*	0.02	This work
Upswimming rate 1	$\alpha = \frac{V_s}{h_l}$	s^{-1}	3.8×10^{-3}	This work
Upswimming rate 2	$\beta = \frac{V_s}{h_p}$	s^{-1}	2.12×10^{-2}	This work
Upswimming rate 3	$\gamma = \frac{V_{eff.}}{h_p}$	s^{-1}	1.60×10^{-2}	This work
Upswimming rate 4	$\delta = \frac{V_{eff}}{h_u}$	s^{-1}	1.43×10^{-2}	This work

is similar and provides the temporal evolution of the mean concentrations as

$$\bar{c}_l^m(t) = \bar{c}_l^{m0} e^{-\alpha t}, \tag{6a}$$

$$\bar{c}_\mu^m(t) = \bar{c}_l^{m\infty} - \bar{c}_l^{m0} \frac{\eta}{\alpha} e^{-\alpha t}, \tag{6b}$$

where the superscript 'm' denotes concentrations in the mesh-only case, and we have defined the rate constants $\alpha = V_s/h_l$, which is as in the porous layer model (but takes a slightly different value because of the different value of h_l, see Supplementary Table S2), and $\eta = V_s/h_u$. For the mesh-only case the concentration in the upper region at long times is given by

$$\bar{c}_u^{m\infty} = \bar{c}_u^{m0} + \bar{c}_l^{m0} \frac{\eta}{\alpha} = \bar{c}_u^{m0} + \bar{c}_l^{m0} \frac{h_l}{h_u}. \tag{7}$$

This corresponds to the concentration in the upper region occurring when all microalgae have swum into it from the lower region.

In the upper region we observe that cells accumulate strongly at the surface. To describe this, we can use a simplification of the Williams and Bees model [26]. By virtue of assumptions 5)–8) above, as shown in Supplementary Appendix SA, the full swimmer conservation equation in the Williams and Bees model simplifies to:

$$\frac{\partial c_u}{\partial t} = -\nabla \cdot [\, V_s\, c_u\, \boldsymbol{k} - D\, \nabla c_u\,], \tag{8}$$

where $\boldsymbol{k}$ is a unit vector pointing upwards and D is the diffusivity, approximated as isotropic, by assumption 7) (see Supplementary Appendix SA for more details). By assumption 1), we have a steady state, so that **(8)** implies

$$V_s\, c_u\, \boldsymbol{k} - D\, \nabla c_u = const., \tag{9}$$

where $\boldsymbol{k}$ is a unit vector pointing upwards. Imposing a no flux condition at the upper boundary (flat for simplicity, assumption viii) requires $(V_s\, c_u\, \boldsymbol{k} - D\, \nabla c_u) \cdot \boldsymbol{k} = 0$ on $z = h$, so that **Equation 9** becomes

$$\frac{dc_u}{dz} = \frac{V_s}{D} c_u, \tag{10}$$

which integrates to

$$c_u = k_1\, e^{\frac{z}{l_p}}, \tag{11}$$

where we have defined a characteristic phototactic accumulation lengthscale $l_p = \frac{D}{V_s}$, and where k_1 is a constant. To find the latter, we use the fact that the average background concentration is given by $\bar{c}_u$, that is, taking $z = 0$ at the bottom of the upper region and $z = h_u$ at its top, $\bar{c}_u = \frac{1}{h_u} \int_0^{h_u} c_u dz$. Thus, integrating **Equation 11** gives $k_1 = \bar{c}_u\, (e^{h_u/l_p} - 1)^{-1}\, h_u/l_p$, so that finally the distribution in the upper region is given by

$$c_u(z, t) = \bar{c}_u(t) \frac{h_u}{l_p} \frac{e^{\frac{z}{l_p}}}{e^{\frac{h_u}{l_p}} - 1}, \tag{12}$$

where that the mean concentration as a function of time, $\bar{c}_u(t)$, is provided by **Equation 4c**.

3 RESULTS

3.1 Initial Condition for the Lower Region

Prior to considering the effect of light on a suspension of *C. reinhardtii* placed in the cuvette, we will consider the initial condition of the suspension in the lower reservoir region, which will be the same starting point for all subsequent experiments. With the blue LED light off, microalgae were

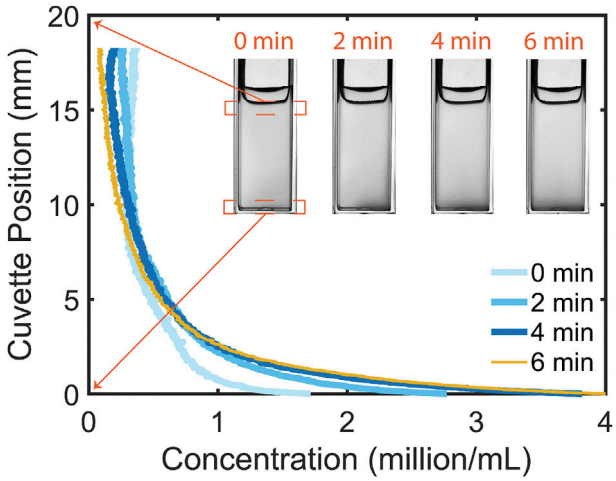

FIGURE 2 | In the absence of phototactic illumination from above microalgae redistribute over the height of the cuvette. A steady distribution can be seen to arise after 4 min.

mixed into the cuvette and the suspension was allowed to stabilize in the presence of only red illumination from the side (see **Figure 1A**), which does not elicit a phototactic response (Supplementary Video S1) [3, 40]. The suspension images and profiles are shown as a time-series in **Figure 2**: over a few minutes, the suspension (initial concentration ~ 1 million/mL) settles into a distribution where the majority of cells reside at the bottom of the cuvette; a steady distribution is observable beyond 4 min. The gradient in concentration already visible for the concentration profile at t = 0 is due to a lag in transferring the cuvette to the imaging setup after mixing: some settling has already occurred at the first instance of imaging. The steady distribution observed beyond 4 min would, for other species of gyrotactic swimming algae such as *Chlamydomonas augustae* [2], also display features known as "bottom-standing plumes" (see also **Figure 1A** in [7]). For *C. reinhardtii*, however, the bottom-standing plume structures are not discernible in the images of the cuvette (though plumes can be seen to descend from its sides, see Supplementary Video S1), though they can be seen in a larger container (see Supplementary Figure S3). It is possible that, for this species, the cuvette width is too narrow to give rise to central bottom-standing plume structures.

3.2 Free Surface: Bulk Photogyrotactic Instabilities

We consider here the effect of light on a suspension of microalgae in a cuvette when the surface of the suspension is free (the metal mesh applied in the next section has been raised above the surface). This experimental scenario can be seen in Supplementary Video S2, stills of which are shown as the sequence in **Figure 3**. Initially the blue LED illumination is switched off and the suspension is distributed with the majority of cells at the bottom, as described in the previous section. Then the LED is switched on, and the cells in suspension phototactically respond to the light, migrating upwards toward the surface (**Figure 3**, t = 3 min). Concomitantly, instabilities arise throughout the suspension, resulting in meandering plumes (**Figure 3**, t = 3 – 5 min). These are of photogyrotactic origin, as discussed below. In the span of ~ 6 minutes phototactic migration appears to have delivered many swimmers to the surface, leaving the bulk of the suspension depleted. This surface accumulation is gravitationally unstable because of the negative buoyancy of surface-accumulated cells: it results in the formation of a plume instability seen to originate from the middle of the meniscus of the suspension surface (**Figure 3**, t = 9 min). The plume structure wiggles around but once formed, is dynamically stable (**Figure 3**, t = 18 min), delivering cells to the bottom of the container. Once they reach this, the microalgae migrate back up to the surface to join the plume, and so forth. When the light is switched off (**Figure 3**, t = LED Off + 17 sec, + 3, 6 min), the phototactic migration toward the surface stops and the surface accumulation sinks as a broader, non-meandering plume. This takes the cells to the bottom of the cuvette, where they once more settle into a distribution similar to the initial one.

3.3 Mesh: New Phototactic Structures

In this section we consider the case of a metal mesh immersed at the top of the microalgal suspension. As described in the methods, the pore size of the mesh is 350 μm, so individual microalgae (~ 5 μm in diameter) easily swim through it. A typical experiment is shown in Supplementary Video S3, stills of which are presented as a sequence in **Figure 4A** (top row). As for the free surface case, blue LED illumination is initially off, and the suspension is distributed with most cells at the bottom (**Figure 4A**, first still). The LED is then switched on and microalgae migrate upward in response to the light (**Figure 4A**, t = 3 min). The response is broadly similar to the free surface case, but there are some interesting differences. One such striking difference is that the mesh creates a pattern of light and shadow to which the microalgae visibly respond

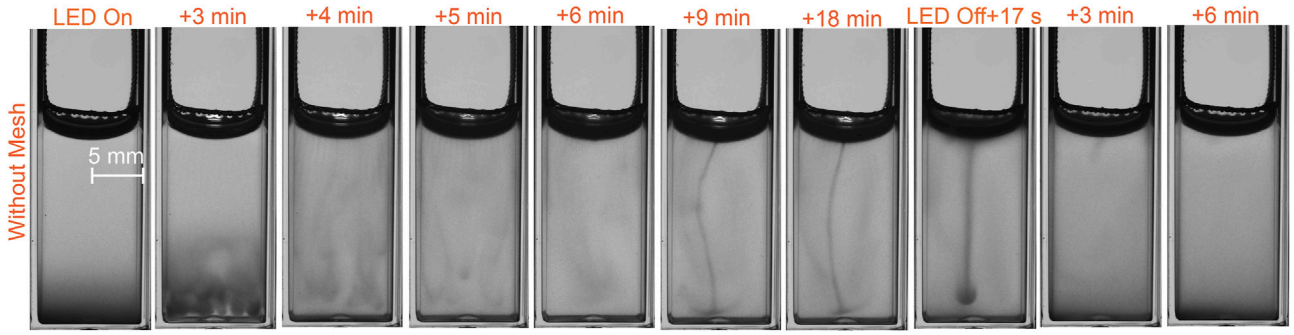

FIGURE 3 | Free surface: photogyrotactic dynamics of a suspension of *C. reinhardtii* microalgae in a cuvette illuminated from the top by a blue LED, and dynamics when the LED is switched off (last three stills).

photogyrotactically, forming accumulations ('phototactic curtains'), see **Figure 4C**. The average width of phototactic curtain feature is 630 ± 53 μm, nearly twice the mesh pore size, showing that the curtains are not the result of shadowing by the mesh, but genuine phototactic structures originating from the response of the microalgae to the local light profile. As in the case of a free surface, when the density of cells phototactically accumulated at the surface becomes too high, a plume of dense cells forms and sinks. However, viscous resistance caused by the mesh pores prevents the plume from completely sinking beyond the mesh, and instead a cloud-like plume structure is seen to be trapped, hovering above the mesh (**Figure 4A**, t = 9, 18 min). Not all the plume-cloud is trapped, negative buoyancy is sufficient to cause some of it to escape through the mesh forming a meandering secondary plume, similar in appearance to the one observed in the free surface case (**Figure 4A**, t = 9, 18 min). While the light is on, these structures appear dynamically stable. As the light is switched off, however, the curtains and cloud structure disperse, cells sink through the mesh, and the escaped plume sinks down straight, again similarly to free surface case (**Figure 4A**, t = LED Off + 19 sec, + 3, 6 min). This emphasizes the stabilizing influence of phototaxis: none of the observed structures could be possible in the absence of the light. Both mesh and light are critical for supporting the plume-cloud.

3.4 Porous Layers: Stabilization of Phototactic Structures and Concentration Gain

We next turn to the case where a porous layer is placed on top of the suspension. As described in the Methods, the porous layer consists of glass beads overlaid onto a metal mesh (the same as was used in the previous section). The beads are around 425 – 600 μm in diameter, which results in interparticle spacings ~ 50 – 200 μm (from microscopic observation). Thus, individual algae ~ 5 μm in diameter can swim through the porous layer. We studied the effect of light on suspensions of microalgae overlaid with porous layers, quantified by the weight of the beads placed on the mesh. A typical experiment with a layer weighing 400 mg is shown in Supplementary Video S4, and stills from this video are presented in **Figure 4B**. As in previous cases, the LED light is initially off and the suspension is distributed with the majority of cells at the bottom (**Figure 4B**, first still). When the LED is switched on, the initial suspension dynamics are similar to the mesh-only case (**Figure 4B**, t = 3 – 6 min), displaying instabilities as the microalgae respond to the light (but with no curtains visible). However, for this case, we were also able to observe clusters of cells swimming upwards as waves in response to the light, see **Figure 5A** for an example. Averaging over five such waves, we found them to have a mean speed of 190 ± 60 μm/s. This is faster than mean swimming speed of individual algal cells, 80 μm/s [38], possibly as a result of advection by upwelling fluid in the lower region of the cuvette generated by the photogyrotactic suspension dynamics. The large deviation in the speed of the waves could also be due to the interaction of the waves with other photogyrotactic structures and up/downwelling flows in the suspension. Once cells have had time to accumulate in the harvest region and on the surface of the suspension, a plume-cloud structure originating at the low point of the meniscus forms above the porous layer (**Figure 4B**, t = 9, 18 min). The plume-cloud appears more diffuse than in the mesh case. The time taken for the plume-cloud to arise in 10 out of 12 experiments used for the analysis is between 6 – 10 min from when the LED light is switched on, as shown in Supplementary Figure S4. Unlike the case of the mesh, the plume does not leak through the porous layer into the suspension: in the presence of light, the viscous resistance offered by the porous layer is sufficient to stabilize the plume-cloud. Instead of sinking the plume-cloud is observed to gradually expand into the upper region. **Figure 5B** charts this expansion. The lateral extent of the plume structure increases the most between 7 and 9 min after the LED has been switched on, when the plume begins to drop and propagate along the porous layer. After that the plume-cloud achieves a steady structure, probably as a result of balance between influx of cells from the surface, where the plume originated at the low point of the meniscus, and loss to the edges of the harvest region (and resorption to the suspension surface by upswimming).

In view of quantifying microalgal concentration in the upper harvest region above the mesh or the mesh + beads porous layer, it is instructive to chart the evolution of the average concentration of the suspension in this region (Supplementary Figure S2). To

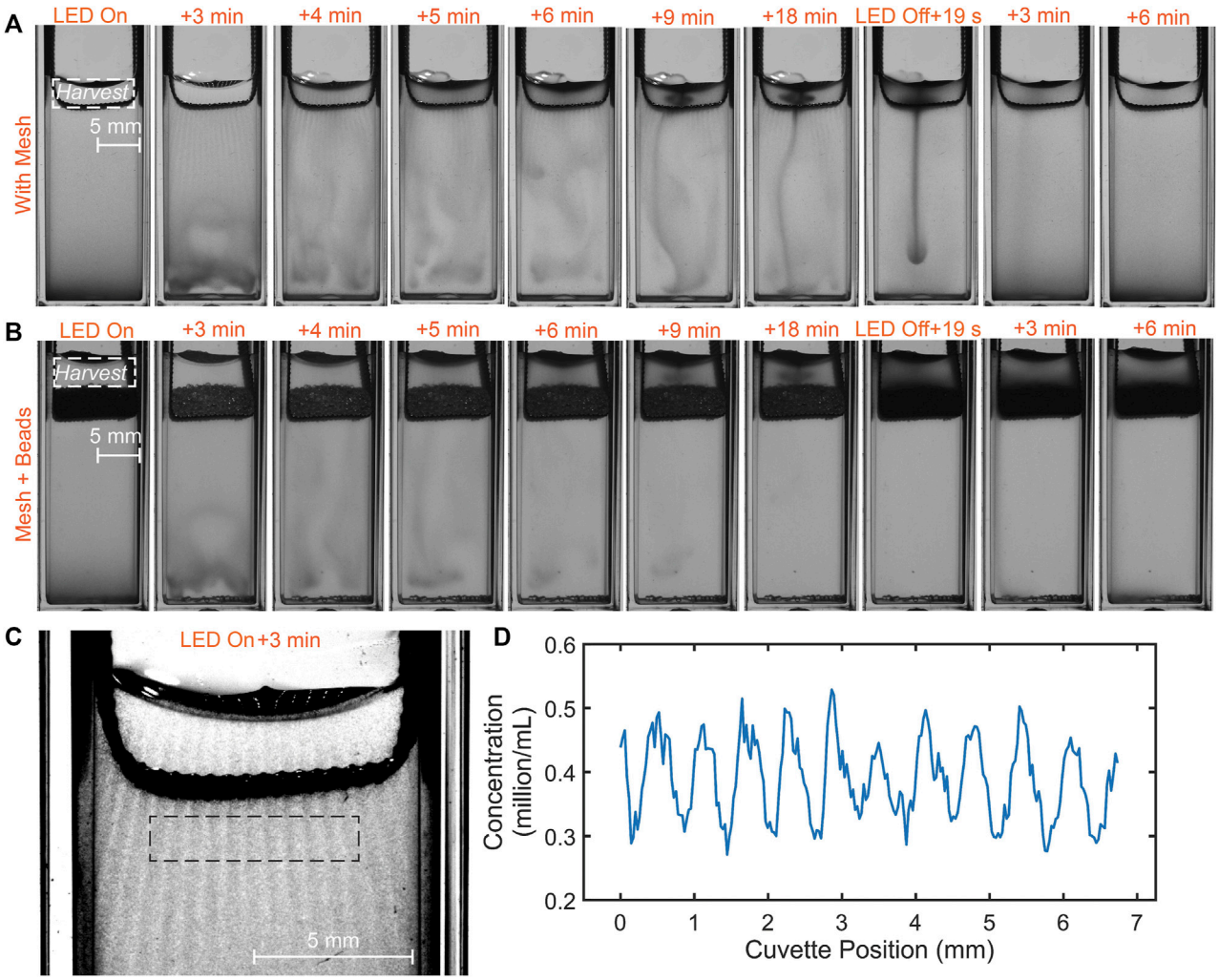

FIGURE 4 | Microalgal suspension dynamics for the case of: **(A)** a mesh; **(B)** mesh + beads (400 mg) placed at the top of the suspension. The dynamics is similar, but there are important differences. Significantly a cloud-like plume is completely trapped between the porous layer and top surface, while in the case of the mesh, it can leak as a thin plume to the suspension below. **(C)** Phototactic "curtain" pattern formed by the accumulation of cells in response to the light and shadow pattern generated by illumination falling on the mesh. **(D)** Curve showing the concentration of algae across the phototactic curtains (mean feature width = 630 ± 53 μm) marked in **(C)**.

identify a porous layer thickness that would not leak into the suspension below, we considered layers of several weights in trial experiments presented in Supplementary Figure S5. We found a general qualitative trend that was similar for all cases: the concentration grows as the light is switched on, and then saturates to a constant value. We focus here quantitatively on the mesh-only case and the "minimally-leaky" mesh + beads (400 mg) case, shown for three repeats in **Figures 6A,B**, respectively. The averaged profiles are shown in **Figure 6C**. This makes it clear that the concentration in the upper harvest region of both the mesh and mesh + beads cases, following a dip in concentration due to phototactic accumulation of cells to the upper surface, grows after the LED is switched on and then tends to saturate. The mesh case, however, saturates earlier, probably because of losses to the lower region, such as the plume visible in **Figure 4A** (9 min). Another interesting quantitative difference between the two cases is the initial rate of concentration, which appears slightly larger for the mesh case. This indicates the concentration process is initially slower when a porous layer is present, than in its absence. As discussed below using the essential model, this makes sense in terms of the microalgae having to make their way through the porous layer, which reduces the swimming speed that sets the concentration rate. The difference in swimming speed will also affect the average time it takes to form the plume, which was measured to be 7.3 ± 0.6 min for the mesh case, while it is 8.7 ± 1.5 min for mesh + beads (Supplementary Figure S4). When the LED is switched off (**Figures 6A–C** inset), the concentration in the upper harvest region is seen to rise briefly before steadily falling. This is because, with the light off, the concentrated algal suspension in the harvest region no longer responds phototactically and cells accumulated to the surface are released, sinking down as dense fluid. The increase in concentration due to the cells coming off the surface shows that our measurements likely underestimate the

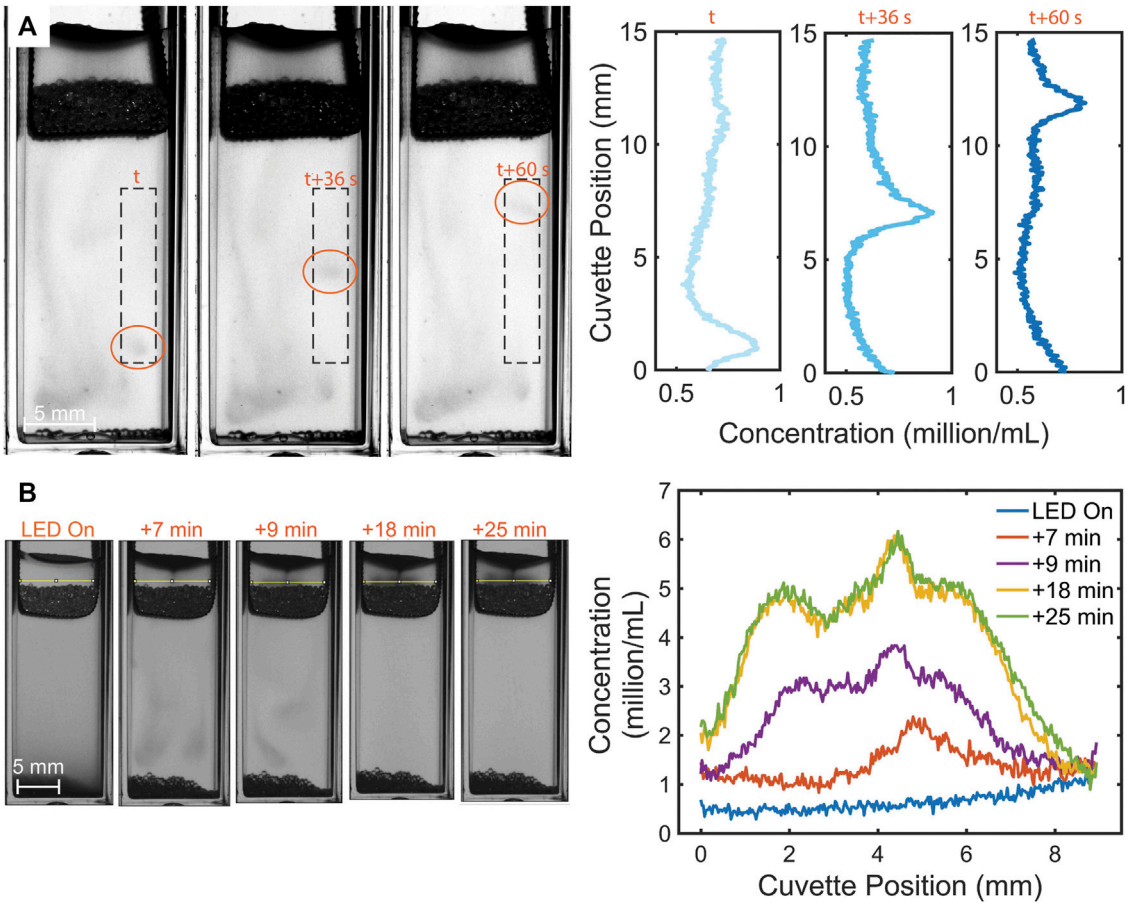

FIGURE 5 | Photogyrotactic dynamics of swimming algae in the mesh + beads case. **(A)** Stills of the algal clusters in the lower region moving upwards as waves with speed ~ 180 μm/s. **(B)** Lateral expansion of the trapped algal plume-cloud formed in the upper harvest region. Its density is seen to increases over time as it expands.

concentration in the upper harvest region because of cells "hidden" at the surface. This could account, at least in part, for discrepancies with model predictions discussed below. For our setup, the time after switching the LED off is optimal for harvesting the suspension, yielding a harvest concentration ≈ 5 million/mL (gain ≈ 4.2 compared to the initial concentration) for the mesh + beads case, as compared to ≈ 4 million/mL cells for mesh-only (gain ≈ 3.6). This highlights the advantage of concentrating using a porous layer. The latter also slows down the rate at which the cells sink back through to the lower region, which depends on the layer thickness.

Also shown in **Figure 6** are profiles charting the temporal evolution of concentration in the lower reservoir region. As for the upper region, we have measured triplicate repeat profiles for the mesh (**Figure 6D**) and mesh + beads (**Figure 6E**), and also evaluated averaged profiles (**Figure 6F**). We see that, after the LED is switched on, the concentration for the mesh and mesh + beads falls, as phototactic swimming into the upper regions depletes the lower region of cells. However, the depletion appears to saturate, and to a higher concentration in the case of mesh-only, reflecting the greater leakiness of the mesh, as discussed below. Insets in **Figures 6D–F** display how, with the LED off, the concentration in the lower region rises due the influx of cells sinking from the upper regions.

3.5 Essential Model Predictions

We have developed a simple model to capture the essential features of the phototactic concentration dynamics, and evaluate it here using parameters for *C. reinhartii* concentrated using a mesh + beads setup, as shown in **Table 1**. In **Figure 7A**, the model prediction using **Equation 4c** for the average concentration of cells $\bar{c}_u(t)$ in the upper harvest region is shown as a function of time (the concentration process starts at time t = 0, "LED on"). Qualitatively, the predicted behaviour is as in the experimental curves (**Figure 6C**), with the concentration initially rising and then saturating. However, quantitatively, the concentration values predicted by the essential model are much larger than those seen experimentally. Indeed, using **Equation 5** and the parameters in **Table 1**, the essential model predicts saturation to a long-time concentration $\bar{c}_u^{\infty} = 8.2 \times 10^6$ cells/ml. This is of the same order of magnitude as, but

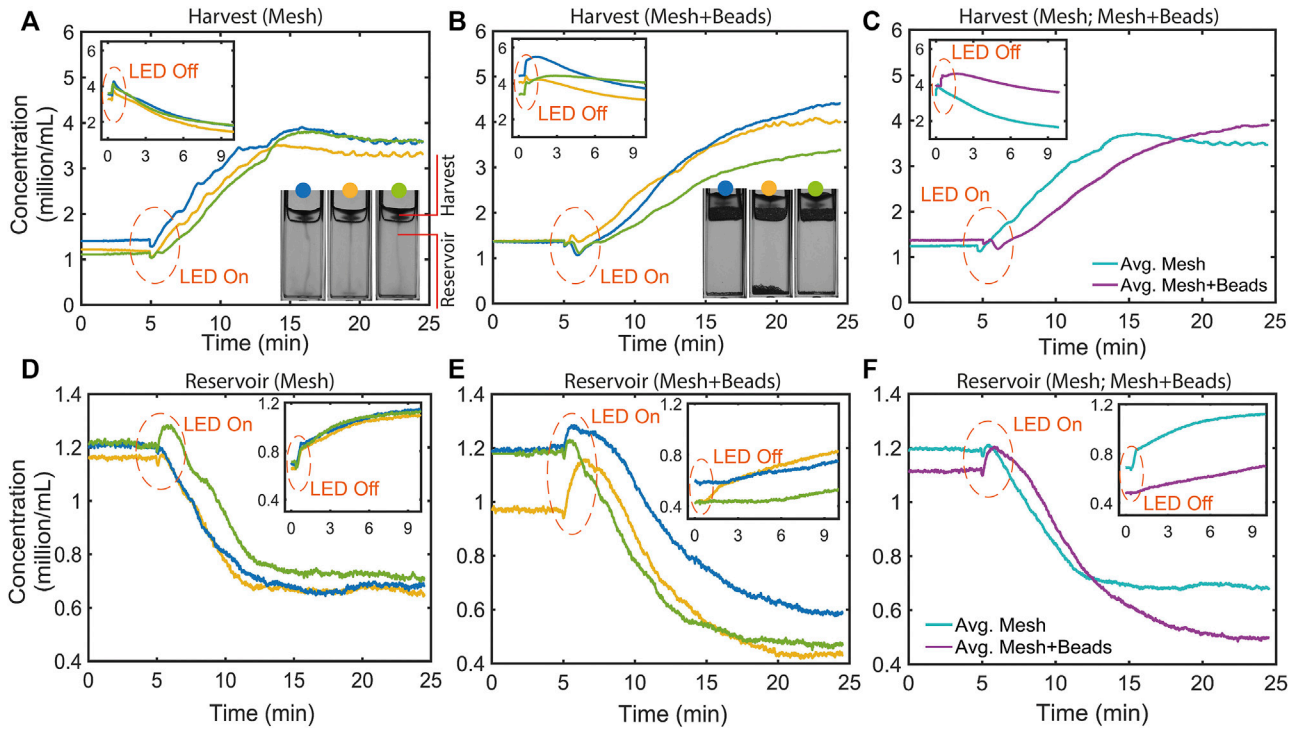

FIGURE 6 | Temporal concentration profiles in the upper harvest region above a mesh or mesh + beads, after the LED is switched on and off (insets), as indicated. **(A)** Three repeats for microalgae phototactically concentrating above the bare mesh. Inset: concentration rise and decay after the LED is switched off. **(B)** As in **(A)**, but for the mesh + beads (400 mg) case. **(C)** Time point average of the concentration profiles shown in **(A, B)**. The concentration for the mesh-only case saturates ~10 min after the LED is switched on, whereas it keeps on increasing towards a higher saturation concentration in the mesh + beads case. When the LED is switched off, the concentration initially increases and then decays, for the reasons discussed in the text. **(D)** Three repeats for profiles in the lower region for the mesh only case. Inset: concentration rise after the LED is switched off. **(E)** As in **(D)** but for the mesh + beads case. **(F)** Time point average of the concentration profiles shown in **(D, E)**. For the mesh-only case the profile decays to a constant value sooner than mesh + beads. The inset shows how the concentrations for both cases rise in the lower region after the LED is switched off, with a greater rise for the more leaky mesh-only case.

approximately double what we observe experimentally ($\approx 4 \times 10^6$ cells/ml). Part of the discrepancy is because, as mentioned above, experimental concentration curves underestimate the concentration in the upper reservoir because of swimmers phototactically accumulated and 'hidden' at the surface. Another possible reason is that the essential model unrealistically ignores mechanisms causing losses: as illustrated by **Equation 5**, $\bar{c}_u^{\infty}$ corresponds to the concentration obtained when all the swimmers from the porous and lower regions swim to the upper region and do not leave it thereafter. In reality, swimmer diffusion will cause cells to be transferred from the upper to the porous region, particularly at longer times when concentration gradients between the regions are large. Another possibility not accounted for by the essential model is that, if swimmers respond to gradients of light (as opposed to just its direction, as assumed in the model), the denser suspension of swimmers in the upper region shades the region below, changing the light gradient and reducing the phototactic speed of swimmers below, and thus the rate of accumulation. **Figure 7A** also shows the model prediction for the concentration in the upper region for the mesh-only case. As in experiment, this is seen to initially rise steeper and saturate at a lower value than the case of mesh + beads; numerically, however, the predicted concentrations ($\bar{c}_u^{\infty} = 7.5 \times 10^6$ cells/ml) are approximately double what we measured experimentally. This is for the same reasons as for the mesh + beads case, and additionally in the mesh-only case there are also losses due to the plume leaking through the mesh, as we have shown (**Figure 4A**, 9 min). The faster rise in concentration observed for the mesh-only case compared to mesh + beads, is due to the difference in upswimming rates in the two cases: for mesh + beads, swimmers are slowed down when they swim through the porous layer. The essential model also allows the prediction of the concentrations in the porous and lower regions, respectively $\bar{c}_p(t)$ and $\bar{c}_l(t)$, which are shown in **Figure 7A**. The lower region concentration is seen to decay exponentially to zero, as swimmers evacuate the lower region by phototactic upswimming. The lower region decay predictions overlap for the mesh and mesh + beads cases, so they are not separately visible in the figure (the prediction equation is the same for these cases, and parameters are practically identical). We can compare these predictions with the experimentally determined concentration profiles. As observed in the previous section, these also decay with time, but not to zero: they saturate to a fixed value (**Figure 6F**), with the mesh-only case reaching a lower value than mesh + beads due to the greater leakiness of

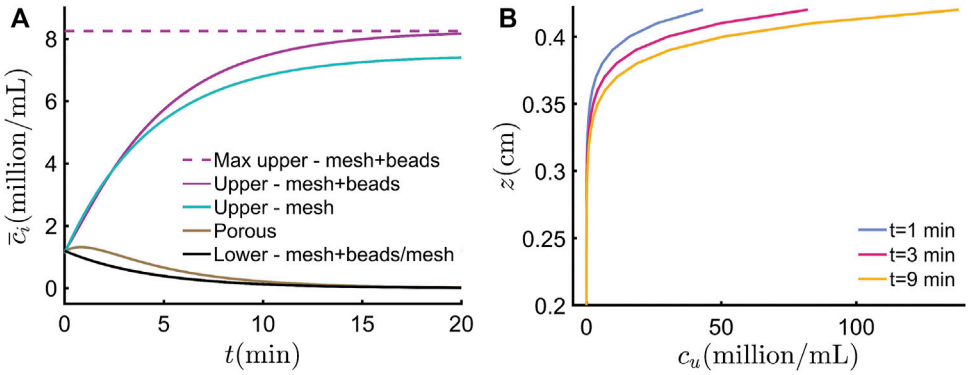

FIGURE 7 | Predictions of the essential model. **(A)** Average concentrations as a function of time since 'LED on' at t = 0 in the upper, porous, and lower regions for the mesh + beads case, and upper and lower regions for the mesh-only case. For both cases, phototactic concentration causes the lower region to evacuate and the upper region to fill up with swimmers, up to a maximum limit, as discussed in the text. For clarity, this limit, shown as a dotted line for the mesh + beads case, is not shown for the mesh-only case. **(B)** Spatial swimmer concentration profiles in the upper region at different times, as shown. The suspension becomes increasingly top-heavy. The plot starts at z = 0.2 cm to make the profiles more evident (the concentration predicted below this level is 0 cells/ml).

the mesh. The essential model fails to predict this saturation and the important difference between the two cases, demonstrating the need to model diffusive transfer and leaking plumes between the regions, and/or a reduction of the phototactic speed. For the porous region, the essential model predicts that the concentration, $\bar{c}_p(t)$, initially rises, due to influx from the lower region outpacing losses to the upper region, and eventually decays to zero. It was not possible to optically image the microalgae in the porous region and obtain the concentration there, so we cannot make a comparison with the essential model prediction in this case.

Assuming phototaxis and diffusion processes are dominant in the upper region, and that these occur faster than the accumulation from the porous region, we can also use the spatial extension of the essential model to chart the distribution of swimming algae in the upper region, which is provided by **Equation 12**. We note that, since this model does not fully account for photogyrotaxis, the predictions are only strictly valid prior to the formation of the plume off the upper surface, which we know from experiment occurs $\approx$ 9 min after turning the light on. In **Figure 7B** the distribution of swimmers is charted at different points in time (prior to plume formation), predicting that the suspension becomes increasingly top-heavy as time progresses. This accumulation, with concentrations reaching $\sim 10^8$ cells/ml close to the upper boundary, is unstable against its own negative buoyancy, and eventually results in the formation of the plume we observe experimentally. As it is not possible to accurately image the accumulation of cells around the meniscus, we did not experimentally quantify the spatial concentration distribution in the upper region. However, the increasing accumulation of swimmers at the surface is clearly discernible in our image sequences, see Supplementary Video S4. The model predicts that the cells accumulate strongly at the top of the upper region, with no sizeable concentration below a certain height. Instead, our image sequences reveal that there is also a nonzero concentration in the bottom of the upper region (indeed that is what we have measured to obtain **Figures 6A–C**). This could be accounted for by losses from the accumulation at the surface to the edge of the cuvette, which are not considered in our model.

4 DISCUSSION

We have shown how light from above can trigger instabilities and upwards migration in an initially quiescent suspension of *C. reinhardtii* microalgae within a rectangular cuvette. By imaging, we qualitatively and quantitatively studied for the first time this migration in the following cases: when a permeable metal mesh is placed at the top of the suspension; when porous layers of beads are overlaid onto the mesh; in the absence of any mesh or layer on the surface. In the latter case, light was seen to drive photogyroactic instabilities in the bulk of the suspension and upwards migration of the cells to the surface, from which, eventually, a plume structure was seen to arise. A similar phenomenology was observed when a mesh was present, except in this case the plume from the surface was partially trapped by the mesh, later giving rise to a secondary plume. By trapping the plume, the mesh allows the concentration of cells in the upper region of the cuvette (also termed "harvest region"), but this is a leaky process. However, when a porous layer of glass beads is overlaid onto the mesh, it is possible to stably concentrate the suspension in the upper harvest region while the light is switched on: the plume from the surface is trapped with minimal leakage. We have charted how the mean concentration in the harvest region varies with time for the case of a mesh with a layer of beads of different weights (thicknesses), showing that a $\approx$ 4-fold concentration is possible for the thickest layer weighing 400 mg (**Figure 6C**). Critically, we have demonstrated that it is the unique combination of light and a moderately thick porous layer of beads that makes the photogyrotactic concentration of cells possible. Without the beads the accumulation of microalgae in the harvest region is

leaky. When the light is switched off, all photogyrotactic structures fall apart, and the microalgal population sinks back down to the initial quiescent state.

We can discuss our findings in terms of what is known about the phototactic and photogyrotactic behaviour of microalgal suspensions. When the LED is switched on, the suspension responds visibly in seconds, similarly to what has been measured for populations responding to light from an optical fibre [23], and corresponding to the time scale for *C. reinhardtii* to perceive light and turn to swim towards it by controlling their flagellar beat [24]. Subsequent to this initial response, the suspension displays instabilities in cell concentration and flow. Some groups of cells rise, moving as waves drifting at the swimming speed of the algae or above, probably advected by upwelling flow; others form stretching plumes; others still sink. This complex behaviour is the result of the interplay of the phototaxis and gyrotaxis of the population, coupled with the fluid dynamics of a negatively buoyant suspension. In the absence of a full photogyrotactic model, whose development is beyond the scope of this paper, it is not possible to account for these observed patterns quantitatively. A lower bound estimate of the timescale for accumulation to the surface leading to the formation of a plume there can, however, be obtained by considering the time for cells to swim straight up to the surface at the maximum phototactic speed. For the mesh + beads (400 mg) case, the mean swimming speed of the microalgae in the lower and upper regions, with heights h_l and h_u, respectively, is V_s, while it is V_{eff}, as given by **Equation 2**, in the porous region with height h_p. The time to reach the surface is then $t \sim (h_l + h_u)/V_s + h_p/V_{eff} \approx 6$ min, using parameters in **Table 1**. For the mesh-only case, there is no porous layer so that $t_m \sim (h_l + h_u)/V_s \approx 5$ min, using parameters in Supplementary Table S2. These values are not too far from the ~9 (7) min it takes for a plume instability to develop from the surface in the mesh + beads (mesh) cases (Supplementary Figure S4). This suggests, as is clear from our concentration data in the harvest region (**Figure 6**), that, in spite of the instabilities observed, phototaxis drives a net flux of cells upwards through the porous layer towards the harvest region, where cells accumulate at the surface. Here they distribute, with maximum concentration at the surface. The concentration becomes increasingly top-heavy (as predicted by our essential model, see **Figure 7B**) and eventually a plume instability develops driven by the negative buoyancy of the suspension. The plume then drops towards the porous layer, but its negative buoyancy is not great enough to sink through it. Instead, the plume is trapped in the harvest region forming a toroidal "plume-cloud" fed from the surface, whose size expands with time to the edge of the harvest region (see **Figure 5B**). Here it appears to stabilize, possibly due to a balance between cell gain from the surface and loss to the suspension at the edges of the cuvette. The surface accumulation and plume-cloud, and all the structures in the lower region, collapse within a few seconds of switching the LED light off. In particular, the concentrated suspension in the harvest region sinks right through the porous layer, though this takes some time for the thick (400 mg) mesh + bead layer. This collapse of the suspension structures demonstrates the essential role of phototaxis in dramatically altering the stability thresholds of the active suspension: none of the structures we have observed can exist without light.

Our essential model provides a qualitative picture of how the average concentration changes in the upper, porous and lower regions, and gives concentration values which agree in order of magnitude with what we have measured. Comparison with experiment, however, reveals that the model fails to quantitatively describe the saturation of the upper and lower concentrations. This in part because our measurements in the upper region underestimate the concentration (missing cells accumulated at the surface). However, as evidenced by the failure of the model to predict saturation in the lower region (compare **Figures 6D**, **7A**), it is likely that quantitative agreement is not possible because critical processes have not been modelled, such as diffusive exchanges between reservoirs and/or shading effects of the cell concentration in the upper region on the phototactic speed. For the upper region, the model was applied to predict a top-heavy distribution of cells, as is observed in our image sequences. The model, however, does not reproduce the concentration of cells visible in the bottom part of the upper region, probably due to a neglect of losses from the surface accumulation at the edge of the cuvette. The model is further limited to the description of the phototactic concentration prior to the formation of the plume-cloud, whose quantitative dynamics require a fully photogyrotactic description. Future studies should develop such a description using continuum models coupling the suspension cell and flow dynamics in response to gravity, flow and light, as has been done by Williams and Bees to describe bioconvection patterns [26]. This will present some challenges. For example, it is as yet unclear which model of the phototactic response of a population agrees quantitatively with experiment. Williams and Bees did not test their model C against experiment [29], and other studies using a similar description to model C did not include gyrotaxis [23, 28]. Alternatively, the adaptive, microscopic model of photoaxis presented in [24] could be used as the basis of an agent-based model (ABM) of the population response, and integrated with known gyrotactic responses implemented in ABMs [41], and coupled to the fluid dynamics (another challenge for ABMs). Numerical and analytical predictions from such models will predict the spatio-temporal patterns in the suspension, including the meandering photogyrotactic plumes, the formation of propagating waves of cells and their concentration in the phototactic curtain structures we have observed. To describe the latter, accounting for the observed width of the curtain pattern, it will be necessary to develop a model coupling the local light profile (optical shadows from the mesh) to the photogyrotactic dynamics. Photogyrotactic models should be developed for the lower, porous and upper regions combined, and should be able predict the characteristic timescales we have observed, such as the time required for plumes to form off the upper surface (Supplementary Figure S4). Such models will also describe how the plume-cloud in the harvest region grows with time, accounting for the curvature in the meniscus (neglected in our essential model) and how this affects the plume formation.

Observation indicates that the plume forms in the lowest point of the meniscus, likely because cells accumulate there. Advanced modelling should also predict how long the mesh or porous layer is able to support the plume against sinking when the LED is on, and how long it takes to sink through the layer when the LED is switched off.

A full account of photogyrotactic dynamics will permit inclusion of processes (such as diffusion and light shading affecting phototactic speed) not included in our essential model. Predictions from these improved photogyrotactic models for the concentration in the upper, porous and lower regions, should provide better agreement with the results shown in **Figure 6**. In particular, it will be interesting to use these refined models to establish the parameters that determine optimal conditions for harvesting microalgae in the upper region. From a practical perspective it is desirable to obtain the largest possible volume of suspension with the highest concentration gain for a given initial mean concentration and critical parameters, such as the height of the lower, porous and upper harvest regions, and the total duration of the concentration process. In addition, it will be desirable to know how strong the light intensity should be for optimal phototactic concentration. This is a parameter which was held fixed in the present study.

Harvesting contributes a significant amount (about 20–30% [36]) of the cost for processing microalgae and bioproducts derived from them. New methods are required to reduces this cost and replace energy-intensive solutions such as centrifugation. In many applications, a concentration factor of 100 upon harvesting is desirable to remove water and allow further bioprocessing of microalgae [36]. Investigations following our study should determine if such a concentration gain, improving on the four-fold gain we have demonstrated, can be achieved using photogyrotaxis alone. Alternatively, photogyrotactic concentration could already be viable as a preliminary concentration step, as is currently done by membrane filtration [42], reducing the time spent on more costly concentration methods, such as centrifugation. Following a demonstration at the milliliter ('cuvette') scale, it is worth investigating if photogyrotactic concentration can be scaled up, and if it can be an energy-efficient (using inexpensive LED or natural light, and exploiting natural swimming energy for concentration), and convenient method of value in industrial microalgal bioprocessing and harvesting. Indeed, for industrially-valuable swimming microalgae, exploiting swimming in response to light, as we have here explored, has not been considered as the basis for an efficient new harvesting method. *Dunaliella salina*, a marine relative of *C. reinhardtii*, is cultured in ponds that are maximum 20 cm deep to allow light penetration for growth [43]. It is known that this microalga can be concentrated when a layer of freshwater is produced, artificially or by rain, at the surface of the pond [43]. The freshwater generates a gradient in the density of the suspension medium, which acts similarly to the porous layer in our study and causes the microalgae to become trapped in the freshwater layer at the surface [44]. The role of photogyrotaxis in this industrially well-known concentration process [43] has not yet been investigated. However, taking into consideration the concentration physics we have uncovered in this study, it could be optimized to produce better microalgal yields from culture ponds. Density gradients cannot be exploited for freshwater microalgae (an aqueous suspending medium less dense than water is not easily found), which require a porous layer to be concentrated by upswimming. In this case, the use of glass beads for the porous layer, as in this study, represents an improvement over Kessler's original suggestion of a fibrous porous layer [35], which, from experience with gravitactic concentration using cotton wool [13, 14, 45], is known to be liable to irreversible cell loss to the fibers (biofouling).

Finally, it is worth remembering that *C. reinhardtii* is a soil-dwelling microalga. Little is known about its ecology within soils [46], but we can speculate that in saturated soils *C. reinhardtii* may migrate across porous layers in response to daylight. Thus, the phenomenology we have uncovered in this work and the methods we have developed can be adapted to better understand the behaviour of *C. reinhardtii* and similar species in their natural environments. It will be very interesting in future studies to investigate the phototactic movements of *C. reinhardtii* in laboratory soil-like porous media, and how this social behaviour affects its photosynthetic growth in topsoil, as well as more "traditional" social behaviours, such as sex [46] and interactions with other soil microbes [47, 48].

DATA AVAILABILITY STATEMENT

The datasets presented in this study can be found in online repositories. The names of the repository/repositories and accession number(s) can be found below: https://doi.org/10.5281/zenodo.5113916.

AUTHOR CONTRIBUTIONS

PP carried out the experiments. OC developed the modelling. PP and OC designed the experiments, analysed the data, and wrote the paper.

ACKNOWLEDGMENTS

We thank K. Leptos for providing the *C. reinhardtii* CC125, M. Bees for a critical reading of the manuscript, and H. Laeverenz Schlogelhofer for the laboratory training provided to PP. OC acknowledges financial support from the Winton Programme for the Physics of Sustainability. PP and OC acknowledge financial support from the British Council through the Newton Bhabha Fellowship Scheme.

SUPPLEMENTARY MATERIAL

The Supplementary Material for this article can be found online at: https://www.frontiersin.org/articles/10.3389/fphy.2021.744428/full#supplementary-material

REFERENCES

1. Wadhams GH, Armitage JP. Making Sense of it All: Bacterial Chemotaxis. *Nat Rev Mol Cel Biol* (2004) 5:1024–37. doi:10.1038/nrm1524
2. Pedley TJ, Kessler JO. Hydrodynamic Phenomena in Suspensions of Swimming Microorganisms. *Annu Rev Fluid Mech* (1992) 24:313–58. doi:10.1146/annurev.fl.24.010192.001525
3. Foster KW, Smyth RD. Light Antennas in Phototactic Algae. *Microbiol Rev* (1980) 44:572–630. doi:10.1128/mr.44.4.572-630.1980
4. Adler J. Chemotaxis in Bacteria. *Science* (1966) 153:708–16. doi:10.1126/science.153.3737.708
5. Bhattacharjee T, Amchin DB, Alert R, Ott JA, Datta SS. Chemotactic Smoothing of Collective Migration. *arXiv* (2021). Available from: http://arxiv.org/abs/2101.04576 (Accessed April 26, 2021).
6. Bretschneider T, Othmer HG, Weijer CJ. Progress and Perspectives in Signal Transduction, Actin Dynamics, and Movement at the Cell and Tissue Level: Lessons from *Dictyostelium*. *Interf Focus.* (2016) 6:20160047. doi:10.1098/rsfs.2016.0047
7. Bees MA. Advances in Bioconvection. *Annu Rev Fluid Mech* (2020) 52:449–76. doi:10.1146/annurev-fluid-010518-040558
8. O'Malley S, Bees MA. The Orientation of Swimming Biflagellates in Shear Flows. *Bull Math Biol* (2012) 74:232–55. doi:10.1007/s11538-011-9673-1
9. Bees MA, Croze OA. Dispersion of Biased Swimming Micro-organisms in a Fluid Flowing through a Tube. *Proc R Soc A* (2010) 466:2057–77. doi:10.1098/rspa.2009.0606
10. Bearon RN, Bees MA, Croze OA. Biased Swimming Cells Do Not Disperse in Pipes as Tracers: A Population Model Based on Microscale Behaviour. *Phys Fluids* (2012) 24:121902. doi:10.1063/1.4772189
11. Hwang Y, Pedley TJ. Bioconvection under Uniform Shear: Linear Stability Analysis. *J Fluid Mech* (2014) 738:522–62. doi:10.1017/jfm.2013.604
12. Cencini M, Franchino M, Santamaria F, Boffetta G. Centripetal Focusing of Gyrotactic Phytoplankton. *J Theor Biol* (2016) 399:62–70. doi:10.1016/j.jtbi.2016.03.037
13. Croze OA, Ashraf EE, Bees MA. Sheared Bioconvection in a Horizontal Tube. *Phys Biol* (2010) 7:046001. doi:10.1088/1478-3975/7/4/046001
14. Croze OA, Bearon RN, Bees MA. Gyrotactic Swimmer Dispersion in Pipe Flow: Testing the Theory. *J Fluid Mech* (2017) 816:481–506. doi:10.1017/jfm.2017.90
15. Durham WM, Kessler JO, Stocker R. Disruption of Vertical Motility by Shear Triggers Formation of Thin Phytoplankton Layers. *Science* (2009) 80323:1067–70. doi:10.1126/science.1167334
16. Elgeti J, Winkler RG, Gompper G. Physics of Microswimmers-Single Particle Motion and Collective Behavior: a Review. *Rep Prog Phys* (2015) 78:056601. doi:10.1088/0034-4885/78/5/056601
17. Rusconi R, Stocker R. Microbes in Flow. *Curr Opin Microbiol* (2015) 25:1–8. doi:10.1016/j.mib.2015.03.003
18. Marchetti MC, Joanny JF, Ramaswamy S, Liverpool TB, Prost J, Rao M, et al. Hydrodynamics of Soft Active Matter. *Rev Mod Phys* (2013) 85:1143–89. doi:10.1103/RevModPhys.85.1143
19. Elgeti J, Winkler RG, Gompper G. Physics of Microswimmers-Ssingle Particle Motion and Collective Behavior: a Review. *Rep Prog Phys* (2015) 78:056601. doi:10.1088/0034-4885/78/5/056601
20. Bastos-Arrieta J, Revilla-Guarinos A, Uspal WE, Simmchen J. Bacterial Biohybrid Microswimmers. *Front Robot AI* (2018) 5:97. doi:10.3389/frobt.2018.00097
21. Prakash P, Abdulla AZ, Singh V, Varma M. Tuning the Torque-Speed Characteristics of the Bacterial Flagellar Motor to Enhance Swimming Speed. *Phys Rev E* (2019) 100:062609. doi:10.1103/PhysRevE.100.062609
22. Prakash P, Abdulla AZ, Singh V, Varma M. Swimming Statistics of Cargo-Loaded Single Bacteria. *Soft Matter* (2020) 16:9499–505. doi:10.1039/d0sm01066a
23. Arrieta J, Barreira A, Chioccioli M, Polin M, Tuval I. Phototaxis beyond Turning: Persistent Accumulation and Response Acclimation of the Microalga Chlamydomonas Reinhardtii. *Sci Rep* (2017) 7:1–7. doi:10.1038/s41598-017-03618-8
24. Leptos KC, Chioccioli M, Furlan S, Pesci AI, Goldstein RE. *An Adaptive Flagellar Photoresponse Determines the Dynamics of Accurate Phototactic Steering in Chlamydomonas* bioRxiv (2018). p. 254714. doi:10.1101/254714
25. Javadi A, Arrieta J, Tuval I, Polin M. Photo-bioconvection: towards Light Control of Flows in Active Suspensions. *Phil Trans R Soc A* (2020) 378:20190523. doi:10.1098/rsta.2019.0523
26. Williams CR, Bees MA. Photo-gyrotactic Bioconvection. *J Fluid Mech* (2011) 678:41–86. doi:10.1017/jfm.2011.100
27. Ogawa T, Shoji E, Suematsu NJ, Nishimori H, Izumi S, Awazu A, et al. The Flux of Euglena Gracilis Cells Depends on the Gradient of Light Intensity. *PLoS One* (2016) 11:e0168114. doi:10.1371/journal.pone.0168114
28. Arrieta J, Polin M, Saleta-Piersanti R, Tuval I. Light Control of Localized Photobioconvection. *Phys Rev Lett* (2019) 123:158101. doi:10.1103/PhysRevLett.123.158101
29. Williams CR, Bees MA. A Tale of Three Taxes: Photo-Gyro-Gravitactic Bioconvection. *J Exp Biol* (2011) 214:2398–408. doi:10.1242/jeb.051094
30. Marshall TJ, Holmes JW, Rose CW. *Soil Physics*. Cambridge University Press (1996). doi:10.1017/CBO9781139170673
31. Martínez-Calvo A, Trenado-Yuste C, Datta SS. *Active Transport in Complex Environments*. *arXiv* (2021). Available from: https://arxiv.org/abs/2108.07011 (Accessed September 16, 2021).
32. Théry A, Wang Y, Dvoriashyna M, Eloy C, Elias F, Lauga E. Rebound and Scattering of Motile *Chlamydomonas* Algae in Confined chambers. *Soft Matter* (2021) 17:4857–73. doi:10.1039/D0SM02207A
33. Brun-Cosme-Bruny M, Bertin E, Coasne B, Peyla P, Rafaï S. Effective Diffusivity of Microswimmers in a Crowded Environment. *J Chem Phys* (2019) 150:104901. doi:10.1063/1.5081507
34. Brun-Cosme-Bruny M, Förtsch A, Zimmermann W, Bertin E, Peyla P, Rafaï S. Deflection of Phototactic Microswimmers through Obstacle Arrays. *Phys Rev Fluids* (2020) 5:093302. doi:10.1103/PhysRevFluids.5.093302
35. Kessler JO Algal Cell Harvesting US4324067A. Available at: https://patents.google.com/patent/US4324067A/en?oq=U.S.+Patent+No.+4324.067 (Accessed April 26, 2021)
36. Fasaei F, Bitter JH, Slegers PM, van Boxtel AJB. Techno-economic Evaluation of Microalgae Harvesting and Dewatering Systems. *Algal Res* (2018) 31:347–62. doi:10.1016/j.algal.2017.11.038
37. Gorman DS, Levine RP. Cytochrome F and Plastocyanin: Their Sequence in the Photosynthetic Electron Transport Chain of Chlamydomonas Reinhardi. *Proc Natl Acad Sci* (1965) 54:1665–9. doi:10.1073/pnas.54.6.1665
38. Jin D, Kotar J, Silvester E, Leptos KC, Croze OA. Diurnal Variations in the Motility of Populations of Biflagellate Microalgae. *Biophysical J* (2020) 119:2055–62. doi:10.1016/j.bpj.2020.10.006
39. Jakuszeit T, Croze OA, Bell S. Diffusion of Active Particles in a Complex Environment: Role of Surface Scattering. *Phys Rev E* (2019) 99:012610. doi:10.1103/PhysRevE.99.012610
40. Goldstein RE, Polin M, Tuval I. Emergence of Synchronized Beating during the Regrowth of Eukaryotic Flagella. *Phys Rev Lett* (2011) 107:148103. doi:10.1103/PhysRevLett.107.148103
41. Croze OA, Sardina G, Ahmed M, Bees MA, Brandt L. Dispersion of Swimming Algae in Laminar and Turbulent Channel Flows: Consequences for Photobioreactors. *J R Soc Interf* (2013) 10:20121041. doi:10.1098/RSIF.2012.1041
42. Monte J, Sá M, Galinha CF, Costa L, Hoekstra H, Brazinha C, et al. Harvesting of Dunaliella salina by Membrane Filtration at Pilot Scale. *Sep Purif Techn* (2018) 190:252–60. doi:10.1016/J.SEPPUR.2017.08.019
43. Borowitzka LJ, Borowitzka MA. Commercial Production of β-carotene by Dunaliella salina in Open Ponds. *Bull Mar Sci* (1990) 47:244–52.
44. Bearon RN, Grünbaum D. Bioconvection in a Stratified Environment: Experiments and Theory. *Phys Fluids* (2006) 18:127102. doi:10.1063/1.2402490
45. Kessler JO. The External Dynamics of Swimming Micro-organisms. *Prog Phycological Res* (1986) 4:257–307.
46. Sasso S, Stibor H, Mittag M, Grossman AR. From Molecular Manipulation of Domesticated Chlamydomonas Reinhardtii to Survival in Nature. *Elife* (2018) 7:e39233. doi:10.7554/eLife.39233
47. Teplitski M, Rajamani S. *Signal and Nutrient Exchange in the Interactions between Soil Algae and Bacteria*, 23. Springer Berlin Heidelberg (2010). p. 413–26. doi:10.1007/978-3-642-14512-4_16

48. Laeverenz Schlogelhofer H, Peaudecerf FJ, Bunbury F, Whitehouse MJ, Foster RA, Smith AG, et al. Combining SIMS and Mechanistic Modelling to Reveal Nutrient Kinetics in an Algal-Bacterial Mutualism. *PLoS One* (2021) 16(5): e0251643. doi:10.1371/journal.pone.0251643

Conflict of Interest: The authors declare that the research was conducted in the absence of any commercial or financial relationships that could be construed as a potential conflict of interest.

Publisher's Note: All claims expressed in this article are solely those of the authors and do not necessarily represent those of their affiliated organizations or those of the publisher, the editors, and the reviewers. Any product that may be evaluated in this article, or claim that may be made by its manufacturer, is not guaranteed or endorsed by the publisher.

frontiers | Frontiers in Physics

ORIGINAL RESEARCH
published: 09 June 2022
doi: 10.3389/fphy.2022.735667

Toward Task Capable Active Matter: Learning to Avoid Clogging in Confined Collectives *via* Collisions

Kehinde O. Aina[1], *Ram Avinery*[2], *Hui-Shun Kuan*[3], *Meredith D. Betterton*[3,4], *Michael A. D. Goodisman*[5] *and Daniel I. Goldman*[2]*

[1]Institute for Robotics and Intelligent Machines, Georgia Institute of Technology, Atlanta, GA, United States, [2]School of Physics, Georgia Institute of Technology, Atlanta, GA, United States, [3]Department of Physics, Department of MCD Biology, University of Colorado Boulder, Boulder, CO, United States, [4]Center for Computational Biology, Flatiron Institute, New York, NY, United States, [5]School of Biological Sciences, Georgia Institute of Technology, Atlanta, GA, United States

Social organisms which construct nests consisting of tunnels and chambers necessarily navigate confined and crowded conditions. Unlike low density collectives like bird flocks and insect swarms in which hydrodynamic and statistical phenomena dominate, the physics of glasses and supercooled fluids is important to understand clogging behaviors in high density collectives. Our previous work revealed that fire ants flowing in confined tunnels utilize diverse behaviors like unequal workload distributions, spontaneous direction reversals and limited interaction times to mitigate clogging and jamming and thus maintain functional flow; implementation of similar rules in a small robophysical swarm led to high performance through spontaneous dissolution of clogs and clusters. However, how the insects learn such behaviors and how we can develop "task capable" active matter in such regimes remains a challenge in part because interaction dynamics are dominated by local, potentially time-consuming collisions and no single agent can survey and guide the entire collective. Here, hypothesizing that effective flow and clog mitigation could be generated purely by collisional learning dynamics, we challenged small groups of robots to transport pellets through a narrow tunnel, and allowed them to modify their excavation probabilities over time. Robots began excavation with equal probabilities to excavate and without probability modification, clogs and clusters were common. Allowing the robots to perform a "reversal" and exit the tunnel when they encountered another robot which prevented forward progress improved performance. When robots were allowed to change their reversal probabilities via both a collision and a self-measured (and noisy) estimate of tunnel length, unequal workload distributions comparable to our previous work emerged and excavation performance improved. Our robophysical study of an excavating swarm shows that despite the seeming complexity and difficulty of the task, simple learning rules can mitigate or leverage unavoidable features in task capable dense active matter, leading to hypotheses for dense biological and robotic swarms.

Keywords: collision-based interaction, collective behavior, multi-robot excavation, swarm robotics, decentralized learning, ant-inspired learning, active matter, confined and crowded conditions

OPEN ACCESS

Edited by:
Natasha Mhatre,
Western University, Canada

Reviewed by:
Chengyi Xia,
Tiangong University, China
Fabio Giardina,
Harvard University, United States

***Correspondence:**
Daniel I. Goldman
daniel.goldman@physics.gatech.edu

Specialty section:
This article was submitted to Social Physics, a section of the journal Frontiers in Physics

Received: *03 July 2021*
Accepted: *02 May 2022*
Published: *09 June 2022*

Citation:
Aina KO, Avinery R, Kuan H-S, Betterton MD, Goodisman MAD and Goldman DI (2022) Toward Task Capable Active Matter: Learning to Avoid Clogging in Confined Collectives via Collisions. Front. Phys. 10:735667. doi: 10.3389/fphy.2022.735667

1 INTRODUCTION

Active matter systems, ensembles of driven "agents", are of much interest in physics for their rich phenomena, which often feature formation of spatially extended structures such as those observed in flocking [1, 2], motility-induced-phase-separation [3–5], giant number fluctuations [6–8] and more [6, 9]. Active systems in confined environments (like within narrow channels) are interesting as structures that form due to collisions and constrained maneuverability in this regime [10–13] decay slowly in time, displaying glassy/supercooled features [11]. Such slow relaxation can lead to deleterious performance of an active system which must perform a "task" (like a group of ants, termites creating tunnels or humans rushing through narrow doors). General physics principles which could allow such active systems to become "task capable" are less understood as the bulk active matter physics focuses on flow and structures that emerge from relatively simple rules among individuals.

Mitigating structure formation in confined systems likely necessitates agents change behavior ("rules") in response to conditions and via interactions with other agents. Studies of such systems are typically the domain of swarm engineering where researchers seek to understand the functional benefits of structure formation. For example, engineers seek to have robot teams achieve goals such as getting aerial swarms to create formations [14] or planar collections of robots to arrange in different patterns [15]. Generically, swarm control schemes may modify a steady-state property of the system such as cluster size [16], pattern formation [17] and locomotion alignment [18]. Such schemes are often represented as functional dependencies between variables, like the orientation being the average of neighbor orientations [1] or the speed decreasing with local particle density [5].

Unfortunately, most control schemes for swarms assume dilute conditions and avoid collisions thus discovery of general principles for task completion (like flow at high speed or low energetic cost) in crowded confined conditions requires new insights in part because real-time adjustment is particularly challenging without a central controller, and with the limited sensing and computation we imposed on the robots, all while dealing with physical noise from their mechanics, jostling and collisions. As a result, conventional planning and control methods that rely on precise or accurate information of the surrounding may not be applicable to achieve coordinated behavior and good traffic flow in such a setting. It is instead useful to discover decentralized learning rules that rely on the unavoidable features of these dense active systems–social and local interactions–to reach effective traffic flow and task performance, under evolving conditions. We wish to understand then broadly how such structures form or dissolve in collectives whose agents possess memory, sensory feedback and even capability to learn over time.

Ants and termites are biological examples of dense and crowded task oriented active systems, where various behaviors (i.e., control schemes) have been naturally selected to aid task performance in such regimes [19, 20] without central control. Ants, for example, cooperatively create nests with complex subterranean networks [21]. They employ no centralized controller or global information, yet are able to excavate soil in dark, narrow and overpopulated conditions [22, 23]. Their tasks usually involve manipulation of soil particles or substrates, transport of bulk pellets through long and narrow tunnels, as well as directed movement to and from their nests [24]. Controlled lab experiments and numerical simulations show that clustering and clogging are prevalent in these conditions [11, 12], similar to "glassy arrests" in non-living active matter [25, 26]. This is due to individuals' persistence in their goals, being unaware or inconsiderate of others', which may lead to clogs that are difficult to resolve when working in narrow, quasi one-dimensional tunnels [12].

Previously we used robots as a robophysical model of the ant tunneling system which facilitated testing of behavioral rules in a controlled environment with noise and complexities of the real physical world [12]. Using the robophysical model we demonstrated how an active confined crowded robot collective could mitigate structure formation (slowly dissolving clogs and jams) via being "lazy" and "giving up". That is, manipulations of workload distribution in this robophysical model collective rationalized our observations of biological ants' strategy unequal workload distributions and probabilistic yielding to oncoming traffic (termed "reversals") demonstrating the importance and utilty of such rules for maintaining optimal tunnel flow. However, we had to program the behaviors in the robots; here we are interested to learn how robots can adjust their behaviors to optimize their workload distributions and retreat behaviors thus providing insight into biological collectives as well as providing principles for robot swarms that must operate in crowded, confined conditions.

Therefore to discover principles by which confined swarms can learn to avoid clogging while performing a useful task (excavation), purely via local information, social interactions and a noisy estimate of their state, here we augment our robophysical swarm to investigate hypotheses for how ant encounters can regulate [27–29] activity by individually learning from collisions. We systematically study the performance of the robots as we subject them to different protocols. We show that clogging can indeed be mitigated, by some individuals learning to "give up" and participate less in digging, where social interactions such as inter-robot collisions and noisy estimates of tunnel length serve as a means of reinforcement in our learning scheme. Our learning scheme provides a robust response to changing conditions, even when individuals acquire noisy or inaccurate information about their environment (tunnel length). We expect that our robophysical model and learning technique will provide guidance for biological hypotheses, as well as inform the design of a robust coordination technique for dense swarms in dynamic and evolving environments. Our results provide an example of the richness of active matter dynamics when the agents can use information to change state to perform and learn to perform tasks.

2 METHODS

Our robots, modified from our previous study [12] are programmed to execute autonomous behaviors independently such as navigation to specific sections in the tunnel and excavation. They are equipped with force sensitive grippers for pellet excavation, an outer shell with capacitive sensing to detect and distinguish two types collisions - robot-robot collisions and robot-wall collisions, as well as terminal rods for charging and detecting the home area (**Figure 1**). The pellets to be excavated are laid at the end of the tunnel are a cohesive granular medium consisting of plastic shells housing loose rare-earth magnets.

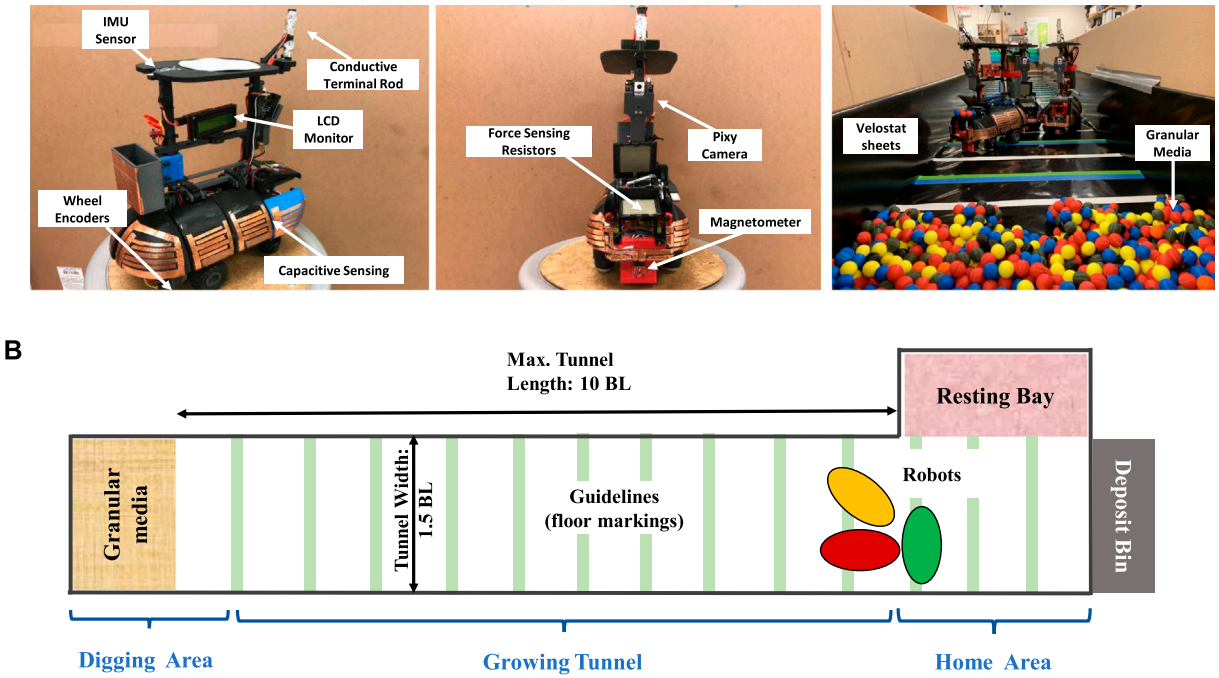

FIGURE 1 | Experimental apparatus consisting of robots and a tunnel. **(A)** Components of an ant robot (two left images): Inertia Measurement Unit (IMU) sensor for absolute orientation; Wheel encoders for localization via robot odometry/dead reckoning; Capacitive touch sensor shells for detecting collisions; Force sensitive resistors for gripper tactile feedback, Magnetometer for detecting pellets and Digging Area; Pixy camera for tunnel navigation and localization; Terminal rod for charging and detection of Home area. In the tunnel (rightmost image): Velostat sheets for lining the tunnel to distinguish robot-robot collision (copper-copper) from robot-wall collision (copper-velostat); Granular media to simulate model cohesive soil excavated by ants **(B)** Schematic diagram of the confined tunnel: a robot starts from the Home Area, decides whether to enter the tunnel and excavate some pellets, or decides to go to the Resting Bay to avoid interference at the tunnel entrance.

Since we are particularly interested in how coordinated group success could be achieved only from physical interactions and local observation of the environment, we do not allow direct robot-to-robot communication or global information to the individuals in the group; our robots rely purely on on-board sensors and make decision based on local sensing and self-reinforcement.

2.1 Collective Task

Our task is a collective excavation scenario: a group of robots must continuously excavate the model granular media in a narrow (1.5 body lengths) and confined tunnel, shown in **Figure 1**. As more pellets are excavated, the tunnel "grows" or changes geometrically as the robots perform their task. A robot starts by leaving the Home area and, using vision, following the guiding trails to the digging area where the cohesive pellets are located. During transit in the tunnel, the robot can detect and distinguish collisions with other robots, as well as collisions with the wall of the tunnel. By sensing a magnetic field, the robots can also detect the pellets. After a successful attempt to excavate, a robot heads home to drop the excavated pellets into a Deposit bin placed on a weighing scale.

Our goal is for the group to excavate as many pellets as possible within a given time. An obvious solution is for the robots to remain constantly active and try to excavate; however as we demonstrated in [12] when all the robots are in such a mode and enter the tunnel concurrently they spend much of their time resolving collisions as a result of competition for space to maneuver and carryout their activities. The resulting traffic jams have robots stuck or stalled due to excessive stress from repeated collisions. This wasted time results in degraded performance, to the extent that fewer robots in the tunnel would excavate faster. The challenge is therefore to use the local information available to individual robots to regulate the congestion and improve group performance under such physical constraints and hindrances. We derive our inspiration from the social behavior of fire ants under crowded and confined conditions [12], and our previous robophysical-model excavation experiment [30], to develop an adaptive learning rule that makes the robots decide when to "give up" digging and when to "take a rest" in a way that significantly improve the performance of the group.

2.2 Robot Controller

We adopt a finite state automaton model [31] which is a common scheme used to control behavior-based robot activities with no global knowledge. A state transition is triggered when a robot senses some physical clues from the environment. Each sensor on the robots has a specific trigger state that enables the robot to transition into another state. **Figure 2** shows the model of individual robot's controller. Each block contains a set of states or sub-states that form a mode or behavior that the robot exhibits. The states and sub-states are as described below:

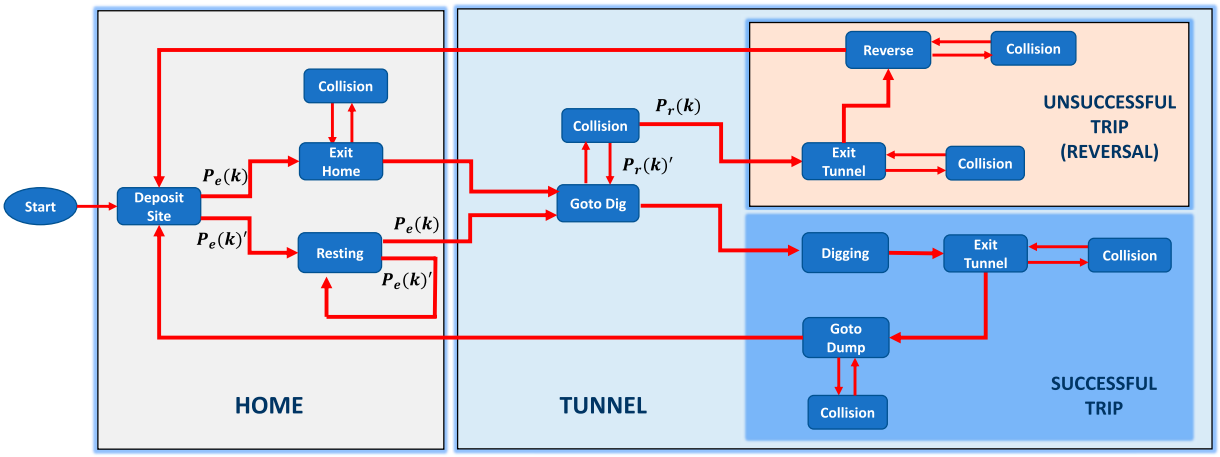

FIGURE 2 | Block diagram for the individual robot controller. State transitions are event-based. P_e: probability of tunnel entry (or go to dig). P_e': probability of resting (or staying at home). P_r: probability of "giving up" after colliding with another robot in the tunnel. P_r': probability of continuing to dig after colliding with anther robot.

1. Goto Dig: This state is triggered at the start of each trip when a robot "decides" whether to dig based on their tunnel entrance probabilities $P_e(k)$.
2. Digging: This state is triggered when the robot is in proximity to the granular media. The magnetometer at the base of the robot detects the magnetic field of the granular media and prompts the robot to start the excavation routine.
3. Exit Tunnel: The robot enters this state from Digging when the Force Sensitive Resistor (FSR) detects sufficient amount of pellets in the gripper. The robot executes several turning maneuvers to exit the digging area and head back home.
4. Goto Dump: This is the state that captures the robot heading home after a successful pellet retrieval (Successful Trip) or unsuccessful pellet retrieval (Unsuccessful Trip). The controller drives the robot out of the tunnel and gets the robot home to the deposit area.
5. Dumping: Robot releases the excavated pellets from its gripper and dumps it in the "Deposit Bin" which is placed on a weighing scale to measure the amount of pellets excavated over time.
6. Exit Home: Robot executes some turning maneuvers to exit the deposit area and enters the tunnel to dig.
7. Collision: This state is triggered when a robot collides with another robot or with the tunnel wall. The robot executes a set of turning maneuvers in an attempt to resolve the collision.
8. Resting: Robot goes to this state at the beginning of a trip if the entrance probability is sampled and the robot decides to rest. The robot follows the guiding trail on the tunnel floor to navigate to the resting area to take a rest and not participate in the tunnel traffic.

We developed a stochastic model with two parameters to control the entrance rate and reversal rate (give-up rate) of the robots so as to regulate tunnel traffic and improve group performance. Let $P_e(k)$ be the tunnel entrance probability and $P_r(k)$ be the reversal probability of each robot at trip attempt number k. A trip begins when a robot samples from the entrance probability, $P_e(k)$ and decides whether to "go in and dig" or "stay at home and rest". This parameter controls the number of robots in the tunnel which directly controls the tunnel density or congestion rate. The reversal probability, $P_r(k)$, on the other hand controls how a robot responds to a collision when it occurs. A robot samples from this parameter and decides if it should "give up" or to continue its journey. With these two parameters, we developed two protocols for studying the effects and performance of fixed social behaviors [12] in multi-robot collective excavation. We use these previously reported fixed behavior protocols [12] as controls to test against the adaptive (learning) behaviors we develop in the next section:

Active Protocol: In this protocol, we fix the tunnel entrance probability $P_e(k)$ to a value of one for each trip for each robot. The reversal probability $P_r(k)$ is set to zero, so the robots do not return home until they are able to collect pellets. This ensures that all the robots are active, trying to dig in the tunnel at all times.

Reversal Protocol: Here we set the reversal probability $P_r(k)$ for each robot to a value greater than zero but less than one, while still keeping the entrance probability to one at all time. This allows the robots to randomly "give up" trying to dig when they collide with other robots in the tunnel.

2.3 Developing an Adaptive Protocol

To go beyond the above fixed behavior protocols and to gain insight into useful social interactions of the confined multi-robot system, we conducted a parameter sweep to find the optimal reversal probabilities that yielded the highest excavation rate in a Cellular Automata (CA) model developed in our previous work [12]; see **Supplementary Section** for detailed description of the model. **Figure 3A** shows the range of excavation rates for varying reversal probability as the tunnel length increases. A closer look at the region with highest excavation rates suggests a non-linear inverse relationship between optimal reversal probabilities and tunnel length. In particular, the optimal probability values drop sharply for short tunnels (less than 5BL) and more gradually for longer tunnels. This gives us inspiration to develop an Adaptive

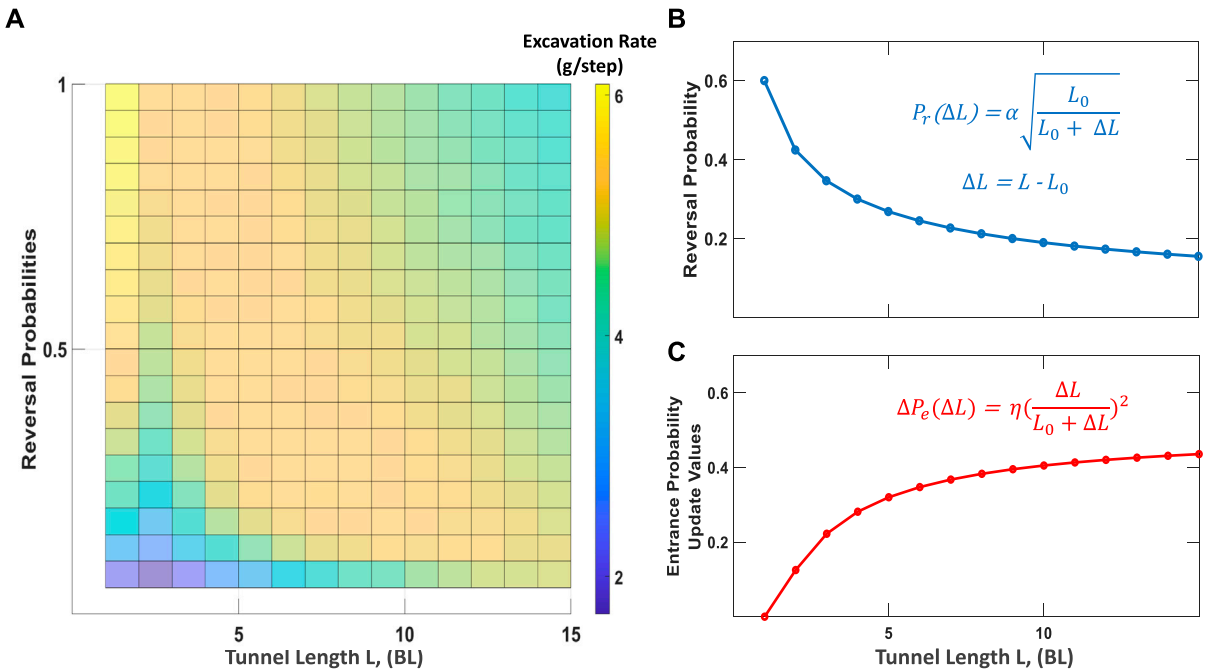

FIGURE 3 | Probability sweep over tunnel length with selected equation models. **(A)** Reversal probability sweep vs. Tunnel length. Plot shows that high to medium reversal probabilities give the highest excavation rate for short tunnels, while low reversal probabilities give the highest excavation rates for long tunnels **(B)** Selected equation for modelling Reversal probabilities as a function of tunnel length for multi-robot experiments **(C)** Learning update value for Entrance probabilities as a function of tunnel length for multi-robot experiments.

Reversal probability function, $P_r(\Delta L)$, that decreases sub-linearly as the tunnel length grows (**Figure 3B** and **Eq. 1** below).

Additionally, ant excavation studies and CA model analysis reveal that an asymmetric or unequal workload distribution improves excavation performance in confined conditions [12, 24]. To attempt to incorporate this principle/strategy in our robophysical system, we develop a self-reinforcement protocol where we model the digging desire of individual robots with a probability P_e, called the "tunnel entrance probability", and update its value based on if a digging attempt performed by a robot was successful (increase P_e by a constant), or unsuccessful (decrease P_e by a constant). Preliminary results showed that this protocol consistently produced an unequal workload distribution with better excavation performance than the Reversal protocol in long tunnels (~10BL). However, this was not the case for short tunnels. Unequal workload strategy did not perform better when the tunnel was short ($<$ 4BL). To account for this phenomenon, we crafted an adaptive "update value" function, ΔP_e, (**Figure 3C** and **Eq. 2** below, which has a small update value when the tunnel is short. We call this the Adaptive Protocol. That is, our adaptive protocol modifies the digging desire of individual robots by using egocentric estimates of the change in tunnel length to update individuals' entrance probability values.

Intuitively, the Adaptive protocol (*via* **Eqs 1**, **2**) suggest that the cost of "giving up" due to collisions (high density) at longer tunnels is substantial, and the strategy to minimize congestion is by deploying fewer workers to dig, or equivalently, more workers to rest. That is, long-duration clogging is more likely to occur in longer tunnels than in short tunnels due to the cascaded effects of multi-body collisions propagated as the robots or ants flow into the tunnel simultaneously. Our adaptive protocol addresses this issue by having the robots modify their entrance probabilities slowly first at the initial stage of digging, then more rapidly at the later stage (**Eq. 2**). ξ is a parameter added to ensure that a resting robot does not remain in resting mode indefinitely (i.e. that P_e does not go to zero) allowing robots to explore their environment, update their estimates of the change in tunnel length, and modify their behaviors if necessary.

$$P_r(\Delta L) = \alpha \sqrt{\frac{L_0}{L_0 + \Delta L}} \tag{1}$$

$$P_e(k, \Delta L) = \begin{cases} P_e(k-1) + \eta \Delta P_e(\Delta L) & \text{if successful trip} \\ P_e(k-1) - \eta \Delta P_e(\Delta L) & \text{if unsuccessful trip} \\ P_e(k-1) + \xi & \text{otherwise (resting)} \end{cases} \tag{2}$$

where:

$\Delta P_e(\Delta L)$ = entrance probability update value
L_0 = initial tunnel length (in robot body lengths)
ΔL = change in tunnel length
ξ = noise or exploration term
α = normalizing constant for reversal probability
η = normalizing constant for tunnel entrance update

and $\Delta P_e(\Delta L) = (\frac{\Delta L}{L_0 + \Delta L})^2$.

The power law expressions of **Eqs 1**, **2** are simple forms that yield the desired behaviors, i.e. rapid change in the reversal and update values

at short tunnels and slow/gradual change at long tunnels (**Figures 3B,C**). Other power law exponents can also be used and will likely result in various degrees of performance gains, as long as the exponent is < 1 for the reversal probability and > 1 for entrance probability update. **Eq. 2** takes a positive sign if the robot is able to get pellets home (successful trip), otherwise it takes a negative sign (unsuccessful trip).

Each time a robot reaches the digging area and excavate pellets, it updates its estimate of the change in tunnel length, ΔL as follows:

$$L(k) = L(k-1) + \gamma\big(L(k)' - L(k-1)\big) \tag{3}$$

$$\Delta L = L(k) - L_0 \tag{4}$$

where:

$L(k)'$ = new measurement of the tunnel length, derived from robot odometry (or dead − reckoning) using the wheel encoder readings.
$L(k)$ = estimate of the tunnel length, averaged over old and new measurements.
$L(k-1)$ = updated value of the tunnel length during the last successful trip
γ = the weighting parameter or learning rate.

A new measurement of the tunnel length, $L(k)'$, is computed when a robot successfully reaches the digging site and excavates pellets. At this time, the tunnel length is derived from the x-component of the robot's location as computed by the robot odometry [32]. The robots use the kinematic model of a differential drive mobile robot based on wheel encoder counts to estimate their absolute displacements in the tunnel. The derivation is provided in the **Supplemental Section**. **Eq. 3** above is an exponential moving average formula that acts as a filter for the estimate of the tunnel length which is used to compute P_r and P_e. It has an important application of reducing noise in a robot's estimate of the tunnel length which might occur when the robots are in multiple collisions. We chose our value of γ to be 0.9 which results in good performance for our experiments. Each robot maintains a separate copy of the equations and updates $P_e(k)$, $P_r(k)$ and ΔL asynchronously according to Algorithm 1 described below.

Algorithm 1: Adaptive Learning Rule Pseudocode.

```
Initialize: k=1, T_r = 60, P_e(k) = 1.0 , P_r(k) = α;
Set experiment duration, T ;
while t < T do
    Sample p ~ U(0, 1) ;
    if p < P_e(k) then
        Goto dig (Active Mode);
        if Contact with a robot then
            Sample q ~ U(0, 1) ;
            if q < P_r(k) then
                Exit tunnel (Give up);
            else
                Continue going to dig;
            end
        else
            Continue going to dig;
        end
        if Robot grabs pellets then
            L(k) = L(k − 1) + γ (L(k)' − L(k − 1)) ;
            ΔL = L(k) − L_0 ;
            Exit tunnel;
        else
            Continue going to dig;
        end
        if Robot gets home with pellets then
            P_e(k) = P_e(k − 1) + η (ΔL / (L_0 + ΔL))^2 ;
        else
            P_e(k) = P_e(k − 1) − η (ΔL / (L_0 + ΔL))^2 ;
        end
        P_r(k) = α sqrt(L_0 / (L_0 + ΔL)) ;
    else
        Rest for T_r seconds (Resting Mode);
        P_e(k) = P_e(k − 1) + ξ;
    end
    k = k + 1;
end
```

The complexity of Algorithm 1 is proportional to the total number of states, S, that the robot visits during an excavation trip. This is denoted as $O(S)$ using the big-O notation. The best-case scenario occurs when the robot does not encounter any collisions but travels from the home area to the digging site and back with pellets. This is likely to occur when there are a few robots in the tunnel and the time to complete a trip (i.e., one pass of the algorithm) is relatively short. On the other hand, the worst-case scenario occurs when the robot encounters and handles collisions in all the states, since collision handling is considered an "intermediate" state (see **Figure 2**). In either case, the amortized run time complexity of the algorithm is O(1) since the number of possible states is bounded and does not depend on any input. Similarly, the space complexity is O(1) since the memory space is fixed and does not grow or depend on any input.

3 EXPERIMENT

We implemented the Adaptive protocol on our physical robots to compare its performance with the Active and Reversal protocols. Unlike in our previous robophysical experiments [12] in which tunnel length and digging probabilities did not change during excavation, here we conducted experiments in which the tunnel increased in length as the robots excavated the granular media (pellets). This both better models growth of tunnels in biological collective excavation [12, 21, 24] and demonstrates how our learning scheme can adapt to dynamic and non-stationary environments. **Figure 4** shows three snapshots of the robot experiment setup.

Because of limitations in the robot's excavation performance per trip, we conducted experiments in the following scheme: initially, the granular media was positioned at one body length in the tunnel ($L_0 = 1$). To model a tunnel increasing in length, the pellets were moved backwards incrementally by one body-length each time the robots made a cumulative deposit increment of 300 g (a camera positioned above a weighing scale recorded the weight of total pellets excavated by the robots). The robots can estimate the tunnel length with a calculation of distance traveled as reported by their wheel encoders (**Figure 1**), and update their reversal and entrance probabilities according to **Eqs 1**, **2** respectively.

At the start of each trial and for each protocol, the entrance probability of the individual robot is set to 1. This ensures that all robots are active and will thus interact with the environment. For the Active and Reversal protocols, the entrance probability remains fixed throughout the duration of the experiment, while for the Adaptive protocol, the entrance probability changes approximately as the inverse square of the tunnel length (**Eq. 2**). This update rule ensures that the robots become less active as the tunnel length increases. Hence, the workload should go from equal to unequal. The η parameter is chosen to ensure that unsuccessful robots decide to rest more often when the tunnel is long, so as to not hinder the performance of the robots that can reach the digging area. If a robot samples from the entrance probability and decides to rest, it navigates to the Resting area and rests for 1 minute. When the resting time is over, the robot samples from the entrance probability again to determine if it should continue to rest or to re-enter the tunnel to dig (**Figure 2**).

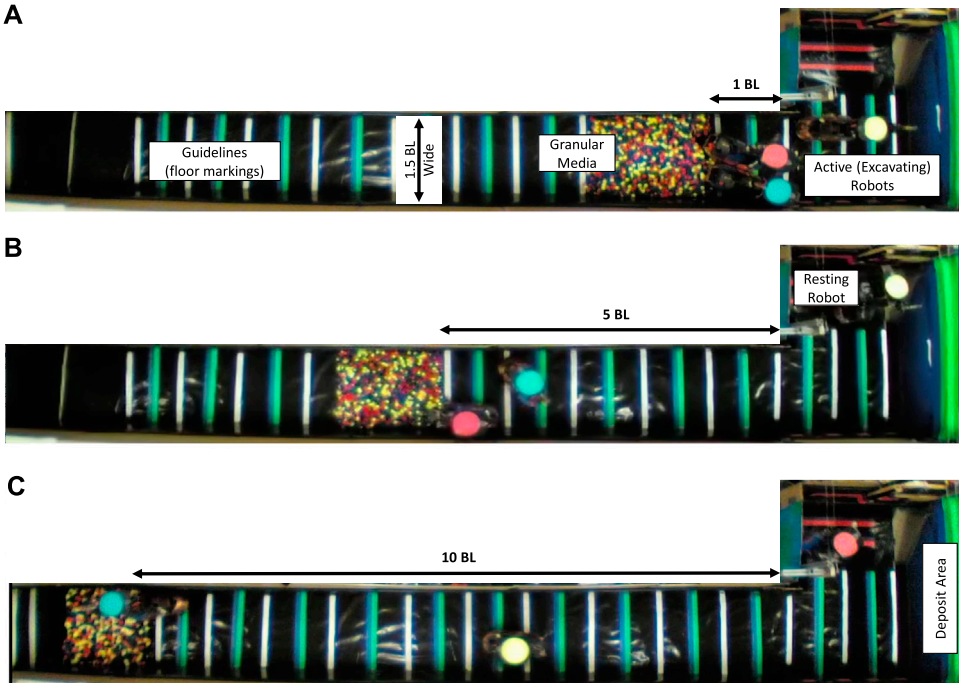

FIGURE 4 | Three snapshots of the top view of multi-robot excavation experiments. **(A)** Pellets at one body-length (1BL) of the tunnel which is the initial position of the pellets at the beginning of each trial, **(B)** pellets at five body-length (5BL) of the tunnel after robots have excavated 1200 g of pellets, **(C)** pellets at ten body-length (10BL) of the tunnel after robots have excavated 2700 g of pellets.

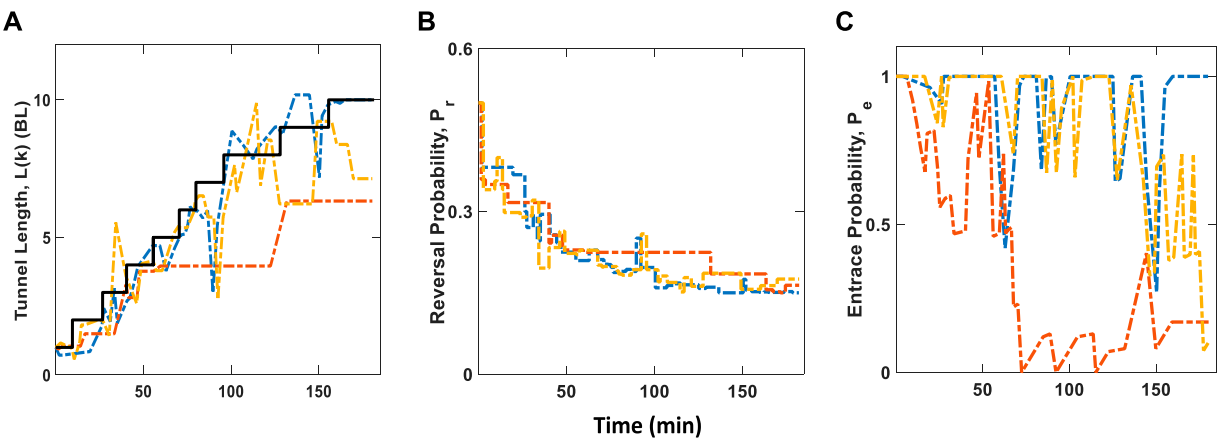

FIGURE 5 | Estimated tunnel length, $L(k)$, Reversal probability, P_r, and Entrance probability, P_e over time for individual robots based on Adaptive rule. Dashed colored lines represent robot A (red), robot B (blue), and robot C (yellow). Solid black line represents actual tunnel length measurement **(A)** Plot shows how individual robots track the actual growing tunnel, based on dead-reckoning method and exponential moving average formula described in **Eq. 3. (B)** Reversal probability values for individual robots as a function of time. These curves closely match the curve described in **Figure 3B (C)** Plot of the entrance probability values over time. This shows how robots initially started off with equal digging "desires" and gradually become unequal "desires" as the tunnel length grows.

For the Reversal protocol, a fixed reversal probability of 0.8 was used for all the robots in all trials. Prior multi-robot experiments demonstrated that such a high reversal probability regulated congestion better than a lower value. For the Adaptive protocol, however, it is desired that the reversal probability drops rapidly for tunnels less than 5BL and saturates quickly for tunnels greater than 5BL. The value of the α parameter–which controls the maximum and minimum values of the reversal probability for the robot experiment–is set to 0.6 which is within the range of values suggested by the parameter sweep plot of **Figure 3A**.

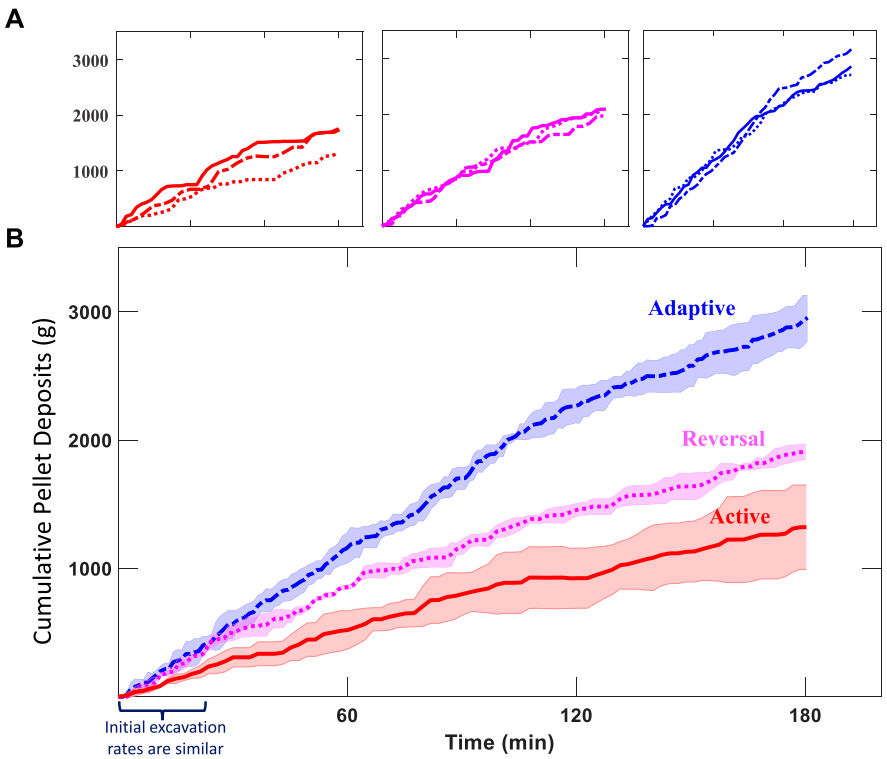

FIGURE 6 | Excavated Pellets vs. Time for three different protocols. Active protocol: all robots have an entrance probability of 1.0 but a reversal probability of 0; Reversal protocol: all robots have an entrance probability of 1.0 and reversal probability of 0.8; Adaptive rule: entrance probability is a function of inverse square of tunnel length, while reversal probability is a function of inverse square-root of tunnel length. **(A)** Individual trial comparison of excavation experiments **(B)** Mean excavated pellets, shaded areas correspond to standard deviation from three experiments.

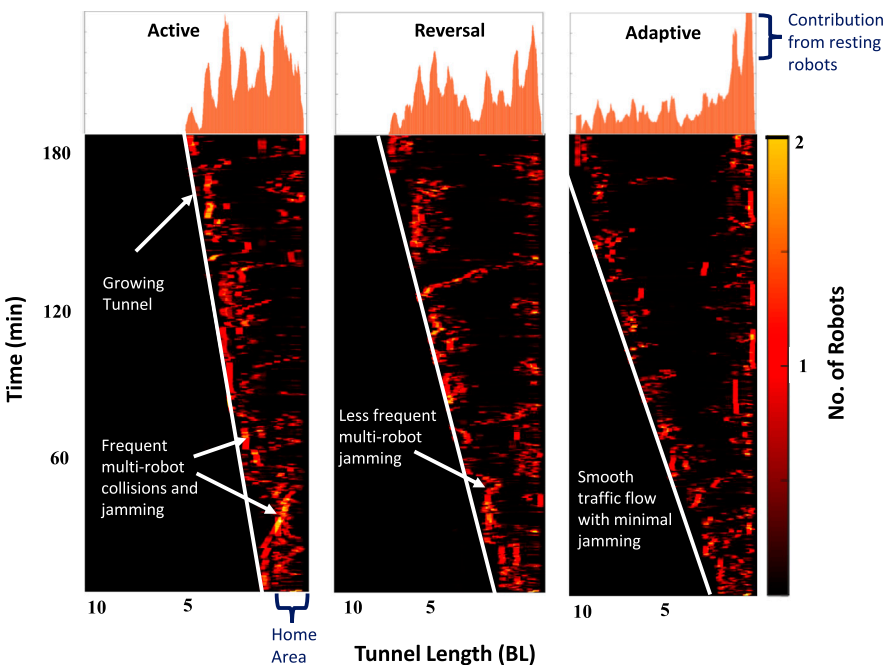

FIGURE 7 | Experimental space-time overlap heat maps of robot positions along the tunnel (x-axis) measured in body-lengths (BL). Y-axis is the time duration of the experiment in minutes. White straight lines show how fast the tunnel grows which depends on the running protocol in the robots. Robots start from the Home area (right side) and transit to the Digging area (left side) continuously while excavating the pellets.

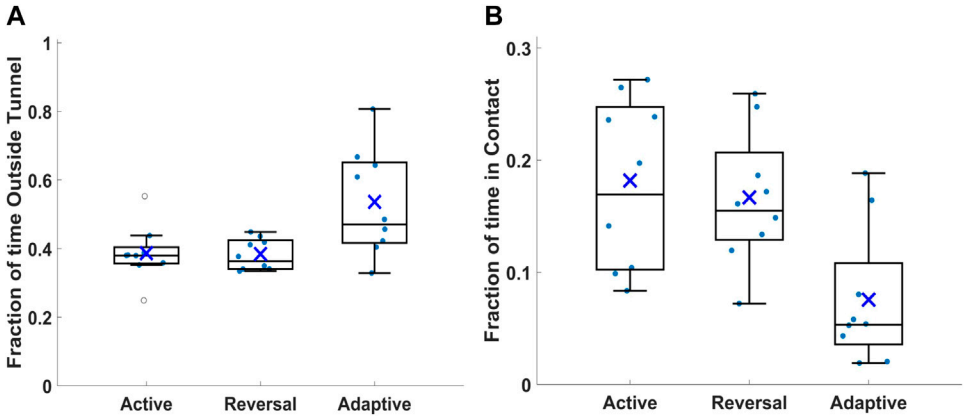

FIGURE 8 | Time spent in various states by individual robots, for the three protocols: Active, Reversal and Adaptive. **(A)** Time spent at the resting and deposition areas **(B)** Time spent in contact with other robots while in the tunnel. Boxes span 25th to 75th percentile, whiskers are between the minimal and maximal values, inner line is the median, × for means, and circles (solid and empty) represent actual data points.

4 RESULTS

In our robot collectives, we implemented the three different protocols and ran three trials for each protocol. Each trial was conducted for 3 h; this duration is set by the capacity on the power-pack of the robots and ensures sensors and actuators are running effectively. The results of these trials are summarized in **Figures 6–9**.

Figure 5 shows the estimated tunnel length, $L(k)$, reversal probabilities, P_r, and entrance probabilities, P_e, for individual robots based on Algorithm 1. **Figure 5A** is the plot of $L(k)$ vs. time which the robots use to estimate the change in tunnel length, ΔL, according to **Eqs 3**, **4**. Since new estimates of tunnel length, $L(k)'$, are derived from the x-component of an individual robot's odometry, it is important to note that wheel slippage can occur when a robot is simultaneously turning and undergoing a collision. This will likely introduce noise in the estimate of the tunnel length, as shown by the fluctuations in the plots of **Figure 5A**. However, the moving average formula of **Eq. 3** will ensure its effect is minimized. In addition, the propagation of noisy measurements is minimized by having the robots reset their odometry measurements at the beginning of each trip, i.e. just before a robot re-enters the tunnel. **Figure 5B** shows that the reversal probability tracks the desired power law expression of **Eq. 1** and **Figure 3B**. **Figure 5C** illustrates how the P_e or "digging desires" of each robot changes from equal to unequal as a function of time, or equivalently, change in tunnel length.

Figure 6 shows a comparison of the cumulative amount of pellets deposited for the three protocols. **Figure 6A** illustrates that the individual trials with the Adaptive rule yield the highest number of pellet deposits for all trials. The graph shows that all protocols produce similar excavation rates at the initial stages of the experiment before they start to diverge as the tunnel length increases. This confirms that the all protocols and trials started with the same initial conditions, except for the reversal probability values in the case of Adaptive and Reversal protocol.

Figure 7 shows space-time plots of the robot trajectories for one of the three trials. The presence of robots in the tunnel is tracked from video captured by a camera positioned above the tunnel. At each time point, the presence of robots is summed over the width of the tunnel and is represented by a single row in the diagram. The adaptive rule produces the fastest tunnel growth, and the map includes some stationary blocks near the Home area which corresponds to resting robots.

Figure 8 explores the portion of time spent by the individual robots either outside of the tunnel (**Figure 8A**)—in the resting or deposition areas–or in contact with each other, while in the tunnel (**Figure 8B**), for the three protocols. The times are quantified based on the robots horizontal position as tracked in the recorded experiments. In **Figure 8B**, robots are considered in contact with others when the horizontal coordinates are less than a body-length apart. We observe that the average time spent outside of the tunnel is roughly the same for the Active and Reversal protocols, at about 40%, but increases a bit for the Adaptive rule (**Figure 8A**). Notably, the Adaptive rule generates a wider variance, indicating some of the robots spend significantly less time in the tunnel than others. Looking at the time spent in contact (**Figure 8B**), we see a narrower distribution for the Reversal than the Active protocol, demonstrating that the Reversal protocol regulates contact time in most cases. More importantly, there is a clear reduction in the average portion of time spent in contact, using the Adaptive rule, from more than 15% using the other protocols, to about 5%.

Figure 9 compares inequality in workload distribution for the Reversal and Adaptive rules, quantified using Lorenz curves. A Lorenz curve presents the cumulative fraction of work done by a cumulative fraction of the population. This curve is convex by definition and an equal workload distribution appears as a straight line between (0,0) and (1,1) A divergence from this straight line indicates unequal workload distribution, where, for example, half of the population is doing less than half of the work. This measure of divergence is usually quantified by the Gini coefficient, G, defined as the ratio of the area between the

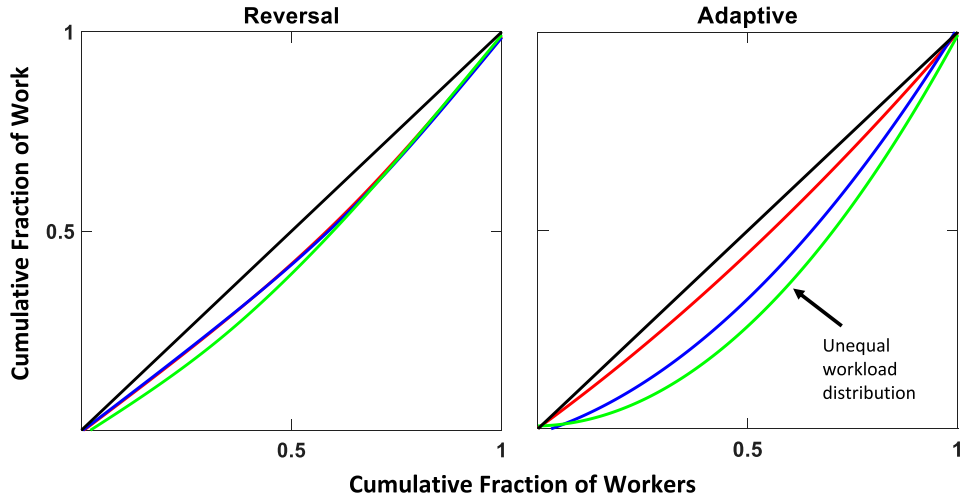

FIGURE 9 | Lorenz curves of robot workload distribution for 1-h "epochs" of 3-h experiment. The curves represent: 1 h duration (red), 2 h duration (blue), and 3 h duration (green). Black solid line represents the line of equality. Cumulative fraction of work is the number of trips the robots took into the tunnel in an attempt to excavate pellets. In Reversal protocol, all robots are mostly inside the tunnel, either going in to excavate pellets or going out to dump or "give-up" and re-enter the tunnel. Adaptive rule on the other hand leads some robots to rest and become less active over time.

Lorenz curve and the line of equality [33]. The curves in **Figure 9** show that the Reversal protocol produces an equal workload distribution with a Gini coefficient of approximately ~0.06. The Adaptive protocol on the other hand produces a strategy that leads to equal workload distribution at short tunnels and unequal workload distribution at long tunnels with a Gini coefficient of ~0.3. This strategy produces the most effective excavation rate in all the experiments. This is smaller than the inequality, in terms of a Gini coefficient, previously reported for ants, of about 0.6 [12], which is due to the larger number of individuals involved in the ant study. Since a tunnel essentially imposes a limit on the number of robots or ants that move through it concurrently without clogging, a larger number of individuals requires a higher degree of inequality to avoid clogging.

5 DISCUSSION

Our results demonstrate that an adaptive strategy, inspired by observations on ant behavior, leads to significant improvements in performance of excavation through a narrow tunnel, by a group of robots.

It was noticed previously that ants are sometimes willing to reverse or "give up", when faced with oncoming traffic [12]. When studied systematically, it was suggested that there is an optimal probabilistic rate for these reversals, which reduces multi-body collisions and jamming events [12]. Indeed, when we implemented probabilistic reversals upon collisions in the robots, we saw improved performance compared to an insistent, non-reversing ("active") behavior (**Figure 6**). Furthermore, our Cellular Automata simulations of the robots suggest that the optimal reversal rate decreases with increasing tunnel length (**Figure 3**), which results from an increase in time wasted working without achieving pellet excavation. When a jam occurs far into the tunnel, a low reversal probability tells the robot not to give up quickly but rather try to resolve congestion locally.

Despite an improvement in performance (**Figure 6**), the willingness to "give up" and reverse did not significantly reduce contacts between the robots in the system when compared with the "active" protocol (**Figure 8**). Ants display another salient collective feature–an unequal workload distribution–which has been demonstrated to improve performance of collective digging in simulation, when compared to an equal workload distribution [12]. We hypothesized that a reinforcement rule employed by the individual robots, governing entrance probabilities P_e (**Figure 2**), could spontaneously result in an unequal workload distribution.

We implemented a reinforcement rule that increases (decreases) the probability to attempt digging with every successful (unsuccessful) digging trip. This reinforcement rule indeed results in the spontaneous formation of unequal participation in digging (**Figure 9**). Our preliminary experiments showed this unequal workload results in reduced performance for short tunnels and increased performance for long tunnels. Taken together with the trend we observed in simulations for optimal reversal rates (**Figure 3**), we decided to implement adaptive rules employed by individual robots, according to the tunnel length, estimated by distance travelled. As a result, an unequal workload distribution emerged that allows them to avoid costly contacts (**Figure 8**) and collectively perform better in an excavation task (**Figure 6**), using noisy estimates (**Figure 5**).

5.1 Relations to Social Insect Collective Dynamics, Active Matter Physics and Swarm Robotics

Given that our work touches on aspects of biological collective behavior, active matter physics and swarm

robotics, we briefly discuss our work in context of these well developed disciplines.

In terms of relation to biology, several studies have revealed that social insects (e.g. ants) modify their individual behaviors in response to specific stimuli experienced in the environment [34–38]. This tendency of individuals to make decisions based on their experience or observation is necessary for organisms' survival and reproduction, and it is termed adaptation or learning [39, 40]. In ants removal of highly active ants from the group results in increased activity by the others [41], suggesting they too use some adaptive strategy. Other studies have also observed adaptation in ant collectives. For example, Buhl et al [42] suggested a feedback model that explains the excavation behavior of ants in a laboratory setting, and Bruce et al [27] suggested that ants use collision information to maintain a desired proximity to others. Thus, we find it reasonable that ants adapt their behaviors based on excavation success which could have a strong relation to collisions (traffic jams) and tunnel length.

Biological systems are known to possess compliant and flexible capabilities which enable them to perform sophisticated maneuvers that are otherwise difficult for their robotic counterparts [43]. For example, Gravish et al [44] studied how antenna deformations provide mechanical support to slipping ants when climbing in confined spaces. Such morphological adaptation of ants makes them excellent excavators in their natural environments [45]. Ants typically generate tunnels that fit about two ant widths and can easily pass each other within them. However, an encounter with three or more ants will take longer to resolve. Our robots also take much longer to resolve 3-robot traffic jams than they do 2-robot collisions, and these become the dominant time cost to be avoided. Thus, strategies for congestion modulation in biological systems may prove applicable in multi-robot real-world scenarios.

In terms of relation of our work to active matter physics, most studies of active matter assume particles remain in a given state (e.g., constant speed movement) and study the global dynamics emerging from such rules. There is typically no "goal" for the global dynamics in such studies. In contrast our system is explicitly "task oriented": from a broad perspective, the system has a mixture of particles with different behaviors that occasionally transition between the different populations (control states) in pursuance of a goal. Thus from a physics perspective it is interesting to ask how desired macroscopic outcomes (e.g., flow of material) must be coupled to microscopic rules which can change in response to macroscopic state (e.g., particles "give up" which detect a slowing of flow). This is particularly interesting in the collisional and dense regimes in part because of challenges for any one agent to know the state of others and active systems must deal with the propensity of such systems to cluster [9, 46, 47], clog and form glassy states [11].

Finally, from a swarm robotics/engineering point of view, while tasks are a critical aspect of making swarms task capable, most work has been conducted in either low density regimes and/or focused on various techniques for collision avoidance [48–52]. This is to ensure safe operation of the robots and to prevent possible catastrophes that may occur in cases of collisions. However, attempting to avoid collisions in crowded and confined conditions could be impractical. This is due to the physical constraint of the environment and/or the uncertainties present in sensor measurements which make collisions inevitable. Even in some cases where accurate measurements are available, the challenges in such environments make robot to be overtly cautious. This conservative behavior would make the robots spend most of their time avoiding collisions rather than advancing the mission of the group.

Recently, researchers have studied scenarios involving small mass and low velocity robots where mild collisions and contacts can be tolerated. In this case, collision can be used as a sensing modality to estimate the state of the environment. For example, [53, 54] developed a probabilistic filtering technique based on inter-robot contacts to localize a team of robots in particular environments. The robots were equipped with binary tactile collision sensors, which provide information for computing the likelihood of a robot to experience collisions in different sections of the environment. In contrast to this, our work uses collisions as a source of reinforcement rather than to estimate the state of the environment. We assume the environment is unknown and dynamic, so our approach can generalize to various scenarios where little domain knowledge is available. This requires our robots to learn to cooperate and adjust to the changes in the environment, including the behavior of other robots, to accomplish their tasks collectively and effectively.

6 CONCLUSION

Active particles performing persistent motion often develop structures consisting of aggregated formations [3–5], especially in confined environments [10–12]. Active matter studies typically involve particles lacking sensing and control that change direction only stochastically. Our robotic system presents a kind of task-oriented active matter, where control is injected to minimize otherwise unavoidable aggregated states and improve collective performance. In this work, collective performance is measured as the rate of pellet collection from the tip of an ever-extending tunnel. This imposed task compels our robots to traverse the entire length of the system (tunnel), to and fro, while encountering any other robot already in it.

Unlike uncontrolled particles, the robots studied here do not stochastically change direction. In fact, when impeded by another robot, they first attempted to maneuver around the robot to continue on their way. This behavior facilitates a "greedy" attempt to maximize individual performance, at the expense of the collective one, and exacerbates formation of aggregates (**Figure 7** and **Figure 8**). On the other hand, we demonstrated that robots can limit time wasted on this persistence through probabilistic reversal, which generates some collective performance gains (**Figure 6**). However, aggregates still form and are expected to increase in frequency with collectives larger than those studied here.

Even in our relatively small groups of robots, to achieve high collective performance that is robust to a changing environment and possibly to group size, we developed a learning control scheme that uses collisions as an information source, which are a noisy proxy for number density in the system. In

robotics, collisions are often viewed as problematic occurrences to be avoided, whereas, they could be an important aspect in the lives of social insects, given the constraints and challenges of their environments. Collisions could serve as fundamentally important information sources that can be harnessed to coordinate the activities of individuals so as to achieve the common goal of the group.

In our multi-robot scenario, we achieved coordination for effective excavation performance by modifying individual robot's response to collision and task desires based on an independent estimate of the tunnel length. We discovered that "giving up", while sacrificing the individual performance, often contributes to the collective performance. We demonstrated that a learning rule that modulates both "giving up" rate and "individual desires" gives a significantly higher group performance than with maladaptive behaviors (**Figure 6**). This technique could be applied to real world scenarios where collisions or physical interactions are unavoidable, or in decentralized task-oriented physical systems where individuals in a group must interact via contacts. We suspect social insects also make good use of collisions to modulate their decision making, in service of a collective goal.

DATA AVAILABILITY STATEMENT

The raw data supporting the conclusions of this article will be made available by the authors, without undue reservation.

AUTHOR CONTRIBUTIONS

KA, H-SK, MB, and DG devised the project, algorithm and experiments. KA developed the robots, algorithms and performed the experiments. KA and RA performed data analysis. KA, RA, MG, and DG contributed to the writing of the manuscript. H-SK, MB, MG, and DG provided insightful discussions and support.

FUNDING

Funding for this research provided by ARO MURI award W911NF-19-1-023, NSF Grant PHY-1205878, NSF Grant IOS-2019799 to MG and DG, and NSF Grant DMR-1725065 to MB.

ACKNOWLEDGMENTS

We are grateful to Andrea W. Richa and Joshua Daymude of Arizona State University for their helpful discussions.

SUPPLEMENTARY MATERIAL

The Supplementary Material for this article can be found online at: https://www.frontiersin.org/articles/10.3389/fphy.2022.735667/full#supplementary-material

REFERENCES

1. Vicsek T, Czirók A, Ben-Jacob E, Cohen I, Shochet O. Novel Type of Phase Transition in a System of Self-Driven Particles. *Phys Rev Lett* (1995) 75: 1226–9. doi:10.1103/physrevlett.75.1226
2. Vicsek T, Zafeiris A. Collective Motion. *Phys Rep* (2012) 517(3):71–140. doi:10.1016/j.physrep.2012.03.004
3. Michael E. Cates and Julien Tailleur. Motility-Induced Phase Separation. *Annu Rev Condensed Matter Phys* (2015) 6(1):219–44.
4. Geyer D, Martin D, Tailleur J, Bartolo D. Freezing a Flock: Motility-Induced Phase Separation in Polar Active Liquids. *Phys Rev X* (2019) 9(3):031043. doi:10.1103/physrevx.9.031043
5. O'Byrne J, Alexandre S, Tailleur J, Zhao Y. An Introduction to Motility-Induced Phase Separation. *arXiv:2112.05024v1* (2021).
6. Ramaswamy. S. The Mechanics and Statistics of Active Matter. *Annu Rev Condens Matter Phys* (2010) 1(1):323–45. doi:10.1146/annurev-conmatphys-070909-104101
7. Dey S, Das D, Rajesh R. Spatial Structures and Giant Number Fluctuations in Models of Active Matter. *Phys Rev Lett* (2012) 108:238001. doi:10.1103/physrevlett.108.238001
8. Ginelli F. The Physics of the Vicsek Model. *Eur Phys J Spec Top* (2016) 225(11-12):2099–117. doi:10.1140/epjst/e2016-60066-8
9. Marchetti MC, Joanny JF, Ramaswamy S, Liverpool TB, Prost J, Rao M, et al. Hydrodynamics of Soft Active Matter. *Rev Mod Phys* (2013) 85:1143–89. doi:10.1103/revmodphys.85.1143
10. Helbing D. Traffic and Related Self-Driven many-particle Systems. *Rev Mod Phys* (2001) 73:1067–141. doi:10.1103/revmodphys.73.1067
11. Gravish N, Gold G, Zangwill A, Goodisman MAD, Goldman DI. Glass-like Dynamics in Confined and Congested Ant Traffic. *Soft Matter* (2015) 11(33): 6552–61. doi:10.1039/c5sm00693g
12. Aguilar J, Monaenkova D, Linevich V, Savoie W, Dutta B, Kuan H-S, et al. Collective Clog Control: Optimizing Traffic Flow in Confined Biological and Robophysical Excavation. *Science* (2018) 361(6403):672–7. doi:10.1126/science.aan3891
13. Garcimartín A, Pastor JM, Ferrer LM, Ramos JJ, Martín-Gómez C, Zuriguel I. Flow and Clogging of a Sheep Herd Passing through a Bottleneck. *Phys Rev E - Stat Nonlinear, Soft Matter Phys* (2015) 91(2):1–7.
14. Abdelkader M, Güler S, Jaleel H, Shamma JS. Aerial Swarms: Recent Applications and Challenges. *Curr Robot Rep* (2021) 2(3):309–20. doi:10.1007/s43154-021-00063-4
15. Schranz M, Umlauft M, Sende M, Elmenreich W. Swarm Robotic Behaviors and Current Applications. *Front Robotics AI* (2020) 7:36. doi:10.3389/frobt.2020.00036
16. Li S, Dutta B, Cannon S, Daymude JJ, Avinery R, Aydin E, et al. Programming Active Cohesive Granular Matter with Mechanically Induced Phase Changes. *Sci Adv* (2021) 7(17):eabe8494. doi:10.1126/sciadv.abe8494
17. Slavkov I, Carrillo-Zapata D, Carranza N, Diego X, Jansson F, Kaandorp J, et al. Morphogenesis in Robot Swarms. *Sci Robot* (2018) 3(25):eaau9178. doi:10.1126/scirobotics.aau9178
18. Reynolds CW. Flocks, Herds and Schools: A Distributed Behavioral Model. *SIGGRAPH Comput Graph* (1987) 21:25–34. doi:10.1145/37402.37406
19. Gordon DM. The Rewards of Restraint in the Collective Regulation of Foraging by Harvester Ant Colonies. *Nature* (2013) 498(7452):91–3. doi:10.1038/nature12137
20. Gordon DM. The Ecology of Collective Behavior in Ants. *Annu Rev Entomol* (2019) 64:35–50. doi:10.1146/annurev-ento-011118-111923
21. Gravish N, Garcia M, Mazouchova N, Levy L, Umbanhowar PB, Goodisman MAD, et al. Effects of Worker Size on the Dynamics of Fire Ant Tunnel Construction. *J R Soc Interf* (2012) 9(77):3312–22. doi:10.1098/rsif.2012.0423
22. Cassill D, TschinkelTschinkel WR, Vinson SB. Nest Complexity, Group Size and Brood Rearing in the Fire Ant, solenopsis Invicta. *Insectes Sociaux* (2002) 49(2):158–63. doi:10.1007/s00040-002-8296-9
23. Gordon DM. The Organization of Work in Social Insect Colonies. *Nature* (1996) 380(6570):121–4. doi:10.1038/380121a0

24. Monaenkova D, Gravish N, Rodriguez G, Kutner R, Goodisman MAD, Goldman DI. Behavioral and Mechanical Determinants of Collective Subsurface Nest Excavation. *J Exp Biol* (2015) 218(9):1295–305. doi:10.1242/jeb.113795
25. Narayan V, Ramaswamy S, Menon N. Long-lived Giant Number Fluctuations in a Swarming Granular Nematic. *Science* (2007) 317(July):105–8. doi:10.1126/science.1140414
26. Janssen LMC. Active Glasses. *J Phys Condens Matter* (2019) 31(50):503002. doi:10.1088/1361-648x/ab3e90
27. Bruce AI, Pérez-Escudero A, Czaczkes TJ, Burd M. The Digging Dynamics of Ant Tunnels: Movement, Encounters, and Nest Space. *Insect Soc* (2019) 66(1):119–27. doi:10.1007/s00040-018-0657-0
28. Sasaki H, Leung H-f. Trail Traffic Flow Prediction by Contact Frequency Among Individual Ants. *Swarm Intell* (2013) 7(4):307–26. doi:10.1007/s11721-013-0085-8
29. Gordon DM. Movement, Encounter Rate, and Collective Behavior in Ant Colonies. *Ann Entomol Soc America* (2021) 114(5):541–6. doi:10.1093/aesa/saaa036
30. Linevich V, Monaenkova D, Goldman DI. Robophysical Study of Excavation in Confined Environments. *Artif Life Robotics* (2016) 21(4):460–5. doi:10.1007/s10015-016-0317-2
31. Panescu D, Dumbrava ş.. Multi-robot Systems: From Finite Automata to Multi-Agent Systems. *IFAC Proc Volumes* (2007) 40(18):121–6. doi:10.3182/20070927-4-ro-3905.00022
32. Ben-Ari M, Mondada F. Robotic Motion and Odometry. In: *Elements of Robotics*. Cham: Springer International Publishing (2018). p. 63–93. doi:10.1007/978-3-319-62533-1_5
33. Paul T, Lutz CC, Rao VD, Goldenfeld N, Robinson GE. Automated Monitoring Reveals Extreme Interindividual Variation and Plasticity in Honeybee Foraging Activity Levels. *Anim Behav* (2014) 95:41–8.
34. Noor MAF. Animal Behavior: An Evolutionary Approach. *BioScience* (1998) 48(10):865–8.
35. Labella TH, Dorigo M, Deneubourg J-L. Division of Labor in a Group of Robots Inspired by Ants' Foraging Behavior. *ACM Trans Auton Adapt Syst* (2006) 1(1):4–25. doi:10.1145/1152934.1152936
36. Feinerman O, Korman A. Individual versus Collective Cognition in Social Insects. *J Exp Biol* (2017) 220:73–82. doi:10.1242/jeb.143891
37. Beshers SN, Fewell JH. Models of Division of Labor in Social Insects. *Annu Rev Entomol* (2001) 46(1):413–40. doi:10.1146/annurev.ento.46.1.413
38. Bonabeau E, Guy T, Deneubourg JL, And G. Quantitative Study of the Fixed Response Threshold Model for the Regulation of Division of Labour in Insect Societies. *Proc R Soc B: Biol Sci* (1996) 263:1565–9.
39. Dukas R. Evolutionary Biology of Insect Learning. *Annu Rev Entomol* (2008) 53(1):145–60. doi:10.1146/annurev.ento.53.103106.093343
40. Papaj DR, Prokopy RJ. Ecological and Evolutionary Aspects of Learning in Phytophagous Insects. *Annu Rev Entomol* (1989) 34:315–50. doi:10.1146/annurev.en.34.010189.001531
41. Charbonneau D, Sasaki T, Dornhaus A. Who Needs 'lazy' Workers? Inactive Workers Act as a 'reserve' Labor Force Replacing Active Workers, but Inactive Workers Are Not Replaced when They Are Removed. *PLOS ONE* (2017) 12(9):e0184074–20. doi:10.1371/journal.pone.0184074
42. Buhl JRM, Deneubourg JL, Grimal A, Theraulaz G. Self-organized Digging Activity in Ant Colonies. *Behav Ecol Sociobiol* (2005) 58(1):9–17. doi:10.1007/s00265-004-0906-2
43. Grimaldi D, Engel MS. *Evolution of the Insects*. Cambridge: Cambridge University Press (2005).
44. Gravish N, Monaenkova D, Goodisman MAD, Goldman DI. Climbing, Falling, and Jamming during Ant Locomotion in Confined Environments. *Proc Natl Acad Sci U.S.A* (2013) 110(24):9746–51. doi:10.1073/pnas.1302428110
45. Nevo E. *Mosaic Evolution of Subterranean Mammals: Regression, Progression, and Global Convergence*. Oxford, UK: Oxford University Press (1999).
46. de Castro P, Diles S, Soto R, Sollich P. Active Mixtures in a Narrow Channel: Motility Diversity Changes Cluster Sizes. *Soft Matter* (2021) 17:2050–61. doi:10.1039/d0sm02052d
47. de Castro P, M. Rocha F, Diles S, Soto R, Sollich P. Diversity of Self-Propulsion Speeds Reduces Motility-Induced Clustering in Confined Active Matter. *Soft Matter* (2021) 17:9926–36. doi:10.1039/d1sm01009c
48. Cai C, Yang C, Zhu Q, Liang Y. Collision Avoidance in Multi-Robot Systems. In: 2007 International Conference on Mechatronics and Automation. Harbin, China: IEEE (2007). p. 2795–800. doi:10.1109/icma.2007.4304002
49. Hennes D, Claes D, Meeussen W, Tuyls K. Multi-robot Collision Avoidance with Localization Uncertainty. In: Proceedings of the 11th International Conference on Autonomous Agents and Multiagent Systems - Volume 1, AAMAS '12. Richland, SC: International Foundation for Autonomous Agents and Multiagent Systems (2012). p. 147–54.
50. Godoy J, Karamouzas I, Guy S, Gini ML. *C-nav : Implicit Coordination in Crowded Multi-Agent Navigation* (2016).
51. Long P, Fan T, Liao X, Liu W, Zhang H, Jia P. Towards Optimally Decentralized Multi-Robot Collision Avoidance via Deep Reinforcement Learning. In: 2018 IEEE International Conference on Robotics and Automation (ICRA). Brisbane, QLD, Australia: IEEE (2018). p. 6252–9. doi:10.1109/icra.2018.8461113
52. Sun D, Kleiner A, Nebel B. Behavior-based Multi-Robot Collision Avoidance. In: 2014 IEEE International Conference on Robotics and Automation (ICRA). Hong Kong, China: IEEE (2014). p. 1668–73. doi:10.1109/icra.2014.6907075
53. Mayya S, Pierpaoli P, Nair G, Egerstedt M. *Collisions as Information Sources in Densely Packed Multi-Robot Systems under Mean-Field Approximations*. Cambridge, MA, USA: Robotics: Science and Systems (2017).
54. Mayya S, Pierpaoli P, Nair G, Egerstedt M. Localization in Densely Packed Swarms Using Interrobot Collisions as a Sensing Modality. *IEEE Trans Robot* (2019) 35(1):21–34. doi:10.1109/tro.2018.2872285

Conflict of Interest: The authors declare that the research was conducted in the absence of any commercial or financial relationships that could be construed as a potential conflict of interest.

Advantages of publishing in Frontiers

OPEN ACCESS
Articles are free to read for greatest visibility and readership

FAST PUBLICATION
Around 90 days from submission to decision

HIGH QUALITY PEER-REVIEW
Rigorous, collaborative, and constructive peer-review

TRANSPARENT PEER-REVIEW
Editors and reviewers acknowledged by name on published articles

Frontiers
Avenue du Tribunal-Fédéral 34
1005 Lausanne | Switzerland

Visit us: www.frontiersin.org
Contact us: frontiersin.org/about/contact

REPRODUCIBILITY OF RESEARCH
Support open data and methods to enhance research reproducibility

DIGITAL PUBLISHING
Articles designed for optimal readership across devices

FOLLOW US
@frontiersin

IMPACT METRICS
Advanced article metrics track visibility across digital media

EXTENSIVE PROMOTION
Marketing and promotion of impactful research

LOOP RESEARCH NETWORK
Our network increases your article's readership